Informational Aspects of Quantum Many-Body Systems

Alexander A. Nico-Katz

A dissertation submitted in partial fulfillment

of the requirements for the degree of

Doctor of Philosophy

of

University College London.

Department of Physics and Astronomy

University College London

July 26, 2023

Dedicated to the memory of my grandfather

I, Alexander A. Nico-Katz, confirm that the work presented in this thesis is my own. Where information has been derived from other sources, I confirm that this has been indicated in the work.

Abstract

The prevailing theme of modern quantum many-body physics is circumscribed by the question: are such systems useful? Can we use them to simulate something, or compute the answer to a problem? Despite this, information-theoretic analyses of quantum many-body systems are rare. This thesis seeks to address that by investigating informational aspects of problems that might be conventionally delegated to the condensed matter community.

I start by investigating 'local memory' in systems that exhibit some form of ergodicity-breaking. A quantitative investigation of how much information is actually retained, and whether or not that information can be accessed, is lacking in this context. I introduce an information-theoretic framework and a criteria by which 'local memory' can be quantitatively defined. I analyze many-body localized (MBL) and quantum scarred systems; both touted to exhibit local memory.

I then investigate entanglement complexity in terms of how compressible a representation of a given state is. I propose a novel kind of geometric entanglement in terms of matrix-product state representations of fixed bond dimension. This representation is more efficient than storing the full state, and so gives an indication of how much information is needed to reconstruct it. By analysing ground state phase diagrams and the ergodic-to-MBL transition, I find that this quantity is exceedingly effective when employed to detect phase boundaries, even in systems where the phases are not known a priori.

Finally, I investigate systems which are informed by the capabilities of current-generation experimental devices. I first consider whether MBL is accessible in quantum dot arrays by investigating the properties of the von Neumann entropy, im-

balance, and number entropy. I then consider phase crossovers in twin-rail quantum dot devices using the statistics of singlet-triplet profiles and the fidelity susceptibility. Finally, I consider idle information loss in an interacting transmon array which simulates IBM's quantum computers.

Impact Statement

Quantum technologies form the backbone of a vast academic-industrial complex. The scope of this complex includes, inter alia: research groups, international initiatives, banks, and private enterprise - all with a vested interest in quantum technology. These interests are in turn backed up by government funding, charities, privately held wealth, and hedge funds. Thus, any quantum research - including my own - cascades through society with far-reaching effects. I here address three sectors impacted by my work: academic, industrial, and socio-ethical.

Academic Impact - The main academic impact of my PhD takes the form of a foundational toolbox: clearly realized techniques for analysing information in realistic condensed matter systems. This impact is incarnate as several publications, with my paper on memory being particularly well-cited. I have also spoken on these topics at two international conferences, and as an invited speaker at Trinity College Dublin. Specific examples include my work on memory in many-body localized systems. This idea of memory was long suspected in the literature, but I provided the first well-founded, information-theoretic investigation thereof. I also identified a gap in the literature - geometric measures of entanglement are founded on separability, which is not a useful perspective to have in many condensed matter systems - and constructed an novel tool to address it.

Industrial Impact - The industrial impact of my work is mainly restricted to the - admittedly large and growing - sector of quantum computing. My work can be applied *in situ* to characterize information flow in existing devices. A widespread application of the techniques I develop in this thesis can also improve information retention in and thus efficiency of quantum technologies in general. My work also

introduces the notion of the 'accessible information game' into condensed matter contexts - which serves as an important stepping stone for developing quantum communication technology. This may eventually have ramifications in terms of global health, energy, and cybersecurity.

Societal and Ethical Impact - The positive societal impact of my research are a distant horizon of potential applications in health, energy, communication, and security. Conversely a technological horizon is ever rife with opportunities to exploit and oppress; and my work in accelerating the realization of this horizon could lead to a poorer understanding of its societal and legislative implications. Regardless, these eventualities are decades away and it is thus tempting to claim that my work is ethically and socially neutral. However: machines we are currently building require the wholesale exploitation of dangerous, unregulated, and often slave labour in e.g. the extraction of rare metals. The texture of daily academic culture is woven of exploitative labour and the cruel treatment of marginalized members of our community - evidenced by dozens of conversations with my colleagues. Societal benefits that my work *may* bring *in the future* do not offset the cruelties that it menaces *today*. I do not have the luxury to claim that my work is ethically neutral. It is not. Thus, I have given a substantial portion of my time during my PhD to community building within the department; as well as widespread and ongoing diversity and inclusivity work, and climate action. The impact this has had is underlined by funding awards from the university, and by exceptional local turnout to events. I will remain vigilant about these aspects of my work as long as I am yet living.

Acknowledgements

A multitude of people have supported me throughout this chapter of my life, and without their collective kindness, insight, and help, this thesis would not exist; and I would be a person far poorer in spirit.

First and foremost, I would like to extend my dearest thanks to my supervisor Prof. Sougato Bose, who has been a constant source of insight, knowledge, and guidance. I value deeply his calm yet joyful attitude towards our work, his consistent kindness to me and to other members of this community, and his ardent support of my independent work. My experience as a member of his group has shaped not only the kind and quality of physicist that I have become, but also the values that I hold important as a member of the wider scientific community.

I want to dearly thank my collaborator Prof. Abolfazl Bayat, who taught me so much in my first year and who guided me through my first two papers. In addition I'd like to thank my collaborators Dr. Gulzat Jaliel, Prof. Charles Smith, Prof. John Goold, Dr. Shane Dooley, Liza Morozova, Dr. Xin Zhang, and Prof. Lieven Vandersypen who have taken a consistent interest in my work, and who have been excellent sources of ideas and physics-related coffee (and remote) chats.

I would like to thank Saad Shaikh for being one of my best friends, and one of my most adamant supporters in the department. As my comrade in arms when it comes to diversity and inclusivity work: I can honestly say that my friendship with him has rendered me a more empathetic and decent human. I also want to thank Pete Bradshaw, who presents as a genius-labrador hybrid, but is in fact an excellent friend. We'll make the project work one day, I swear. Thanks as well to Prof. Sergey Yurchenko and the entire PandA team, for all the fun we've had and

the good we've done while having it.

I'd also like to thank Sergey, Jonathan, Tony, Charles, and everyone in the EXOMOL group who have welcomed me unquestioningly into their group's Friday after-work drinks. I still don't really know what any of you actually do. Something similar goes to all the people in HEP who have broadened my horizons, and my cocktail proclivities; in particular my good friends Fern, Veera, Sim, and Abi. Finally I want to thank my friends in Sougato's group: Dylan, Daniele, Roopayan, Eva, Farhan, Bin, and Debarshi.

To my family: my parents and brother and sisters and uncles and aunts and cousins, I love you deeply, even if we should all try and see each other a little more. For my mum, who is an eternally supportive source of adventure and inspiration. For my dad, who is a colourful and kind man who I have valued reconnecting with. I want to thank my Savta for her strength and kindness, for the excellent conversation, for taking a deep and genuine interest in my values and my life, and - in the words of my uncle - for feeding me.

Thanks to Cass for being Cass, for the chaos, and for eternally encouraging me to be me. Thanks to Shana for the wild dispossession, the art and the fire, and all the good coffee chats, and all the good book recommendations. Thanks to FAMILILY, I love you all so much more than I can possibly say. And thanks to Isolde, James, Jacob, Max, and Clare; for all the joy we've shared and will share.

For Ali, there's not much that I can write here that I haven't already inscribed on the inside cover of some other book elsewhere. Thank you for sharing the past few years of my life with me. You're my best friend, and I love you.

UCL Research Paper Declaration Form: referencing the doctoral candidate's own published work(s)

1. **For a research manuscript that has already been published** (if not yet published, please skip to section 2)**:**

   (a) **What is the title of the manuscript?** Information-theoretic memory scaling in the many-body localization transition

   (b) **Please include a link to or doi for the work:** 10.1103/PhysRevB.105.205133

   (c) **Where was the work published?** Physical Review B

   (d) **Who published the work?** American Physical Society

   (e) **When was the work published?** 25 May 2022

   (f) **List the manuscript's authors in the order they appear on the publication:** Alexander Nico-Katz, Abolfazl Bayat, and Sougato Bose

   (g) **Was the work peer reviewed?** Yes

   (h) **Have you retained the copyright?** No

   (i) **Was an earlier form of the manuscript uploaded to a preprint server (e.g. medRxiv)? If 'Yes', please give a link or doi** Yes, DOI: 10.48550/arXiv.2009.04470

   If 'No', please seek permission from the relevant publisher and check the box next to the below statement:

   ☐ *I acknowledge permission of the publisher named under 1d to include in this thesis portions of the publication named as included in 1c.*

2. **For a research manuscript prepared for publication but that has not yet been published** (if already published, please skip to section 3)**:**

   (a) **What is the current title of the manuscript?** N/A

   (b) **Has the manuscript been uploaded to a preprint server 'e.g.**

medRxiv'?

If 'Yes', please please give a link or doi: N/A

(c) **Where is the work intended to be published?** N/A

(d) **List the manuscript's authors in the intended authorship order:** N/A

(e) **Stage of publication:** N/A

3. **For multi-authored work, please give a statement of contribution covering all authors** (if single-author, please skip to section 4)**:** All authors contributed equally to the inception and development of the ideas contained within the work. ANK carried out all numerics and plotting. ANK and AB co-wrote the manuscript, with SB contributing to the introductory and concluding sections.

4. **In which chapter(s) of your thesis can this material be found?** Chapter 2

e-Signatures confirming that the information above is accurate (this form should be co-signed by the supervisor/ senior author unless this is not appropriate, e.g. if the paper was a single-author work)**:**

Candidate:

Date:

Supervisor/Senior Author signature (where appropriate)**:**

Date:

UCL Research Paper Declaration Form: referencing the doctoral candidate's own published work(s)

1. **For a research manuscript that has already been published** (if not yet published, please skip to section 2)**:**

   (a) **What is the title of the manuscript?** Memory hierarchy for many-body localization: Emulating the thermodynamic limit

   (b) **Please include a link to or doi for the work:** 10.1103/PhysRevResearch.4.033070

   (c) **Where was the work published?** Physical Review Research

   (d) **Who published the work?** American Physical Society

   (e) **When was the work published?** 25 July 2022

   (f) **List the manuscript's authors in the order they appear on the publication:** Alexander Nico-Katz, Abolfazl Bayat, and Sougato Bose

   (g) **Was the work peer reviewed?** Yes

   (h) **Have you retained the copyright?** No

   (i) **Was an earlier form of the manuscript uploaded to a preprint server (e.g. medRxiv)? If 'Yes', please give a link or doi** Yes, DOI: 10.48550/arXiv.2111.01146

   If 'No', please seek permission from the relevant publisher and check the box next to the below statement:

   ☐ *I acknowledge permission of the publisher named under 1d to include in this thesis portions of the publication named as included in 1c.*

2. **For a research manuscript prepared for publication but that has not yet been published** (if already published, please skip to section 3)**:**

   (a) **What is the current title of the manuscript?** N/A

   (b) **Has the manuscript been uploaded to a preprint server 'e.g.**

medRxiv'?

If 'Yes', please please give a link or doi: N/A

(c) **Where is the work intended to be published?** N/A

(d) **List the manuscript's authors in the intended authorship order:** N/A

(e) **Stage of publication:** N/A

3. **For multi-authored work, please give a statement of contribution covering all authors** (if single-author, please skip to section 4)**:** All authors contributed equally to the inception and development of the ideas contained within the work. ANK carried out all numerics and plotting. ANK and AB co-wrote the manuscript, with SB contributing to the introductory and concluding sections.

4. **In which chapter(s) of your thesis can this material be found?** Chapter 2

e-Signatures confirming that the information above is accurate (this form should be co-signed by the supervisor/ senior author unless this is not appropriate, e.g. if the paper was a single-author work)**:**

Candidate:

Date:

Supervisor/Senior Author signature (where appropriate)**:**

Date:

UCL Research Paper Declaration Form: referencing the doctoral candidate's own published work(s)

1. **For a research manuscript that has already been published** (if not yet published, please skip to section 2)**:**

   (a) **What is the title of the manuscript?** Entanglement-complexity geometric measure

   (b) **Please include a link to or doi for the work:** 10.1103/PhysRevResearch.5.013041

   (c) **Where was the work published?** Physical Review Research

   (d) **Who published the work?** American Physical Society

   (e) **When was the work published?** 24 January 2023

   (f) **List the manuscript's authors in the order they appear on the publication:** Alexander Nico-Katz, and Sougato Bose

   (g) **Was the work peer reviewed?** Yes

   (h) **Have you retained the copyright?** No

   (i) **Was an earlier form of the manuscript uploaded to a preprint server (e.g. medRxiv)? If 'Yes', please give a link or doi** Yes, DOI: 10.48550/arXiv.2207.05052

   If 'No', please seek permission from the relevant publisher and check the box next to the below statement:

   ☐ *I acknowledge permission of the publisher named under 1d to include in this thesis portions of the publication named as included in 1c.*

2. **For a research manuscript prepared for publication but that has not yet been published** (if already published, please skip to section 3)**:**

   (a) **What is the current title of the manuscript?** N/A

   (b) **Has the manuscript been uploaded to a preprint server 'e.g.**

medRxiv'?

If 'Yes', please please give a link or doi: N/A

(c) **Where is the work intended to be published?** N/A

(d) **List the manuscript's authors in the intended authorship order:** N/A

(e) **Stage of publication:** N/A

3. **For multi-authored work, please give a statement of contribution covering all authors** (if single-author, please skip to section 4)**:** ANK developed the early ideas contained within this work. Both authors developed and shaped the work. ANK carried out all numerics and plotting and wrote the manuscript, with SB contributing to the introductory and concluding sections.

4. **In which chapter(s) of your thesis can this material be found?** Chapter 3

e-Signatures confirming that the information above is accurate (this form should be co-signed by the supervisor/ senior author unless this is not appropriate, e.g. if the paper was a single-author work)**:**

Candidate:

Date:

Supervisor/Senior Author signature (where appropriate)**:**

Date:

UCL Research Paper Declaration Form: referencing the doctoral candidate's own published work(s)

1. **For a research manuscript that has already been published** (if not yet published, please skip to section 2)**:**

   (a) **What is the title of the manuscript?** N/A

   (b) **Please include a link to or doi for the work:** N/A

   (c) **Where was the work published?** N/A

   (d) **Who published the work?** N/A

   (e) **When was the work published?** N/A

   (f) **List the manuscript's authors in the order they appear on the publication:** N/A

   (g) **Was the work peer reviewed?** N/A

   (h) **Have you retained the copyright?** N/A

   (i) **Was an earlier form of the manuscript uploaded to a preprint server (e.g. medRxiv)? If 'Yes', please give a link or doi** N/A
   If 'No', please seek permission from the relevant publisher and check the box next to the below statement:

   ☐ *I acknowledge permission of the publisher named under 1d to include in this thesis portions of the publication named as included in 1c.*

2. **For a research manuscript prepared for publication but that has not yet been published** (if already published, please skip to section 3)**:**

   (a) **What is the current title of the manuscript?** Identifying Many-Body Localization in Realistic Dot Arrays

   (b) **Has the manuscript been uploaded to a preprint server 'e.g. medRxiv'?**
   If 'Yes', please please give a link or doi: Yes, DOI: 10.48550/arXiv.2301.08246

(c) **Where is the work intended to be published?** Physical Review B

(d) **List the manuscript's authors in the intended authorship order:** Alexander Nico-Katz, Gulzat Jaliel, Paola Atkinson, Thomas A. Mitchell, David A. Ritchie, Charles G. Smith, Sougato Bose

(e) **Stage of publication:** Responding to Referee Feedback

3. **For multi-authored work, please give a statement of contribution covering all authors** (if single-author, please skip to section 4)**:** ANK, GJ, CGS, and SB equally contributed to the ideas and development of the work. ANK carried out all numerics. GJ carried out all experimental characterizations and imaging. PA, TAM, and DAR contributed to device fabrication. ANK wrote the manuscript, GJ contributing to the section regarding experimental characterizations. CGS and SB contributed to the introductory and concluding sections.

4. **In which chapter(s) of your thesis can this material be found?** Chapter 4

e-Signatures confirming that the information above is accurate (this form should be co-signed by the supervisor/ senior author unless this is not appropriate, e.g. if the paper was a single-author work)**:**

Candidate:

Date:

Supervisor/Senior Author signature (where appropriate)**:**

Date:

Contents

List of Figures

List of Tables

Chapter 1

Introduction

"Thou didst not turn in contempt from my childish play in among dust, and the steps that I heard in my playroom are the same that are echoing from star to star."

— Rabindranath Thakur

"Physics is not important."

— Shankar Das Sarma
The first (and only)
time we ever met.

The prevailing questions that surround quantum many-body systems are oddly utilitarian: what are their value? Can these systems be controlled, harnessed, and eventually exploited? Can we use them to simulate, calculate, optimize, or communicate? These questions - consciously or otherwise - inform the state-of-the-art. These questions dictate the way that many people frame their research interests, and thus how they channel those research interests into grant applications. In academic settings these questions have fractured, spawning further questions that have, in turn, coalesced into vast fields of interrelated research. Resource theories of quantum entanglement, quantum algorithms, and the extent (or indeed, existence) of quantum speedup and advantage over classical algorithms are all examples of this vague question brought into sharp focus by very clever people with very large grants. In corporate settings these questions are posed in tandem with the promise

of a lucrative future. In social settings the lay public - in pubs, and bars, and parties, and over their dinner tables, and on their balconies - discuss these questions; pondering how the widely advertised quantum horizon will change our lives.

This has, of course, all come to a head with the advent of the noisy intermediate-scale quantum (NISQ) device [1]. A half-century of research and innovation on a global scale has led to the creation of, inter alia, mesoscale electronic quantum devices (e.g. quantum dots and wires), lattices of trapped ions, atom chips, and superconducting qubits. We now have actual, functioning, quantum computers - even if they are still a bit rough around the edges.

Despite this the field that is best poised to answer these questions remains fairly unexcavated. Quantum information theory has been, and continues to be, mostly concerned with either many replicas of individual states, or small non-interacting systems passed through some quantum channel. Interdisciplinary work has begun to bridge the gap between information-theoretic and condensed matter frameworks, but there is still much that each can learn from the other. The rising interest in ergodicity-breaking quantum systems is an additional incentive in building these interdisciplinary connections. Information and thermalization have long formed a symbiotic relationship: classical information theory was formed, in part, by analogy to thermalization. The fields were parted suddenly by the advent of quantum theory, but the discovery of ergodicity-breaking quantum phenomena admits the possibility that they can be slowly reunited.

This thesis is devoted to exploring and building these interdisciplinary connections, with the focus shifting through two broad movements sundered by an interlude. In Chapter 2 I will use direct imports from quantum information theory to interrogate information retention and in quantum many-body systems exhibiting ergodicity breaking. Such systems are often touted as sporting ‘local memory’ where information encoded into a subsystem can be locally retrieved at a later time. Thus, these systems are obvious candidates as sub-components - e.g. memory registers - of larger quantum computers and devices; and a framework for analyzing information retention in such systems is thus desirable. In Chapter 3 I introduce a

novel extension of the geometric measure of entanglement which exploits the matrix product state formalism. I then use this measure to probe the ground-state phase diagrams of four systems of increasing complexity, as well as an ergodic-localized transition. This study reveals that the novel measure is particularly suited to the identification of phase boundaries, and may serve as a useful exploratory probe in future research. This chapter is the 'interlude' of the thesis, and draws more broadly on purely informational principles than the other two. Finally, in Chapter 4 I interrogate informational aspects of various state-of-the-art NISQ devices - including von Neumann and number entropies, divergences between probability distributions, and the Holevo quantity. The general structure of this chapter takes the repetitive form of device-model-quantity: I introduce an experimental device, then I discuss the model that simulates the device, finally I investigate some of the model's properties. The three NISQ devices I consider in this thesis are: single-rail quantum dot arrays simulated by an extended Fermi-Hubbard model, twin-rail quantum dot arrays simulated by an antiferromagnetic Heisenberg ladder, and IBM's quantum computers simulated by an extended Bose-Hubbard model. All the model parameters are in turn informed by experimental characterizations - connecting the results of this thesis to realistic experiment.

1.1 Summary of Results

Each chapter of this thesis focuses on a different broad topic: memory in Chapter 2, entanglement-complexity in Chapter 3, and realistic NISQ devices in Chapter 4. They are, of course, interrelated and share themes that focus on bridging the gap between condensed matter and quantum information theory. The results of each chapter are split into two rough halves, the first half of each chapter is focused on work that has already been finished and exists either as a publication or as an online preprint. The latter half of each chapter focuses on unpublished and ongoing work that extends the principles developed in the first half. In general, the parts of this thesis that are yet unpublished present very interesting results, but do not lend themselves as well to detailed interrogation or interpretation as the published

parts. In this section I synopsize the results of each chapter. I also detail which parts of this thesis exist in print already, and which are ongoing research project. This information is covered here such that the internal flow of each chapter remains uninterrupted.

Chapter 2 focuses on interrogating local memory in non-ergodic quantum systems, namely in a toy model of MBL and in a scarred systems. I first introduce the 'accessible information game' is introduced in Section 2.1, which leads to the introduction of a brief set of criteria that define a memory quantifier. The results for MBL are shown in Section 2.2. For a small system of $L = 16$ particles I find that an information-theoretic reinterpretation of the imbalance - a quantity widely used in to characterize memory in MBL - drastically underestimates the amount of information retained by a subsystem in the MBL phase. By introducing several other memory quantifiers, which I benchmark with the von Neumann entropy, I determine that the Holevo quantity captures the most information, followed by a configurational version of the mutual information. I then investigate the ergodic-MBL transition and perform scaling analyses to extract critical exponents. I find that artificially dephasing certain quantities yields scaling results consistent with the Harris bound $\nu > 2$, a rarity in the literature surrounding small-scale analyses of the MBLT. This suggests that the MBL phase in the thermodynamic limit consists of blocks which have dephased with respect to each other, an idea I evidence by investigating localization in the XX (non-interacting) and Heisenberg (interacting) models. In Section 2.3 I investigate memory in the context of quantum scars realized in a Dzyaloshinskii-Moriya interacting spin-1 chain. I find a retention of information similar to that of the MBL case which is robust to small perturbations of the Hamiltonian. This suggests that scars may be suitable as memory registers - though the protocol I investigate only encodes a single classical bit. Whether or not scarred systems can sustain more complicated protocols is an open question. The sections on memory quantifiers, MBL, and the ergodic-MBL transition, have been adapted from work published in Physical Review B and Physical Review Research in Refs. [2] and [3] respectively. The work on scars is, at the time of writing,

ongoing and still in its infancy.

Chapter 3 is concerned with a novel re-imagining of the geometric measure of entanglement from the perspective of tensor networks. I introduce the matrix product state formalism and construct the novel measure - which I dub an 'entanglement-complexity' measure - in Section 3.1. The results of applying this measure to ground state phase analyses of a variety of systems is shown in Section 3.2. This application reveals that my new measure can detect phases of matter which the conventional geometric entanglement cannot. Moreover, by tuning the bond dimension of the underlying matrix product states, different phases of a system can be slowly revealed in increasing detail. I then use this measure to investigate ground state entanglement in a scarred system and find a strange periodicity that is yet unexplained. Since scarce few known ground states in condensed matter physics are separable, but ground states generally have area-law entanglement, I contend that this measure is a much more useful probe of entanglement and of phase diagrams in condensed matter contexts. I also investigate mid-spectrum eigenstates and the ergodic-MBL transition in Section 3.3 which yields no surprising results - a critical point of $h_c \sim 3.5$ with no concrete scaling results is found. However, this does provide a case study for how my new measure can be applied in such a context. The sections introducing the measure and applying the measure to ground state phase diagrams have been adapted from work published in Physical Review Research in Ref. [4]. The ground state phase diagram of the scarred model is ongoing research that is not yet published.

Chapter 4 addresses different informational topics across a variety of different experimental NISQ devices. The structure of this chapter is quite different, in each section I first introduce the experimental device and theoretical model, then I investigate several properties of the device given realistic characterizations of the model parameters. In Section 4.1 I investigate the accessible regimes, and possibility of detecting MBL, in modern small-scale $L \leq 10$ quantum dot arrays. The results suggest that current generation arrays are close to accessing MBL, but that differentiating MBL from other phases is a difficult task. Most notably I identify

a 'frozen' non-MBL insulating phase which experimental quantum dot arrays may realize. By investigating a variety of quantities, I determine that local charge sensing alone can identify MBL and uniquely demarcate it from this frozen phase. In Section 4.2 I investigate ground states of twin-rail quantum dot arrays realizing an antiferromagnetic Heisenberg ladder. In particular I focus on profiles of singlet-triplet measurements and the fidelity susceptibility which appear to track each other as the model parameters are scanned across a phase crossover. I then incorporate disorder and finite time quenches which may transport the state of the system away from the ground state. The results of this extended analysis indicates that modern experimental systems can indeed access this crossover, and accurate ground state preparation is possible. Finally, in Section 4.3 I analyze transmon arrays which simulate the natural underlying dynamics of IBM's superconducting quantum computers. By invoking the Holevo quantity and Loschmidt echo, I investigate idle information loss - information lost locally due to the accretion of long-range entanglement and information spreading. These results place certain constraints on some characterizations of IBM devices. I suggest how IBM's characterizations could be improved, and that in-situ experimental analyses of these quantities may provide insight into how information is distributed and lost in modern quantum computers. The section on MBL in quantum dot arrays has been adapted from the work in Ref. [5]. The sections on twin-rail quantum dot arrays and IBM's devices are comprised of research that is still ongoing.

1.2 The Informational Approach

Claude Shannon's Promethean text *'A Mathematical Theory of Communication'* is both a bedrock beneath, and a glittering minaret that rises over, the fields of the natural sciences[1] [6]. The central result of this work is the most widely-accepted mathematical definition of the rather nebulous term 'information'. Information, according to Shannon, should be envisaged through the lens of communication. A single message drawn from an ensemble of possible messages only becomes

[1] Evidenced by it's monstrous citation count that rivals the population of Oxford.

'information' once it has been passed through a (typically noisy) channel to another party who then tries to reconstruct it. The informational content of the message is thusly related to how reliably communication between the two parties succeeds.

Consider, for example, the state of a coin. When uncontextualized and lying on the stained wood of a Soho bar, the coin means nothing. It is only when Alice encodes a message into the coin: "heads I want another round, tails I want to leave", passes it through the noisy channel of being slid across the bar to Bob, and Bob's subsequent inspection of it, that it comes to bear meaning. That it comes to bear *information*. Clearly if the noisy channel is too noisy, if their colleague Eve grabs the coin in transit and flips it a few times, then the information is erased. Bob cannot figure out - from the state of the coin alone - what message Alice intended to send.

This perspective: wherein information and its physical embodiment are characterized by increasingly complicated communication games played between Alice and Bob, is the 'informational approach' I allude to throughout this thesis. A version of this game is discussed in detail in Section 2.1 at the start of Chapter 2, and relevant information-theoretic concepts are introduced throughout the text. This preliminary section is dedicated to introducing the central concept of entropy in classical and quantum contexts, and impressing upon the reader the value of such an informational approach.

1.2.1 Classical Shannon Theory

Systems that have a degree of uncertainty in their *possible* states are generally better at bearing information. A flat coin has only two states, it can only encode a binary decision: a yes or a no, a one or a zero, a single 'bit' of information. The state of a dice is clearly richer, it can take one of six values and thus more information can be encoded into it. These six values may - however - be harder to distinguish. The bleary-eyed, overworked, two-pints-down Bob may have difficulty distinguishing five and six; and its a lot harder for Alice to slide a die without rolling it than slide a coin without flipping it. This interplay between uncertainty and distinguishability is a topic I shall revisit in Chapter 2 in the context of quantum channels.

Given uncertainty's central role in classical information theory, a precise quan-

tification $H(\cdot)$ thereof is required. Consider the finite scheme $\{p_i, \rho_i\}$ of N states wherein the state ρ_i occurs with probability p_i. In classical physics, the states ρ_i are all distinct and fully distinguishable. There are several intuitive relations that $H(\cdot)$ should satisfy [7, 8]:

1. $H(\cdot)$ should be continuous in the p_i.

2. $H(\cdot)$ should be maximized for equiprobable events $p_i = 1/N$. This corresponds to a system with maximal uncertainty, and the value of $H(\cdot)$ should reflect that.

3. $H(\cdot)$ should be expandable, i.e. the inclusion of a new state ρ_{N+1} which cannot occur $p_{N+1} = 0$ should not change $H(\cdot)$. This reflects the intuition that anything outside the scope of the system in question should not affect it.

4. $H(\cdot)$ of a joint system AB where A and B are two finite schemes should satisfy the relation

$$H(AB) = H(A) + H_A(B) \tag{1.1}$$

   where $H_A(B)$ is the uncertainty of B *given* the state of A. This intuitively captures the notion that the uncertainty we have about the joint system AB is not just the uncertainty we have about A and B independently. Knowing A may *inform* us about B, and hence the state of B is conditioned upon A. More specifically $H_A(B) \leq H(B)$ with equality only for when A and B are independent. This fact is not necessarily true for quantum systems, an idea I touch on later in the discussion of the coherent information in Section 2.1.3.

Collectively, these principles are known as the 'Shannon-Khinchin' axioms, and they can uniquely be satisfied by the equation

$$H(\{p_i\}) = -\sum_i p_i \log p_i \tag{1.2}$$

where $p_i \log p_i \doteq 0$ for $p_i = 0$, and where the logarithm is in any fixed base [6]. Throughout this thesis, I will use logarithm base two unless otherwise indicated.

This allows us to interpret many results in terms of bits of information. The quantity of Eq. (1.2) is referred to as the *entropy* of the scheme due to its analogical form to and historical relationship with the thermodynamic entropy introduced by Ludwig Boltzmann in his famous H-theorem. This connection is perhaps most solemnly recognized in the fact that Boltzmann's grave bears his entropy relation on its front, and Shannon's grave - over four thousand miles apart - bears his on its reverse.

Considering again the fair coin and the fair die discussed above, the uncertainty in the state of the coin is $H(\{1/2,1/2\}) = \log 2 = 1$, and the uncertainty in the state of die is $H(\{1/6,\cdots,1/6\}) = \log 6 \approx 2.585$. This latter fact implies that the exact state of the die can be inferred - at minimum - with between two and three binary queries. An example may be: (i) is the state even or odd (ii) is the state one or six (iii) is the state two or five. These questions will *always* exactly determine the state of the die, either after asking (ii) or after asking (iii). On average, 2.585 queries will be required.

From the above formative ideas, the field of classical information theory was formalized and codified. Coding theorems, compression algorithms, telecommunications, codebreaking, and the fundamental principles of modern classical computation followed; and humanity charged headlong into the age of information - the age of unrestricted *communication*. Some sociological thinkers suggest that this age is now coming to an end [9, 10]; but it is not an understatement to say that Shannon's paper is a keystone in the foundations of modernity. With the advent of quantum computers on the horizon: these informational principles, transposed into a quantum-mechanical context, are as relevant as ever.

1.2.2 Quantum Shannon Theory

A quantum theory of information starts with the substitution of our classical ensemble with an ensemble of *quantum* states $\{p_i, \rho_i\}$. Without any additional information about which state has been selected from this ensemble, an observer receives the combined state $\rho = \sum_i p_i \rho_i$ where ρ is a trace-unity positive semi-definite Hermitian operator with real eigenvalues λ_i that sum to unity $\sum_i \lambda_i = 1$. These eigenvalues can thus be interpreted as the probabilities that the state ρ will be observed in its

various eigenstates. The von Neumann entropy is defined as the Shannon entropy over the eigenvalues, i.e. the vector of effective probabilities:

$$S(\rho) = -\sum_i \lambda_i \log \lambda_i = -\mathrm{Tr}\left[\rho \log \rho\right] \tag{1.3}$$

where $S(\cdot)$ is definitionally invariant under change of basis, and is an intrinsic property of the ensemble $\{p_i, \rho_i\}$. The von Neumann entropy in this context quantifies the uncertainty an observer has in the state of $S(\rho)$ but - unlike the classical case - that uncertainty can arise when information is distributed non-locally. In the classical theory, the joint system AB has entropy that is strictly greater than or qual to the entropy of either A or B individually. This can be seen by invocation of the final Shannon-Khinchin axiom discussed above $H(AB) \geq H(A)$ with equality only at $H_A(B) = 0$, i.e. when knowledge of A fully determines B. The same is not true of quantum systems, wherein information can be distributed between two disjoint systems A and B. In the quantum theory it is perfectly possible for the von Neumann entropy of the joint system $S(\rho^{AB})$ to be far less than the entropy of a subsystem $S(\rho^A)$. This non-local distribution of information is called 'entanglement', a topic that is central to this thesis. In particular Chapter 3 and parts of Chapter 4 focus heavily on investigating quantum entanglement and entropy directly. It is also used to benchmark results in Chapter 2.

Another major difference that comes into play when considering information and communication via quantum states is the fact that the quantum states ρ_i may not be distinguishable. Indeed if the ρ_i are fully distinguishable (mutually commuting) then they are themselves the eigenstates of ρ and the situation reduces to the classical case where the eigenvalues $\lambda_i = p_i$. Non-orthogonality of the ρ_i is not just a possible feature of quantum information theory, it is central and necessary. A failure to exploit the essentially quantum nature of the states causes the whole thing to reduce to the classical theory.

Given the discussion of the Shannon-Khinchin axioms above, it in unsurprising that the von Neumann entropy is maximized for equiprobable eigenvalues $\lambda_i = 1/N$. This however bears a very different interpretation when it comes to the quantum

theory. Due to the lack of guarantee that the quantum states are distinguishable, maximally uncertain states are no longer necessarily useful for bearing information. Consider two extremes: an ensemble of orthogonal (classical) states which yields $\rho = \mathbb{I}/N$ where $\mathbb{I}$ is the $N \times N$ identity matrix, and an ensemble of states arbitrarily close to the identity $\rho_i \sim \mathbb{I}/N$ which also yield $\rho = \mathbb{I}/N$. Clearly the first ensemble is excellent as a source for encoding messages, whilst the second is completely useless - the states are barely distinguishable. Despite this, both have high von Neumann entropies and - if we naïvely interpret the result by analogy to the classical theory - both should be equally useful sources. This may seem a contrived example, but in systems with little memory where information is rapidly erased, this exact process becomes quite important. If we have a very noisy channel that tends to send all input states to the identity, then this situation arises exactly. I discuss this in more detail in Section 2.1.2 where I introduce the Holevo quantity - a bound on the classical capacity of a quantum channel with accounts for this exact behaviour.

Throughout the rest of this thesis, informational principles such as the relative entropy and the mutual information are invoked. These principles inform how well the systems in question can bear and transmit information, how useful they are from a technological and industrial perspective, and how they may fit into the accelerating age of information. Even where the results of this thesis aren't direct information-theoretic imports: objects like the divergence between probability distributions and entropic quantities still bear strong connections to classical and quantum information theory.

1.3 Equilibrium, Ergodicity, Thermalization, and Chaos

The nature of equilibria has been a continual focus of scientific attention for more than a century. From early toiling by Maxwell and Gibbs, through the lost Viennese cafés in which Loschmidt and Boltzmann argued over sachertorte, flanked by the blossoming twin fields of probability and information theory whose first strained steps were guided by the efforts of Shannon and Khinchin and Kolmogorov, and

distilled down through the accurately-trained scientific legions of the twentieth century arrived statistical mechanics: the theory of equilibrium.

In the classical theory, the ergodic hypothesis - that generic classical systems visit every part of the phase space admitted by macroscopic conservation laws - leads naturally to thermalization. Ergodicity can be used to justify a foundational principle of statistical mechanics: the principle of equal a priori probabilities which states that different (allowed) microstate configurations of the system are equally likely to occur. Statistical mechanics then assigns each microstate to a macrostate, and thus - after agglomerating all the microstates - to each macrostate a finite probability. Macroscopic quantities can then be calculated by averaging over ensembles of macrostates, with the underlying probability distributions governed by the microscopic features of the system.

Whilst the nature of these ensembles, how they are formed and how they can give rise to macroscopic physics, are well understood; why such a procedure should give such good results is generally not. Real experiments are usually made on a single system, not a vast ensemble; and the common arguments for the validity of the underlying principles either appeals to the ergodic hypothesis[2] or a coarse-graining procedure which shatters dynamical reversibility. These significant gaps in the physical foundation aren't the only Damoclean threat to statistical mechanics; and - as with almost every pinnacle attained by the physical sciences before the advent of the 1920s - the question of reconciling classical statistical physics with the quantum revolution eventually reared from the billows [11].

The bridling issue is that of phase space: the prevailing approaches to classical statistical mechanics rely on a well-defined phase space, or the ability to demarcate well-defined phase space volumes [11]. This is precisely what is implied by my above discussion regarding the assignation of microstates to macrostates. A fundamental feature of quantum mechanics however is that conjugate variables (in the case of quantum analogy to classical phase space, position and momentum) do not commute, and thus the precision to which they can be defined is limited by a

[2]Proven only for a few systems such as the Sinai billiard.

corresponding Heisenberg uncertainty relation. This means that conventional phase spaces, and volumes within those phase spaces, cannot be defined [12]. This also afflicts notions of 'chaos' in quantum systems. Classically, chaos is often characterized by the exponentially rapid divergence as $\sim e^{\lambda t}$ of nearby trajectories in phase space - characterized by the Lyapunov exponent λ. Due to the unitarity of closed system dynamics, the distance between two quantum states is preserved: $\langle\psi|U^{\dagger}(t)U(t)|\psi+\delta\psi\rangle$ is a constant in time. Thus novel ways of defining chaos via random matrix theory, and of extracting Lyapunov exponents by e.g. OTOCs, have been introduced.

However, equilibration, thermalization, and chaos are *known* to occur in quantum systems. We can observe it. The existence of steady-state solutions to Lindblad master equations, the relaxation of observables in closed quantum systems to values uncorrelated with the initial state, and the prevalence of systems with chaotic Wigner-Dyson level statistics. This last fact is in fact a consequence of a working definition of chaos in quantum systems - that chaotic Hamiltonians give the same results as random matrices with identical symmetries [13]. One of the most significant questions in the study of quantum many-body systems is how we can understand the mechanism by which thermalization occurs in a closed quantum system. A close second is how can this mechanism be broken.

1.3.1 The Eigenstate Thermalization Hypothesis

As indicated in the preceding discussion, a precise definition of thermalization and the mechanisms by which it occurs in a quantum-mechanical context are still up for debate. However, several attempts to define quantum thermalization have been made which do not reference phase space; the most notable incarnation being the eigenstate thermalization hypothesis (ETH). As the ETH is not directly relevant to the methodology or results of this thesis, but still undergirds much of the literature upon which this thesis is built, I briefly give an overview of it here. For more information see Refs. [11] and [14], two well-known and in-depth reviews of the topic.

In a nutshell, the eigenstate thermalization hypothesis (ETH) proposes one

possible mechanism by which a closed quantum system can be said to have self-'thermalized'. Originally proposed in the seminal work of Deutsch [15] and Srednicki [16, 17], it is easiest understood by following the similarly foundational work of Rigol et al. in Ref. [18], which I summarize. The expectation value of a generic observable $\hat{A}$ in a closed system with Hamiltonian H, eigenvectors $|\alpha\rangle$, and corresponding eigenvalues E_α evolves as

$$\langle \hat{A}(t) \rangle = \sum_{\alpha,\beta} C_\alpha^* C_\beta e^{i\left(E_\alpha - E_\beta\right)t} A_{\alpha\beta} \tag{1.4}$$

where $A_{\alpha\beta} = \langle \alpha | \hat{A} | \beta \rangle$, and the probability amplitudes C_α are fixed by the choice of initial state. For long times non-degenerate eigenvalues E_α yield thusly incommensurate off-diagonal oscillations $E_\alpha - E_\beta \neq 0$, and the long-time value should fluctuate around

$$\langle \hat{A}(t) \rangle_D = \sum_\alpha |C_\alpha|^2 A_{\alpha\alpha}. \tag{1.5}$$

If the steady-state value of the observable relaxes at all, then it is reasonable to assume that it will relax to this value. One can interpret Eq. (1.5) as an observable averaged over the diagonal ensemble, and denote it by the subscript $\langle \cdot \rangle_D$. We can now compare this generic prediction of quantum mechanics to the predictions of an appropriately chosen statistical ensemble: the microcanonical ensemble (denoted by the subscript $\langle \cdot \rangle_M$), from which the equilibrium value of the same observable $\hat{A}$ is

$$\langle \hat{A}(t) \rangle_M = \frac{1}{\mathcal{N}_{E_0,\Delta E}} \sum_{\alpha \in \mathbb{E}} A_{\alpha\alpha} \tag{1.6}$$

where $\mathbb{E}$ is the set of all α such that the corresponding eigenvalue E_α is close enough in energy to the energy of the initial state $\mathbb{E} = \{\alpha \mid |E_\alpha - E_0| < \Delta E\}$ for some appropriately chosen energy window ΔE, and where $\mathcal{N}_{E_0,\Delta E}$ is the cardinality of $\mathbb{E}$. The equivalence of results from diagonal and microcanonical ensembles

$$\langle \hat{A}(t) \rangle_D = \langle \hat{A}(t) \rangle_M \tag{1.7}$$

is a statement supported by classical analogy, extensive numerical confirmation,

and - in scant few cases - rigorous proof, but is still, generically, conjecture; and implicitly forms half of the 'hypothesis' in the acronym 'ETH'. The explicit part of the 'hypothesis' is the proposed explanation for the equivalence in Eq. (1.7): that the eigenstate expectation values of a few-body operator *themselves* are almost equal in a small enough energy window

$$A_{\alpha\alpha} = \langle\alpha|\hat{A}|\alpha\rangle \approx \langle\hat{A}\rangle_M \quad \forall\ \alpha \in \mathbb{E}. \tag{1.8}$$

The ETH thus reveals a mechanism of thermalization which appears far removed from the type we are used to in classical mechanics: each eigenstate *itself* is a thermal state in the sense expectation values of observables calculated with it yields the steady-state 'thermalized' value. In general, non-thermal states are in fact complicated coherent superpositions of these eigenstates which in turn yield non-thermal expectation values. The ETH is well summarized by an ansatz first proposed by Srednicki in Ref. [17] to describe the matrix elements of observables in the system's eigenbasis:

$$A_{\alpha\beta} = A(\overline{E})\delta_{\alpha\beta} + e^{-S(\overline{E})/2} f_O(\overline{E},\omega) R_{\alpha\beta} \tag{1.9}$$

where $\overline{E} = (E_\alpha - E_\beta)/2$ is the average energy of the eigenstates α and β, $\omega = E_\beta - E_\alpha$, $S(\overline{E})$ is the thermodynamic entropy, $A(\overline{E}) = \langle\hat{A}\rangle_M$ is the microcanonical average over states close in energy to $\overline{E}$, $f_O(\overline{E},\omega)$ is a smooth function of its arguments, and $R_{\alpha\beta}$ is a random variable with zero mean and unit variance [11]. If the system exhibits symmetries which divide the energy shell into disparate sectors, then those sectors may independently follow the ETH.

For the purposes of this thesis, the most relevant part of Eq. (1.9) is the smoothness of $A(\overline{E})$. When $A(\overline{E})$ is smooth then eigenstates with energy close to $\overline{E}$ have similar expectation values, Eq. (1.8) is satisfied, and the ETH holds. When $A(\overline{E})$ rapidly varies, then Eq. (1.8) fails, as does the ETH. It is in this sense, once the ETH has been violated which in turn leads to a breakdown of the equivalence in Eq. (1.7), that the quantum system fails to thermalize. Such non-thermalizing quantum sys-

tems, far-from-equilibrium, are important to the rest of this thesis.

1.3.2 Many-Body Localization

Many-body localization (MBL) is a phenomenon wherein certain quantum systems fail to thermalize. As my discussion up to this point indicates, the word 'thermalize' here can mean different things to different people. Moreover, a confluence of theoretical, numerical, and experimental breakthroughs that occurred in the late twentieth through early twenty-first centuries reinvigorated the field of MBL and ergodicity-breaking in general. As such, the field of MBL has gone through an array of paradigmatic shifts since the roots of its inception in 1958 [3].

MBL was originally envisaged as a kind of Anderson localization which was robust to interactions [19] - quantum wavefunctions describing interacting many-body systems could be localized by disordered fields in a similar way to classical wave localization in disordered materials. This was the ultimate result of the seminal work by Basko, Altshuler, and Aleiner in Ref. [20] and published in 2006. This behemoth of a work proved the existence of wavefunction localization in (closed) disordered conductors in the presence of electron-electron interactions. The condensed matter community jumped at the chance to study this novel phase of matter and the early golden age of MBL research began. Some landmark results include, inter alia: Pal and Huse's foundational numerical study of the transition of a system into an MBL phase in 2010 [21], the groundbreaking work of Schreiber et al. who first experimentally probed the MBL phase in 2015 [22], and Imbrie's construction of exact local integrals of motion for an MBL model in 2016 [23]. These landmark results were informed by a dedicated decade of theoretical, numerical, and experimental study - the results of which have been condensed into a handful of exceptional review articles[4] [24–27].

[3] These paradigm shifts have also rendered MBL a deeply funny field to work in. Based on my discussions with my contemporaries at conferences: some people swear by MBL, some people don't think it exists at all. Some people think that phenomenological approaches to the ergodic-MBL transition are the future of the field, others find this to be a deep and fundamental betrayal for the sake of citations. Some people are so bored of averaging over random samples that they're quitting the field altogether. I once saw someone sarcastically cite the actual 1852 Occam's Razor article as a comeback to a comment on the arXiv. It's a spectacular melting pot of personalities and perspectives, and I love it.

[4] Incidentally the review of Abanin, Altman, Bloch, and Serbyn of Ref. [24] was the earliest

Gradually the hallmark features of MBL were collated and distilled by the scientific community: (i) strong ergodicity-breaking and ETH violation in the MBL phase [24], (ii) a rich many-body localization phase transition (MBLT) across the entire spectrum with highly debated properties [21, 28–36], and (iii) emergent integrability and associated local memory [23, 37–40] which provides a lucrative testbed for applications in quantum computing. Further characteristics of MBL which emerge from these general features include: the relaxation of observables - most notably the imbalance [22, 41–46] and prevalence of area-law entangled mid-spectrum eigenstates [31, 32, 47–50], the slow logarithmic growth of entanglement entropies [41, 50–56] and spatial correlation functions [57–59]. Across the ergodic-MBL transition, the unfolded level statistics themselves undergo a quantitative transition [21, 29, 53, 60–65], and myriad other signatures have been found in myriad other quantities [42, 57, 66, 67]. Devices in which MBL has been experimentally realized include ultracold atoms and ions in optical lattices [22, 44, 45, 68–70], and superconducting qubits [71], with recent evidence suggesting that extant transmon-based quantum computers naturally tread a delicate line between localization and chaos [72].

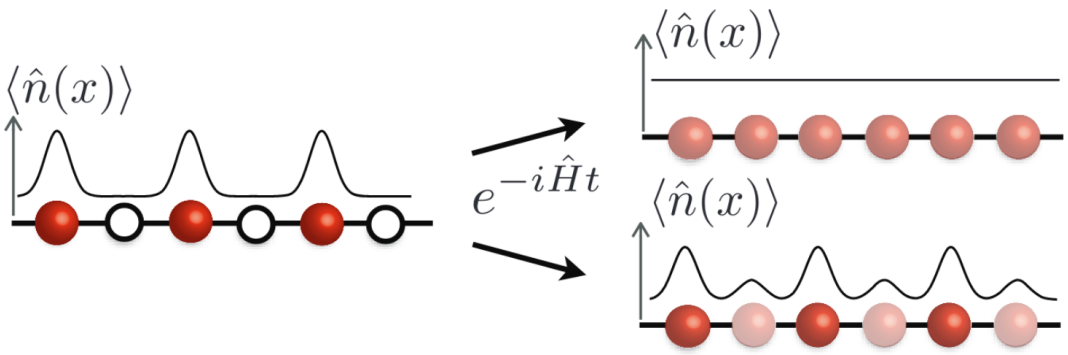

Figure 1.1: Schematic of a state initialized in a non-thermal density wave configuration that, after unitary evolution, either relaxes to a thermal configuration or retains some memory about its initial state. Figure retrieved from Ref. [24].

It is in the above phenomenological sense that a system 'fails to thermalize'. Neglecting the precise underlying mechanism: the absence of thermalization is

article I ever remember reading on the subject of MBL - right at the start of my PhD. Sitting next to Maksym and listening to Dmitry deliver (remotely) the keynote talk at a conference years later is a fond memory of mine.

manifest in a system wherein local excitations do not spread, wherein the initial state of a subsystem is locally preserved and can be retrieved. A schematic example of this is shown in Fig. 1.1 wherein the features of the initial state of some closed interacting system are either erased (thermalization) or retains some memory of its initial state (MBL).

Mechanically, a simple explanation of many-body localization can be found in terms of energetic suppression of certain transitions. In a closed system with quenched disorder, a single-site change typically incurs an energy cost of the order of the (random) disorder strength. This means that two quantum states which are spatially close (in the sense that only a few local operations are required to transform one into the other) are energetically separated. On the other hand, states which are energetically close are typically spatially separated, requiring an extensive number of operations to change one into the other. Given the fact that a closed system cannot overcome this energetic gap by exchanging constituents with an environment: the system is necessarily localized. MBL specifically occurs when can the new channels opened up by interactions cannot provide the energy required to surmount single-particle localization.

A more nuanced, modern, understanding of MBL is driven by the discovery of (quasi) local integrals of motion (LIOMs) and the diagonalization of MBL Hamiltonians in terms of l-bits $\hat{\tau}_j$: local operators dressed with non-local corrections that exponentially fall off with distance [23, 38, 40]. The Hamiltonian of the system deep in the MBL phase can be rewritten in terms of z-components of these l-bits as follows:

$$H = \sum_i J_i \hat{\tau}_i^z + \sum_{ij} J_{ij} \hat{\tau}_i^z \hat{\tau}_j^z + \sum_{ijk} J_{ijk} \hat{\tau}_i^z \hat{\tau}_j^z \hat{\tau}_j^z + \cdots .$$

This reveals a new mechanism for MBL: as a version of the underlying 'clean' system, in which the emergent l-bits dephase with respect to each other but cannot flip or exchange with each other. Essentially, transport can still occur *within* the support of an l-bit, but not *between* them.

Finally, it is worth outlining a categorical ambiguity present in literature, and that I necessarily perpetrate throughout this thesis. Both 'many-body localization'

(referring to the general phenomenon) and 'many body localized' (the state of a specific system) bear the acronym 'MBL'. Typically one can determine which is meant by context, but it does lead to some strange turns of phrase; the same system can 'exhibit MBL' or 'be MBL' depending on which the author means. Highlighting this is not just pedantry on my part, there is an ongoing (sometimes heated) argument in literature about whether the many-body localized phase exists as a specific and stable phase of matter, or whether a system simply exhibits many-body localization for an interim period.

1.3.3 The Many-Body Localization Transition

As discussed in the previous section, an thermalizing system exhibits strikingly different behaviour to a localized one. A natural question to ask is what the transition between the two looks like? As it turns out the characterization and analysis of the ergodic-MBL transition forms a rich seam of physics. Unlike conventional quantum phase transitions [73], the MBL transition (MBLT) takes place across the spectrum [24, 26, 27, 74]; making its analysis a far more elaborate task than that of other quantum critical systems. An additional difficulty is manifest the fact that each eigenstate appears to localize at a different disorder strength, a feature known as the mobility edge [26, 29, 75]. Advancements in quantum simulators have paved the way for experimental attempts to probe the transition [44, 67, 71, 76–79] and an array of theoretical breakthroughs have resulted in a general debate over the nature of the transition itself [21, 28–36, 80].

I summarize features of disorder-induced transitions and the MBLT in the following subsections, but I first discuss general finite-size scaling theory and data collapse for continuous transitions in Section 1.3.3.1. The topic of finite-size scaling is relevant to several sections of this thesis, and necessarily prefaces the discussion of the MBLT. I then discuss disorder-induced transitions in Section 1.3.3.2, addressing the analytical results of Harris [81] and developments thereof by Chayes et al. and Chandran et al. [82, 83]. Finally, I briefly discuss some general numerical results which inform much of MBLT literature up to this point, as well as the results of Chapter 2.

1.3.3.1 Finite-Size Scaling Theory

The characteristic feature of a continuous phase transition, the feature which drives the transition itself, is the existence and divergence of some underlying correlation length ξ [84]. As the critical point is reached $\lambda \to \lambda_c$, ξ diverges as

$$\xi \sim \frac{1}{|\lambda - \lambda_c|^{\nu}} \tag{1.10}$$

with critical exponent $\nu > 0$. In this sense, we can intuit the critical value λ_c as *where* the transition takes place, and the critical exponent ν as *how fast* it takes place (i.e. how fast the correlation length diverges). Typically, we cannot access the underlying correlation length directly, and the system-specific question of how to do so implicitly has driven innovation in the field; see for example the Thouless time and energy first introduced in the context of Anderson localization in Ref. [85] and the modern discussion thereof in e.g. Refs. [86, 87]. An appropriately selected quantity $O_\infty(\lambda)$ will diverge at the critical point in a similar fashion to the underlying characteristic length

$$O_\infty(\lambda) \sim \frac{1}{|\lambda - \lambda_c|^{\zeta}} \sim \xi^{\zeta/\nu}. \tag{1.11}$$

where the scaling exponent ζ determines how quickly $O_\infty(\lambda)$ diverges, and so the ratio ζ/ν can be intuited as how closely our quantity tracks the effect of diverging ξ.

For a finite system however, there is an upper limit to ξ; the (smallest) physical extent of the system L (though I will consider one-dimensional systems for the rest of this thesis). For a finite-sized quantity $O_L(\lambda)$, this length takes the place of ξ close to the critical point:

$$O_L(\lambda) \sim L^{\zeta/\nu} \quad \text{for} \quad \lambda \to \lambda_c \tag{1.12}$$

which, in conjunction with the idea that - at the critical point - the quantity should

follow a scaling law [88], yields the celebrated finite-size scaling ansatz:

$$O_\infty(\lambda) = \xi^{\zeta/\nu} f(L/\xi) \tag{1.13}$$

which describes the bulk behaviour of the quantity close to the critical point. We note that our scaling function $f(\cdot)$ is arbitrary provided it satisfies two crucial conditions [89]:

$$f(L/\xi) \begin{cases} = \text{const.} & \text{if} \quad L \gg \xi \\ \sim (L/\xi)^{\zeta/\nu} & \text{if} \quad L \ll \xi \end{cases} \tag{1.14}$$

which ensure the behaviour of Eq. (1.11) and Eq. (1.12) respectively. A convenient (and commonplace) choice of scaling function which renders our ansatz more tractable by eliminating explicit ξ dependence is $f(\cdot) = \cdot^{\zeta/\nu} g(\cdot^{1/\nu})$ where unspecified $g(\cdot)$ satisfies conditions similar to those in Eq. (1.14) such that they still hold for our specified scaling function. This yields our tractable scaling ansatz for a continuous phase transition [90]:

$$O_\infty(\lambda) = L^{\zeta/\nu} g(L^{1/\nu}|\lambda - \lambda_c|). \tag{1.15}$$

The process of data collapse can now be used to extract the critical value λ_c, and critical exponents ν and ζ, simply by calculating the quantity $O_\infty(\lambda)$ for a range of λ at varying scales L. The procedure involves rescaling

$$\begin{aligned} O'_\infty(\lambda) &= L^{-\zeta/\nu} O_\infty(\lambda) \\ \lambda' &= L^{1/\nu}|\lambda - \lambda_c| \end{aligned}$$

such that $O'_\infty(\lambda) = g(\lambda')$, which is free from explicit dependence on L, ξ, and all critical values and exponents. As such, all rescaled curves are identical and should fall upon each other: the well-known 'data collapse'. The art is simply in finding the optimal values of λ_c, ν, and ζ for which the collapse succeeds.

The collapse is systematically affected by finite-size effects, as the ansatz works only in the limit of the bulk $L \to \infty$. We can also see the seeds of scale invari-

ance, either as a function of the rescaling, or in the case that the scaling exponent $\zeta = 0$ where we would see the unscaled curves cross at a single point, regardless of L.

1.3.3.2 Disorder-Induced Transitions

At the heart of the theory of disorder-induced transitions is the celebrated Harris criterion $\nu > 2/d$, used to determine whether or not an existing continuous phase transition in an undisordered (uniform) system persists under the addition of quenched disorder [81, 91]. We will now heuristically re-derive the criterion and point out its flaws by considering a clean system of dimension d exhibiting a continuous phase transition. As discussed in Section 1.3.3.1, such a transition has an underlying correlation length that diverges as $\xi \sim |\lambda - \lambda_c|^{-\nu}$ as we approach the critical point $\lambda \to \lambda_c$. We can consider the clean system to consist of sub-regions of volume ξ^d which - by the definition of the correlation length - do not depend on each other. Under the addition of quenched disorder (to bonds or sites) the n-th sub-region's critical value $\lambda_c^{(n)}$ changes slightly. Since the effect of quenched disorder on each sub-region has been averaged over ξ^d i.i.d. random variables, the unbiased estimator for the variance of these $\{\lambda_c^{(n)}\}$ is given by:

$$s^2_{\lambda_c} \sim \frac{1}{\xi^d - 1} \tag{1.16}$$

In the thermodynamic limit where ξ isn't bounded by unfortunate physicality, unbiased corrections to the standard deviation and the -1 in the radicand of Eq. (1.16)) can both be neglected such that the standard deviation of the $\{\lambda_c^{(n)}\}$ is of the order $s_{\lambda_c} \sim \xi^{-d/2}$. From this and our general form for the correlation length in a continuous phase transition we find that the fluctuations in λ_c due to the addition of quenched disorder is of the order $s_{\lambda_c} \sim |\lambda - \lambda_c|^{d\nu/2}$. For the clean phase transition to be stable under the addition of quenched disorder - it suffices that the original critical value λ_c is not dominated by these fluctuations:

$$|\lambda - \lambda_c| > |\lambda - \lambda_c|^{d\nu/2} \tag{1.17}$$

from which we can determine the Harris criterion $\nu > 2/d$ by simple comparison of the exponents on the left and right hand sides. Intuitively, for $\nu > 2/d$, the disorder is less and less relevant at larger scales and the critical properties in the thermodynamic limit are determined by the zero-randomness model. For $\nu < 2/d$, the opposite is true, disorder becomes more relevant at larger scales and the critical properties in the thermodynamic limit are determined by the infinite-randomness model.

Despite it's widespread citation, the original (heuristic) formulation of the Harris criterion in 1974 (see Ref. [81]) is of limited use. There are four relevant features of the above derivation which limit its usefulness in the modern studies of disorder-driven transitions: i) the underlying correlation length ξ is accessible, ii) it necessarily references an existing clean transition; devoid of quenched disorder, iii) it uses the continuous phase transition (power-law) form for ξ, and iv) it considers systems in the thermodynamic limit wherein ξ is unbounded by the physical extent of the system. Unfortunately, the bulk of modern analyses of disorder-induced transitions i) use quantities (spatial and otherwise) or heuristic correlation lengths (such as the Thouless time) ii) have no clean counterpart without quenched disorder, iii) are not necessarily continuous phase transitions, and iv) are limited in system size.

Due to these shortcomings, there have been considerable advancements made in our understanding and generalization of the Harris criterion. Notably the work of Chayes-Chayes-Fisher-Spencer (CCFS) in Ref. [82] and Chandran-Laumann-Oganesyan (CLO) in [83] which address some of these issues. Despite this, very little about the functional form of the famous formula $\nu > 2/d$ has changed. Indeed in the forty years that span the publication of Harris' seminal work in 1974, and the work of Chandran, Laumann, and Oganesyan in 2015, the defining feature of disorder-driven transitions still fits into a few letters:

$$\nu \geq \frac{2}{d+2a} \tag{1.18}$$

making Harris' original qualitative inquiry an exceptional examples of an 'educated guess'. Despite this, arguments have been made that the Harris bound is irrele-

vant to MBL, either because the transition is of a Kosterlitz-Thouless type (making the scaling ansatz invalid) [35, 36, 92, 93], or - as discussed by Cecile Monthus in Ref. [80] - because the averaging over the ξ^d i.i.d random variables is not explicit but happens implicitly over eigenstates, and as such the crucial central limiting behaviour of Eq. (1.16) is not seen.

1.3.3.3 Numerical Results for the MBLT

Numerical results for the MBLT fall into two broad groups. The limitation of exact numerics to small system sizes ($L \sim 20$) makes extracting the behaviour of the system in the thermodynamic limit challenging. Scaling analyses in such systems are riddled with pathological finite-size effects and thus almost all small-scale numerical analyses strongly violate the Harris bound. Such analyses typically assume a continuous phase transition and find $1 \leq \nu \leq 1.5$. A few notable exceptions [66, 94] that capitalize on quantities which are robust to finite-size effects satisfy the Harris bound. In contrast, large phenomenological approaches - though blind to microscopic features of the system - have had markedly more success: either consistently achieving this bound [30, 34, 95–98], or supporting the idea that the transition is of a Kosterlitz-Thouless type [35]. It has also been suggested by Khemani et al. in Ref. [32] that there are two universality classes at play: one that is accessible to small-scale analyses which doesn't need to satisfy the Harris bound, and one that is accessible to large-scale analyses which does. These universality classes are loosely identifiable as the infinite-randomness and zero-randomness cases discussed in Section 1.3.3.2.

1.3.4 Quantum Scars

Quantum many-body scars are a kind of 'weak' ergodicity breaking behaviour found in certain systems. Weak ergodicity breaking occurs when the ETH is satisfied for *most* of the system's eigenstates, but a select few eigenstates dramatically violate it [13, 100]. A quantum scar is a band of these ETH-violating eigenstates which 'scar' the spectrum. These scars effectively embed a non-thermalizing system *within* an large thermalizing space. Systems initialized in the scarred subspace

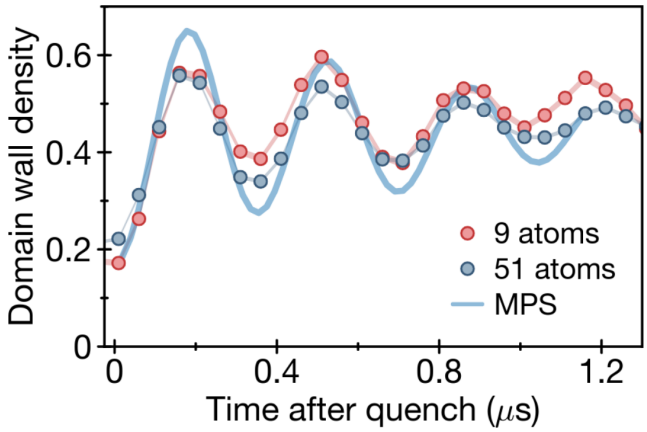

Figure 1.2: Experimental evidence of revivals in the domain wall density in a scarred system. The revivals are independent of system size. Figure retrieved from Ref. [99].

will behave as though decoupled from the thermalizing bulk of the spectrum. Thus, systems with quantum scars can exhibit unique kinds of non-thermal behaviour for very specific initial state configurations.

The precise mechanisms that lead to the existence of quantum scars are yet unknown - though the prevailing explanation is that the Hilbert space of a complicated system can fragment into a myriad of dynamically decoupled sectors which may not appear if one only examines global conservation laws [13, 101]. However, as with MBL, the features of scarred systems are being thoroughly examined and documented. The main feature of scarred systems are sharp quantum revivals of states initialized within the scarred subspace, quantified by e.g. a Loschmidt echo [102, 103]. In practice, a state initially prepared in the scarred subspace will appear to be erased - as though the system has thermalized - then will suddenly re-emerge at a time much less than the recurrence times of the full closed system. This effect is shown in Fig. 1.2 retrieved from Ref. [99], the landmark work of Bernien et al. which shows revivals in the domain wall density of a Rydberg array that have a size-independent frequency. This has led to scars too being touted as having a kind of 'memory' which may be accessible and technologically exploitable. I interrogate this claim in Section 2.3, and investigate the ground state phase diagram of a scarred system in Section 3.2.4.

Ultimately, scars do not form an overwhelming part of this thesis. Where they

do appear, I mostly use them as an example of another setting in which non-ergodic effects may lead to local memory. This, in turn, warrants their investigation through the lens of the informational approach. As such this overview is intentionally cursory, and I would direct the interested reader towards Refs. [13] and [104], two excellent and detailed reviews of the topic.

References

[1] John Preskill. Quantum computing in the NISQ era and beyond. *Quantum*, 2:79, aug 2018.

[2] Alexander Nico-Katz, Abolfazl Bayat, and Sougato Bose. Information-theoretic memory scaling in the many-body localization transition. *Physical Review B*, 105(20):205133, 2022.

[3] Alexander Nico-Katz, Abolfazl Bayat, and Sougato Bose. Memory hierarchy for many-body localization: Emulating the thermodynamic limit. *Physical Review Research*, 4(3):033070, 2022.

[4] Alexander Nico-Katz and Sougato Bose. Entanglement-complexity geometric measure. *Physical Review Research*, 5(1):013041, 2023.

[5] Alexander Nico-Katz, Gulzat Jaliel, Paola Atkinson, Thomas A Mitchell, David A Ritchie, Charles G Smith, and Sougato Bose. Identifying many-body localization in realistic dot arrays. *arXiv preprint arXiv:2301.08246*, 2023.

[6] Claude Elwood Shannon. A mathematical theory of communication. *The Bell system technical journal*, 27(3):379–423, 1948.

[7] A Ya Khinchin. *Mathematical foundations of information theory*. Courier Corporation, 2013.

[8] Velimir M. Ilić and Miomir S. Stanković. Generalized shannon–khinchin axioms and uniqueness theorem for pseudo-additive entropies. *Physica A: Statistical Mechanics and its Applications*, 411:138–145, 2014.

[9] Charlie Magee. The age of imagination: Coming soon to a civilization near you. In *Second International Symposium: National Security & National Competitiveness: Open Source Solutions*, volume 1, 1993.

[10] Rita J King. The emergence of a new global culture in the imagination age. *British Council*, 2007.

[11] Luca D'Alessio, Yariv Kafri, Anatoli Polkovnikov, and Marcos Rigol. From quantum chaos and eigenstate thermalization to statistical mechanics and thermodynamics. *Advances in Physics*, 65(3):239–362, May 2016.

[12] J. von Neumann. Proof of the ergodic theorem and the h-theorem in quantum mechanics. *The European Physical Journal H*, 35(2):201–237, sep 2010.

[13] Sanjay Moudgalya, B Andrei Bernevig, and Nicolas Regnault. Quantum many-body scars and hilbert space fragmentation: a review of exact results. *Reports on Progress in Physics*, 85(8):086501, jul 2022.

[14] Masahito Ueda. Quantum equilibration, thermalization and prethermalization in ultracold atoms. *Nature Reviews Physics*, 2(12):669–681, 2020.

[15] J. M. Deutsch. Quantum statistical mechanics in a closed system. *Phys. Rev. A*, 43:2046–2049, Feb 1991.

[16] Mark Srednicki. Chaos and quantum thermalization. *Phys. Rev. E*, 50:888–901, Aug 1994.

[17] Mark Srednicki. The approach to thermal equilibrium in quantized chaotic systems. 32(7):1163–1175, jan 1999.

[18] Marcos Rigol, Vanja Dunjko, and Maxim Olshanii. Thermalization and its mechanism for generic isolated quantum systems. *Nature*, 452(7189):854–858, Apr 2008.

[19] P. W. Anderson. Absence of diffusion in certain random lattices. *Phys. Rev.*, 109:1492–1505, Mar 1958.

[20] D.M. Basko, I.L. Aleiner, and B.L. Altshuler. Metal–insulator transition in a weakly interacting many-electron system with localized single-particle states. *Annals of Physics*, 321(5):1126–1205, May 2006.

[21] Arijeet Pal and David A. Huse. Many-body localization phase transition. *Physical Review B*, 82(17), Nov 2010.

[22] Michael Schreiber, Sean S. Hodgman, Pranjal Bordia, Henrik P. Lüschen, Mark H. Fischer, Ronen Vosk, Ehud Altman, Ulrich Schneider, and Immanuel Bloch. Observation of many-body localization of interacting fermions in a quasirandom optical lattice. *Science*, 349(6250):842–845, 2015.

[23] John Z. Imbrie. On many-body localization for quantum spin chains. *Journal of Statistical Physics*, 163(5):998–1048, Apr 2016.

[24] Dmitry A. Abanin, Ehud Altman, Immanuel Bloch, and Maksym Serbyn. Colloquium: Many-body localization, thermalization, and entanglement. *Rev. Mod. Phys.*, 91(2):21001, 2019.

[25] Rahul Nandkishore and David A. Huse. Many-body localization and thermalization in quantum statistical mechanics. *Annual Review of Condensed Matter Physics*, 6(1):15–38, mar 2015.

[26] Fabien Alet and Nicolas Laflorencie. Many-body localization: An introduction and selected topics. *Comptes Rendus Physique*, 19(6):498–525, sep 2018.

[27] Dmitry A. Abanin and Zlatko Papić. Recent progress in many-body localization. *Ann. Phys. (Leipzig)*, 529(7):1700169, 2017.

[28] Tarun Grover. Certain general constraints on the many-body localization transition, 2014.

[29] David J. Luitz, Nicolas Laflorencie, and Fabien Alet. Many-body localization edge in the random-field Heisenberg chain. *Phys. Rev. B*, 91(8):081103, 2015.

[30] Andrew C. Potter, Romain Vasseur, and S. A. Parameswaran. Universal properties of many-body delocalization transitions. *Phys. Rev. X*, 5(3):031033, 2015.

[31] Vedika Khemani, S. P. Lim, D. N. Sheng, and David A. Huse. Critical properties of the many-body localization transition. *Phys. Rev. X*, 7:021013, Apr 2017.

[32] Vedika Khemani, D. N. Sheng, and David A. Huse. Two universality classes for the many-body localization transition. *Phys. Rev. Lett.*, 119:075702, Aug 2017.

[33] Thimothée Thiery, François Huveneers, Markus Müller, and Wojciech De Roeck. Many-body delocalization as a quantum avalanche. *Physical Review Letters*, 121(14), Oct 2018.

[34] Anna Goremykina, Romain Vasseur, and Maksym Serbyn. Analytically solvable renormalization group for the many-body localization transition. *Phys. Rev. Lett.*, 122:040601, Jan 2019.

[35] Philipp T. Dumitrescu, Anna Goremykina, Siddharth A. Parameswaran, Maksym Serbyn, and Romain Vasseur. Kosterlitz-thouless scaling at many-body localization phase transitions. *Physical Review B*, 99(9), Mar 2019.

[36] Alan Morningstar, David A. Huse, and John Z. Imbrie. Many-body localization near the critical point. *Physical Review B*, 102(12), Sep 2020.

[37] Maksym Serbyn, Z. Papić, and Dmitry A. Abanin. Local conservation laws and the structure of the many-body localized states. *Phys. Rev. Lett.*, 111:127201, Sep 2013.

[38] David A. Huse, Rahul Nandkishore, and Vadim Oganesyan. Phenomenology of fully many-body-localized systems. *Phys. Rev. B*, 90:174202, Nov 2014.

[39] V. Ros, M. Müller, and A. Scardicchio. Integrals of motion in the many-body localized phase. *Nuclear Physics B*, 891:420–465, Feb 2015.

[40] Anushya Chandran, Isaac H. Kim, Guifre Vidal, and Dmitry A. Abanin. Constructing local integrals of motion in the many-body localized phase. *Phys. Rev. B*, 91:085425, Feb 2015.

[41] David J. Luitz, Nicolas Laflorencie, and Fabien Alet. Extended slow dynamical regime close to the many-body localization transition. *Phys. Rev. B*, 93(6):060201, 2016.

[42] Fernando Iemini, Angelo Russomanno, Davide Rossini, Antonello Scardicchio, and Rosario Fazio. Signatures of many-body localization in the dynamics of two-site entanglement. *Phys. Rev. B*, 94(21):214206, 2016.

[43] Emanuele Levi, Markus Heyl, Igor Lesanovsky, and Juan P. Garrahan. Robustness of many-body localization in the presence of dissipation. *Physical Review Letters*, 116(23), Jun 2016.

[44] Jae-yoon Choi, Sebastian Hild, Johannes Zeiher, Peter Schauß, Antonio Rubio-Abadal, Tarik Yefsah, Vedika Khemani, David A Huse, Immanuel Bloch, and Christian Gross. Exploring the many-body localization transition in two dimensions. *Science*, 352(6293):1547–1552, 2016.

[45] Henrik P. Lüschen, Pranjal Bordia, Sean S. Hodgman, Michael Schreiber, Saubhik Sarkar, Andrew J. Daley, Mark H. Fischer, Ehud Altman, Immanuel Bloch, and Ulrich Schneider. Signatures of many-body localization in a controlled open quantum system. *Physical Review X*, 7(1), Mar 2017.

[46] Pranjal Bordia, Henrik Lüschen, Sebastian Scherg, Sarang Gopalakrishnan, Michael Knap, Ulrich Schneider, and Immanuel Bloch. Probing slow relax-

ation and many-body localization in two-dimensional quasiperiodic systems. *Phys. Rev. X*, 7(4):041047, 2017.

[47] J. Eisert, M. Cramer, and M. B. Plenio. Area laws for the entanglement entropy - a review. *Rev. Mod. Phys.*, 82:277–306, Feb 2010.

[48] Tarun Grover. Certain General Constraints on the Many-Body Localization Transition. 2014.

[49] Bela Bauer and Chetan Nayak. Area laws in a many-body localized state and its implications for topological order. *J. Stat. Mech.: Theory Exp.*, 2013(09):09005, 2013.

[50] Jonas A. Kjäll, Jens H. Bardarson, and Frank Pollmann. Many-body localization in a disordered quantum ising chain. *Phys. Rev. Lett.*, 113(10):1–7, 2014.

[51] Marko Žnidarič, Tomaž Prosen, and Peter Prelovšek. Many-body localization in the Heisenberg XXZ magnet in a random field. *Phys. Rev. B*, 77(6):064426, 2008.

[52] Jens H. Bardarson, Frank Pollmann, and Joel E. Moore. Unbounded growth of entanglement in models of many-body localization. *Phys. Rev. Lett.*, 109:017202, Jul 2012.

[53] Loïc Herviou, Jens H. Bardarson, and Nicolas Regnault. Many-body localization in a fragmented hilbert space. *Phys. Rev. B*, 103:134207, Apr 2021.

[54] Maksym Serbyn, Z. Papić, and Dmitry A. Abanin. Universal slow growth of entanglement in interacting strongly disordered systems. *Phys. Rev. Lett.*, 110:260601, Jun 2013.

[55] Rajeev Singh, Jens H Bardarson, and Frank Pollmann. Signatures of the many-body localization transition in the dynamics of entanglement and bipartite fluctuations. *New Journal of Physics*, 18(2):023046, Feb 2016.

[56] Ken Xuan Wei, Chandrasekhar Ramanathan, and Paola Cappellaro. Exploring Localization in Nuclear Spin Chains. *Phys. Rev. Lett.*, 120(7):070501, 2018.

[57] Soumya Bera and Arul Lakshminarayan. Local entanglement structure across a many-body localization transition. *Phys. Rev. B*, 93(13):134204, 2016.

[58] Giuseppe De Tomasi, Soumya Bera, Jens H. Bardarson, and Frank Pollmann. Quantum Mutual Information as a Probe for Many-Body Localization. *Phys. Rev. Lett.*, 118(1):48–50, 2017.

[59] Yevgeny Bar Lev, Guy Cohen, and David R. Reichman. Absence of diffusion in an interacting system of spinless fermions on a one-dimensional disordered lattice. *Phys. Rev. Lett.*, 114(10):100601, 2015.

[60] Vadim Oganesyan and David A. Huse. Localization of interacting fermions at high temperature. *Phys. Rev. B*, 75(15):155111, 2007.

[61] Jonas A. Kjäll. Many-body localization and level repulsion. *Phys. Rev. B*, 97:035163, 2018.

[62] Pedro Ponte, Z. Papić, François Huveneers, and Dmitry A. Abanin. Many-body localization in periodically driven systems. *Physical Review Letters*, 114(14), Apr 2015.

[63] Bitan De, Piotr Sierant, and Jakub Zakrzewski. On intermediate statistics across many-body localization transition, 2021.

[64] Pil Hun Song and Dima L Shepelyansky. Low energy transition in spectral statistics of 2D interacting fermions. *Phys. Rev. B*, 61:15546–15549, Jun 2000.

[65] Piotr Sierant, Dominique Delande, and Jakub Zakrzewski. Many-body localization due to random interactions. *Phys. Rev. A*, 95:021601, Feb 2017.

[66] Johnnie Gray, Sougato Bose, and Abolfazl Bayat. Many-body localization transition: Schmidt gap, entanglement length, and scaling. *Phys. Rev. B*, 97(20):201105, 2018.

[67] Ming Gong, Gentil D. de Moraes Neto, Chen Zha, Yulin Wu, Hao Rong, Yangsen Ye, Shaowei Li, Qingling Zhu, Shiyu Wang, Youwei Zhao, and et al. Experimental characterization of the quantum many-body localization transition. *Physical Review Research*, 3(3), Jul 2021.

[68] J. Smith, A. Lee, P. Richerme, B. Neyenhuis, P. W. Hess, P. Hauke, M. Heyl, D. A. Huse, and C. Monroe. Many-body localization in a quantum simulator with programmable random disorder. *Nat. Phys.*, 12(10):907–911, 2016.

[69] Alexander Lukin, Matthew Rispoli, Robert Schittko, M. Eric Tai, Adam M. Kaufman, Soonwon Choi, Vedika Khemani, Julian Léonard, and Markus Greiner. Probing entanglement in a many-body-localized system. *Science*, 364(6437):256–260, 2019.

[70] Antonio Rubio-Abadal, Jae Yoon Choi, Johannes Zeiher, Simon Hollerith, Jun Rui, Immanuel Bloch, and Christian Gross. Many-Body Delocalization in the Presence of a Quantum Bath. *Phys. Rev. X*, 9(4):041014, 2019.

[71] P. Roushan, C. Neill, J. Tangpanitanon, V. M. Bastidas, A. Megrant, R. Barends, Y. Chen, Z. Chen, B. Chiaro, A. Dunsworth, A. Fowler, B. Foxen, M. Giustina, E. Jeffrey, J. Kelly, E. Lucero, J. Mutus, M. Neeley, C. Quintana, D. Sank, A. Vainsencher, J. Wenner, T. White, H. Neven, D. G. Angelakis, and J. Martinis. Spectroscopic signatures of localization with interacting photons in superconducting qubits. *Science*, 358(6367):1175–1179, 2017.

[72] Christoph Berke, Evangelos Varvelis, Simon Trebst, Alexander Altland, and David P. DiVincenzo. Transmon platform for quantum computing challenged by chaotic fluctuations. *Nature Communications*, 13(1), may 2022.

[73] S. Sachdev. *Quantum phase transitions*. Cambridge University Press, Cambridge, second edition, 2011.

[74] Rahul Nandkishore and David A Huse. Many-body localization and thermalization in quantum statistical mechanics. *Annu. Rev. Condens. Matter Phys.*, 6(1):15–38, 2015.

[75] Maksym Serbyn, Z. Papic, and Dmitry A. Abanin. Criterion for many-body localization-delocalization phase transition. *Phys. Rev. X*, 5(4):21–27, 2015.

[76] Kai Xu, Jin Jun Chen, Yu Zeng, Yu Ran Zhang, Chao Song, Wuxin Liu, Qiujiang Guo, Pengfei Zhang, Da Xu, Hui Deng, Keqiang Huang, H. Wang, Xiaobo Zhu, Dongning Zheng, and Heng Fan. Emulating Many-Body Localization with a Superconducting Quantum Processor. *Phys. Rev. Lett.*, 120(5):050507, 2018.

[77] Chen Zha, V.M. Bastidas, Ming Gong, Yulin Wu, Hao Rong, Rui Yang, Yangsen Ye, Shaowei Li, Qingling Zhu, Shiyu Wang, and et al. Ergodic-localized junctions in a periodically driven spin chain. *Physical Review Letters*, 125(17), Oct 2020.

[78] Qiujiang Guo, Chen Cheng, Hekang Li, Shibo Xu, Pengfei Zhang, Zhen Wang, Chao Song, Wuxin Liu, Wenhui Ren, Hang Dong, Rubem Mondaini, and H. Wang. Stark many-body localization on a superconducting quantum processor, 2020.

[79] Qiujiang Guo, Chen Cheng, Zheng-Hang Sun, Zixuan Song, Hekang Li, Zhen Wang, Wenhui Ren, Hang Dong, Dongning Zheng, Yu-Ran Zhang, and et al. Observation of energy-resolved many-body localization. *Nature Physics*, 17(2):234–239, Sep 2020.

[80] Cécile Monthus. Many-body-localization transition in the strong disorder limit: Entanglement entropy from the statistics of rare extensive resonances. *Entropy*, 18(4), 2016.

[81] A. B. Harris. Effect of random defects on the critical behaviour of Ising models. *Journal of Physics C Solid State Physics*, 7(9):1671–1692, May 1974.

[82] J. T. Chayes, L. Chayes, Daniel S. Fisher, and T. Spencer. Finite-size scaling and correlation lengths for disordered systems. *Phys. Rev. Lett.*, 57:2999–3002, Dec 1986.

[83] A. Chandran, C. R. Laumann, and V. Oganesyan. Finite size scaling bounds on many-body localized phase transitions, 2015.

[84] Michael E. Fisher and Michael N. Barber. Scaling theory for finite-size effects in the critical region. *Phys. Rev. Lett.*, 28:1516–1519, Jun 1972.

[85] J T Edwards and D J Thouless. Numerical studies of localization in disordered systems. *Journal of Physics C: Solid State Physics*, 5(8):807–820, apr 1972.

[86] Maksym Serbyn, Z. Papić, and Dmitry A. Abanin. Thouless energy and multifractality across the many-body localization transition. *Physical Review B*, 96(10), Sep 2017.

[87] Piotr Sierant, Dominique Delande, and Jakub Zakrzewski. Thouless time analysis of anderson and many-body localization transitions. *Phys. Rev. Lett.*, 124:186601, May 2020.

[88] Alvaro Corral, Rosalba Garcia-Millan, and Francesc Font-Clos. Exact derivation of a finite-size scaling law and corrections to scaling in the geometric galton-watson process. *PLOS ONE*, 11(9):e0161586, Sep 2016.

[89] E Brézin. An investigation of finite size scaling. *Journal de Physique*, 43(1):15–22, 1982.

[90] John Cardy. *Finite-size scaling*. Elsevier, 2012.

[91] Harris A Brooks. The 'harris criterion' lives on. *Journal of Physics: Condensed Matter*, 28(42):421006, aug 2016.

[92] Jan Šuntajs, Janez Bonča, Tomaž Prosen, and Lev Vidmar. Quantum chaos challenges many-body localization. *Physical Review E*, 102(6), Dec 2020.

[93] Nicolas Laflorencie, Gabriel Lemarié, and Nicolas Macé. Chain breaking and kosterlitz-thouless scaling at the many-body localization transition in the random-field heisenberg spin chain. *Physical Review Research*, 2(4), Nov 2020.

[94] Zheng-Hang Sun, Jian Cui, and Heng Fan. Characterizing the many-body localization transition by the dynamics of diagonal entropy. *Phys. Rev. Research*, 2:013163, Feb 2020.

[95] Ronen Vosk, David A. Huse, and Ehud Altman. Theory of the many-body localization transition in one-dimensional systems. *Phys. Rev. X*, 5(3):031032, 2015.

[96] Philipp T. Dumitrescu, Romain Vasseur, and Andrew C. Potter. Scaling theory of entanglement at the many-body localization transition. *Physical Review Letters*, 119(11), Sep 2017.

[97] Shi Xin Zhang and Hong Yao. Universal Properties of Many-Body Localization Transitions in Quasiperiodic Systems. *Phys. Rev. Lett.*, 121(20):206601, 2018.

[98] Alan Morningstar and David A. Huse. Renormalization-group study of the many-body localization transition in one dimension. *Physical Review B*, 99(22), Jun 2019.

[99] Hannes Bernien, Sylvain Schwartz, Alexander Keesling, Harry Levine, Ahmed Omran, Hannes Pichler, Soonwon Choi, Alexander S. Zibrov, Manuel Endres, Markus Greiner, Vladan Vuletić, and Mikhail D. Lukin.

Probing many-body dynamics on a 51-atom quantum simulator. *Nature*, 551(7682):579–584, Nov 2017.

[100] Anushya Chandran, Thomas Iadecola, Vedika Khemani, and Roderich Moessner. Quantum many-body scars: A quasiparticle perspective. *Annual Review of Condensed Matter Physics*, 14(1):443–469, 2023.

[101] Pablo Sala, Tibor Rakovszky, Ruben Verresen, Michael Knap, and Frank Pollmann. Ergodicity breaking arising from hilbert space fragmentation in dipole-conserving hamiltonians. *Phys. Rev. X*, 10:011047, Feb 2020.

[102] Christopher J Turner, Alexios A Michailidis, Dmitry A Abanin, Maksym Serbyn, and Zlatko Papić. Weak ergodicity breaking from quantum many-body scars. *Nature Physics*, 14(7):745–749, 2018.

[103] C. J. Turner, A. A. Michailidis, D. A. Abanin, M. Serbyn, and Z. Papić. Quantum scarred eigenstates in a rydberg atom chain: Entanglement, breakdown of thermalization, and stability to perturbations. *Phys. Rev. B*, 98:155134, Oct 2018.

[104] Maksym Serbyn, Dmitry A Abanin, and Zlatko Papić. Quantum many-body scars and weak breaking of ergodicity. *Nature Physics*, 17(6):675–685, 2021.

Chapter 2

Memory in Ergodicity-Breaking Systems

"A way a lone a last a loved a long the"

— James Joyce

"You say memory too much."

— Abolfazl Bayat
Giving me feedback on our article.

In this chapter I examine the idea of 'local memory', a feature of certain condensed matter systems in which subsystems retain information about their initial state (see e.g. Refs [1, 2]). By interrogating the meaning of 'local memory' as it is used in contemporary literature, I contend that the current working quantifications of memory (for there are several) are either loose, underdeveloped, or not particularly useful. Exploiting the 'accessible information game' - an import from the quantum information community - as a bedrock on which to build an operational definition of memory, I define a brief criteria by which quantifiers of memory can be identified. I then apply this criteria, as well as several other quantities widely used in quantum information theory, to interrogate memory in two popular types of ergodicity-breaking condensed matter contexts: MBL and quantum scars. The introductory sections of this chapter, as well as the analysis of MBL in Section 2.2 is adapted from my published works in Refs. [3, 4].

I argue in Section 2.1 that the definitions (for there are several) of 'memory' in a condensed matter context are woefully loose, underdeveloped, and not particularly useful. It is in this context that I introduce the 'accessible information game', an import from the quantum information community that I can exploit as the bedrock for an operational definition of memory. This leads to a brief criteria which a true information-theoretic quantifier of memory must satisfy.

I draw attention to Section 2.1.2 and Section 2.1.3 which concerned with the Holevo quantity and the quantum coherent information respectively. These two quantities are critical to this chapter and encapsulate generally useful ideas surrounding the 'accessible information game' which is played throughout this entire thesis. The Holevo quantity in particular is incarnated into several forms throughout this thesis. For interested readers, much of these sections are covered in far greater detail in Preskill's famous quantum computation notes (see Ref. [5]); though I do not adapt from these notes directly.

I subsequently apply the devised definitions and quantities to analyses of memory in two popular types of ergocity-breaking condensed matter systems: MBL in Section 2.2 and quantum scars in Section 2.3. In the context of MBL, I find that its value as a hard drive- as a store of memory over time - is well founded; though extant studies fail to capture how much information is actually retained. This investigation also reveals some interesting features regarding how subsystems may decohere with respect to each other in the thermodynamic limit. However, in the context of quantum scars, their value as memory stores is a much more nebulous problem. I find certain highly-constructed contexts in which they exhibit exceptional memory, retaining information at exponential timescales, though this seems to be a fragile phenomenon.

2.1 The Accessible Information Game

The 'accessible information game' is a term coined[1] in the quantum Shannon entropy section of Preskill's famous quantum computation notes. There it appears

[1] Presumably by either Preskill or Kitaev. I don't know exactly who wrote exactly what.

exactly twice, framed first as a game played by Bob when "Alice finds it easier to send signals [...] which are imperfectly distinguishable rather than mutually orthogonal", and secondly when an "experimental physicist tries to measure an unknown classical force using a quantum system as a probe" [5]. This chapter (as well as some sections of future chapters) concerns itself with the former case, though transplanted into the context of many-body condensed matter systems. The latter case is also a subject of considerable interest which represents a rising current in quantum theory which I briefly touch upon in Chapter 4: quantum metrology and sensing. However, I do not consider the ramifications of this framework on metrology and sensing in this thesis.

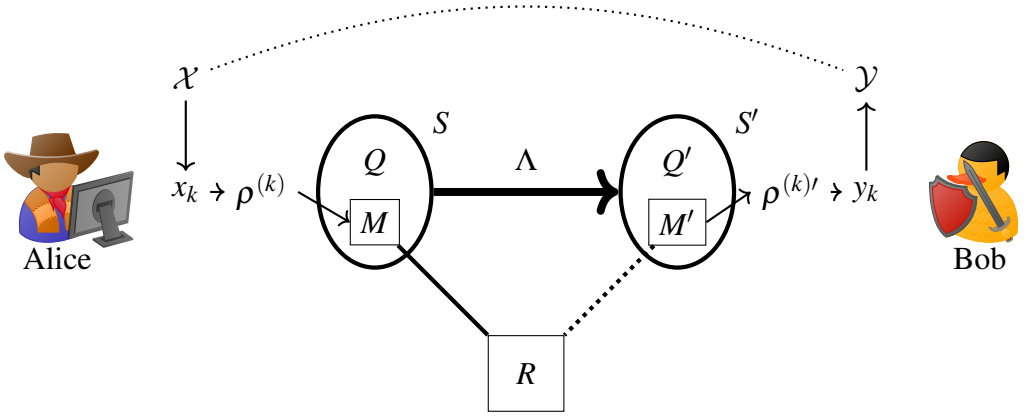

Figure 2.1: Schematic of the 'accessible information game' played by Alice and Bob. Classical information x_k drawn by Alice from $\mathcal{X}$ is encoded in the quantum state $\rho^{(k)}$ and loaded into the message register M of some larger system S. After being passed through the channel Λ and measured by Bob to produce some output y_k that defines a prior $\mathcal{Y}$, the game is decided by how well Bob can reconstruct $\mathcal{X}$ from his observed $\mathcal{Y}$.

The game itself is played thusly: Alice encodes a classical message x_k (a random variable drawn from the ensemble $\mathcal{X} = \{p_k, x_k\}$) as either classical (incoherent) or quantum (coherent) information into the state $\rho^{(k)}$ of a subsystem M the 'message register', which is in contact with the rest of the system Q such that $S = Q \cup M$. S then evolves under some CPTP quantum channel Λ, and Bob performs some measurements on the message register M' of the resulting system S' and receives a decoded message y_k which defines a prior Y. Alice and Bob may both optionally access a reference state R which is a purification of the initial state of the message

register M. The game is decided by how well Bob can reconstruct X from Y, and is shown schematically in Fig. 2.1.

The key twist in this thesis is that S is actually - rather than simply in principle - a messy, complicated, many-body quantum system. In this context, the abstract framework above can be understood as encapsulating a vast range of protocols in current-generation quantum devices, from conventional communication between two parties, to information storage or 'local memory' if Alice and Bob decide to treat M as a quantum 'hard drive' of sorts. That is to say that they are the same person who discards all information about X after encoding $\rho^{(k)}$ into M, and who returns later to reconstruct the information using only M'. Clearly, if modern noisy-intermediate-scale quantum (NISQ) devices are ever to be taken seriously as actual computational platforms, these protocols need to be theoretically understood and experimentally interrogated. This chapter investigates the latter protocol: the nature and quantification of 'local memory' in many-body quantum systems, and the consequent potential value of such systems as quantum 'hard drives'.

2.1.1 What Is, and Isn't, Memory: An Operational Definition

Despite the fact that 'local memory' is widely quoted in the literature, especially in MBL literature, it is infrequently the subject of direct investigation. In this section I leverage the ideas of Section 2.1 into an operational definition of a true memory quantifier. I then discuss the ways in which memory has been captured in MBL systems before, and outlines their shortcomings. Given the framing of condensed matter systems as mediating an 'accessible information game', it is natural to leverage that framing into an actual definition of 'local memory'.

The operational definition of a memory quantifier that I suggest, as preempted by the preceding section Section 2.1, is extremely simple. A memory quantifier should satisfy two criteria: (i) it should yield a number of bits of information that can be extracted from the system in question and (ii) it should contain non-trivial temporal correlations with reference to some initial state. Despite the simplicity of these requirements, many widely-used signatures of information spreading or retention in a condensed matter context do not satisfy them; I outline relevant examples

below.

In theoretical and experimental studies alike 'memory' is most frequently discussed in terms of non-zero steady-states of appropriate observables, notably quantities derived from local magnetization or occupancy measurements [1, 6–10]. Should these measurements systematically coincide with similar measurements made on the initial state of the system, then system has retained some 'local memory' of those initial features. A generic starting point for constructing quantities of this kind is the autocorrelation function:

$$F(t) = \left\langle \hat{W}(0)\hat{W}(t) \right\rangle \tag{2.1}$$

of some appropriate observable $\hat{W}$. The premier example here is the imbalance, used extensively in MBL literature and to great effect in landmark experiments (see, for example, Ref. [11–15]). It is defined in terms of local fermionic number expectation values $\langle \hat{n}_j(t) \rangle = n_j(t)$ where j indexes sites on a lattice. If the initial system is in some charge density wave configuration then the aggregate deviation of the $n_j(t)$ from their initial values $n_j(0)$ quantifies how well the system remembers its initial number configuration. The prototypical example, for a system of spinless fermions such that $n_j(t) \in [0,1]$ and initialised in the charge density wave state $|0,1,0,\cdots,0,1\rangle$, the imbalance is defined as:

$$\mathcal{I}(t) = \frac{N_e(t) - N_o(t)}{N_e(t) + N_o(t)} \tag{2.2}$$

where $N_{e(o)} = \sum_{j \in \text{even}(odd)} n_j(t)$ is the total number of fermions on even (odd) sites. The initial state has all even sites unoccupied, and all odd sites occupied, so $\mathcal{I}(0) = 1$. As the system evolves, it can either thermalize to homogeneity such that the initial configuration is lost $\lim_{t\to\infty} \mathcal{I}(t) = 0$, else it can relax to a state which is either correlated $\lim_{t\to\infty} \mathcal{I}(t) > 0$ or anti-correlated $\lim_{t\to\infty} \mathcal{I}(t) < 0$ with the initial configuration.

It is often argued that a more sophisticated grasp of memory can be attained by

investigating the growth of the out-of-time-order correlator (OTOC)

$$O^{WV}(t) = \left\langle [W(t), V(0)]^{\dagger} [W(t), V(0)] \right\rangle_{\beta} \tag{2.3}$$

for some appropriately chosen, spatially separated, operators $\hat{W}$ and $\hat{V}$, which initially commute. The angle braces $\langle \cdot \rangle_{\beta}$ here denote the thermal average at inverse temperature β. Originally envisaged as an analogy to the classical Poisson bracket as a measure of quantum chaos, it can also be interpreted as an indirect measure of information scrambling: the speed and strength with which the effect of the perturbation $\hat{V}$ is felt by the distant $\hat{W}$ tells us how quickly information is carried through the system. In ergodic systems the effect of the perturbation spreads rapidly and the OTOC grows exponentially in time $O^{WV}(t) \sim e^{\lambda_L t}$ at a rate governed by the Lyapunov exponent λ_L; whilst in the localized phase this growth appears logarithmic or power-law [16, 17].

More precisely, the OTOC quantifies the spreading of the support of the operator $\hat{W}(t)$ onto the support of the operator $\hat{V}$. If they share support, then information about one can be non-locally inferred from the other. Thus an OTOC depends on an appropriate choice of operators, has no clear interpretation in terms of how may bits of information can actually be extracted from a subsystem, and is exceedingly difficult to measure experimentally.

Finally, local memory can be inferred without appealing to explicit temporal correlations by monitoring, e.g., the growth of entanglement entropies, spatial correlators, the spatial mutual information, and the emergence of local integrals of motion [18, 19]. Some of these quantities have obvious bit-wise informational interpretations, or are advantageously blind to the specifics of measurement procedure, but unilaterally lack any kind of temporality.

In summary, the prevailing methods by which memory is accessed in MBL systems all have respective strengths and shortcomings. The dynamics of local observables like the magnetization and imbalance are experimentally tractable and temporally connect the initial conditions with late-time measurements; but can be rendered useless by a poor choice of measurement basis, and do not immedi-

ately quantify how much information - in bits - can be extracted from a subsystem. OTOCs, whilst much more sophisticated and theoretically invaluable, suffer similarly from the specification of perturbation/measurement operators and the lack of a bitwise interpretation, and aren't readily accessible to experimental. Quantities like the entropy and spatial mutual information are informational, but lack the temporal correlations necessary to act as true memory quantifiers.

Over the next few sections I introduce and compare a myriad of quantities, most of which satisfy these conditions of a memory quantifier and which interrogate memory in different ways.

2.1.2 The Holevo Quantity

The Holevo quantity - first introduced by Alexander Holevo in Ref. [20][2] - quantifies the maximum amount of accessible (classical) information in a given system. This definition is worth unpicking in detail as it undergirds the definition of the quantum coherent information discussed in Section 2.1.3, and is bluntly wielded as a memory quantifier throughout much of this thesis.

Formally, one can consider Alice encoding the elements $\{x_k\}$ of an alphabet X in the states $\{\rho^{(k)}\}$, each with probability p_k. Alice then passes these states, each bearing some classical information, to Bob who may then perform any generic positive operator-valued measure (POVM) measurements on it. The readout of these measurements yield to Bob a corresponding alphabet Y of classical outcomes $\{y_k\}$, each with probability q_k. The accessible information is then defined as the mutual information

$$H(X:Y) = H(X) + H(Y) - H(X,Y) \tag{2.4}$$

where $H(X) = -\sum_j p_j \log_2 p_j$ is the Shannon entropy of X, $H(Y)$ is the corresponding Shannon entropy of Y, and $H(X,Y)$ is their joint entropy[21]. The Holevo quantity is solely a function of the input ensemble $\{p_k, \rho^{(k)}\}$ and is defined as follows

$$C(\{p_k,\rho^{(k)}\}) = S\left(\sum_k p_k \rho^{(k)}\right) - \sum_k p_k S\left(\rho^{(k)}\right) \tag{2.5}$$

[2]I must admit that I have not read this paper - it is written in Russian.

where $S(\rho) = -\mathrm{Tr}[\rho \log_2 \rho]$ is the von Neumann entanglement entropy. The defining feature of the Holevo quantity is that it upper-bounds the accessible information

$$H(X:Y) \leq C(\{p_k, \rho^{(k)}\}) \tag{2.6}$$

and thus represents the upper limit on how much information about X Bob can reconstruct given Y after X has been passed through a quantum channel. This result is called the Holevo bound, or Holevo's theorem. The proof of the inequality of Eq. (2.6) is simply and elegantly given in the excellent textbook of Nielsen and Chaung (see Ref. [22]), as are several applications of the Holevo quantity.

It is worth discussing some important features of the Holevo quantity of Eq. (2.5) before applying it in earnest to condensed matter systems. First of all it is entirely independent of the measurements made by Bob, any increase in the Holevo quantity - and a commensurate increase in the maximum possible accessible information - is completely controlled by Alice. This makes some intuitive sense, the inequality defines only an *upper* bound. Bob can always perform a pointless or stupid measurement, or spill his coffee all over Y, and whilst the accessible information $H(X:Y)$ decreases, the Holevo quantity does not. Bob can, in these situations, just select a better POVM or tidy his desk a bit before trying to do quantum physics. However the best that dear Bob can possibly do, even with a generous EPSRC grant and perfectly commuting measurements, is ultimately contingent on Alice's ensemble.

Secondly, if Alice can tune the ensemble $\{p_k, \rho^{(k)}\}$ freely, the Holevo quantity can be maximized by setting all the $\rho^{(k)}$ to pure orthogonal states and setting all p_k equal. This corresponds to Alice encoding and transmitting her classical message by writing it down on a sheet of paper and just handing it to Bob - no quantumness required. Again, Bob can always screw this up by being a clumsy idiot, but in theory he can always determine X perfectly - he can just read it.

The true power of the Holevo quantity, and the upper bound it defines, lies somewhere between these two extremes. Let's assume that I have been too harsh on Bob, and that he's really is trying his best. Let's also assume that Alice's messages

are closer perhaps to a conventional alphabet - that she has very limited control over the states $\rho^{(k)}$, but can tune freely the probabilities p_k with which she transmits states to Bob. This, with the kind of oracular foreshadowing that only fiction authors and natural scientists can produce in their writing, is very close to the situation of transmitting messages via condensed matter systems. Alice wants to embed a message to Bob in a system which may have impurities, nonlinear interaction terms, and which will likely carry her prepared state $\rho^{(k)}$ to one that she cannot easily predict $\rho^{(k)\prime}$. This is a kind of noisy channel [23]. It is, of course, $\rho^{(k)\prime}$ that Bob receives and experiments upon. Hence, Alice cannot consistently and reliably predict or affect the states themselves, but can tweak the probabilities with which she inputs certain messages into her messy condensed matter system. It is in this framework that the game of communication and of memory retention becomes a fascinating question immediately relevant to the world of modern quantum simulation.

I formalize the above discussion by defining $\rho^{(k)\prime}$ in terms of a generic completely-positive trace preserving (CPTP) map Λ which enacts an arbitrary quantum channel $\rho^{(k)\prime} = \Lambda[\rho^{(k)}]$, resulting in a reformulated Holevo quantity

$$C\left(\left\{p_k, \Lambda\left[\rho^{(k)}\right]\right\}\right) = S\left(\sum_k p_k \Lambda[\rho^{(k)}]\right) - \sum_k p_k S\left(\Lambda\left[\rho^{(k)}\right]\right) \tag{2.7}$$

that is more generic than the original, and makes explicit that the classical messages are being passed through some quantum channel Λ which encapsulates layers of encoding, transmission, transformation, and decoding. Now the maximum amount of accessible information is contingent not only on Alice's ensemble $\{p_k, \rho^{(k)}\}$, but also the channel Λ through which she passes the state to Bob.

Furthermore, this reformulation highlights a few specific cases in which the Holevo quantity excels as a memory quantifier. Firstly it is clearly invariant under change of basis of the outcome $\Lambda[\rho^{(k)}] \to U\Lambda[\rho^{(k)}]U^\dagger$; this sidesteps all problems with Bob making a 'poor measurement'. Consider, for example, that Bob measures the two-state ensemble of X eigenstates $\{\rho_0 = |+\rangle\langle+|, \rho_1 = |-\rangle\langle-|\}$ in

the Z basis; even though the states are distinguishable and the single bit message $\{x_0 = 0, x_1 = 1\}$ can be perfectly retrieved, Bob has failed to do so due to a poor choice of measurement basis. This is ultimately due to the fact that the Holevo quantity is an intrinsic property of the ensemble $\{p_k, \Lambda[\rho^{(k)}]\}$, but it is still a fact worth explicating as - in future sections - I will consider the kind of results that Bob can *actually* achieve rather than *optimally* achieve. Secondly, and far more subtly, generic quantum channels can both increase *and* decrease the von Neumann entanglement entropy [5]. This means that states $\{\rho^{(k)}\}$ that are initially distinguishable can be transmitted to states which are indistinguishable, e.g. $\Lambda[\rho^{(k)}] = |0\rangle\langle 0| \ \forall \ k$. The Holevo quantity can be understood in the context of this fact as a delicate interplay between distinguishability and purity. If the $\Lambda[\rho^{(k)}]$ cannot be distinguished, or if they are maximally mixed, then the terms in Eq. (2.7) cancel and no information can be transmitted. Purity doesn't matter if your states aren't distinguishable, and distinguishability reduces as the states become more and more mixed. Though the examples we've outlined here are extreme, I will encounter a milder form of this behaviour later, wherein initially distinguishable pure states are mixed and rendered less distinguishable, causing the Holevo quantity to decrease.

Concluding this section, I note that the rightmost term in the definition of Eq. (2.7) is simply the mean von Neumann entanglement entropy of the states $\Lambda[\rho^{(k)}]$. Given that $\sum_k p_k \Lambda[\rho^{(k)}]$ can - at best - be the scaled identity operator $\mathbb{I}_{\dim(\mathcal{H}_\rho)}/\dim(\mathcal{H}_\rho)$ of dimension equal to the dimension $\dim(\mathcal{H}_\rho)$ of the Hilbert space in which the $\{\rho^{(k)}\}$ live, the Holevo quantity is upper-bounded in turn by the quantity

$$C(\{p_k, \rho^{(k)}\}, \Lambda) \leq \log_2 \dim(\mathcal{H}_\rho) - \sum_k p_k S(\Lambda[\rho^{(k)}]) \tag{2.8}$$

which I can interpret as quantifying the purity of the ensemble states $\rho^{(k)}$. This interpretation is of importance to the results of Section 2.2 and is a crucial benchmark given the discussion of purity and distinguishability outlined above. Additionally, given that the von Neumann entanglement entropy is widely-used in condensed matter theory as a signature of phase transitions and as evidence of information being distributed in non-local degrees of freedom, this connection serves as a useful

comparative benchmark.

2.1.3 The Quantum Coherent Information

The quantum coherent information is defined in terms of some generic system Q passed through some channel Λ and a reference system R that purifies the original state of the system Q [24]. The reference system is held 'in hand' and does not evolve (i.e. Λ only acts on Q). The definition of the quantum coherent information is simply a reformulation of the classical accessible information of Eq. (2.4) using von Neumann entanglement entropies instead of Shannon entropies

$$I_q(R\rangle Q) = S(\Lambda[\rho]^Q) - S(\Lambda[\rho]^{RQ}) \tag{2.9}$$

where ρ is the initial pure state of the entire system, $\Lambda[\rho]^Q$ is the final state of the system Q and $\Lambda[\rho]^{RQ}$ is the final state of the combined system RQ. The quantum coherent information is thought to play a similar role in quantum information theory as the mutual information does in classical information theory, satisfying equivalent quantum data processing inequalities [22]. Despite this, it does not yet have the clear informational interpretation that the Holevo quantity has.

The most notable feature of the coherent information of Eq. (2.9) is that it can be either positive or negative. The same is not true of the analogous classical quantity: the joint Shannon entropy can be decomposed as $H(R,Q) = H(R|Q) + H(Q)$ such that the entropy of the joint system can never be less than the entropy of a subsystem $H(R,Q) \geq H(Q)$. Thus the direct classical analogy of Eq. (2.9) wherein von Neumann entropies are replaced with Shannon entropies can never be positive. Thus the quantum coherent information can be used as a signature of non-classicality - signifying information that can only be stored by exploiting quantum coherence [24].

2.2 Memory in the Many-Body Localized Heisenberg Spin Chain

A key concept in MBL is the emergence of memory: the local retention of information about initial conditions. Memory is necessarily temporal and thus typically discussed through dynamical quantities such as the imbalance, steady-states of local observables, or deduced from entanglement and correlation spreading [7, 8, 15, 25–27]. As discussed in Section 2.1.1, these quantities may or may not actually capture memory.

By instead computing the Holevo quantity in Eq. (2.5) for a given input ensemble $\{p_k, \rho^{(k)}\}$ and environment state $|e\rangle$ under the action of the map $\mathcal{E}[\cdot]$ one can directly quantify how much information, in bits, can be extracted locally from the system s at time t about its initial state. This is indeed a direct, dynamical quantification of local memory in the subsystem s. The use of this quantity and several other memory quantifiers in characterising the ergodic-MBL transition is the subject of the rest of this section.

2.2.1 The Disordered Heisenberg Spin Chain

The Heisenberg chain with quenched random disorder has been used extensively in literature as a toy model of MBL, and I continue that tradition in this thesis. Enforcing periodic boundary conditions, the model is governed by the Hamiltonian

$$H = J \sum_{j=1}^{L} \vec{S}_j \cdot \vec{S}_{j+1} + \sum_{j=1}^{L} h_j S_j^z \tag{2.10}$$

where $\vec{S}_j = (S_j^x, S_j^y, S_j^z)^\top$ is a vector of the standard spin-1/2 operators, and where h_j are quenched random variables drawn uniformly from the interval $[-h, h]$ where h characterizes the disorder strength. For small system sizes, this model localizes at a critical value near $h_c \gtrsim$ [28, 29] in a fashion that looks like a second-order phase transition. However, as discussed in Section 1.3.3, the ergodic-MBL transition is not yet well understood: the apparent critical value changes dramatically as a function of system size and the transition may belong to different universality classes [30–

32].

The model of Eq. (2.10) is widely used for good reason. Short-range interactions admit simple tensor network treatments of the system. With the inclusion of a ZZ anisotropy the system can be tuned between interacting and non-interacting versions. Different forms for the h_i can lead to staggered or quasi-random Z fields with different localizing effects. It is simple, easy to implement, and highly flexible. Exploitation of these advantages in the context of MBL have in turn yielded novel advances in the analysis and simulation of condensed matter systems in general, see e.g. Refs. [33, 34].

2.2.2 The Subsystem 'Hard Drive' Protocol

In the system of L spin-1/2 particles governed by the Heisenberg model of Eq. (2.11), I can identify a subsystem of l particles (our message register) and there encode pure separable messages of the form

$$\rho^{(k)} = |x_1^{(k)}, x_2^{(k)}, \cdots, x_l^{(k)}\rangle\langle x_1^{(k)}, x_2^{(k)}, \cdots, x_l^{(k)}| = |x_k\rangle\langle x_k| \tag{2.11}$$

in which $x_i^{(k)} \in \{\uparrow, \downarrow\}$ encodes either zero $0 \rightarrow \uparrow$ or one $1 \rightarrow \downarrow$, i.e. the state of a single classical bit. In the context of the accessible information game discussed in Section 2.1, the messages $x_1^{(k)} x_2^{(k)} \cdots x_l^{(k)}$ are the classical messages x_k drawn from some alphabet $\mathcal{X}$ that Alice has encoded in the state $\rho^{(k)}$ of the message register M. The message register in this case is simply the first l sites of our model, within which the 2^l different possible classical messages that comprise the alphabet $\mathcal{X}$ can be encoded in the 2^l mutually orthogonal (and thus perfectly distinguishable) computational basis states. The message register is then embedded in an environment of size $L - l$ which is initially prepared in a pure quantum state $|E\rangle\langle E|$, this is our complement Q to the message register M such that the combined system S is the entire Heisenberg chain. The combined state of message and environment is of size L, and is initially given by the quantum state $\rho^{(k)} \otimes |E\rangle\langle E|$.

For notational convenience, I incorporate this embedding, time evolution under the Hamiltonian of Eq. (2.11), and eventual extraction of the state of the message

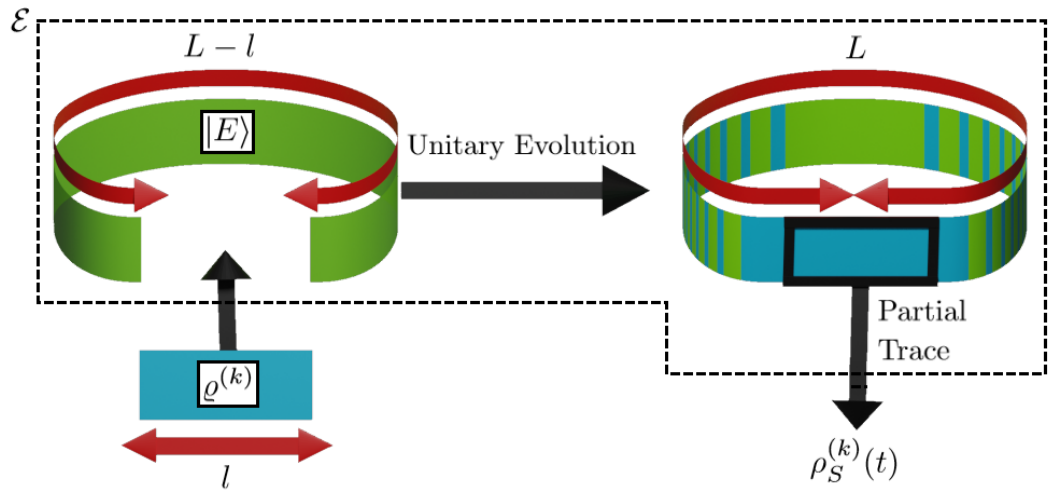

Figure 2.2: Schematic diagram of the procedure by which individual messages $\rho^{(k)}$ are transmitted via the channel Λ.

register (i.e. the partial trace over the degrees of freedom in the environment E) all into the channel Λ. The action of Λ on $\rho^{(k)}$ is thus given by

$$\Lambda^r[\rho^{(k)}] = \mathrm{Tr}_Q\left[e^{-iHt}\left(\rho^{(k)}\otimes|E\rangle\langle E|\right)e^{iHt}\right] = \rho^{(k)}(t) \tag{2.12}$$

where I have added a superscript r to the channel to serve as a notational reminder than H and E are *specific realizations* of the Hamiltonian and environment states (though for compactness I omit explicit superscripts on these symbols and on $\rho^{(k)}(t)$), and thus that Λ^r only represents a single realization of the channel. Later on I will have to average not only over the message index k, but also over many different realizations of our channel (indexed by r).

This procedure is shown schematically in Fig. 2.2, and essentially defines a kind of quantum 'hard drive'. Information initially localized within the message may bleed out into the environment during transmission, represented in the schematic by blending of the blue message with the green environment. A subsystem M embedded into a larger system Q that I want to encode information into and then retrieve at a later time. I can quantify the maximum quality of this data retrieval with the Holevo quantity of Section 2.1.2, but in practice - and as I shall demonstrate in the rest of this chapter - this protocol can admit different quantifiers of memory, different Hamiltonians, the incorporation of dissipative baths, and ar-

bitrary encoding and decoding procedures. In conjunction with the criteria given in Section 2.1.1, this general protocol gives a clear operational definition for 'local memory of initial conditions' and a systematic method for analyzing local memory in condensed matter systems by treating them as hard drives.

2.2.3 Four Hierarchical Informational Quantities

The results in the next section mainly centre on the Holevo quantity as defined in Eq. (2.7). However, it is flanked by three other quantities which inform the discussion of memory in different ways. Two are quantifiers of memory (as per the criteria laid out in Section 2.1.1) that depend on the kind of measurements that can be employed by Bob - one of which is a direct information-theoretic analogy to the imbalance of Eq. (2.2). I also discuss the simple modification of the von Neumann entanglement entropy of Eq. (2.6) which - though subtly devoid of temporal correlation and thus useless as a memory quantifier - serves as an upper-bound for all other quantities. All four quantities are summarised in Table 2.1, and defined and discussed in detail below. In this section I introduce and discuss these quantities, how they are constructed, and what they may tell us about memory in condensed matter systems.

Quantity	Memory Quantifier	Measurements	Definition
VNE	No	Full State Tomography	Eq. (2.13)
Holevo	Yes	Full State Tomography	Eq. (2.14)
CMI	Yes	Global Measurements on M	Eq. (2.18)
SSMI	Yes	Local Measurements in M	Eq. (2.16)

Table 2.1: Summary of the four quantities discussed in Section 2.2.3 based on two features: whether they hold the status of a valid memory quantifier based on the criteria laid out in Section 2.1.1, and what measurements need to be made to construct the quantity[3].

For notational convenience, I first introduce three averages: message averaging over the index k will be written out explicitly as it informs our discussion of which

[3]Full state tomography here means full extraction of all the elements of the state vector (density operator) describing the pure (mixed) state of a system (subsystem) in some convenient basis.

quantities are true memory quantifiers and takes a different form for each quantity. Channel averaging over different channel realizations Λ^r is denoted by angle brackets $\langle\cdot\rangle$, and in the case of disordered systems it is here that disorder averaging takes place. The combined effect of message averaging, channel averaging (typically a geometric mean), and normalization between zero and unity is denoted by a bar $\overline{\cdot}$. The normalization of each memory quantifier allows us to compare them directly, even for different message sizes l. This normalization also endows each memory quantifier with an additional interpretation: as the a kind of density or rate of information transfer. That is to say, the amount of information - in bits - that can be reliably transmitted per component of the message register M.

The first quantity of relevance is the simple modification of the von Neumann entropy introduced in Eq. (2.6) and the associated discussion:

$$\overline{P(t)} = 1 - \overline{S(t)} = \frac{1}{l}\left\langle l - \sum_k p_k S(\rho^{(k)}(t)) \right\rangle. \tag{2.13}$$

This modified von Neumann entropy is bounded as $0 \leq \overline{P(t)} \leq 1$, and upper bounds all further quantities. In the perfect transmission regime, wherein $\Lambda^r[\rho^{(k)}] = \rho^{(k)} = |x_k\rangle\langle x_k|$, all terms in the sum are zero and the upper limit $\overline{P(t)} \to 1$ is saturated; in the complete scrambling limit each $\rho^{(k)}(t) \to \mathbb{I}/2^l$, all terms in the sum are $p_k l$, and I saturate the lower limit $\overline{P(t)} \to 0$.

Though the presence of p_k in Eq. (2.13) suggests the existence of temporal correlations - promoting this quantity to the status of a memory quantifier - this is not in fact true. Consider again the channel which sends all initial states $\{\rho^{(k)}\}$ to the single pure state $|0\rangle$. Clearly this channel is entirely useless for transmitting information, but Eq. (2.13) still saturates the upper limit $\overline{P(t)} \to 1$. Rather, the quantity $\overline{P(t)}$ characterizes the average *instantaneous* mixedness of the ensemble $\{\rho^{(k)}(t)\}$, not how well that ensemble can actually bear information from the past or into the future.

The Holevo quantity can consequently be interpreted as a minor correction to Eq. (2.13) that compensates for this issue by taking state distinguishability into

account:

$$\overline{C(t)} = \frac{1}{l}\left\langle S\left(\sum_k p_k \rho^{(k)}(t)\right) - \sum_k p_k S(\rho^{(k)}(t))\right\rangle \tag{2.14}$$

clearly the new term saturates to l as $\sum_k p_k \rho^{(k)}(t) \to \mathbb{I}/2^l$, which occurs both when all the states $\{\rho^{(k)}(t)\}$ are maximally mixed, and - more crucially - when all the states $\{\rho^{(k)}(t)\}$ are pure and orthogonal. In the former case, the second term also saturates and $\overline{C(t)} \to 0$. In the latter case, the first term can be interpreted as capturing the distinguishability of the $\{\rho^{(k)}(t)\}$ and saturates to l, the second term is driven to zero, and $\overline{C(t)} \to 1$. I note that the $\{\rho^{(k)}(t)\}$ need not be identical to the $\{|x_k\rangle\}$ in order for the Holevo quantity to saturate: if our channel simply rotates some initial states as follows $\{|x_k\rangle\} = \{|0\rangle, |1\rangle\} \to \{\rho^{(k)}(t)\} = \{|+\rangle, |-\rangle\}$, where $|\pm\rangle = (|0\rangle \pm |1\rangle)/\sqrt{2}$, then the Holevo quantity will still saturate $\overline{C(t)} = 1$. It is in this sense that the Holevo quantity is 'optimal', it enforces Bob's hypothetical use of the optimal measurement basis. The fact that the Holevo quantity is independent of measurement basis (and Bob's decoding protocol) is unique amongst the quantities in the following paragraphs.

Motivated by the local single-site measurements which can be readily made in a range of experimental quantum simulators, I also consider the maximum information that can be gleaned about the initial configuration of *individual* sites within the message register. The joint probability that a site j in the message $\rho^{(k)} = |x_k\rangle\langle x_k|$ is initialized in the state σ and then measured at time t in the state σ' is given by:

$$p_{k,j}(\sigma, \sigma', t) = \mathrm{tr}\left[P_j^{\sigma} \rho^{(k)}\right] \mathrm{tr}\left[P_j^{\sigma'} \rho^{(k)}(t)\right] \tag{2.15}$$

where $P_j^{\sigma} = |\sigma_j\rangle\langle\sigma_j|$ is the local projection operator onto the state σ at site j. I then define the average single-site mutual information

$$\overline{I_s(t)} = \left\langle \sum_{k,\sigma,\sigma'} p_k \tilde{p}_k(\sigma, \sigma', t) \log_2 \frac{\tilde{p}_k(\sigma, \sigma', t)}{\tilde{p}_{k,\Sigma}(\sigma, t)\tilde{p}_{k,\Sigma'}(\sigma', t)} \right\rangle \tag{2.16}$$

where $\tilde{p}_k(\sigma, \sigma', t) = \sum_j p_{k,j}(\sigma, \sigma', t)/l$ and where $p_{k,\Sigma}(\sigma, t) = \sum_{\sigma'} \tilde{p}_k(\sigma, \sigma', t)$ and $p_{k,\Sigma'}(\sigma', t) = \sum_{\sigma} \tilde{p}_k(\sigma, \sigma', t)$ are the marginal distributions of our site-averaged ini-

tial and final state variables respectively. This is a natural information-theoretic extension of the imbalance in the sense that Eq. (2.16) is the information that can be gleaned at time t about the initial conditions using only the measurements taken when computing the imbalance (i.e. single-site measurements in a fixed, predetermined, basis). If the state of each individual site, as measured in a basis specified by the P_j^σ, is locally preserved then $\overline{I_s(t)}$ saturates to unity. If the single-site states are not preserved - either because the channel scrambles the message, or if they rotate into new states that measurements P_j^σ cannot distinguish, then $\overline{I_s(t)} \to 0$. There is a crucial note to be made here which is that I am free to choose when to take the message average (over k) and the site average (over j). Our choice of taking the site average at the level of individual probabilities, and the message average at the level of disorder/environment (channel) averaging may, at first, appear arbitrary; but our justifications follow four simple ideas: (i) an average at the level of probabilities *must be taken*; without averaging the protocol sends a single message with probability unity, and as such cannot bear information. This can be verified by inspection of the definition of $\overline{I_s(t)}$ in Eq. (2.16) (ii) For a given site, the rest of the message effectively forms part of the environment, as such a change in message corresponds to a change in the channel, motivating our decision to average over both simultaneously (iii) This definition of the SSMI is analogous to the conventional construction of the imbalance which averages over each site first, then over realizations (iv) results for taking the combined order - with both site and message averaging at the level of individual probabilities - yield no scaling results, and show an overall decrease in informational content with increasing system size; indicating that this decoding protocol is functionally useless.

One can extend the above idea to the entire message register, taking measurements in the basis of the message states themselves. In this case, the outcome of the measurements is one of the 2^l spin configurations (the computational basis). The joint probability $p(k,k',t)$ of sending the state $|x_k\rangle$ and measuring the state $|x_{k'}\rangle$ at

time t is given by the diagonal elements

$$p(k,k',t) = p_k \langle x_{k'}|\rho^{(k)}(t)|x_{k'}\rangle = p_k \rho^{(k)}_{k'k'}(t). \tag{2.17}$$

I then define the normalized configurational mutual information for this joint probability as

$$\overline{I_c(t)} = \frac{1}{l}\left\langle \sum_{kk'} p(k,k',t)\log_2 \frac{p(k,k',t)}{p_K(k,t)p_{K'}(k',t)} \right\rangle \tag{2.18}$$

where $p_K(k,t) = \sum_{k'} p(k,k',t)$ and $p_{K'}(k',t) = \sum_k p(k,k',t)$ are the marginal distributions of our initial and final state variables respectively. Importantly, this construction is exactly the Holevo quantity of Eq. (2.14) in the full decoherence limit, in which $\rho^{(k)}(t)$ is replaced by a decohered density matrix $\rho^{(k)}_D(t)$ with all off-diagonal elements set to zero

$$\rho^{(k)}(t) \to \rho^{(k)}_D(t) = \mathrm{diag}(\rho^{(k)}_{11}(t), \rho^{(k)}_{22}(t), \cdots, \rho^{(k)}_{2^l 2^l}(t)). \tag{2.19}$$

I derive this property by first considering the CMI over a single channel realization $I^r_c(t)$:

$$I^r_c(t) = \frac{1}{l}\sum_{kk'} p(k,k',t)\log_2 \frac{p(k,k',t)}{\sum_s p(k,s,t)\sum_{s'} p(s',k',t)} \tag{2.20}$$

such that

$$\overline{I_c(t)} = \langle I^r_c(t)\rangle . \tag{2.21}$$

I note that: while I carry out the derivation in the basis of computational message states $\{|x_k\rangle\}$, any suitable basis can - in principle - be used instead. I insert the probabilities of Eq. (2.18) into Eq. (2.20) and resolve the first marginal distribution $\sum_s p(k,s,t) = p_k$ trivially by the unit-trace condition of $\rho^(k)(t)$[4]. Splitting up the logarithm, and cancelling relevant terms then yields

$$I^r_c(t) = \frac{1}{l}\sum_{kk'} p_k \rho^{(k)}_{k'k'}(t)\log_2 \rho^{(k)}_{k'k'}(t) - \frac{1}{l}\sum_{kk'} p_k \rho^{(k)}_{k'k'}(t)\log_2 \sum_{s'} p_{s'}\rho^{(s')}_{k'k'}(t). \tag{2.22}$$

[4]The second marginal distribution $\sum_{s'} p(s',k',t)$ involves all message states and is generally non-trivial.

I note that, by constructing an operator with the $\rho^{(k)}_{k'k'}(t)$ as eigenvalues, the sums over k' can be replaced with appropriate traces and some terms will take the form of von Neumann entropies. A naturally suitable operator is the fully decohered (in the computational basis) operator $\rho^{(k)}_D(t)$, defined in Eq. (2.19), which trivially has the $\rho^{(k)}_{k'k'}(t)$ as eigenvalues. I can then recast $I^r_c(t)$ in terms of traces as follows:

$$I^r_c(t) = \frac{1}{l}\sum_k p_k \mathrm{Tr}\left[\rho^{(k)}_D(t)\log_2\rho^{(k)}_D(t)\right] - \frac{1}{l}\mathrm{Tr}\left[\left(\sum_k p_k\rho^{(k)}_D(t)\right)\log_2\left(\sum_s p_s\rho^{(s)}_D(t)\right)\right] \tag{2.23}$$

which, when rewritten in terms of the von Neumann entropy $S(\rho) = -\mathrm{Tr}\rho\log_2\rho$, yields the Holevo quantity over decohered states $\rho^{(k)}_D(t)$:

$$I^r_c(t) = \frac{1}{l}S\left(\sum_k p_k\rho^{(k)}_D(t)\right) - \frac{1}{l}\sum_k p_k S(\rho^{(k)}_D(t)). \tag{2.24}$$

demonstrating, by analogy to Eq. (Eq. (2.14)), that the configurational mutual information as I have constructed it is just the Holevo quantity in the full decoherence limit. Though I have chosen the computational basis for our derivation, any suitable (orthonormal) basis can be used. I can intuit that different choices of basis yield different diagonal elements in the $\rho^{(k)}_D(t)$, and act as effective modifications to the eigenvalues of all the $\rho^{(k)}(t)$ at once. The 'optimality' of the Holevo quantity as discussed above can now also be understood in the sense that it uses the true eigenvalues of the $\rho^{(k)}(t)$ rather than those of the a basis-dependent decohered operators$\rho^{(k)}_D(t)$. This is equivalent to performing measurements in the eigenbasis of each *individual* message $\rho^{(k)}(t)$, rather than fixing a measurement basis from the outset.

I emphasize here that the decohering process of Eq. (2.19) occurs only *after* full unitary evolution up to time t. Thus, while it destroys coherence within the message register at the time of measurement, it doesn't preclude the build up of long-range coherence during the unitary evolution of the full system.

Finally, I draw attention to an important feature of the memory quantifiers in that they are each constructed using different kinds of measurements. The Holevo

quantity requires full tomography of the subsystem, the CMI requires measurements in a fixed global basis on the subsystem, and the SSMI requires the same measurements as the imbalance: namely local measurements in a fixed basis. As such, these quantities give us a useful quantification of the maximum amount of information that can be extracted from a subsystem given the kinds of measurement apparatus available to Bob - a crucial point when considering the potential of MBL systems in quantum computational settings. I summarize all quantities, the measurements required to construct them, and their status as memory quantifiers in Table 4.1.

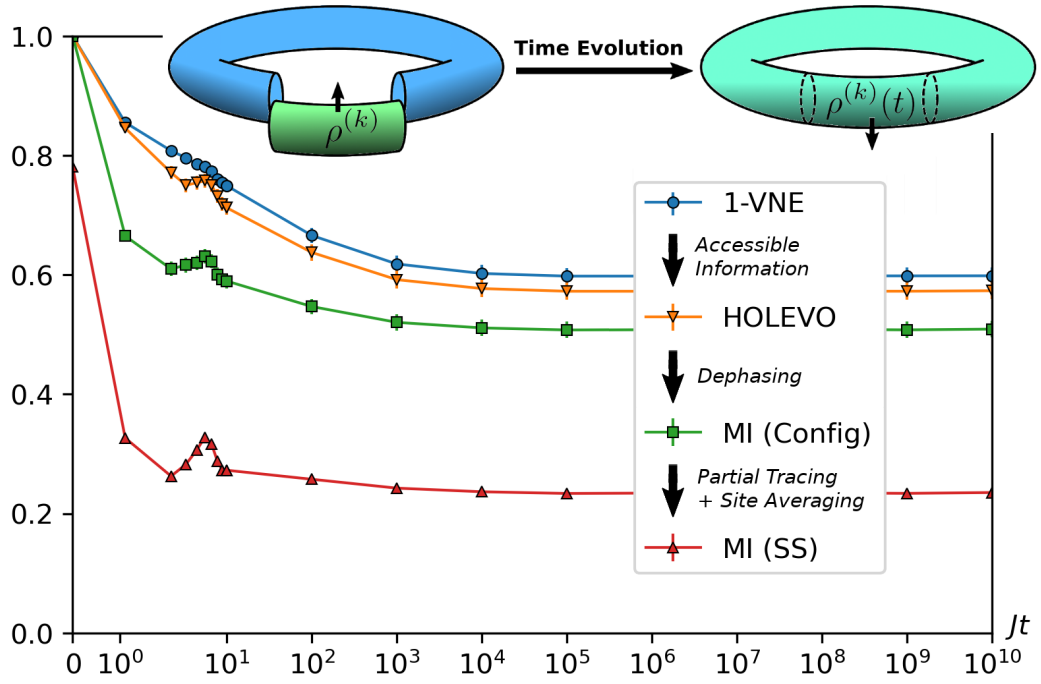

Figure 2.3: Hierarchy of channel-averaged informational quantities against time (normalized between 0 and 1) for disorder strength $h = 4$ in the middle of the MBLT. The schematic shows the action of a single channel realization on a single contiguous message state initialized in the state $\rho^{(k)} = \rho^{(k)} = |x_k\rangle\langle x_k|$. The peak at $Jt \approx 8$ occurs when the information carried away from the message first interacts with itself, causing transient revival. Error bars shown where visible.

2.2.4 Results and Finite-Size Scaling Analyses

In this section, I interrogate the quantities discussed in Section 2.2.3 in the context of the disordered Heisenberg model of Eq. (2.11). With the exception of a few results at the end of this section, I mainly consider pure environment states $|E\rangle\langle E|$ which are simply random product states of the Z eigenstates $\{|\uparrow\rangle, |\downarrow\rangle\}$.

I compare all quantities with respect to two standards. Firstly, which better captures local memory in terms of the number of bits of information preserved in the subsystem over time. Secondly, which better captures the critical properties of system Eq. (2.10) as I scan h across the MBLT, i.e. how strongly each quantity violates the Harris bound $\nu > 2$ (for a one-dimensional system, see Section 1.3.3.1).

The behaviour of the four quantities $\overline{P(t)}$, $\overline{C(t)}$, $\overline{I_c(t)}$, and $\overline{I_s(t)}$ as a function of time are shown in Fig. 2.3 for a system of size $L = 16$, message register size $l = 4$ and disorder strength $h/J = 4$. From Fig. 2.3, one can clearly see that these quantities form a strict hierarchy at all times. Indeed, I conjecture that the four quantities obey the following inequality for all choices of L, l and h

$$1 - \overline{S(t)} \geq \overline{C(t)} \geq \overline{I_c(t)} \geq \overline{I_s(t)} \tag{2.25}$$

In Appendix A, I strictly prove that $1 - \overline{S(t)} \geq \overline{C(t)} \geq \overline{I_c(t)}$. The last part of the inequality of Eq. (2.25), namely the CMI upper bounding the SSMI, has been extensively verified through numerical simulation and is intuitively sensible: internal dephasing and our tracing out parts of a system should not increase the information that one can glean from it.

Indeed all the inequalities of Eq. (2.25) have intuitive origins in quantum information: as discussed in the section Section 2.2.3, the Holevo quantity is a correction to $1 - \overline{S(t)}$ that specifically addresses whether or not information in the subsystem is accessible given optimal measurements. The CMI is simply the Holevo quantity after all final message states have been passed through the fully dephasing channel in Eq. (2.19), and by the monotonicity of the Holevo quantity under such a channel the inequality $\overline{C(t)} \geq \overline{I_c(t)}$ is evident. This is illustrated in the legend of Fig. 2.3, showing the hierarchy and the intuitive informational reasons for its existence. Thus, from a quantum informational perspective, the hierarchy of Eq. (2.25) is unsurprising. However, exploiting this informational framework and placing the hierarchy in the context of MBL reveals an important consequence: the imbalance - widely used as a quantifier of local memory in MBL - via its informational counterpart $\overline{I_s(t)}$, drastically underestimates memory in MBL systems. In the worst cases the use of

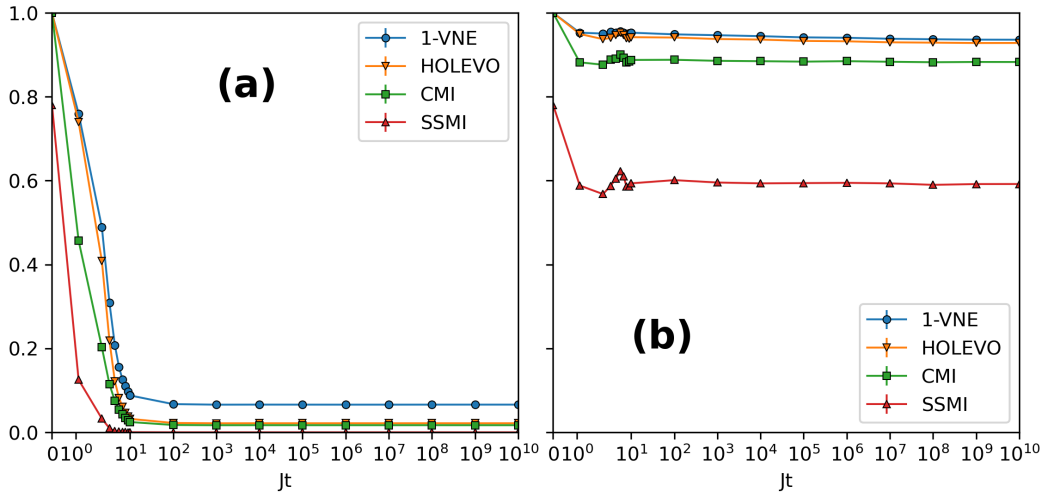

Figure 2.4: Dynamics of the four informational quantities for $L = 16$, $l = 4$ on extreme sides of the MBLT **(a)** $h = 0.1$, **(b)** $h = 16$, results for the middle of the MBLT ($h = 4$) are given in main text. In all cases, a strict hierarchy is seen, and the system convincingly relaxes to a steady-state at exponential times. Error bars shown where visible.

$\overline{I_s(t)}$ erases almost two thirds of the accessible information according to the Holevo quantity.

A final feature of Fig. 2.3 and Fig. 2.4 is that all the four quantities have readily reached a steady-state within very small error bars, even in the midst of the MBLT. This allows us to define time-independent steady-state quantities:

$$\overline{O}^{(ss)} = \lim_{t\to\infty} \overline{O(t)} \approx \overline{O(T)} \tag{2.26}$$

where O can be any of our four quantities, and where I take exponential time scales of $T = 10^{10}\ Jt$ for all subsequent results. These steady states can be used for investigating the scaling analysis across the MBL transition point, which is the subject of the rest of this section.

In the context of this problem there are two relevant length scales: the message length l and the total system size L. Inspired by Ref. [28, 35] and as discussed in Section 1.3.3.1, it is expected that the steady state values follow a finite size ansatz of the form

$$\overline{O}^{(ss)} = L^{-\zeta/\nu} f(l/L, L^{1/\nu}(h - h_c)) \tag{2.27}$$

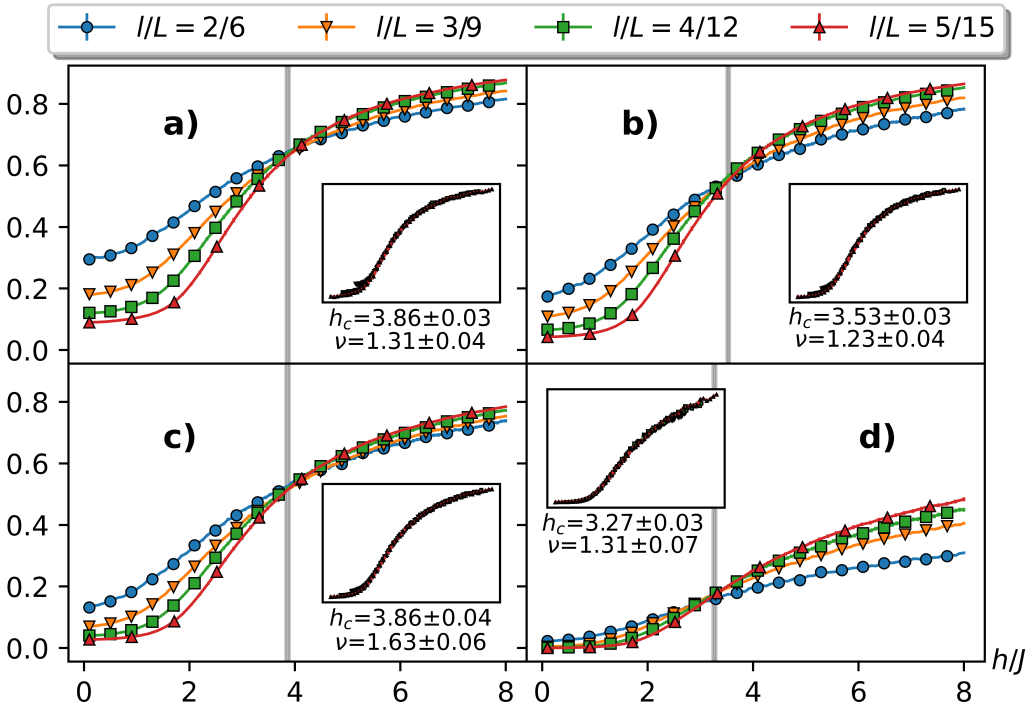

Figure 2.5: Disorder-averaged steady-state values of (normalized) informational quantities as a function of disorder strength. The message-to-system size ratio for all panels is $l/L = 1/3$. The panels show: **(a)** von Neumann entropy **(b)** Holevo quantity **(c)** CMI **(d)** SSMI. Insets show the corresponding data collapse for the three largest systems. Every fifth point is marked for legibility, and error bars shown where visible.

where h_c is the critical point, ν and ζ are critical exponents and $f(\cdot,\cdot)$ is an unspecified function. By fixing the ratio as $l/L = 1/3$, I plot $\overline{O}^{(ss)}$ as a function of h for various system sizes in Fig. 2.5**(a)**-**(d)** for the four quantities, respectively. As is clear from the figure, all four quantities show a crossover wherein curves of different system sizes intersect. The existence of this crossover suggests scale-invariant behaviour, indicates that $\zeta = 0$, and determines the critical value h_c for each quantity. Interestingly, the critical point h_c determined by the SSMI is far lower than the ones deduced from the other three quantities.

I here use a more elaborate scaling analysis based on the principle of data collapse [36, 37]. This, in conjunction with the ansatz of Eq. (2.27) allows us to systematically determine h_c, ζ, and ν as discussed in Section 1.3.3.1. Carrying out these data collapses with variable ζ revealed that that $\zeta \approx 0$ for all quantities, hence

I set $\zeta = 0$ for the rest of this section. Respective data collapses for each quantity are shown in the insets of Fig. 2.5**(a)**-**(d)**, each yielding slightly different optimal values for ν and h_c.

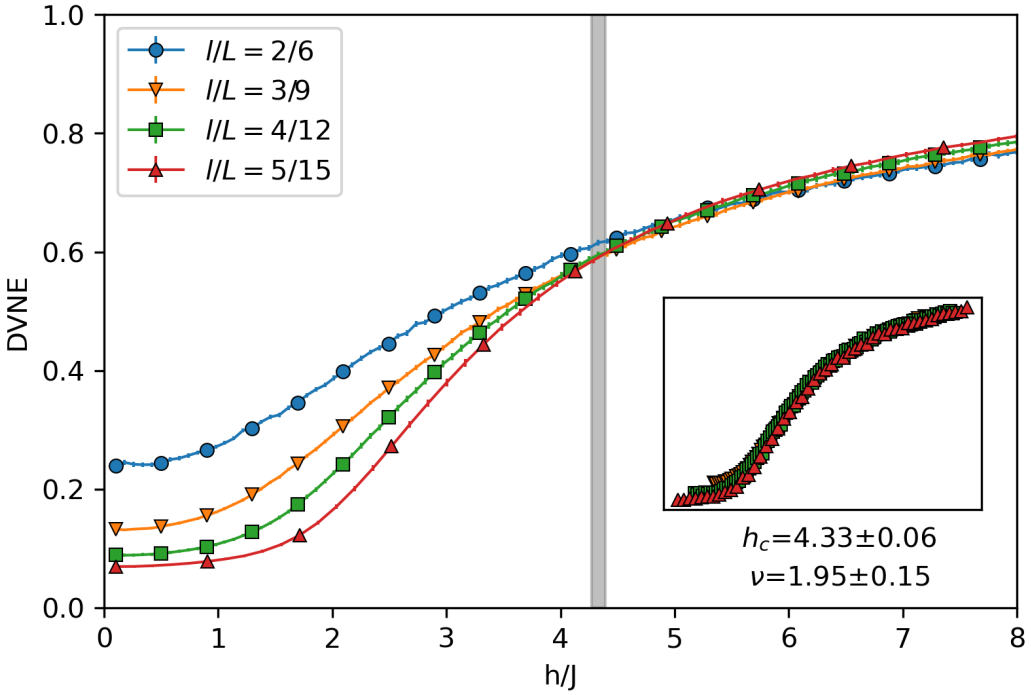

Figure 2.6: Channel-averaged DVNE as a function of disorder strength. Every fifth point is marked for readability, and error bars shown where visible. The inset shows the corresponding data collapse of the largest three systems.

These resulting optimal values for h_c and ν are depicted in Fig. 2.7(a). Similar to many previous studies: small system sizes lead to systematic underestimation of the critical value ν, bounded analytically for this system by $\nu \geq 2$ [35, 38, 39]. The von Neumann entropy $\nu = 1.31 \pm 0.04$, the Holevo quantity $\nu = 1.23 \pm 0.04$, and the SSMI $\nu = 1.31 \pm 0.07$ all violate the Harris bound to a similar extent. Unexpectedly, all three of these quantities are outperformed in terms of Harris bound violation by the CMI which attains a critical exponent of $\nu = 1.63 \pm 0.06$, a remarkably high value for such small system sizes. In this sense one can state that the CMI captures less information than the Holevo quantity (see the hierarchy of Fig. 2.3) but better captures the behaviour of the MBLT in the sense that it violates the Harris bound to a lesser extent. Finally, the SSMI performs badly both as the worst quantity with which to capture retained information, and as a quantity which violates the Harris

bound to a much greater extent than the CMI. It also underestimates the critical h_c with respect to all other quantities. This indicates that the SSMI, and thus the widely used imbalance, are poor scaling quantities which cannot precisely capture properties of the MBLT. As such the SSMI, and by extension the imbalance, are not useful quantifiers of local memory in any arena other than situations where - due to the simple measurements they require - they are the only ones available. Additional scaling results for a message-to-system size ratio of $l/L = 1/4$ are shown in Fig. 2.8 wherein no new behaviour can be seen that has not already been discussed.

The significantly higher values of ν for the CMI may suggest that this quantifier better captures the behaviour of Eq. (2.10) in the thermodynamic limit than the other quantities. Since the CMI is the decohered counterpart of the Holevo quantity, it indicates that throwing away the off-diagonal coherences improves scaling results. For small systems, where these off-diagonal quantum coherences persist, I propose that it is beneficial to artificially set them to zero at the end of a simulation, or to only extract diagonal elements in experiment.

To further support this, I compute the decohered von Neumann entropy (DVNE) by decohering the message register $\rho \to \rho_D$ according to Eq. (2.19) before evaluating the von Neumann entropy of Eq. (2.13). This is essentially the Shannon entropy of diagonal elements in the computational basis, and has been used (in some form) occasionally in the context of MBL before [7, 40, 41]. The obtained critical values of h_c and ν are also shown in Fig. 2.7**(a)**. The effect of artificial dephasing according to Eq. (2.19) is shown in Fig. 2.7 by black arrows. Remarkably, the von Neumann entropy of artificially dephased quantum states yields a critical value $\nu = 1.95 \pm 0.15$ consistent with the Harris bound [38] and closer to large-system analyses of the MBLT. Again, similar results can be found in the $l/L = 1/4$ case of Fig. 2.8 .

I conjecture that this may be because artifically decohering the message subsystem imitates the kind of effects that occur in the thermodynamic limit. The decohering of a subsystem in the thermodynamic limit is a direct consequence of interactions. I investigate this comparing the steady state Holevo quantity and its

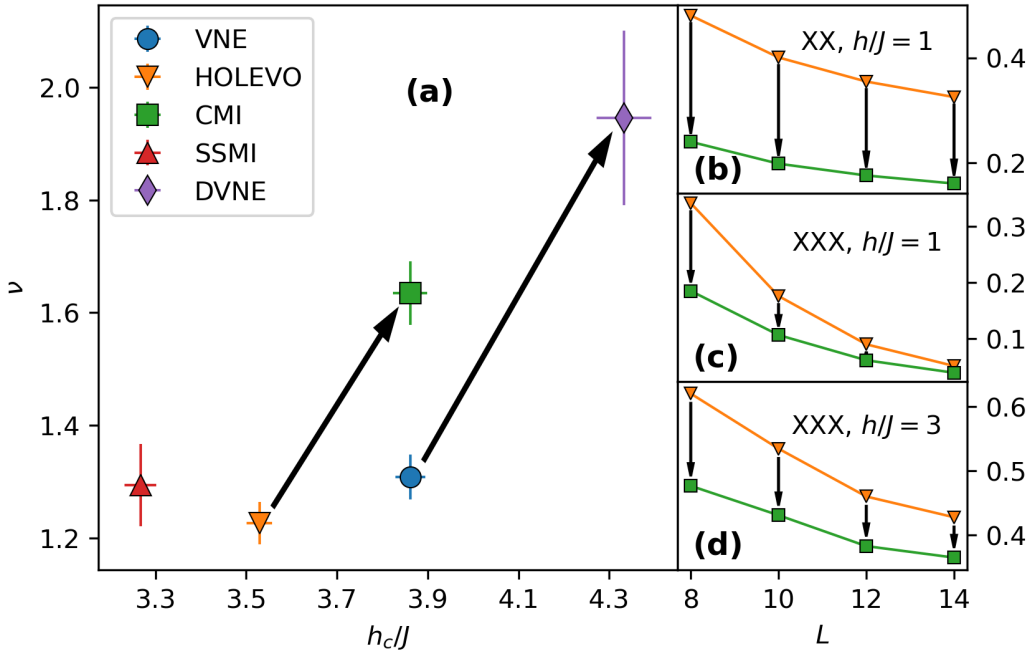

Figure 2.7: Main panel (a) shows the extracted critical values h_c and exponents ν for all memory quantifiers and the DVNE for a message-to-system size ratio $l/L = 1/3$. Inset panels (b)-(d) compare the Holevo quantity and its decohered counterpart, the CMI, for the XX and Heisenberg (XXX) models. Artificial dephasing is indicated by the arrows.

decohered counterpart, the CMI, directly in systems with and without interactions across the MBLT, and for a range of system sizes L. In Fig. 2.7**(b)** I replace the interacting Heisenberg (XXX) Hamiltonian of Eq. (2.10) with the non-interacting (XX) Hamiltonian. For the non-interacting case, the figure shows slight - if any - convergence between the Holevo quantity and the CMI as the system size L increases; even for small disorder strengths $h/J = 1$. In Fig. 2.7**(c)**-**(d)** I return to the Heisenberg Hamiltonian. For small disorder strengths $h/J = 1$, the Holevo quantity and the CMI quickly converge as the system size increases. Even close to the transition point $h/J = 3$, one can see from Fig. 2.7**(c)** that the curves converge as L increases, albeit the convergence is slowed. This evidences the fact that the dephasing of the subsystem slows down near the MBL transition point and thus larger system sizes are required to emulate thermodynamic behaviour. Thus wholly quantum quantities may fail to capture the Harris bound $\nu \geq 2$ in small finite systems $L \sim 20$. Essentially, rather than completing this convergence by taking L to a suf-

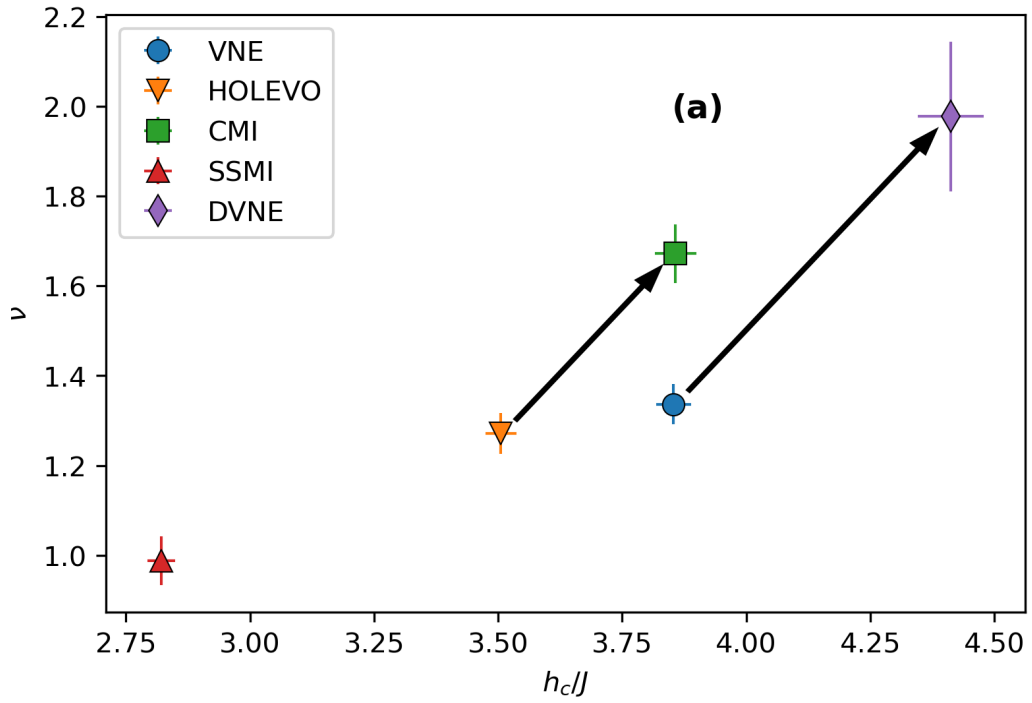

Figure 2.8: Extracted critical values and exponents for the memory quantifiers for the message-to-system size ratio $l/L = 1/4$. Black arrows show artificial decohering.

ficiently large value, our suggestion approximates it by artificially decohering the subsystem instead.

I note here that this procedure enforces a particular understanding of the nature of the MBL state in the thermodynamic limit: as a product state of dephased subsystems. Thus I can only conjecture that this procedure emulates the thermodynamic limit, though this conjecture is supported by some preliminary evidence (namely Fig. 2.7(b)-(d)) and is similar to the LIOM picture of the MBL phase [2, 35, 42]. What I can state definitively is that this procedure considerably reduces the extent to which the analytic Harris bound is violated in small systems, which in turn is evidence that such an enforcement may be plausible.

2.2.5 Outlook

By drawing on principles from quantum information theory, and structuring an investigation of local memory from the perspective of the accessible information game, I determined a set of brief criteria for constructing a true memory quantifier.

I subsequently introduced several such quantifiers in the context of MBL, and established a systematic hierarchical order among them. This serves as a foundation not just for future study of memory in MBL, but - as I shall demonstrate in Section 2.3 and Section 4.3 of Chapter 4 - in broader condensed matter contexts.

With respect to MBL specifically, our findings show that the Holevo quantity represents the best quantifier of memory in terms of number of bits of information retained over time. This is unsurprising, as the Holevo quantity is a direct import from quantum information theory that quantifies the maximum classical capacity of a given channel. Surprisingly, the informational version of the widely-used imbalance performs the worst - suggesting that extant literature drastically underestimates the amount of information actually retained. Furthermore when characterizing the MBL transition using these memory quantifiers I find that, though the Holevo quantity may the best quantifier of memory itself, the CMI - its decohered counterpart - best captures the critical properties of the MBLT. Motivated by this, I compared the von Neumann entropy of a small subsystem to its decohered variant and discovered that it too outperforms its quantum, coherent, counterpart; yielding a critical exponent consistent with the Harris bound. A plausible conclusion of this analysis is that finite-size effects can be mitigated just by deliberately decohering the final state of the message register. This provides a significant theoretical and experimental advantage: in theory one can drastically improve small-system scaling results and may even be able to emulate the thermodynamic limit by deliberately throwing away information. In experiment one may only needs to measure the diagonal elements of the reduced density matrix instead of extremely demanding state tomography. Ultimately these results not only shed light on memory and the thermodynamic limit in MBL systems, but provide a solid test case for how a systematic investigation of memory in any condensed matter system should look.

2.3 Memory in Quantum Many-Body Scars

In a complementary vein to MBL, quantum scars represent another example of ergodicity-breaking in many-body condensed matter systems - though its mech-

anism and manifestation is quite different (see Section 1.3.4). And, again in a complementary vein to MBL, scars are said to retain a certain 'memory' of their initial conditions [43–45]. This is usually characterized by periodic revivals in a Loschmidt echo, with systems initialized in a scarred subspace returning to their initial configuration at regular intervals which are much shorter than the full system recurrence times [46, 47].

In this section I interrogate memory in a specific scarred system, the spin-1 Dzyaloshinskii-Moriya interacting chain, by applying the 'accessible information game' discussed in Section 2.1 and applied to MBL in Section 2.2. This time, I extend the study to open systems, wherein the role of the large environment states of Section 2.2 are replaced by Markovian baths. In this context, the quantum coherent information introduced in Section 2.1.3 also becomes relevant.

2.3.1 The Scarred Dzyaloshinskii-Moriya Interacting Spin Chain

As a framework for studying a scarred model, I consider a system of N spin-1 particles that realize the Hamiltonian:

$$\hat{H} = \sum_{j,j'}^{N} \lambda_{j,j'} \left(e^{i\phi} \hat{S}_j^+ \hat{S}_{j'}^- + \text{h.c.} \right) + \Omega \sum_{j=1}^{N} [(\hat{S}_j^x)^2 - (\hat{S}_j^y)^2] \tag{2.28}$$

where the spin-1 raising operator is:

$$\hat{S}^+ = \sqrt{2}\,[|+1\rangle\langle 0| + |0\rangle\langle -1|]\,, \tag{2.29}$$

the lowering operator is $\hat{S}^- = (\hat{S}^+)^\dagger$, and the remaining operators are defined as $\hat{S}^x = (\hat{S}^+ + \hat{S}^-)/2$ and $\hat{S}^y = -i(\hat{S}^+ - \hat{S}^-)/2$. This model exhibits quantum scarring for all values of the model parameters $\lambda_{j,j'}$, $\phi = k\pi$, and Ω; though as I show later $\Omega \neq 0$ dramatically curtails the size of the scarred subspace. At integer k the model becomes a spin-1 XX model, and for half-integer k the system realizes a Dzyaloshinskii-Moriya interaction (DMI). Notably the model parameter $\lambda_{j,j'}$ can vary with the site indices j and j', and is not subject to any restrictions. The scars

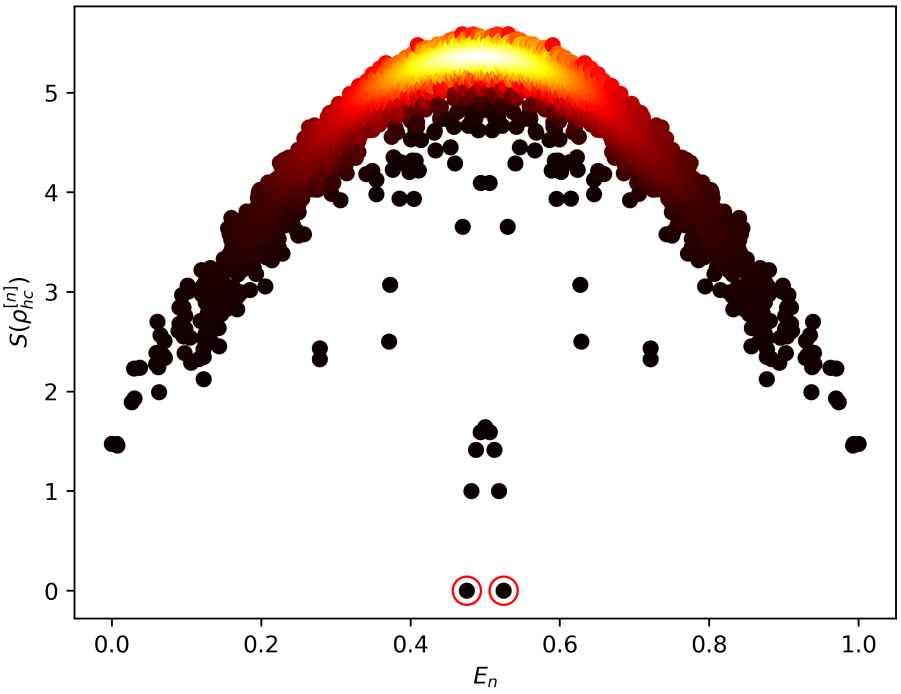

Figure 2.9: The entanglement entropy S of the half-system reduced density matrices $\rho_{hc}^{[n]}$ of the energy eigenstates $|E_n\rangle$; normalized such that the spectrum of eigenenergies lies in the interval $E_n \in [0,1]$. The two QMBS states $|\mathbb{X}_\pm\rangle$, circled in the diagram above, have no entanglement $S_E = 0$, and are well-separated from the bulk states.

persist for arbitrary, potentially long-range, $\lambda_{j,j'}$. For the purposes of this thesis, I use the generic functional form

$$\lambda_{j,j'} = \lambda/|j-j'|^\alpha \tag{2.30}$$

where λ tunes the strength of the coupling, and α tunes the range of the interaction. Given the periodicity of the model with respect to the phase ϕ I restrict it to the interval $\phi \in [0,\pi]$ without loss of generality.

I now define two product states which are eigenstates of the Hamiltonian of Eq. (2.28) at the DMI point $\phi = \pi/2$:

$$|\mathbb{X}_\pm\rangle \equiv |\pm\rangle|\pm\rangle|\pm\rangle|\pm\rangle\ldots, \tag{2.31}$$

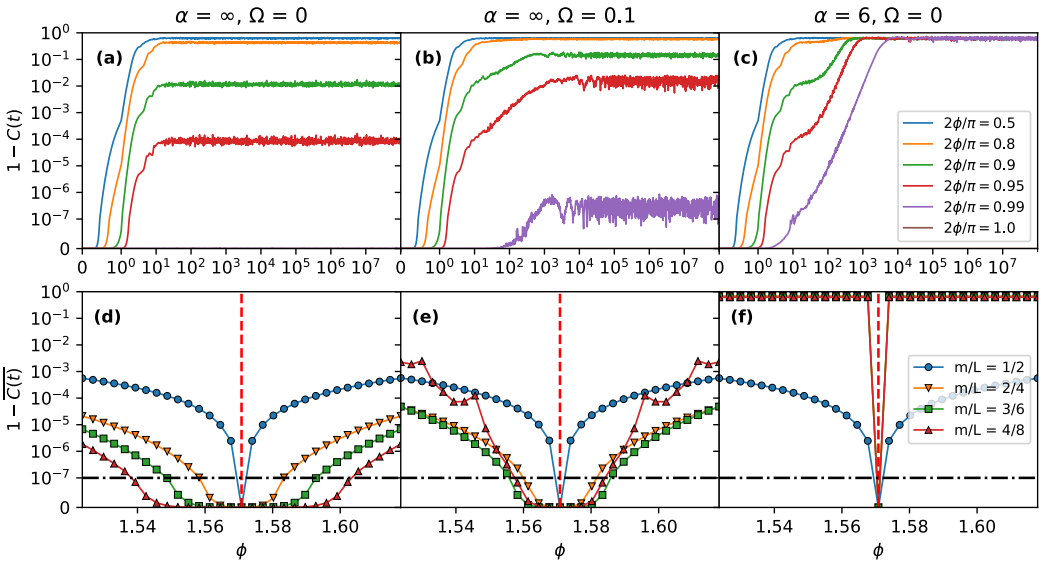

Figure 2.10: Top row **(a)-(c)** shows one minus the Holevo quantity over time for various values of the system parameters. Bottom row **(d)-(f)** show corresponding steady-state values at exponential times $\lambda t_f \sim 10^{10}$ for addressable registers of size $m = L/2$ of the left half of the system. Flat regions below the dash-dotted black lines in panels **(d)-(f)** correspond to 'stable' regions wherein perfect information retention is attained despite imperfect scars.

where $|\pm\rangle = (|+1\rangle \pm |-1\rangle)/\sqrt{2}$. In Fig. 2.9 I plot the half-system entanglement entropies of all energy eigenstates for a particular choice of model parameters $N = 8$, $\phi = \pi/2$, $\Omega = 0.1$, $\lambda = 1$, and $\alpha = 2$. This is a widespread method of evidencing quantum scarring by identifying bands of eigenstates well-separated from the bulk [46, 48–50]. The individual eigenstates of Fig. 2.9 are coloured by density, with brighter regions corresponding to a higher density of states. From Fig. 2.9 one can clearly see a bright bulk and a pair of well-separated states with zero entanglement - identified by red circles. These zero entanglement eigenstates are precisely the states $|\mathbb{X}_\pm\rangle$ discussed above. The band of states between these two product states and the bulk are other potential scar states that coalesce into a flatter band for $\Omega = 0$ - it is in this sense that non-zero Ω disrupts the scars latent in the system.

2.3.2 Stable Memory Away From Perfect Scarring

Given the product scar states $|\mathbb{X}_{\pm}\rangle$ of Eq. (2.31), it is natural to encode a single classical bit of information into the system by assigning

$$0 \to |\mathbb{X}_{+}\rangle, \quad 1 \to |\mathbb{X}_{-}\rangle. \tag{2.32}$$

This represents the simplest possible non-trivial message that a system can bear, and serves as a crucial benchmark. After all, if a system fails to reliably store the state of even a single classical bit, it cannot reasonably be said to have any kind of useful 'memory'.

After the encoding Eq. (2.32) of the state of a single classical bit into the system, one can measure m sites at a later time t_f and try to reconstruct the state of this encoded bit. Once again, given the framing of the 'accessible information game', the efficacy of this protocol is quantified by the Holevo quantity, which yields the number of classical bits of information that can be retrieved given optimal measurements on the final state. I assume that both messages are equally likely $p_0 = p_1 = 1/2$ to occur in our alphabet, such that the Holevo quantity as introduced in Section 2.1.2 takes the form

$$C(t) = S\left(\frac{1}{2}\left[\rho_0^S(t) + \rho_1^S(t)\right]\right) - \frac{1}{2}\left[S\left(\rho_0^S(t)\right) - \frac{1}{2}S\left(\rho_1^S(t)\right)\right]. \tag{2.33}$$

In Fig. 2.10 panels **(a)**-**(c)**, I show $1 - C(t)$ against time for several different choices of our Hamiltonian parameters ϕ, α, and Ω for a system of $N = 8$ particles. Here, I take the m measureable sites to be the entire left half of the system $m = L/2$. As expected, perfect scarring at $\phi = \pi/2$ renders $|\mathbb{X}_{\pm}\rangle$ as eigenstates and results in a value of zero for all graphs - implying perfect classical information retention. When probing the stability of this perfect information retention to changes in the Hamiltonian parameters, I find that memory is stable to small changes in ϕ and Ω - with exponentially small deviations from a perfect bitrate of $C(t) = 1$. This is shown for nearest-neigbour interactions in Fig. 2.10 panel **(a)** for $\Omega = 0$ and **(b)** for $\Omega = 0.1$, wherein small deviations from $\phi = \pi/2$ result in a minor loss of information

over time which eventually equilibrates to an oscillation around a steady-state value. However for long-range interactions, even ones that fall off rapidly $\alpha = 6$, these memory effects are essentially destroyed. This is shown in Fig. 2.10**(c)** in which all curves aside from $\phi = \pi/2$ eventually converge to unity indicating complete information loss. Regardless, during the interim period up to times of $t \sim 10^3$, a significant amount of information is retained. Thus, even though the long-range interacting scarred system is not capable of retaining information indefinitely, it may still be valuable as an interim memory register for use in-situ - a quantum many-body RAM if you will.

In panels Fig. 2.10**(d)**-**(f)** I formalize this notion of stability by taking the time-average of the respective curves in **(a)**-**(c)**

$$\overline{C(t)} = \int_0^{t_f} C(t)\mathrm{d}t \tag{2.34}$$

and analyzing the steady-state deviation of the Holevo quantity from unity. If $1-\overline{C(t)} < \varepsilon$, where ε is some threshold probability, for some interval $\phi \in [\pi/2 - \phi_\varepsilon, \pi/2 + \phi_\varepsilon]$ that is non-vanishing with system size, then we can say that memory is 'stable' with respect to perturbations in ϕ. Strikingly, just such a stability can be seen in Fig. 2.10**(d)** for a threshold probability $\varepsilon = 10^{-7}$ denoted by a horizontal black dash-dotted line. The places where individual curves fall below this line correspond to stable regions as per my definition above. As a function of the double scaling in the message-to-system size ratio m/L, it is easy to identify 'plateaus' in which larger systems are more stable to perturbations in ϕ than smaller systems. This stability breaks down slightly for deviations in Ω as shown in Fig. 2.10**(e)**, wherein the plateaus follow no predictable behaviour in system size and the curves deform. Stability vanishes entirely for long-range interactions as shown in Fig. 2.10**(f)**, though again a study at intermediate times up to $t \sim 10^3$ might reveal a kind of interim stability.

Perhaps most interestingly, taking the m sites to lie *anywhere else* in the system destroys stability entirely. This is shown in Fig. 2.11a for m/L sites taken in the middle of the system. Increasing system size results in a corresponding increasingly

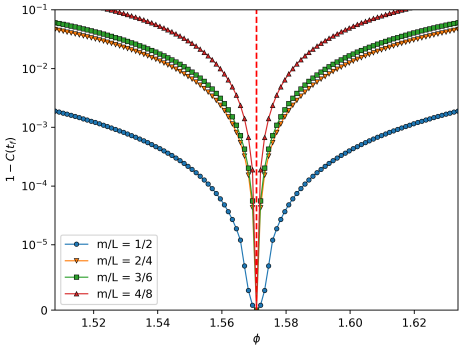

(a) One minus the steady-state Holevo quantity at exponential times $\lambda t_f \sim 10^{10}$ for addressable registers of size $m = L/2$ in the middle of the system.

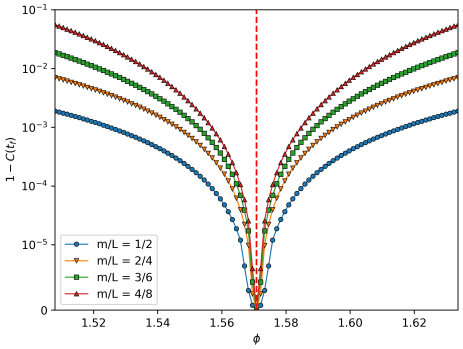

(b) One minus the steady-state Holevo quantity at exponential times $\lambda t_f \sim 10^{10}$ for addressable registers of size $m = 1$ of the leftmost site of the system.

rapid failure of the system to retain information. This may suggest that the results of Fig. 2.10 are simply edge effects - that perhaps the classical state of the system is encoded into the state of a locked edge qubit. However this doesn't seem to be the case, as evidenced in Fig. 2.11b wherein I instead take $m = 1$ to be the leftmost qubit, there is no significant increase in information retention compared to the m/L sites in the middle of the system, and there is a dramatic decrease in information retention when compared to Fig. 2.10**(d)**. This suggests that the information is truly distributed across an extensive portion of the register of m/L sites.

Given the above results, it seems that realistic systems, which will not perfectly enact scarring, can still serve as effective memory registers provided an extensive number of sites can be addressed. However, the value of quantum many-body scars as practical stores of classical memory - even in the simplest toy case - is a complicated interplay between how finely the Hamiltonian can be tuned, the system size, and the specifics of the measurement protocol. For example, if the Hamiltonian in the lab can be finely tuned, but few sites can be measured at a single time, then smaller registers are better as memory stores. If more sites can be measured, then larger registers are better. If the Hamiltonian cannot be finely tuned, then faster measurement times are better.

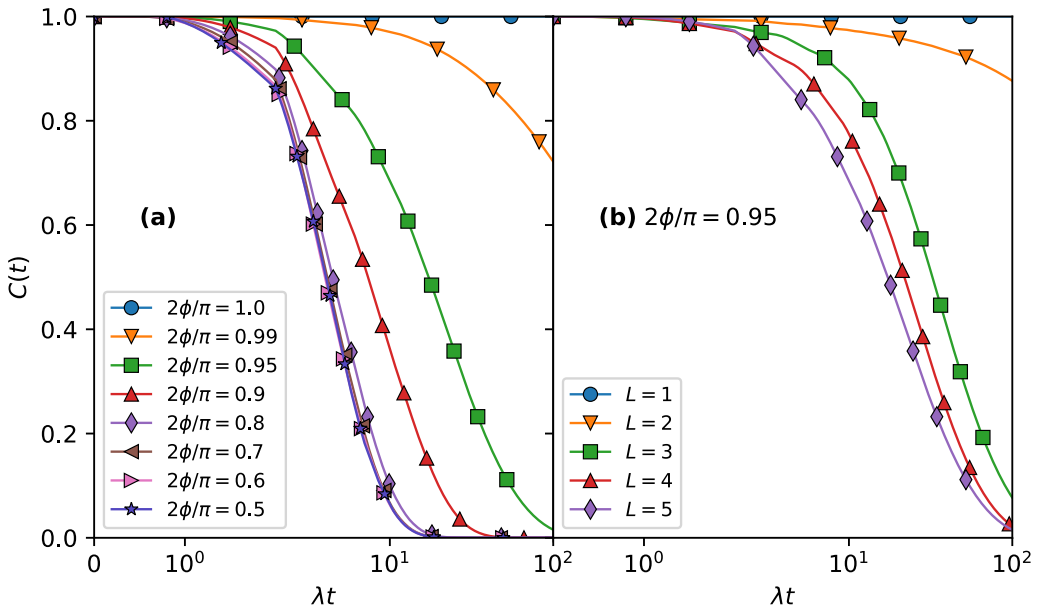

Figure 2.12: Holevo quantity of the open DMI chain with X noise over time for **(a)** varying ϕ and fixed system size $L = 6$ and **(b)** verying system size L and fixed $\phi = 0.95\pi/2$.

2.3.3 Memory in an Open Scarred System

A natural extension of the results of the previous section is an investigation of how well an *open* scarred system can retain information. Generally, an environment will leach information that is either lost into an extensive number of constituents, or discarded entirely if no record of the environment is retained (in a Markovian bath for example). In this case, it is possible to both investigate the Holevo quantity - though this time for an addressable register $m = L$ which takes up the entire system - and the quantum coherent information.

As discussed in Section 2.1.3, the capacity of a system to transmit information via quantum coherence can be quantified by the quantum coherent information:

$$\mathcal{I}(R\rangle S(t)) = S(\rho^S(t)) - S(\rho^{RS}(t)) \tag{2.35}$$

where R is a purification of $\rho^S(0)$. Due to fact that I am taking the messages as equiprobable, the initial state $\rho^S(0)$, which is an even mixture of $|\mathbb{X}_+\rangle$ and $|\mathbb{X}_-\rangle$, is

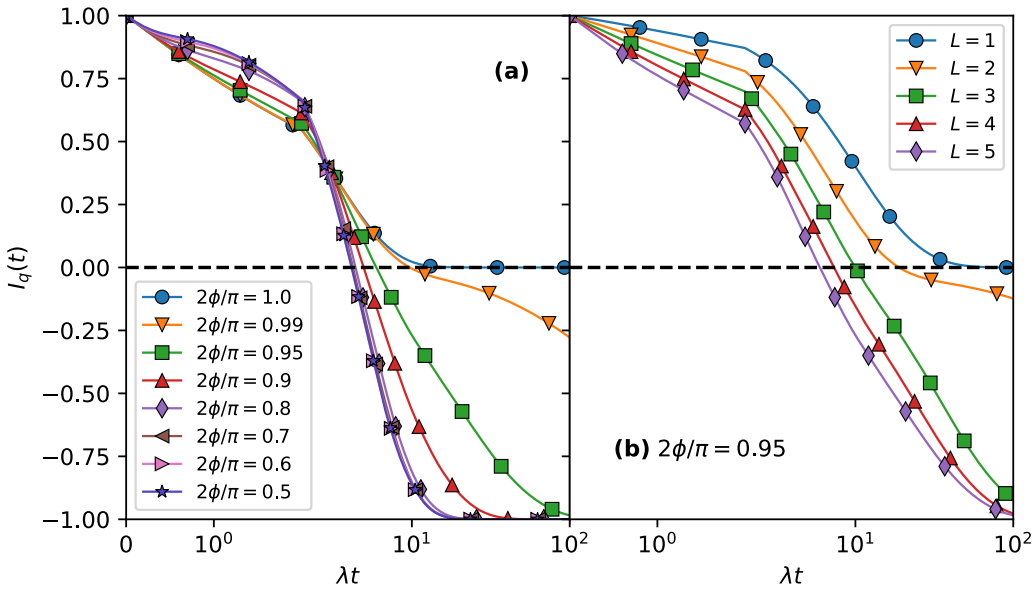

Figure 2.13: Quantum coherent information of the open DMI chain with X noise over time for **(a)** varying ϕ and fixed system size $L = 6$ and **(b)** verying system size L and fixed $\phi = 0.95\pi/2$.

purified by the cat state

$$|\psi(0)\rangle = \frac{|0\rangle_R|\mathbb{X}_+\rangle_S + |1\rangle_R|\mathbb{X}_-\rangle_S}{\sqrt{2}}; \tag{2.36}$$

an even superposition of our two messages entangled with the reference system R which consists of a single two-level system.

To model the Markovian environments, I invoke the Lindblad equation for the time evolution of the mixed state $\rho^S(t)$:

$$\dot{\rho}_S(t) = -i\,[H, \rho_S(t)] + \gamma \sum_j L_j \rho_S(t) L_j^\dagger - \frac{1}{2}\left\{L_j^\dagger L_j, \rho_S(t)\right\}. \tag{2.37}$$

where L_j are jump operators that describe the possible processes the system can undergo once coupled to its environment. The parameter γ tunes the strength of the interaction between environment and system, and I take it to be independent of j. I consider three different on-site jump operators throughout this section, corresponding to different kinds of environmental noise: X, Z, and $+$, enacted by local operators $L_j = S_j^x$, S_j^z, and S_j^+ respectively.

It is instructive at this junction to investigate the effects of these operators on the states $|\mathbb{X}_-\rangle$. This will inform the forthcoming results. For completeness, the relevant spin-1 operators in the Z-basis are as follows:

$$S^x = \frac{1}{\sqrt{2}}\begin{pmatrix} 0 & 1 & 0 \\ 1 & 0 & 1 \\ 0 & 1 & 0 \end{pmatrix}, \quad S^z = \begin{pmatrix} 1 & 0 & 0 \\ 0 & 0 & 0 \\ 0 & 0 & -1 \end{pmatrix}, \quad S^+ = \sqrt{2}\begin{pmatrix} 0 & 1 & 0 \\ 0 & 0 & 1 \\ 0 & 0 & 0 \end{pmatrix}. \tag{2.38}$$

By direct calculation, S^x annihilates $|-\rangle$ and interconverts the states $|+\rangle \longleftrightarrow |0\rangle$. This means that jump operators of the form $L_j = S^x_j$ should have no effect on the state $|\mathbb{X}_-\rangle$ and drive the state $|\mathbb{X}_+\rangle$ towards a mixed state which is orthogonal to $|\mathbb{X}_-\rangle$. Thus, the two states remain distinguishable despite the effect of the channel. The operator S^z interconverts $|+\rangle \longleftrightarrow |-\rangle$ and drives the system towards a mixed state of the two - leading to indistinguishability and the erasure of information. The operator S^+ has the expected effect of mapping both states $|\pm\rangle$ to mixed states of $|0\rangle$ and $|1\rangle$, and so again erases any information encoded in the original state of the system. This rough analysis gives us insight into the type of noise that the system may be resistant to, namely X noise.

For the rest of this section I consider systems of $L = 6$ particles with $\Omega = 0$, $\alpha = 2$, and $\lambda = 1$ in the Hamiltonian of Eq. (2.28). I also fix the strength of the environmental coupling $\gamma = 0.1$ and evoltuion times of $\lambda t = 10^2$ throughout. This choice of parameters, specifically the setting of $\Omega = 0$, is to isolate the behaviours that one might see in the 'ideal' scarred system without any other kind of interaction. The Lindblad equation of Eq. (2.37) is directly constructed and numerically integrated using a sparse brute force fourth order Runge-Kutta scheme[5].

The Holevo quantity in the context of X noise is shown in Fig. 2.12. Panel

[5]The ability to access larger system sizes is curtailed first by my decision to numerically integrate the Lindblad equation which scales as $O(\Omega^2)$ where Ω is the dimensionality of the system, then by the local dimensionality $d = 3$ due to my consideration of spin-1 particles, and finally by the inclusion of ancillae qubits in the calculation of the quantum coherent information which multiply the dimensionality of the problem by an additional factor of 2. Altogether the problem scales as $O(3^{2L+\log_3 4})$. In terms of a conventional qubit problem, the $L = 6$ system corresponds to numerical integration of an ~ 21 qubit chain; which is close to the limit for exact diagonalization studies on conventional hardware.

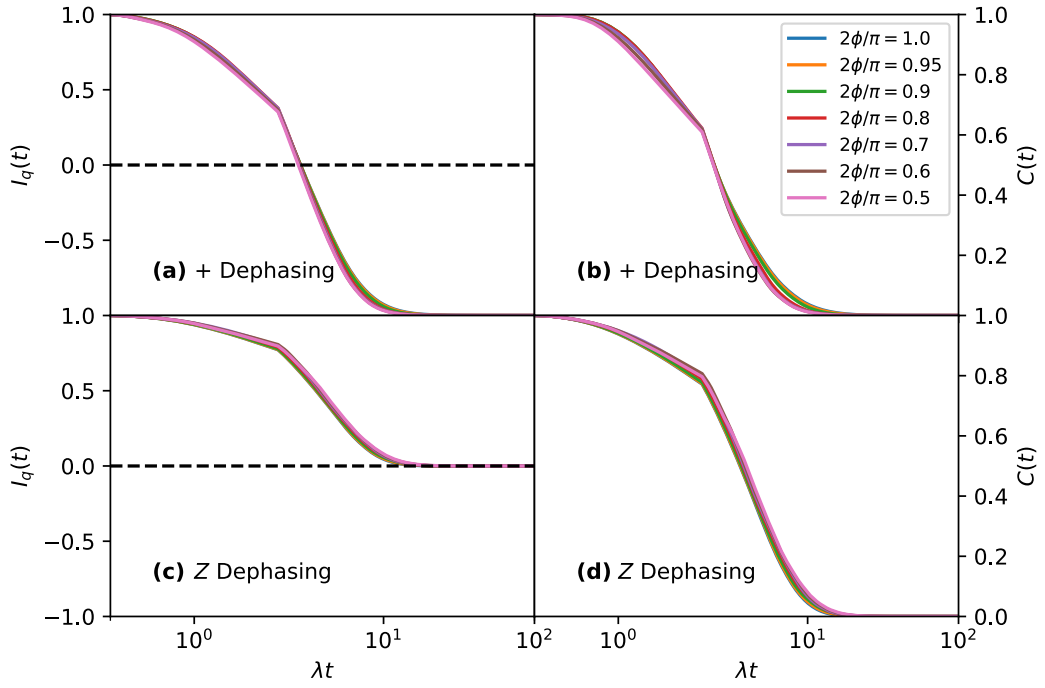

Figure 2.14: Informational quantities against time for varying ϕ and different kinds of jump operators. **(a)** Quantum coherent information and + operators. **(b)** Holevo quantity and + operators. **(c)** Quantum coherent information and Z operators. **(d)** Holevo quantity and Z operators.

(a) shows results for a fixed system size $L = 6$ at varying ϕ. Strikingly, even in a noisy system coupled to the environment, there is perfect retention of classical information at the exact scarring point $\phi = \pi/2$. This can be explained by the discussion above, wherein the mixed state that the jump operators $L_j = S_j^x$ drive $|\mathbb{X}_+\rangle$ towards is still fully distinguishable from the state $|\mathbb{X}_-\rangle$. As ϕ varies away from $\pi/2$, $|\mathbb{X}_-\rangle$ is no longer a scar eigenstate and so is gradually affected more and more by the noise, resulting in this distinguishability being slowly degraded over time. As can be seen from Fig. 2.12**(a)**, even minor deviations in $\phi = 0.95\pi/2$ induce rapid information loss. Only when ϕ deviates from the exact scarring point by 1% at $\phi = 0.99\pi/2$ can we see any kind of significant information retention at intermediate times $\lambda t = 10^2$. Moreover, this information loss becomes dramatically more pronounced as the system size increases. This is evidenced in panel **(b)** of Fig. 2.12 in which a deviation to $\phi = 0.95\pi/2$ manifests as only a slight drop in preserved information for $L = 2$, but almost total erasure for $L > 2$.

The quantum coherent information $I_q(t)$ for the same system is shown in Fig. 2.13 and it fares no better in the arena of open system dynamics. As discussed in Section 2.1.3, a positive value for $I_q(t)$ (shown as a dashed black line) indicates strictly non-classical behaviour; i.e. the existence of some degree of quantum coherence in the relevant basis. As evidenced by Fig. 2.13**(a)** this non-classicality is rapidly lost in the open system - all curves quickly drop from the maximum value to zero or below. Interestingly the exact scar at $\phi = \pi/2$ preserves some of the quantum coherent information $I_q(t) = 0$ even at late times, whilst deviation from $\phi = \pi/2$ results in a quantum coherent information that falls towards $I_q(t) = -1$ instead. This suggests that some information can be preserved, but that it may be encoded classically rather than within the specifics of quantum coherences between states. Again, the ability of a system to preserve information after detuning from exact scarring $\phi = \pi/2$ falls off rapidly with system size, as shown in Fig. 2.13**(b)**.

In general this is unsurprising. Dephasing channels like the one I consider here drive states towards incoherent diagonal mixed states. As such only information that Alice encoded classically (i.e. in diagonal elements) persists and is accessible by Bob [51]. Thus one can simultaneously see a rapid falling off of the quantum coherent information, yet a persistent non-zero value of the Holevo quantity. Interestingly, this is reflected in the fact that the behaviour of Fig. 2.13 *after* the loss of non-classicality when $I_q(t)$ crosses zero, is almost identical to the behaviour of the Holevo quantity shown in Fig. 2.12. This suggests a potentially concrete connection between the quantum coherent information and channel capacities.

Finally, the encoding even of even a classical bit of information in the states $|\mathbb{X}_{\pm}\rangle$ is ruined entirely by different kinds of noise. The $+$ and Z noise are considered by invoking jump operators S_j^+ and S_j^z respectively.. For $+$ operators, results are shown in Fig. 2.14**(a)** and **(b)** for the quantum coherent information and Holevo quantity over time respectively. For Z operators, corresponding results are shown in Fig. 2.14**(c)** and **(d)**. All quantities aside from the quantum coherent information for Z operators (panel **(c)**) drop rapidly to their minimum values. This corresponds to total erasure of all information. As discussed before, the fact that S^x annihilates

$|-\rangle$ means that even after the channel has run its course, the resulting states are still distinguishable. Thus the system in question is resistant to a certain specific type of noise, but not to noise in general.

Ultimately this section represents a preliminary investigation of memory in scarred systems in open and closed contexts. Many questions have arisen in the course of this investigation, some of which I outline here but defer to my future work. First of all, does a more concrete connection between the Holevo quantity and the quantum coherent information, as suggested by the similarities between Fig. 2.12**(a)** and Fig. 2.13**(a)**? Secondly, are there other systems which bear the latent ability to postpone or entirely halt the loss of quantum coherence? Finally, are these properties strengthened by the fact that we have been working in the scarred subspace? This final question in particular represents a real, exploitable, use case for quantum scars in the context of quantum information processing and computing.

2.4 Outlook

In this chapter I have introduced the accessible information game, the Holevo quantity, and the quantum coherent information, in the context of non-ergodic quantum systems. In doing so I defined a brief criteria for determining whether or not a quantity in a 'memory quantifier'. In Section 2.2, I used a range of these memory quantifiers to determine how reliably MBL systems store information over time. This addresses a long-standing notion in MBL literature wherein they are held to have a kind of 'local memory'. I find that MBL systems indeed exhibit memory, with - in extreme cases - up to 95% of the data encoded within an MBL subsystem retained over time. However, the main extant quantifier of this memory, the imbalance, drastically underestimates this. My subsequent scaling analyses also revealed that the best quantifier of memory, the Holevo quantity, does not best capture the ergodic-MBL transition. I subsequently suggest that scaling results can be improved by discarding information, enforcing a procedure that the system would carry out automatically in the thermodynamic limit. The results of this analysis show that by discarding off-diagonal elements of subsystem density matrices, scaling analyses

yield coefficients consistent with the Harris criterion. This is a rarity in small-scale MBL literature.

In Section 2.3 I analyze the Holevo quantity and coherent information in both open and closed scarred systems. By encoding the simplest possible classical message - the state of a single bit - into the system, I was able to analyze whether or not claims of 'memory' in scarred systems are as well-founded as the similar claim of MBL systems. In closed systems, my results show that, whilst the scarred system exhibits a kind of robust memory which preserves information perfectly over time; it is very fragile to certain changes in the Hamiltonian. Moreover, the information seems to be non-locally encoded in the state of edge sites. In open systems, potential signatures of information retention were found, but only for certain kinds of noise. Ultimately these results suggest that scarred systems could generally exhibit a kind of memory, but that it is so delicate and fragile that it cannot reliably store even the state of a single bit. I contend that scarred memory is not as robust and general-purpose as MBL memory; and that the latter makes for a better quantum 'hard drive'. I conclude the section by suggesting ways in which these preliminary findings could be extended.

References

[1] Rahul Nandkishore and David A Huse. Many-body localization and thermalization in quantum statistical mechanics. *Annu. Rev. Condens. Matter Phys.*, 6(1):15–38, 2015.

[2] Dmitry A. Abanin and Zlatko Papić. Recent progress in many-body localization. *Ann. Phys. (Leipzig)*, 529(7):1700169, 2017.

[3] Alexander Nico-Katz, Abolfazl Bayat, and Sougato Bose. Information-theoretic memory scaling in the many-body localization transition. *Physical Review B*, 105(20):205133, 2022.

[4] Alexander Nico-Katz, Abolfazl Bayat, and Sougato Bose. Memory hierarchy

for many-body localization: Emulating the thermodynamic limit. *Physical Review Research*, 4(3):033070, 2022.

[5] J. Preskill. Chapter 10. quantum shannon theory. *Lecture Notes for Physics 229: Quantum Information and Computation.*, 1998.

[6] Arijeet Pal and David A. Huse. Many-body localization phase transition. *Physical Review B*, 82(17), Nov 2010.

[7] Emanuele Levi, Markus Heyl, Igor Lesanovsky, and Juan P. Garrahan. Robustness of many-body localization in the presence of dissipation. *Physical Review Letters*, 116(23), Jun 2016.

[8] Pedro Ponte, Z. Papić, François Huveneers, and Dmitry A. Abanin. Many-body localization in periodically driven systems. *Physical Review Letters*, 114(14), Apr 2015.

[9] J. Smith, A. Lee, P. Richerme, B. Neyenhuis, P. W. Hess, P. Hauke, M. Heyl, D. A. Huse, and C. Monroe. Many-body localization in a quantum simulator with programmable random disorder. *Nat. Phys.*, 12(10):907–911, 2016.

[10] Anushya Chandran, Isaac H. Kim, Guifre Vidal, and Dmitry A. Abanin. Constructing local integrals of motion in the many-body localized phase. *Phys. Rev. B*, 91:085425, Feb 2015.

[11] Michael Schreiber, Sean S. Hodgman, Pranjal Bordia, Henrik P. Lüschen, Mark H. Fischer, Ronen Vosk, Ehud Altman, Ulrich Schneider, and Immanuel Bloch. Observation of many-body localization of interacting fermions in a quasirandom optical lattice. *Science*, 349(6250):842–845, 2015.

[12] Henrik P. Lüschen, Pranjal Bordia, Sean S. Hodgman, Michael Schreiber, Saubhik Sarkar, Andrew J. Daley, Mark H. Fischer, Ehud Altman, Immanuel Bloch, and Ulrich Schneider. Signatures of many-body localization in a controlled open quantum system. *Physical Review X*, 7(1), Mar 2017.

[13] Pranjal Bordia, Henrik Lüschen, Sebastian Scherg, Sarang Gopalakrishnan, Michael Knap, Ulrich Schneider, and Immanuel Bloch. Probing slow relaxation and many-body localization in two-dimensional quasiperiodic systems. *Phys. Rev. X*, 7(4):041047, 2017.

[14] Kai Xu, Jin Jun Chen, Yu Zeng, Yu Ran Zhang, Chao Song, Wuxin Liu, Qiujiang Guo, Pengfei Zhang, Da Xu, Hui Deng, Keqiang Huang, H. Wang, Xiaobo Zhu, Dongning Zheng, and Heng Fan. Emulating Many-Body Localization with a Superconducting Quantum Processor. *Phys. Rev. Lett.*, 120(5):050507, 2018.

[15] Pranjal Bordia, Henrik P. Lüschen, Sean S. Hodgman, Michael Schreiber, Immanuel Bloch, and Ulrich Schneider. Coupling identical one-dimensional many-body localized systems. *Physical Review Letters*, 116(14), Apr 2016.

[16] Yu Chen. Universal logarithmic scrambling in many body localization. *arXiv preprint arXiv:1608.02765*, 2016.

[17] Juhee Lee, Dongkyu Kim, and Dong-Hee Kim. Typical growth behavior of the out-of-time-ordered commutator in many-body localized systems. *Physical Review B*, 99(18):184202, 2019.

[18] A. Chandran, A. Pal, C. R. Laumann, and A. Scardicchio. Many-body localization beyond eigenstates in all dimensions. *Phys. Rev. B*, 94(14):57–62, 2016.

[19] David Pekker, Bryan K. Clark, Vadim Oganesyan, and Gil Refael. Fixed points of wegner-wilson flows and many-body localization. *Phys. Rev. Lett.*, 119:075701, Aug 2017.

[20] A. S. Holevo. Bounds for the quantity of information transmitted by a quantum communication channel. *Probl. Peredachi Inf.*, 9(3):3–11, 1973.

[21] Wojciech Roga, Mark Fannes, and Karol Zyczkowski. Universal bounds for

the holevo quantity, coherent information, and the jensen-shannon divergence. *Phys. Rev. Lett.*, 105(4):040505, 2010.

[22] Michael A. Nielsen and Isaac L. Chuang. *Quantum Computation and Quantum Information: 10th Anniversary Edition*. Cambridge University Press, USA, 10th edition, 2011.

[23] Benjamin Schumacher and Michael D. Westmoreland. Sending classical information via noisy quantum channels. *Phys. Rev. A*, 56:131–138, Jul 1997.

[24] Benjamin Schumacher and Michael A Nielsen. Quantum data processing and error correction. *Physical Review A*, 54(4):2629, 1996.

[25] David J. Luitz, Nicolas Laflorencie, and Fabien Alet. Extended slow dynamical regime close to the many-body localization transition. *Phys. Rev. B*, 93(6):060201, 2016.

[26] Michael J. Gullans and David A. Huse. Dynamical purification phase transition induced by quantum measurements. *Phys. Rev. X*, 10:041020, Oct 2020.

[27] Thomas Klein Kvorning, Loïc Herviou, and Jens H. Bardarson. Time-evolution of local information: thermalization dynamics of local observables, 2021.

[28] Vedika Khemani, S. P. Lim, D. N. Sheng, and David A. Huse. Critical properties of the many-body localization transition. *Phys. Rev. X*, 7:021013, Apr 2017.

[29] Nicolas Laflorencie, Gabriel Lemarié, and Nicolas Macé. Chain breaking and kosterlitz-thouless scaling at the many-body localization transition in the random-field heisenberg spin chain. *Physical Review Research*, 2(4), Nov 2020.

[30] Vedika Khemani, D. N. Sheng, and David A. Huse. Two universality classes for the many-body localization transition. *Phys. Rev. Lett.*, 119:075702, Aug 2017.

[31] R. K. Panda, A. Scardicchio, M. Schulz, S. R. Taylor, and M. Žnidarič. Can we study the many-body localisation transition? *EPL*, 128(6):40–42, 2019.

[32] Piotr Sierant and J Zakrzewski. Can we observe the many-body localization? *arXiv preprint arXiv:2109.13608*, 2021.

[33] Vedika Khemani, Frank Pollmann, and S. L. Sondhi. Obtaining highly excited eigenstates of many-body localized hamiltonians by the density matrix renormalization group approach. *Phys. Rev. Lett.*, 116:247204, Jun 2016.

[34] Piotr Sierant, Dominique Delande, and Jakub Zakrzewski. Thouless time analysis of anderson and many-body localization transitions. *Phys. Rev. Lett.*, 124:186601, May 2020.

[35] A. Chandran, C. R. Laumann, and V. Oganesyan. Finite size scaling bounds on many-body localized phase transitions, 2015.

[36] Jonas A. Kjäll, Jens H. Bardarson, and Frank Pollmann. Many-body localization in a disordered quantum ising chain. *Phys. Rev. Lett.*, 113(10):1–7, 2014.

[37] Anders W. Sandvik. Computational studies of quantum spin systems. *AIP Conference Proceedings*, 1297(1):135–338, 2010.

[38] A. B. Harris. Effect of random defects on the critical behaviour of Ising models. *Journal of Physics C Solid State Physics*, 7(9):1671–1692, May 1974.

[39] J. T. Chayes, L. Chayes, Daniel S. Fisher, and T. Spencer. Finite-size scaling and correlation lengths for disordered systems. *Phys. Rev. Lett.*, 57:2999–3002, Dec 1986.

[40] Luca D'Alessio and Anatoli Polkovnikov. Many-body energy localization transition in periodically driven systems. *Annals of Physics*, 333:19–33, Jun 2013.

[41] Zheng-Hang Sun, Jian Cui, and Heng Fan. Characterizing the many-body localization transition by the dynamics of diagonal entropy. *Phys. Rev. Research*, 2:013163, Feb 2020.

[42] Maksym Serbyn, Z. Papić, and Dmitry A. Abanin. Local conservation laws and the structure of the many-body localized states. *Phys. Rev. Lett.*, 111:127201, Sep 2013.

[43] Kyungmin Lee, Ronald Melendrez, Arijeet Pal, and Hitesh J. Changlani. Exact three-colored quantum scars from geometric frustration. *Physical Review B*, 101(24), jun 2020.

[44] Hongzheng Zhao, Adam Smith, Florian Mintert, and Johannes Knolle. Orthogonal quantum many-body scars. *Phys. Rev. Lett.*, 127:150601, Oct 2021.

[45] M. R. Lambert, Shan-Wen Tsai, and Shane P. Kelly. Quantum memory at an eigenstate phase transition in a weakly chaotic model. *Phys. Rev. A*, 106:012206, Jul 2022.

[46] Christopher J Turner, Alexios A Michailidis, Dmitry A Abanin, Maksym Serbyn, and Zlatko Papić. Weak ergodicity breaking from quantum many-body scars. *Nature Physics*, 14(7):745–749, 2018.

[47] Sanjay Moudgalya, B Andrei Bernevig, and Nicolas Regnault. Quantum many-body scars and hilbert space fragmentation: a review of exact results. *Reports on Progress in Physics*, 85(8):086501, jul 2022.

[48] C. J. Turner, A. A. Michailidis, D. A. Abanin, M. Serbyn, and Z. Papić. Quantum scarred eigenstates in a rydberg atom chain: Entanglement, breakdown of thermalization, and stability to perturbations. *Phys. Rev. B*, 98:155134, Oct 2018.

[49] Michael Schecter and Thomas Iadecola. Weak ergodicity breaking and quantum many-body scars in spin-1 x y magnets. *Physical review letters*, 123(14):147201, 2019.

[50] Shane Dooley. Robust quantum sensing in strongly interacting systems with many-body scars. *PRX Quantum*, 2:020330, May 2021.

[51] Robin Blume-Kohout, Hui Khoon Ng, David Poulin, and Lorenza Viola. Information-preserving structures: A general framework for quantum zero-error information. *Phys. Rev. A*, 82:062306, Dec 2010.

Chapter 3

An Entanglement-Complexity Geometric Measure

"Happiness, free, for everyone, and let no one be forgotten!"

— Arkady and Boris Strugatsky

"I would like to make a confession which may seem immoral: I do not believe in Hilbert space anymore."

— John von Neumann
Also Basil Hiley every time we talk.

The preceding chapter detailed how tools from the quantum information community can be used to quantify information retained by the state of a dynamically evolving system about its initial conditions. This took the form of an 'accessible information game' in which we tried to extract as much information as possible from some known final state. In this chapter, the game is reversed: how much information do we need to *keep* in order to accurately represent a given state? And what insight can this reversal provide with respect to condensed-matter systems?

A sweepingly successful answer to this reversed question takes the form of tensor network approaches to quantum state representation. A quantum state that is represented in full by a number of elements exponential in system size can instead be represented by a linear number of fixed-size tensors. Moreover, certain

classes of quantum state actually have an *efficient* representation as a tensor network, wherein very little information about the quantum state is lost, even when the fixed size of the tensors is taken to be relatively small. In essence, when much of the exponentially large Hilbert space is irrelevant and can be discarded [1]. The result can be dramatic, later on in this chapter I consider ground states systems with five-hundred constituent spin-1 particles. An exact representation would require storing $3^{512} \approx 10^{244}$ complex numbers[1]. Tensor network approaches dropped this down to about ten million, a literal $\mathcal{O}(10^{237})$ speedup.

In this chapter I propose a new geometric measure of entanglement based on tensor networks, specifically the matrix-product state (MPS) formalism. They key advantage of this measure over extant measures is that it does not rely on separability, which allows it to address a wide class of condensed-matter contexts which the conventional geometric measure cannot. In essence, the MPS representation of a state becomes efficient when the amount of entanglement in a state is limited in some way. States with a low amount of entanglement permit exact (or close to exact) representations as MPS of low bond dimension, whilst states with a large amount of complicated entanglement structures require an MPS of large bond dimension that approaches the dimension of the total original Hilbert space [2, 3]. I thus construct a geometric measure of entanglement without appealing to separability by *reversing* this approach: the entanglement of a given state can be quantified by how much a low-χ MPS *fails* to represent it. This chapter concerns itself with the definition of this new geometric measure, additional motivations and discussions surrounding it, and the application of the measure to ground state phase diagrams and mid-spectrum eigenstate analyses. These analyses reveal that the MPS-derived entanglement-complexity geometric measure of entanglement is a potentially powerful tool for interrogating quantum systems and identifying phase transitions.

[1] Given a rough Fermi-style estimate of 10^{80} atoms in the observable universe, lets figure out what storing this number would look like. If every isolated atom in our observable universe was transmuted into an individual universe in its own right, and if each of the atoms in each of those universes was once again transmuted into its own sovereign universe, then if a single bit of information was etched upon every atom in all the unfolding, cascading cosmos, we could store about 0.0003% of the data required to modern floating-point precision. I did it with a laptop because a clever dude called Guifre Vidal wrote some papers in 2008.

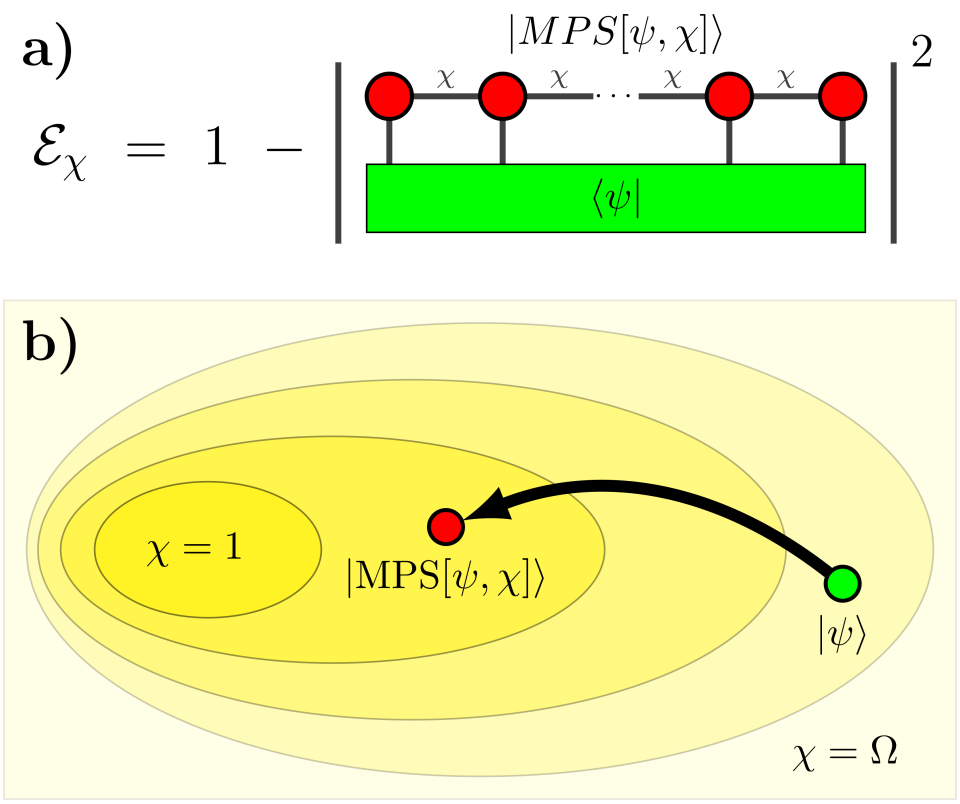

Figure 3.1: Schematics showing **a)** the diagrammatic equation for our generalization of the geometric entanglement (an overview of this diagrammatic notation is given in Appendix B) and **b)** a Hilbert space which has been organized into nested manifolds of states with perfect representations as MPS of bond dimension χ. The $\chi = 1$ manifold is a manifold of product states, and the full Hilbert space is attained as $\chi \to \Omega$ where Ω is the total dimension of the space. The compression procedure of a state $|\psi\rangle$ into its MPS representation $|\mathrm{MPS}[\psi,\chi]\rangle$ is given by the black arrow.

I begin by reviewing separability and extant separability-based geometric measures of entanglement in Section 3.1.1. I then summarize some important details of the MPS formalism in Section 3.1.2 before introducing my tensor network theoretic entanglement-complexity geometric measure in Section 3.1.3. In Section 3.2 I apply my geometric measure to a wide array of condensed matter systems; namely the $J_1 - J_2$ model and three variations on the spin-1 Haldane chain. Here I directly contrast it to the conventional geometric measure of entanglement of Wei and Goldbart introduced in Ref. [4]. This investigation reveals that different values of the bond dimension χ reveal new phases or features of phase diagram which are invisible to the conventional geometric entanglement. This establishes a class of measures

which together form a set of highly tunable exploratory tools. Finally, I address mid-sprectrum eigenstates in the context of many-body localization in Section 3.3, establishing the value of the measure away from ground-state phase transitions. Together, this demonstrates a range of contexts in which the entanglement-complexity measure exhibits striking advantages; offering a novel approach by which systems with limited but non-separable entanglement structures can be investigated using geometric measures. Much of this chapter is based on the published work of Ref. [5].

3.1 Geometric Measures of Entanglement

The defining feature of a geometric measure of entanglement takes the form of some set of states $\mathcal{S}$ which can be identified as being 'not entangled', and some distance function $f(\psi,\phi)$ between the state $|\psi\rangle$ that we are interested in and the states $|\phi\rangle \in \mathcal{S}$. Minimizing f yields a quantity which is interpreted as a geometric measure of entanglement: the distance between $|\psi\rangle$ and the closest non-entangled state. If the minimum value of f is zero then the state $|\psi\rangle$ is not entangled; anything otherwise heralds entanglement.

Conventional geometric measures of entanglement are defined as the distance of the quantum state in question to its nearest counterpart in a set of separable or k-separable states [6]. In essence directly conflating 'entanglement' with 'separability'. These measures have been exceedingly valuable when it comes to quantifying entanglement. A significant advantage of geometric measures is that they confer on us the ability to study bulk entanglement *globally* as opposed to measures which impose physical cuts (see e.g. the half-chain entanglement entropy, Schmidt gap, or negativity). They have seen widespread use in quantum information and in the investigation of bi-partite and multi-partite entanglement structures [4, 7–10]. Indeed the conventional definition of multi-partite entanglement is given in terms of separability [11, 12]. However, many systems yield states which have interesting, simple, entanglement structures that are not separable into any partitions of the system into subsystems. For a salient example, see the AKLT state discussed in Section 3.2.2. The rest of this section discusses separability, and then a reformulation

of the geometric entanglement based on the MPS formalism which does not appeal to separability in quantifying entanglement.

3.1.1 Separability and the Conventional Geometric Measures

Separability is an idea that is foundational to the definition of entanglement in many contexts. A separable state of N parties is one which can be prepared by acting locally on each of the N parties - without requiring long-range operations [13]. The eight cups of coffee I drink each day are separable; I prepare each one individually. This thesis is also separable. Despite the fact I have prepared each part in reference to its neighbours and its purpose in the tapestry of the whole, anything I want to change can be changed *locally*. Even if adding new information to the third chapter necessitates my inclusion of appropriate definitions in the first, I can simply make the changes sequentially and locally, mediating the relationship between the changes via classical communication (i.e. my personal notes). Quantum mechanical systems, however, may exhibit non-separability; wherein they simply cannot be prepared in this fashion. The canonical undergraduate examples are Bell pairs, though many of the complicated states which arise in the natural evolution of a quantum state under some Hamiltonian are in some way non-separable.

To be precise, the state of a system described in terms of N parties is called N-partite. If the state of an N-partite system can be prepared by acting on only N parties, then it is 'fully separable' or just 'separable'[2]. Note that this definition is subject to arbitrary re-partitioning, it is generally possible to divide a system into an arbitrary quantity of parties. For example, my eight daily coffees from the example above can be partitioned into 'morning' and 'afternoon' coffees (bi-partite description); or into my 'wake up coffees', 'physics cafe chat coffees', and 'coffees I don't need, but want' (tri-partite). Indeed I could subdivide the coffees further, each individual coffee into a nice hot first half, and a dreadful cold second half (16-partite). Quantum systems are the same and despite the fact that an obvious partitioning

[2]Much of the literature uses 'separable' and 'fully separable' interchangeably, as I do throughout this thesis. When referring to states that are only partially separable into $k < N$ partitions, I refer to them using the phrase k-separable to avoid ambiguity.

might represent itself[3], separability remains an difficult thing to pin down without choosing some a priori way of partitioning the system. Finally, if a state of N parties can be partitioned into $k < N$ parties wherein acting on these k parties locally prepares the full state, then the state is said to be k-separable. These k-separable states can be written as a product state of k parties which may be *internally* entangled but do not share entanglement *between* them [14–16]. The above discussion of full and k-separability becomes important later, where a poor choice of partitioning results in an only slightly entangled system registering as highly non-separable.

Given the above notion of separability, it is natural to define a set states which are fully separable $\mathcal{S}$, and define a distance function between elements of this set and the state in question $|\psi\rangle$. As introduced by Wei and Goldbart in the seminal publication of [4], when the distance measure is taken to be the state fidelity, this quantity $\mathcal{E}$ is known as the geometric measure of entanglement or 'geometric entanglement' for short. It is defined as:

$$\mathcal{E} = \min_{\phi} \left[1 - |\langle \psi | \phi \rangle|^2\right] \tag{3.1}$$

wherein the minimization of the quantity over $|\phi\rangle \in \mathcal{S}$ locates the state $|\phi\rangle$ which is closest to $|\psi\rangle$. The prevailing generalization of this quantity considers instead minimization over $|\phi\rangle \in \mathcal{S}_k$ where $\mathcal{S}_k$ the set of all k-separable states $\mathcal{S}_k$.

These quantities have seen widespread success, notably in the identification and analysis of bi-partite and genuine multi-partite entanglement [4, 7–10, 14, 17]. Despite this, Eq. (3.1) and its immediate generalization in terms of k-separability have one major shortcoming: they cannot readily differentiate between simple and complicated entanglement structures. A product state of entangled Bell pairs, for example, will saturate Eq. (3.1) despite its trivial structure, and one can conceive of states with which are *entirely* non-separable but have simple entanglement structures - e.g. the AKLT state [2, 18]. Thus, whilst a generalization of the geometric entanglement from the perspective of separability is invaluable, there are contexts

[3]For example, N interacting fermions should almost always be partitioned into N parties, and not $3N/2$ partitions wherein we have transformed half the fermions into Majorana fermions just for the accursed fun of it.

where a different generalization is more appropriate. I introduce just such a generalization through the exploitation of matrix product state (MPS) representations in the coming section.

3.1.2 The Matrix Product State Representation

The central object of the MPS formalism is the MPS itself: a representation of an arbitrary pure state $|\psi\rangle$ as a product of local tensors. This representation is formed by repeated reshaping and decomposition of the original state until it has been factorized into the MPS form, a process we briefly review here. For additional details see Refs. [2, 3], and for a brief introduction to diagrammatic tensor notation[4] see Appendix B. Starting from the generic pure state

$$|\psi\rangle = \sum_{\{j\}}^{d} c_{j_1,j_2,\cdots,j_N} |j_1, j_2, \cdots, j_n\rangle, \tag{3.2}$$

where the j indices are 'physical' indices which account for physical degrees of freedom, we combine the indices $j_2, j_3 \cdots, j_N$, reshape the tensor, and perform a singular value (Schmidt) decomposition across the physical indices j_1 and $(j_2, j_3, \cdots, j_N)$:

$$c_{j_1,(j_2,\cdots,j_N)} = \sum_{s_2} U_{j_1,s_2} S_{s_2,s_2} V^{\dagger}_{s_2,(j_2,j_3,\cdots,j_N)}. \tag{3.3}$$

The matrix U is left-unitary, $V^{\dagger}$ is right-unitary, and S is a diagonal matrix of the descending singular values across the bi-partition, of which some may be degenerate or exactly zero.

These singular values determine the quality of the decomposition: low singular values contribute less to the decomposition and can be discarded without a significant decrease in the fidelity of our MPS representation. The bond dimension χ is the positive integer number of these singular values that we choose to keep and quantifies the amount of information retained by our MPS. In general, the more singular values we discard at every partition, the more compressed and less exact our MPS representation becomes. It is here that the concept of entanglement complex-

[4] Also called 'Penrose' notation after it's creator.

ity becomes important: since the number of singular values across a bi-partition is an entanglement measure in its own right, states with less entanglement have more singular values equal or close to zero that can be readily discarded, and have correspondingly good low-χ MPS representations [1, 19]. The more entanglement there is in a system, and the more complicated its structure is, the higher the bond dimension required to achieve a good MPS representation [3].

Returning to our derivation of the MPS representation we reshape and suppress redundant rows and columns in the singular matrix and separate out the indices (j_1, s_2) and $(s_2, j_2, j_3 \cdots, j_N)$:

$$c_{j_1,j_2,\cdots,j_N} = \sum_{s_2} U_{j_1,s_2} S_{s_2,s_2} V^{\dagger}_{s_2,j_2,j_3,\cdots,j_N}. \tag{3.4}$$

We can now incorporate S into $U_{j,s} \to A^{[j]}_s$ and $V^{\dagger} \to \widetilde{V}^{\dagger}$ as is convenient, where we have relabeled U in accordance with notational convention:

$$c_{j_1,j_2,\cdots,j_N} = \sum_{s_2} A^{[j_1]}_{s_2} \widetilde{V}^{\dagger}_{s_2,j_2,j_3,\cdots,j_N}. \tag{3.5}$$

Repeating this procedure on $\widetilde{V}^{\dagger}$ across the next physical bi-partition using the combined indices (s_2, j_2) and $(j_3, j_4, \cdots, j_N)$ yields

$$c_{j_1,j_2,\cdots,j_N} = \sum_{s_2,s_3} A^{[j_1]}_{s_2} A^{[j_2]}_{s_2,s_3} \widetilde{V}^{\dagger}_{s_3,j_3,j_4,\cdots,j_N}. \tag{3.6}$$

By continually decomposing the resulting $\widetilde{V}^{\dagger}$ we finally arrive at the MPS representation of our tensor c

$$c_{j_1,j_2,\cdots,j_N} = \sum_{\{s\}} A^{[j_1]}_{s_1,s_2} A^{[j_2]}_{s_2,s_3} A^{[j_3]}_{s_3,s_4} \cdots A^{[j_N]}_{s_N,s_1}. \tag{3.7}$$

The s indices are 'auxiliary' indices which connect neighbouring tensors and describe the internal degrees of freedom (thus they can be conveniently gauged). The auxiliary index s_1 connecting the first and final tensors has been inserted to account for closed boundary conditions; in the case of open boundary conditions it can be

safely suppressed such that the first and final A matrices become vectors.

The final state, by Eq. (3.2) and Eq. (3.7), is thus

$$|\mathrm{MPS}[\psi,\chi]\rangle = \sum_{\{j\},\{s\}} A^{[j_1]}_{s_1,s_2} A^{[j_2]}_{s_2,s_3} \cdots A^{[j_N]}_{s_N,s_1} |j_1, j_2, \cdots, j_n\rangle \tag{3.8}$$

where the size of the A matrices is limited by the bond dimension χ which in turn controls the fidelity of the MPS decomposition $|\langle\psi|\mathrm{MPS}[\psi,\chi]\rangle|$. For clarity we must forego the usual notation $|\psi[A]\rangle$ for the MPS representation of a state as a parametrization in terms of the A matrices, instead introducing new notation $|\mathrm{MPS}[\psi,\chi]\rangle$ which clearly displays the bond dimension χ (rather than leaving it implicitly defined as the dimension of the A matrices) and reframes the decomposition of a state into its MPS representation as a compression procedure rather than an exact parametrization:

$$|\psi\rangle \rightarrow |\mathrm{MPS}\,[\psi,\chi]\rangle. \tag{3.9}$$

In the case that (i) the original state $|\psi\rangle$ has a low amount of entanglement, or that (ii) the bond dimension χ of the MPS representation is sufficiently high, the compression of Eq. (3.9) is close to lossless and the final MPS $|\mathrm{MPS}\,[\psi,\chi]\rangle$ is close to the initial state $|\psi\rangle$.

I conclude this section with four pertinent parting notes. Firstly, that the decomposition of Eq. (3.9) is not necessarily optimal in the sense that it minimizes the distance between the initial state and its MPS representation. This is due to the fact that different orderings of the decomposition over all physical bi-partitions do not yield identical results. Generally however, the greedy approach I use - sweeping left to right - is good enough. In addition, it is worth noting that once a state is *in* MPS form (such as the output states of the DMRG algorithms that follow), truncating that MPS can indeed be optimal. One simply discards the cached singular values [3]. Secondly, that the decomposition is not unique, as can be seen by simply gauging the bonds e.g. $A^{[j_1]}A^{[j_2]} = (A^{[j_1]}X)(X^{-1}A^{[j_2]}) = \widetilde{A}^{[j_1]}\widetilde{A}^{[j_2]}$; however this corresponds to a local change of basis and does not affect the physical properties of the MPS. Thirdly, that the number (and value) of the singular values across a bi-partition does

not change under local operations, rendering it a genuine entanglement measure [20]. Finally, that the manifold of MPS states of a fixed bond dimension χ contains the manifolds of all MPS states of strictly lower bond dimension: with the $\chi = \Omega$ manifold being identical to the full Hilbert space and the $\chi = 1$ manifold being identical to the set of all fully-separable states (no entanglement is present across any physical cut). The restructuring of Hilbert space into these nested manifolds, and the decomposition process of Eq. (3.9) on a generic state, are shown schematically in panel **b)** of Fig. 4.1.

3.1.3 The Entanglement-Complexity Geometric Measure

In contrast to the separability-based generalization of the geometric measure discussed in Section 3.1 which involved a minimization over the set of k-separable states, the generalization that I propose is the minimization of Eq. (3.1) over the manifold of MPS of fixed bond dimension χ:

$$\mathcal{E}_\chi = 1 - |\langle\psi|\mathrm{MPS}[\psi,\chi]\rangle|^2 \tag{3.10}$$

and is shown in diagrammatic tensor notation in panel **a)** of Fig. 4.1. I have omitted the minimization from our notation because, as discussed in Section 3.1.2 and noted in Ref. [3], this minimization happens implicitly during the decomposition of Eq. (3.9). The generalization Eq. (3.10) quantifies the representability of $|\psi\rangle$ as an MPS $|\mathrm{MPS}[\psi,\chi]\rangle$ of bond dimension χ, and is geometric in that this representability is quantified in terms of a distance function between $|\psi\rangle$ and the closest (constrained) state to it $|\mathrm{MPS}[\psi,\chi]\rangle$. I also note that, similarly to the $(k > N)$-separable generalization for an N-partite system, $E_{\chi>1} = 0$ does not necessarily mean that there is no entanglement; rather that the entanglement present is not sufficient enough to frustrate representation as an MPS of bond dimension χ. Given these two points, and the discussion of the role of the bond dimension χ in Section 3.1.2, the generalization Eq. (3.10) can be interpreted as the geometric entanglement from the perspective of entanglement complexity as opposed to k-separability.

Intuitively, rather than organizing the full Hilbert space into nested sets of k-

separable states like existing generalizations of the geometric entanglement, the MPS formalism organizes Hilbert space into nested manifolds of states with exact fixed-χ MPS representations (see panel **b)** of Fig. 4.1). This picture moves us away from separability and towards the alternative, nuanced understanding of entanglement complexity given by the MPS formalism. This nested structure also implies, as every MPS manifold contains the manifolds of strictly lower bond dimension within it, the hierarchy $\mathcal{E}_1 \geq \mathcal{E}_2 \geq \cdots \mathcal{E}_\Omega$ where Ω is the total dimension of the full Hilbert space. Definitionally, and conveniently, the geometric entanglement of Eq. (3.1) and my generalization of Eq. (3.10) coincide $\mathcal{E} = \mathcal{E}_1$ at $\chi = 1$ which defines a manifold of product states [2]; this has been noted in Ref. [21] which uses the $\chi = 1$ MPS representation to efficiently calculate the geometric entanglement - though it lacks an extension to higher bond dimensions. The restructuring of Hilbert space and interpretation of entanglement from the perspective of complexity rather than separability results in a quantity which, when it is extended to higher bond dimensions $\chi > 1$, captures behaviour which the geometric entanglement cannot.

Finally I remark that whilst MPS have been used in conjunction with the geometric entanglement before, these works focus on efficient calculation of existing measures, rather than in the construction of new measures. See e.g. Refs. [7, 10, 21, 22]. The calculation of $\mathcal{E}_\chi$ via the application of Eq. (3.10) to a range of interesting condensed-matter systems is the subject of the rest of this chapter.

3.2 Entanglement-Complexity as a Signature of Ground State Phase Transitions

In this section, I apply the introduced entanglement-complexity geometric measure $\mathcal{E}_\chi$ to a range of different Hamiltonians of increasing complexity. These Hamiltonians undergo various ground state phase transitions as a function of the Hamiltonian parameters, and serve to illustrate the capabilities of the measure $\mathcal{E}_\chi$. The first two models are the J_1-J_2 model in Section 3.2.1 and the spin-1 Haldane chain in Section 3.2.2 around the Majumdar-Ghosh and AKLT points respectively. These mod-

els showcase the basic features of $\mathcal{E}_\chi$ in very well-understood settings. I then discuss an ansiotropic Haldane chain with a complicated phase diagram in Section 3.2.3, which has seven different phases and exhibits critical behaviour belonging to several different university classes. Finally I investigate an anisotropic Dzyaloshinskii–Moriya interacting spin chain in Section 3.2.4, the ground state phase diagram of which is - to the best of my knowledge - not yet known.

The centrally important feature revealed by these analyses is that the quantity $\mathcal{E}_\chi$ for sufficient $\chi \ll \Omega$ is capable of detecting *all* phase boundaries for the considered systems. Ultimately, this suggests that the entanglement-complexity geometric measure $\mathcal{E}_\chi$ may be a powerful tool for the investigation of systems wherein the phase diagram is not yet explicitly known.

3.2.1 Phase Diagram of the J_1-J_2 Chain around the Majumdar-Ghosh Point

The first model of interest is the $J_1 - J_2$ model around the Majumdar-Ghosh point. At this point, for open boundary conditions, the unique ground state becomes a product state of entangled singlets [23]. Such a ground state has an exact representation as an MPS of bond dimension $\chi = 2$ and is $N/2$-separable, thus we would expect $\mathcal{E}_2$ to identify the Majumdar-Ghosh point exactly. The $J_1 - J_2$ model is defined by the Hamiltonian

$$H = J_1 \sum_j^n \vec{S}_j \cdot \vec{S}_{j+1} + J_2 \sum_j^n \vec{S}_j \cdot \vec{S}_{j+2} \tag{3.11}$$

where $\vec{S}_j$ are vectors of standard spin-1/2 operators. The Majumdar-Ghosh point is here found at $J_2 = J_1/2$.

Fixing $J_1 = 1$, I evaluate the generalized geometric entanglements $\mathcal{E}_1$ and $\mathcal{E}_2$ across the Majumdar-Ghosh point using two-site DMRG implemented to reach ground states of Eq. (3.11) for large system sizes ($N = 256$). These results are shown in Fig. 3.2, from which we can see clearly that - despite an initial peak at small system sizes - the conventional geometric entanglement completely fails to identify the point in the thermodynamic limit, whilst the $\chi = 2$ generalization successfully

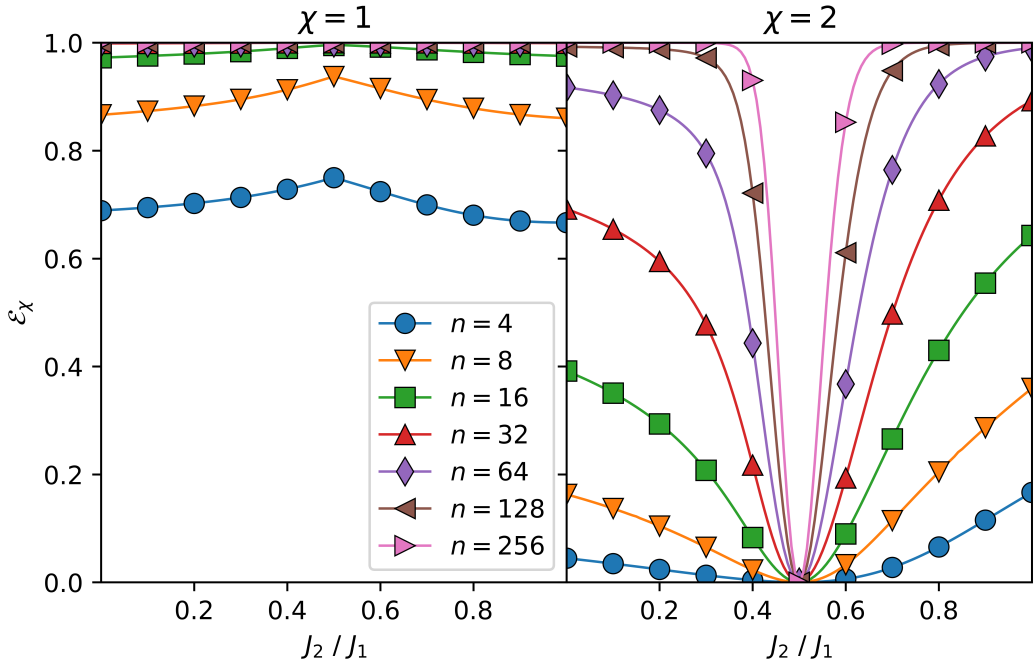

Figure 3.2: The **(left)** geometric entanglement $\mathcal{E}_1$ and **(right)** its first non-trivial generalization $\mathcal{E}_2$ of the $J_1 - J_2$ ground state across the Majumdar-Ghosh point. Whilst the conventional geometric entanglement initially shows a small peak at the Majumdar-Ghosh point, only $\mathcal{E}_2$ successfully locates the ground state in the thermodynamic limit.

captures the expected behaviour. Despite the clear advantage of $\mathcal{E}_2$ in this context, existing generalizations of the geometric entanglement based on k-separability can also detect the $N/2$-separable Majumdar-Ghosh ground state.

3.2.2 Phase Diagram of the Affleck-Kennedy-Lieb-Tasaki Model

In contrast to the previous section, wherein the Majumdar-Ghosh ground state is not fully separable but is $N/2$-separable and thus detectable via conventional generalizations of the geometric measure, here I demonstrate a situation where the any kind of separability is entirely irrelevant. The Affleck-Kennedy-Lieb-Tasaki (AKLT) ground state is a valence bond solid with an exact MPS representation of bond dimension $\chi = 2$ but which is at best 1-separable (i.e. not separable into subsystems) [2]. It can be prepared as the ground state of the spin-1 extended Haldane

chain

$$H = \sum_j^N \vec{S}_j \cdot \vec{S}_{j+1} + \frac{J_{\mathrm{AKLT}}}{3} \sum_j^N \left(\vec{S}_j \cdot \vec{S}_{j+1} \right)^2 \tag{3.12}$$

where $\vec{S}_j = (S_j^x, S_j^y, S_j^z)^\top$ are vectors of spin-1 operators. At the point $J_{\mathrm{AKLT}} = 1$, the ground state of Eq. (3.12) becomes the AKLT ground state with MPS representation:

$$A^{[+]} = \sqrt{\frac{2}{3}}\sigma^+, \quad A^{[0]} = \frac{1}{\sqrt{3}}\sigma^z, \quad A^{[-]} = \sqrt{\frac{2}{3}}\sigma^- \tag{3.13}$$

where the $\sigma^\pm$ and σ^z operators are the standard pauli ladder and z operators [2, 3, 18, 24]. In this setting it is clear that $\mathcal{E}_2$ should be able to detect the AKLT ground state, whilst the geometric entanglement and its k-separable generalizations cannot. I take open boundary conditions, and fix the elements of $\vec{S}_1$ and $\vec{S}_N$ (where N is

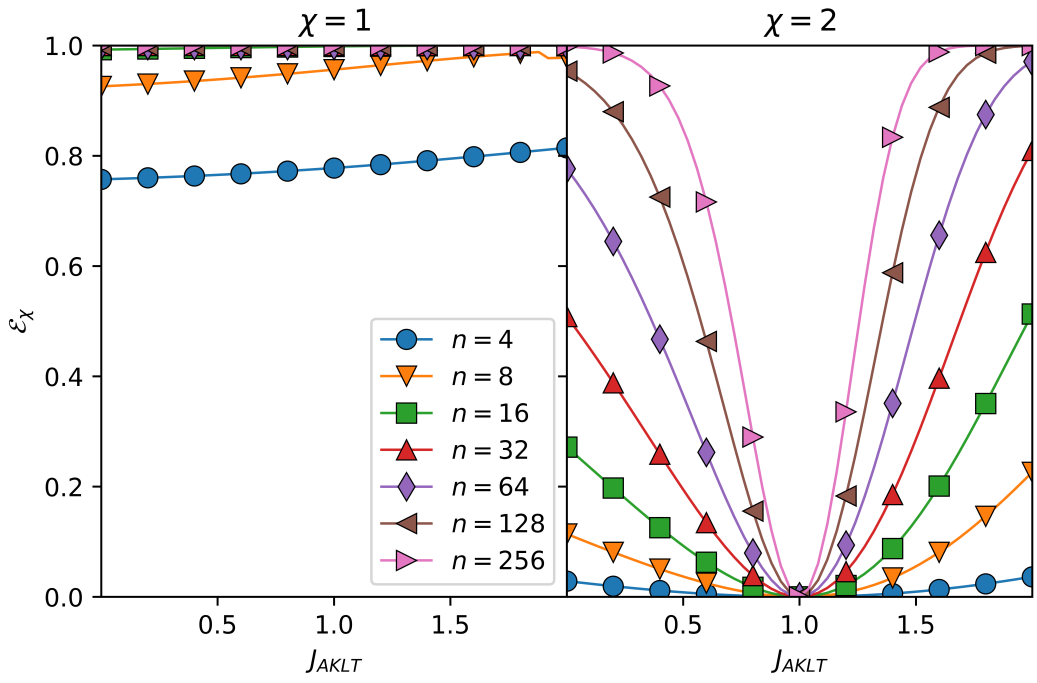

Figure 3.3: The **(left)** geometric entanglement $\mathcal{E}_1$ and **(right)** our generalized $\chi = 2$ counterpart E_2 of the ground state of Eq. (3.12) across the AKLT point. Only our generalization successfully locates the AKLT ground state.

the system size) as spin-1/2 operators to lift the fourfold ground state degeneracy [25]. I then probe the system's ground state using the geometric entanglement $\mathcal{E}_1$ and its first non-trivial generalization $\mathcal{E}_2$. I use two-site DMRG implemented to access large system sizes up to $N = 256$ [2, 26, 27]. The results are shown in

Fig. 3.3, from which we can see that the geometric entanglement $\mathcal{E}_1$ fails to detect the AKLT point at all, even in small systems in which it hasn't yet saturated to unity, whilst our $\chi = 2$ generalization $\mathcal{E}_2$ successfully identifies the ground state in the thermodynamic limit.

3.2.3 Phase Diagram of the Anisotropic Haldane Chain

The fact that the toy problems of the previous sections are best captured by $\mathcal{E}_2$ instead of $\mathcal{E}_1$ is - whilst an excellent demonstration of why the entanglement-complexity generalization is valuable - fairly obvious given the properties of the Majumdar-Ghosh and AKLT ground states. In both of these cases, the exact MPS representation is either well-known, or obvious. Now let us consider a case where this no longer holds, wherein the optimal value of χ is not known *a priori* and may in fact vary across the phase diagram. In this setting, higher generalizations $\chi \geq 2$ should gradually reveal more and more details about the known phase diagram of the system in question.

The system I consider is the anisotropic Haldane chain

$$H = J \sum_{j=0}^{L-1} \vec{S}_j \cdot \vec{S}_{j+1} + D \sum_{j=0}^{L} \left(S_j^z\right)^2 + E \sum_{j=0}^{L} \left(S_j^x\right)^2 - \left(S_j^y\right)^2 \tag{3.14}$$

where the parameter D tunes the strength of uniaxial anisotropies, and E tunes the strength of rhombic anisotropies. The Hamiltonian of Eq. (3.14) is widely used, albeit often with one of the anisotropic terms set to zero, in the modelling of realistic spin systems [28, 29] (also see Ref. [30] and the references therein).

The ground state phase diagram of the system is shown in panel **a)** of Fig. 3.4. There are seven distinct phases: the three Néel-like phases, the large-$E_x/E_y/D$ phases, and - most notably - the central gapped Haldane phase. We discuss these where relevant throughout the rest of this section. There are a litany of associated phase transitions in different universality classes, but we will only briefly mention the three Gaussian transitions between the Haldane phase and the large-$E_x/E_y/D$ phases (marked as red dots with arrows through them in panel **a)** of Fig. 3.4) [5] [32].

[5] For a more detailed discussion of the phase transitions see Ref. [31] and the references therein.

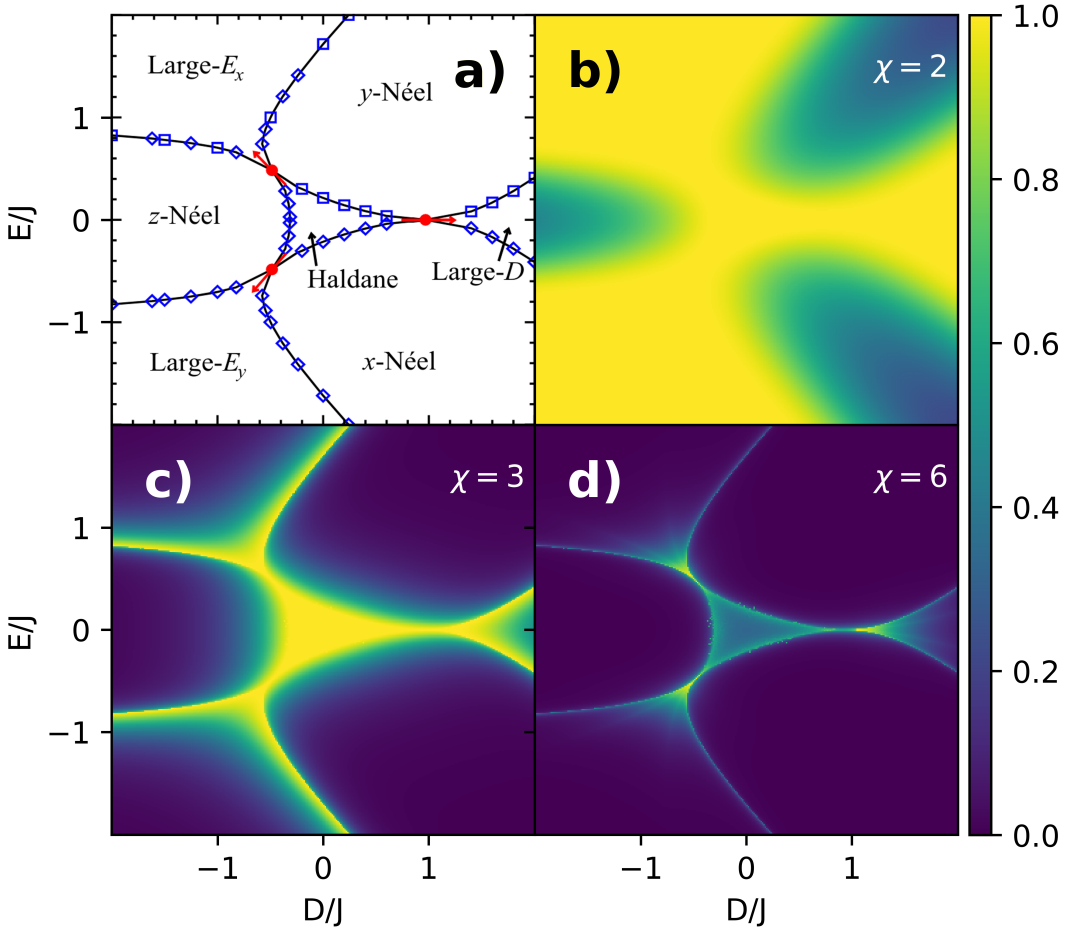

Figure 3.4: The ground state phase diagram of the anisotropic Haldane model of Eq. (3.14). Panel **a)** shows the phase diagram as determined in Ref. [31] (reproduced with permission). Panels **b)-d)** show $\mathcal{E}_\chi$ of the ground state for $\chi = 2,3,6$ respectively. The ground states were calculated for a system of $n = 512$ sites using two-site DMRG [2, 26, 27].

In this section, I consider an anti-ferromagnetic $J > 0$ coupling and so the ground state prefers maximal values $S^z_j = \pm 1$ everywhere, the different phases occur when this antiferromagnetic coupling and the anisotropies tuned by D and E assist or frustrate each other. The system is symmetric around $E = 0$ as a negative E simply corresponds to an inversion of x and y axes on each site. The ground states of each phase are best understood in terms of single-site ground states everywhere except the Haldane phase around $D = E = 0$, and it is from this perspective that they are discussed them below. The point $D = E = 0$ itself is adiabatically connected to the AKLT ground state, as evidenced by the continuity of Fig. 3.3 across the interval $J_{\text{AKLT}} \in [0,1]$, and thus the Haldane phase is best understood as having similar

properties to the valence bond solid of the AKLT point.

As shown in panel **a)** of Fig. 3.5, the geometric entanglement $\mathcal{E}_1$ is close to saturation across the entire region of phase space I investigate $D \in [0,2]$ and $E \in [0,2]$. This is simply due to the fact that - even in regions where single-site terms begin to dominate - the antiferromagnetic coupling still generates some entanglement. As the single-site terms dominate fully $D/J \to \infty$ or $E/J \to \infty$, the geometric entanglement should once again become a useful investigative tool as the ground states become products of single-site ground states.

In contrast to the geometric entanglement, my entanglement-complexity generalization $\mathcal{E}_\chi$ reveal more and more features of the phase diagram as a function of increasing χ; a feature related to the fact that the different phases have different entanglement structures which are best captured by MPS of different bond dimensions. This is shown in panels **b)-d)** of Fig. 3.4 where the phases of Eq. (3.14) are captured by $\mathcal{E}_\chi$ for $\chi = 2,\ 3,\ 6$ respectively.

Panel **b)** shows the first non-trivial generalization $\mathcal{E}_2$ which successfully identifies states deep in the $x/y/z$-Néel phases. These phases occur when the system's ground state is close to a Néel state ($\chi = 1$) of eigenstates $|S_j^{x/y/z} = \pm 1\rangle$ respectively. In the z-Néel phase this is assisted by low E which prefers $|S_j^x = 0\rangle$ eigenstates and the antiferromagnetic coupling J itself. In the x-Néel and y-Néel phases this is assisted by positive D which prefers $|S_j^z = 0\rangle$. As such all three Néel states aren't frustrated away from their respective phase boundaries and these regions are revealed by low bond dimension $\chi = 2$.

Panel **c)** shows $\mathcal{E}_3$ which reveals the full extent of the Néel phases and successfully identifies the large-$E_x/E_y/D$ phases. The former is due to slight frustration that each of the Néel phases experience close to their phase boundaries, an MPS of bond dimension $\chi = 2$ simply does not capture enough information near these boundaries. The latter is due to the fact that each of the large-$E_x/E_y/D$ phases is frustrated. The large-E_x/E_y phases have ground states close to product states of $|S_j^{x/y} = \pm 1\rangle$ but this is frustrated directly by negative D and the antiferromagnetic coupling J which prefer eigenstates $|S_j^z = \pm 1\rangle$. The large-D phase experiences a

similar frustration, but entirely between the antiferromagnetic coupling and large positive D. We can also infer the existence of the Haldane phase around $D = E = 0$, but not any of its properties or its phase boundaries.

Panel **d)** shows $\mathcal{E}_6$ which further narrows the phase boundaries and finally reveals the Haldane phase itself. A clear decrease of in $\mathcal{E}_6$ can be seen in the Haldane phase indicating that it is area-law entangled; a feature of the fact that the ground state at $D = E = 0$ is adiabatically connected to the area-law AKLT ground state. In fact the AKLT ground state is a good approximation of the true ground state near $D = E = 0$ in general [33, 34]. The reason the Haldane phase is only captured by a slightly higher bond dimension $\chi = 6$ compared to the other phases is simply due to the fact that all the terms of the Hamiltonian are of the same order, the system is thus highly frustrated, and is slightly more entangled - though it is still ultimately a valence bond solid similar in structure to the AKLT ground state and can still be represented efficiently as an MPS.

Investigation of this phase diagram at much higher values of $\chi = 8, 16, 32$ is shown in Fig. 3.5. Unlike in Fig. 3.4, the color scale is logarithmic to ensure visibility of E_χ even in the large-χ regime wherein the fidelity of the MPS representation is very high almost everywhere. Panel **b)** of Fig. 3.5 shows $\mathcal{E}_8$ in which the Haldane phase has become very clearly defined, reinforcing the idea that - whilst it is more entangled than the other phases' ground states and the AKLT state - it is still area-law entangled and admits a low-χ MPS representation as expected. Panels **c)** and **d)** show $\mathcal{E}_{16}$ and $\mathcal{E}_{32}$ respectively in which we see an exponential drop-off in the fidelity loss due to high bond dimension MPS representations. The critical regions near the Gaussian critical points from the Haldane phase to the large-$E_x/E_y/D$ phases are the brightest regions; this aligns with the understanding that - close to criticality - low-χ MPS representations generally fail. An interesting aspect of these plots that may warrant further research is that the phase diagram persists even at high bond dimension, suggesting a potential scaling in bond dimension and fidelity.

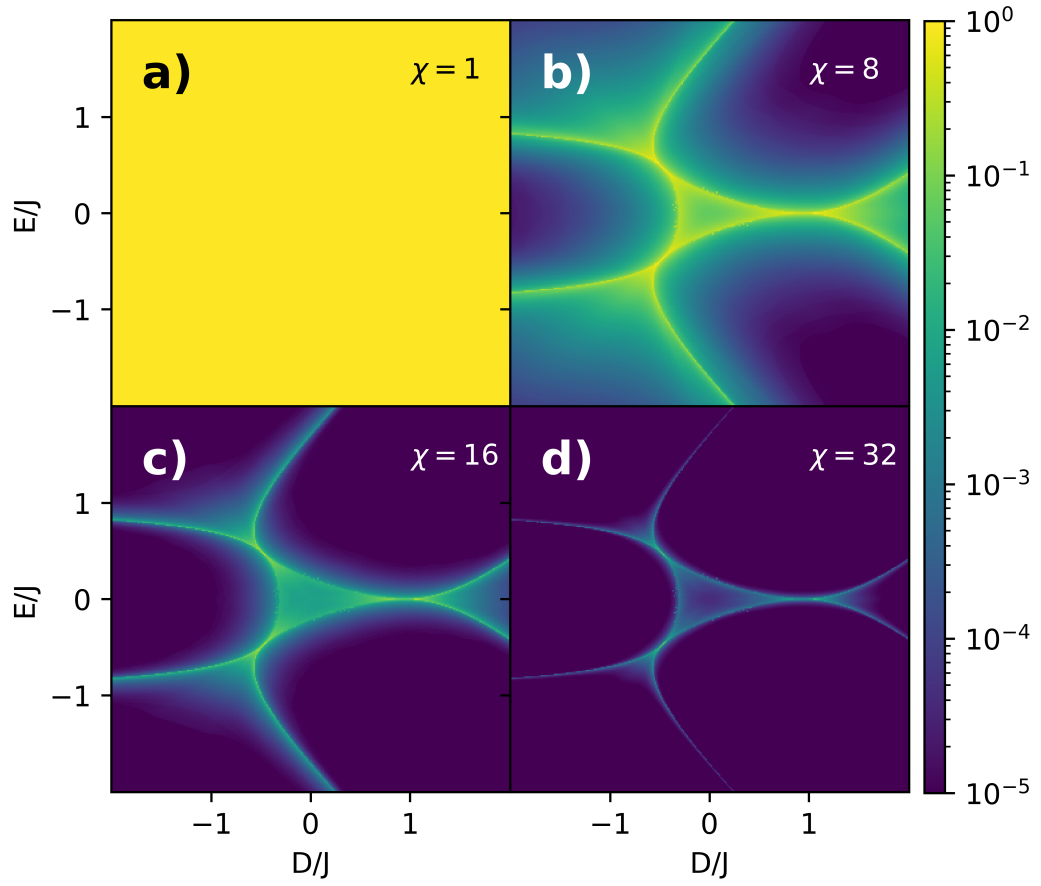

Figure 3.5: The ground state phase diagram of the anisotropic Haldane model of Eq. (3.14). Panel **a)** shows the geometric entanglement $\mathcal{E}_1$. Panels **b)-d)** show $\mathcal{E}_\chi$ of the ground state for $\chi = 8, 16, 32$ respectively. The ground state was calculated for a system of $n = 512$ sites using two-site DMRG implemented using an extension of quimb [35].

3.2.4 Phase Diagram of a Anisotropic Spin-1 Dzyaloshinskii–Moriya Interacting Chain

Concluding this section, I consider a novel model with a ground state phase diagram that has not - to the best of my knowledge - been investigated in any detail. Thus, unlike in all previous toy models of this section, neither I nor anyone else have any idea what this ground state phase diagram is going to look like[6]. The model in question is a hybrid of the scarred spin-1 chain with interactions that can be tuned between XXZ and Dzyaloshinskii–Moriya interactions first introduced in Section 2.3.1, and the rhombic anisotropy terms introduced in Section 3.2.3. It is

[6] It's weird.

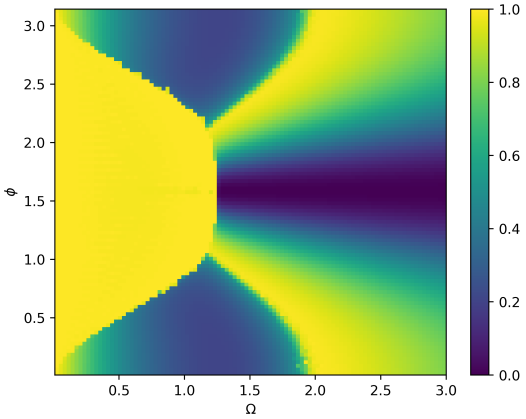

(a) The geometric entanglement $\mathcal{E}_1$ across the ground state phase diagram at various ϕ and Ω. System size $N = 50$.

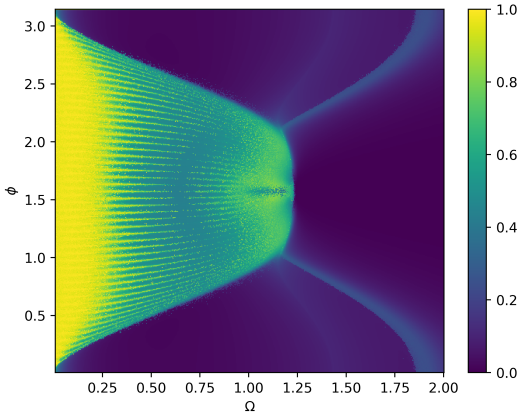

(b) The $\chi = 2$ generalization of the geometric entanglement $\mathcal{E}_2$ across the ground state phase diagram. System size $N = 50$.

defined as follows:

$$H = J \sum_{j}^{N-1} \left(e^{i\phi} S_j^+ S_{j+1}^- + \text{h.c.} \right) + \Omega \sum_{j}^{N} \left(S_j^x \right)^2 - \left(S_j^y \right)^2 \tag{3.15}$$

where S_j^α are standard spin-1 operators, and where I have taken open boundary conditions. This model exhibits quantum scarring for $\Omega = 0$ [36]. The ground state phase diagram is determined using two-site DMRG for a system of $N = 50$ spins, with results for the conventional geometric entanglement $\mathcal{E}_1$ shown in Fig. 3.6a and for the $\chi = 2$ generalization $\mathcal{E}_2$ in Fig. 3.6b.

The results of this blind, probative investigation are striking. The conventional geometric entanglement $\mathcal{E}_1$ does successfully identify broad regimes and possible novel phases in the model of Eq. (3.15). However, the entanglement-complexity geometric measure $\mathcal{E}_2$ reveals a strange internal structure within those phases. The striations that appear in the leftmost bright region are the most interesting feature - the number of striations that appear is equal to the system size (other sizes not shown). This may suggest the existence of an $L\phi$-dependence in the ground state - though I defer an actual, detailed, investigation of this phase diagram to future research. Ultimately this section, whilst a brief and cursory presentation of results, demonstrates the potential value of $\mathcal{E}_\chi$ as an exploratory tool for investigating systems which are not so thoroughly understood, e.g. in systems where optimal values of χ are not known *a priori*.

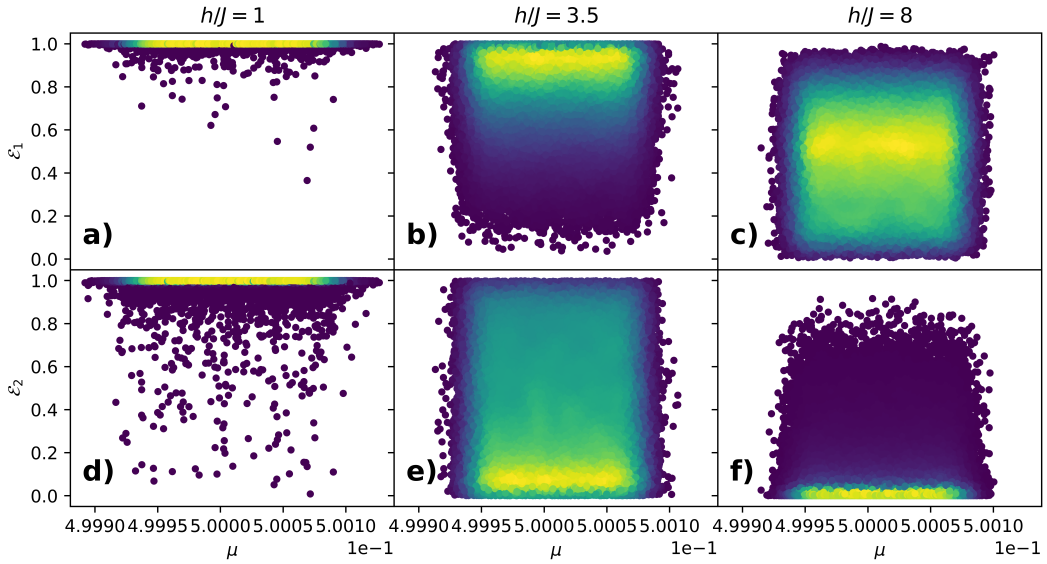

Figure 3.7: Geometric measures $\mathcal{E}_1$ and $\mathcal{E}_2$ of mid-spectrum eigenstates of Eq. (2.10) for a range of disorder strengths h/J across the MBLT. Each column shows a different disorder strength: **a),d)** in the ergodic regime $h/J = 1$, **b),e)** near the middle of the ergodic-MBL transition $h/J = 3.5$, and **c),f)** in the MBL regime $h/J = 8$. Brighter yellow coloration indicates a higher density of states. The dimensionless quantity $\mu \in [0,1]$ is the energy of the eigenstate relative to extremal eigenenergies, with $\mu = 0$ corresponding to the ground state energy, and $\mu = 1/2$ to the middle of the spectrum.

3.3 Entanglement-Complexity of a Many-Body Localized System

As discussed in Section 1.3.2 many body localization (MBL) is one possible mechanism by which an interacting many-body quantum system fails to thermalize. The precise definition of thermalization in this context is still debated (see Section 1.3.1); but certain hallmarks of MBL have been well established. Notable features of MBL include: the emergence of local memory, the breakdown of internal energy and particle transport, local integrals of motion, and mid-spectrum eigenstates exhibiting area-law like entanglement entropy [37–39]. Whilst the first feature was examined in the previous chapter, this chapter concerns itself with the last. MBL states are area law entangled, exhibiting simple short-range entanglement structures. Despite this, they are generally non-separable and exhibit limited genuine multi-partite entanglement. Because of this, conventional geometric measures

of entanglement are generally useless at diagnosing the onset of MBL. However, area-law states admit efficient representations as low bond dimension MPS, and hence my entanglement-complexity generalizations can meet considerably more success in diagnosing MBL. It is worth explicitly noting here that the MBL transition takes place across the entire spectrum and is a departure from the ground state transitions I have considered thus far in this chapter.

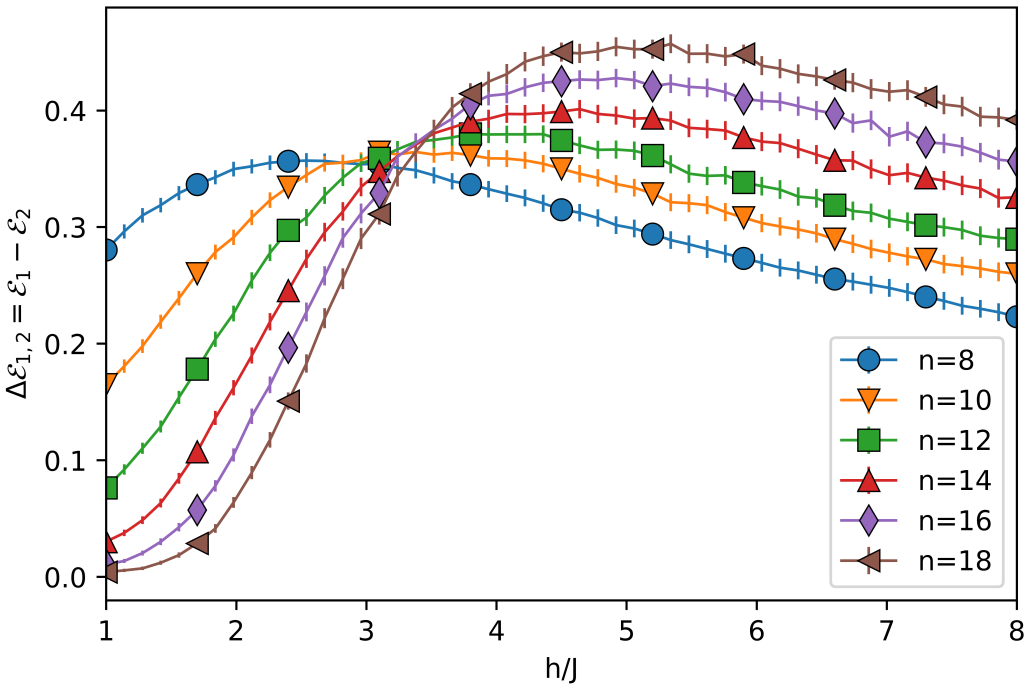

Figure 3.8: The difference $\Delta\mathcal{E}_{1,2} = \mathcal{E}_1 - \mathcal{E}_2$ between the conventional $\mathcal{E}_1$ and generalized $\mathcal{E}_2$ geometric entanglements across the ergodic-MBL transition. Each data point is over 512 disorder realizations and 10 mid-spectrum eigenstates per disorder realization. Error bars shown where visible.

Once again, let us consider the prototypical Heisenberg Hamiltonian comprised of n spin-$1/2$ particles with quenched z-field disorder of Eq. (2.10). This model is discussed in detail in Section 2.2.1. The ratio of disorder strength to Heisenberg coupling h/J tunes the model and for large disorder $h/J \gg 1$, the system is MBL. I consider systems of size up to $n = 18$ which, whilst too small to extract reliable thermodynamic properties of MBL through e.g. conventional scaling analyses (see Section 1.3.3.1 and Section 2.2.4), allows us to differentiate ergodic and localized regimes [40, 41].

I first investigate $\mathcal{E}_\chi$ for individual mid-spectrum eigenstates across the MBL transition using both the conventional geometric entanglement $\mathcal{E}_1$ in panels **a)-c)** and the bond dimension $\chi = 2$ generalization $\mathcal{E}_2$ in panels **d)-f)** of Fig. 3.7. Each panel shows $\mathcal{E}_\chi$ for 1024 samples of 100 mid-spectrum eigenstates, for a total of 102400 data points, these are then coloured according to a Gaussian kernel density estimation wherein brighter yellow coloration indicates a higher density of states. From panels **a)** and **d)** we see that both $\mathcal{E}_1$ and $\mathcal{E}_2$ are high in the ergodic regime $h/J = 1$, implying the well-known property that mid-spectrum eigenstates of generic Hamiltonians are volume-law and thus have no efficient representation as low bond dimension MPS. Panels **b)** and **e)** indicate that, close to the transition point $h/J = 3.5$, $\mathcal{E}_1$ remains high, but the average value of $\mathcal{E}_2$ - despite the existence of many individual eigenstates which have $\mathcal{E}_2$ far from zero - drops suddenly. This implies that eigenstates are far from product states, but are starting to become area-law entangled as low dimension MPS representations become increasingly viable. Finally panels **c)** and **f)** show slightly lower values of $\mathcal{E}_1$ and near-zero values of $\mathcal{E}_2$ in the MBL regime $h/J = 8$. This indicates that, in addition to almost all the eigenstates being area-law entangled with highly efficient MPS representations, many of the states also have considerable overlap with product states. This suggests that we are witnessing the onset of behaviour similar to the $h/J \to \infty$ case where all ground states simply become product states of local S^z_j eigenstates.

Given the results of Fig. 3.7 and the associated discussion, notice that $\mathcal{E}_1$ and $\mathcal{E}_2$ coincide in the ergodic phase $\mathcal{E}_1 = \mathcal{E}_2 = 1$, diverge near the ergodic-MBL transition point, and tend to coincide again deep in the MBL phase $\mathcal{E}_1 = \mathcal{E}_2 = 0$. This is due to the fact that MPS of bond dimension $\chi = 1$ and $\chi = 2$ are both equally bad representations of thermal states on the ergodic side of the transition, and both equally exact representations of product states on the extreme $h/J \to \infty$ MBL side of the transition. This behaviour is captured by the equation

$$\Delta\mathcal{E}_{\chi_1,\chi_2} = \mathcal{E}_{\chi_1} - \mathcal{E}_{\chi_2}, \tag{3.16}$$

which is strictly non-negative and bounded in the interval $[0,1]$ for $\chi_1 < \chi_2$ [7]. Quantitatively Eq. (3.16) captures how much the fidelity of the MPS representation of a given state improves when we increase the bond dimension $\chi_1 \to \chi_2$.

In the following analyses, I average $\Delta\mathcal{E}_{1,\chi} = \mathcal{E}_1 - \mathcal{E}_\chi \geq 0$ over 512 realizations of the Hamiltonian and 10 mid-spectrum eigenstate samples for each of these realizations. The results of this analysis for $\Delta\mathcal{E}_{1,2}$ are shown in Fig. 3.8 where we can clearly see $\Delta\mathcal{E}_{1,2} \to 0$ in the ergodic regime, climbing throughout the critical region, and decreasing linearly towards zero deep in the localized regime. In the transition region we can see a crossover point around $h/J \sim 3.5$ (considering the largest three sizes available) indicating scale-invariant behaviour around the region where the critical point $h_c \geq 3.5$ is usually found for similar small systems in this model [42]. I also note a slight drift of this crossover which is not an atypical pathology in extant analyses at similar scales. Whilst $\mathcal{E}_\chi$, and by extension Eq. (3.16) cannot diverge by definition, its gradient can: a feature shown clearly in Fig. 3.8 close to $h/J = 3.5$ with steeper gradients for larger system sizes.

I extend this study by considering $\Delta\mathcal{E}_{1,\chi}$ for $\chi > 2$ up to $\chi = 16$. It is important to note here that due to the restructuring of Hilbert space into a hierarchy of nested manifolds of MPS with fixed bond dimension there is an associated hierarchy $\mathcal{E}_1 \geq \mathcal{E}_2 \geq \cdots \geq \mathcal{E}_\Omega$ in the generalized geometric entanglement. Two corollaries to this fact are: (i) that $\Delta\mathcal{E}_{1,\chi} \geq 0$ with equality only when the state in question is a product state or when $\chi = 1$, and (ii) that there exists a similar hierarchy in $\Delta\mathcal{E}_{1,\chi}$:

$$\Delta\mathcal{E}_{1,2} \leq \Delta\mathcal{E}_{1,3} \leq \cdots \leq \Delta\mathcal{E}_{1,\Omega}. \tag{3.17}$$

The hierarchy of Eq. (3.17) is shown in Fig. 3.9 for a system of size $n = 18$, where one can also see a clear peak emerging in the critical region near $h/J = 3.5$ as the bond dimension is increased. Given that I consider considerable values (relative to the low system size) of the bond dimension $\chi = 16$; this result supports the argument that all low or intermediate bond dimension MPS representations are

[7] A trivial feature of the nested structure of the variational manifolds shown in Fig. 3.1, i.e. that increasing the size of the variational parameter space will never produce a worse representation of the state.

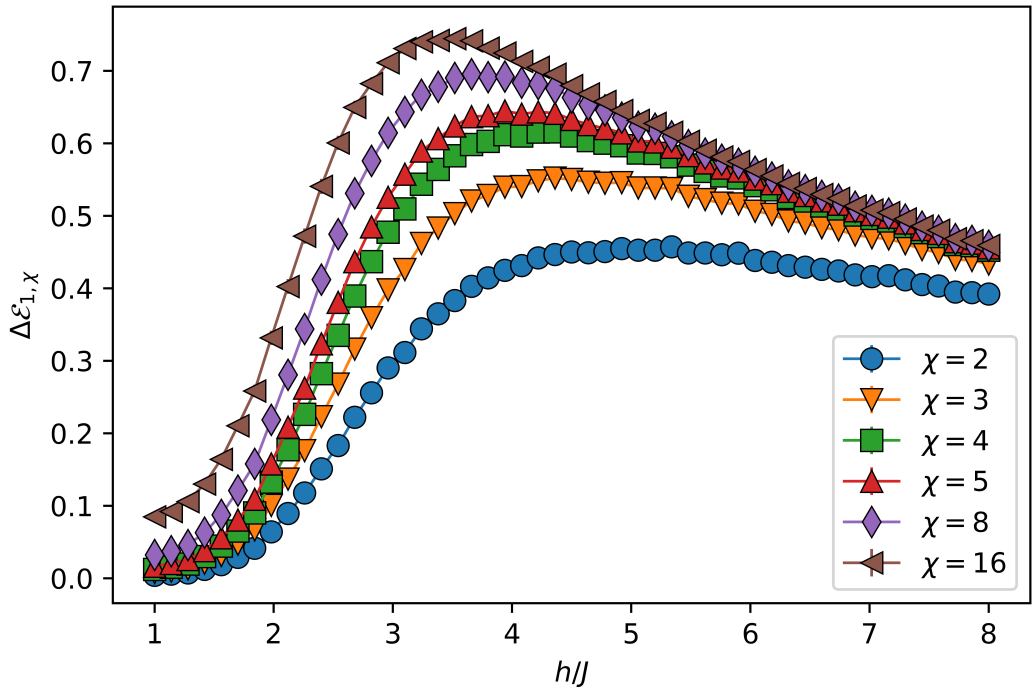

Figure 3.9: The relative generalized geometric entanglement $\Delta\mathcal{E}_{1,\chi}$ across the ergodic-MBL transition for different values of χ in a system of size $n = 18$.

equally poor in the ergodic regime, and become equally good in the MBL regime. The similarity of the curves in Fig. 3.9 also suggests that the coarse-graining of entanglement enforced by MPS representations of low bond dimension does not erase the qualitative features of the transition. It does, however, suggest that the exact quantitative features change considerably, as changing the bond dimension seems to induce a logarithmic drift in the peak. This further supports the argument that the quantity $\Delta\mathcal{E}_{1,\chi}$ is not useful as a scaling quantity in the context of MBL[8].

To capstone my investigation of MBL via the entanglement-complexity geometric measure, I also present results for $\Delta\mathcal{E}_{1,\chi}$ for a range of different values of χ and different system sizes, the results of which are shown in Fig. 3.10. The main features of all panels are similar to Fig. 3.8: a characteristic intersection of lines that suggests scale-invariance close to $h/J = 3.5$, and the drift of this point with increasing system size n. In essence, no new qualitative information is revealed by accessing higher values of χ aside from a more pronounced critical peak in Fig. 3.9.

[8] Additionally, I personally could not find good data collapses in any of the $\Delta\mathcal{E}_{\chi_1,\chi_2}$.

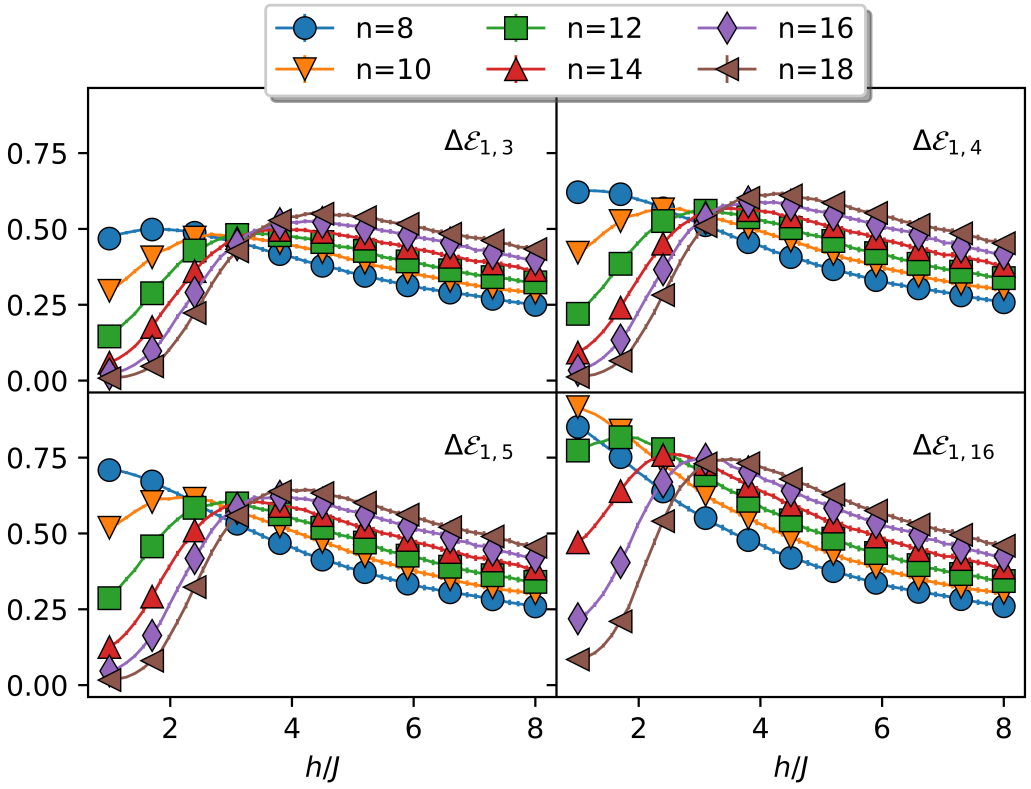

Figure 3.10: The relative generalized geometric entanglement $\Delta\mathcal{E}_{1,\chi}$ across the ergodic-MBL transition for different values of χ and different system sizes.

This all indicates that the properties of $\mathcal{E}_1$ and $\mathcal{E}_2$ together suffice to characterize the MBLT. Of course this may change at larger system sizes, or for systems that exhibit different kinds of ergodicity-breaking.

3.4 Outlook

In this chapter I have introduced a scalable geometric measure of entanglement that does not appeal to separability. Rather, through the MPS formalism and the bond dimension χ, my approach focuses an alternative understanding of entanglement in terms of entanglement complexity: the efficiency of state representation under entanglement coarse-graining. This change in perspective yields a novel geometric measure of entanglement $\mathcal{E}_\chi$ which succeeds in contexts where the conventional geometric entanglement (coincident with $\mathcal{E}_1$) and its immediate k-separable generalization cannot. I additionally note that, due to the advantageous fact that $\mathcal{E}_\chi$ is still derived from an overlap between two states, it may also retain the positive feature of

being an experimentally measurable quantity through e.g. a SWAP test [43, 44] or MPS tomography [45]. I have demonstrated the value of $\mathcal{E}_\chi$ in a variety of different contexts. Firstly, at the Majumdar-Ghosh and AKLT points, which can be detected by my geometric measure $\mathcal{E}_2$ but not necessarily by the conventional geometric entanglement $\mathcal{E}_1$. Secondly, I found that the known phases of the anisotropic Haldane model, each having their distinct signature in entanglement-complexity, are gradually revealed by $\mathcal{E}_\chi$ as χ is varied; these phases are invisible to the conventional geometric entanglement. Thirdly, in a more exploratory setting, I found several interesting features of the phase diagram of a hitherto uninvestigated system - the anisotropic DMI interacting spin-1 chain.

Finally, in the context of MBL and away from ground state analyses, $\mathcal{E}_\chi$ and relative entanglements $\Delta\mathcal{E}_{\chi_1,\chi_2}$ provides a tunable quantification of the transition between volume and area law entangled eigenstates across the spectrum. I do note that the results of this paper rely on accurate generation of the target state $|\psi\rangle$, which may not always be possible for some systems e.g. an experimentally prepared state, or a state obtained by some numerical procedure for which convergence is difficult. The question of extending the measure $\mathcal{E}_\chi$ to target states which are only partially known is an interesting future topic of research.

References

[1] Guifré Vidal. Efficient classical simulation of slightly entangled quantum computations. *Phys. Rev. Lett.*, 91:147902, Oct 2003.

[2] Ulrich Schollwöck. The density-matrix renormalization group in the age of matrix product states. *Annals of Physics*, 326(1):96–192, Jan 2011.

[3] Román Orús. A practical introduction to tensor networks: Matrix product states and projected entangled pair states. *Annals of Physics*, 349:117–158, 2014.

[4] Tzu-Chieh Wei and Paul M. Goldbart. Geometric measure of entanglement

and applications to bipartite and multipartite quantum states. *Physical Review A*, 68(4), oct 2003.

[5] Alexander Nico-Katz and Sougato Bose. Entanglement-complexity geometric measure. *Physical Review Research*, 5(1):013041, 2023.

[6] Gabriele De Chiara and Anna Sanpera. Genuine quantum correlations in quantum many-body systems: a review of recent progress. *Reports on Progress in Physics*, 81(7):074002, jun 2018.

[7] Qian-Qian Shi, Romá n Orús, John Ove Fjærestad, and Huan-Qiang Zhou. Finite-size geometric entanglement from tensor network algorithms. *New Journal of Physics*, 12(2):025008, feb 2010.

[8] Aditi Sen(De) and Ujjwal Sen. Channel capacities versus entanglement measures in multiparty quantum states. *Phys. Rev. A*, 81:012308, Jan 2010.

[9] Anindya Biswas, R. Prabhu, Aditi Sen(De), and Ujjwal Sen. Genuine-multipartite-entanglement trends in gapless-to-gapped transitions of quantum spin systems. *Physical Review A*, 90(3), sep 2014.

[10] Sudipto Singha Roy, Himadri Shekhar Dhar, Aditi Sen(De), and Ujjwal Sen. Tensor-network approach to compute genuine multisite entanglement in infinite quantum spin chains. *Phys. Rev. A*, 99:062305, Jun 2019.

[11] Otfried Gühne and Géza Tóth. Entanglement detection. *Physics Reports*, 474(1-6):1–75, apr 2009.

[12] Ryszard Horodecki, Paweł Horodecki, Michał Horodecki, and Karol Horodecki. Quantum entanglement. *Rev. Mod. Phys.*, 81:865–942, Jun 2009.

[13] W. Dür and J. I. Cirac. Classification of multiqubit mixed states: Separability and distillability properties. *Phys. Rev. A*, 61:042314, Mar 2000.

[14] M. Blasone, F. Dell'Anno, S. De Siena, and F. Illuminati. Hierarchies of geometric entanglement. *Physical Review A*, 77(6), jun 2008.

[15] Andreas Gabriel, Beatrix C. Hiesmayr, and Marcus Huber. Criterion for k-separability in mixed multipartite states. *Quantum Info. Comput.*, 10(9):829–836, sep 2010.

[16] Aditi Sen De and Ujjwal Sen. Bound genuine multisite entanglement: Detector of gapless-gapped quantum transitions in frustrated systems, 2010.

[17] Debasis Sadhukhan, Sudipto Singha Roy, Amit Kumar Pal, Debraj Rakshit, Aditi Sen(De), and Ujjwal Sen. Multipartite entanglement accumulation in quantum states: Localizable generalized geometric measure. *Phys. Rev. A*, 95:022301, Feb 2017.

[18] Ian Affleck, Tom Kennedy, Elliott H. Lieb, and Hal Tasaki. Rigorous results on valence-bond ground states in antiferromagnets. *Phys. Rev. Lett.*, 59:799–802, Aug 1987.

[19] Jens Eisert and Hans J. Briegel. Schmidt measure as a tool for quantifying multiparticle entanglement. *Physical Review A*, 64(2), jul 2001.

[20] J Sperling and W Vogel. The schmidt number as a universal entanglement measure. *Physica Scripta*, 83(4):045002, mar 2011.

[21] Peiyuan Teng. Accurate calculation of the geometric measure of entanglement for multipartite quantum states. *Quantum Information Processing*, 16(7):1–18, 2017.

[22] Colin G. West and Tzu-Chieh Wei. Global and short-range entanglement properties in excited, many-body localized spin chains. 2016.

[23] Chanchal K. Majumdar and Dipan K. Ghosh. On Next-Nearest-Neighbor Interaction in Linear Chain. I. *Journal of Mathematical Physics*, 10(8):1388–1398, August 1969.

[24] D. Perez-Garcia, F. Verstraete, M. M. Wolf, and J. I. Cirac. Matrix product state representations. *Quantum Info. Comput.*, 7(5):401–430, jul 2007.

[25] Keola Wierschem and Pinaki Sengupta. Characterizing the haldane phase in quasi-one-dimensional spin-1 heisenberg antiferromagnets. *Modern Physics Letters B*, 28(32):1430017, dec 2014.

[26] Steven R. White. Density-matrix algorithms for quantum renormalization groups. *Phys. Rev. B*, 48:10345–10356, Oct 1993.

[27] U. Schollwöck. The density-matrix renormalization group. *Rev. Mod. Phys.*, 77:259–315, Apr 2005.

[28] Marcel den Nijs and Koos Rommelse. Preroughening transitions in crystal surfaces and valence-bond phases in quantum spin chains. *Phys. Rev. B*, 40:4709–4734, Sep 1989.

[29] Shaolong Ma, Collin Broholm, Daniel H. Reich, B. J. Sternlieb, and R. W. Erwin. Dominance of long-lived excitations in the antiferromagnetic spin-1 chain nenp. *Phys. Rev. Lett.*, 69:3571–3574, Dec 1992.

[30] Jie Ren, Yimin Wang, and Wen-Long You. Quantum phase transitions in spin-1 xxz chains with rhombic single-ion anisotropy. *Physical Review A*, 97(4), apr 2018.

[31] Yu-Chin Tzeng, Hiroaki Onishi, Tsuyoshi Okubo, and Ying-Jer Kao. *Physical Review B*, 96(6), aug 2017.

[32] Wei Chen, Kazuo Hida, and B. C. Sanctuary. *Physical Review B*, 67(10), mar 2003.

[33] L. Campos Venuti, C. Degli Esposti Boschi, and M. Roncaglia. Long-distance entanglement in spin systems. *Physical Review Letters*, 96(24), jun 2006.

[34] Olga V. Maximova, Sergey V. Streltsov, and Alexander N. Vasiliev. Long range ordered, dimerized, large-d and haldane phases in spin 1 chain compounds. *Critical Reviews in Solid State and Materials Sciences*, 46(4):371–383, 2021.

[35] Johnnie Gray. quimb: a python library for quantum information and many-body calculations. *Journal of Open Source Software*, 3(29):819, 2018.

[36] Shane Dooley. Robust quantum sensing in strongly interacting systems with many-body scars. *PRX Quantum*, 2:020330, May 2021.

[37] Rahul Nandkishore and David A. Huse. Many-body localization and thermalization in quantum statistical mechanics. *Annual Review of Condensed Matter Physics*, 6(1):15–38, mar 2015.

[38] Fabien Alet and Nicolas Laflorencie. Many-body localization: An introduction and selected topics. *Comptes Rendus Physique*, 19(6):498–525, sep 2018.

[39] Dmitry A. Abanin and Zlatko Papić. Recent progress in many-body localization. *Ann. Phys. (Leipzig)*, 529(7):1700169, 2017.

[40] Piotr Sierant, Dominique Delande, and Jakub Zakrzewski. Thouless time analysis of anderson and many-body localization transitions. *Phys. Rev. Lett.*, 124:186601, May 2020.

[41] R. K. Panda, A. Scardicchio, M. Schulz, S. R. Taylor, and M. Žnidarič. Can we study the many-body localisation transition? *EPL (Europhysics Letters)*, 128(6):67003, feb 2020.

[42] Vedika Khemani, S. P. Lim, D. N. Sheng, and David A. Huse. Critical properties of the many-body localization transition. *Phys. Rev. X*, 7:021013, Apr 2017.

[43] Adriano Barenco, André Berthiaume, David Deutsch, Artur Ekert, Richard Jozsa, and Chiara Macchiavello. Stabilization of quantum computations by symmetrization. *SIAM Journal on Computing*, 26(5):1541–1557, 1997.

[44] Harry Buhrman, Richard Cleve, John Watrous, and Ronald de Wolf. Quantum fingerprinting. *Phys. Rev. Lett.*, 87:167902, Sep 2001.

[45] B. P. Lanyon, C. Maier, M. Holzäpfel, T. Baumgratz, C. Hempel, P. Jurcevic, I. Dhand, A. S. Buyskikh, A. J. Daley, M. Cramer, M. B. Plenio, R. Blatt, and C. F. Roos. Efficient tomography of a quantum many-body system. *Nature Physics*, 13(12):1158–1162, sep 2017.

Chapter 4

Informational Aspects of Quantum Simulators

"The Worldly Hope men set their Hearts upon Turns Ashes – or it prospers; and anon, Like Snow upon the Desert's dusty Face, Lighting a little hour or two – is gone."

— Omar Khayyám

This chapter concerns itself with informational aspects of realistic current-generation quantum simulators, namely quantum dot arrays and superconducting quantum computers. Whilst previous chapters addressed informational ideas in the context of abstract theoretical models, each model discussed in this chapter simulates a real NISQ device. The devices considered are current generation or near-future, and represent an oncoming frontier of tunable, controllable, many-body systems.

The specific 'informational aspects' I consider are incarnated as, inter alia, widely-used canonical objects such as the von Neumann entropy and number entropy, the statistics of singlet-triplet measurement outcomes, the fidelity susceptibility[1], the Holevo quantity, and Loschmidt echos. The chapter first addresses the possibility of detecting MBL in one-dimensional quantum dot arrays in Section 4.1. Twin-rail quantum dot arrays are then discussed in Section 4.2, with an eye to detecting phase transitions via singlet-triplet measurements. Finally information

[1]The fidelity susceptibility is 'informational' in the sense that is is proportional to the quantum fisher information which governs how precisely properties of the system can be determined from measurements made on the system.

scrambling in superconducting quantum computers (specifically IBM's transmon computing devices) is addressed in Section 4.3.

4.1 Identifying Many-Body Localization in Quantum Dot Arrays

Many-body localization (MBL), the breaking of ergodicity and corresponding arrest of transport in disordered strongly-correlated quantum systems [1–4], has become increasingly accessible in a wide array of experimental systems. Devices in which MBL has been experimentally realized include ultracold atoms and ions in optical lattices [5–8], and superconducting qubits [9]. A natural, yet hitherto unrealized, setting in which to explore MBL is that of semiconducting quantum dot arrays (QDA). Such systems are promising simulators of fermionic systems in both 1D and 2D [10, 11], they are highly tunable and different lattice geometries can be readily fabricated: in short an ideal testbed for MBL. Despite this, modern arrays are realistically limited to few dots, readout can be noisy, and - as they are extremely sensitive to environmental electrostatic discharge - they can be damaged during fabrication, handling, or general use during the experimental process. Thus, whilst the detection of MBL in realistic current-generation quantum dot arrays is both a crucial proof-of-concept for such arrays as generic quantum testbeds, it is also fraught with difficulties. A number of questions naturally arise: can current-generation realistic arrays access MBL regimes? How can we reliably identify MBL in such arrays? And - given how fragile these systems are - what are the minimal measurements required to do so?

In this section I address the above questions by first characterizing the double-dot properties of a state-of-the-art device and extrapolating the rough parameter ranges of an extended Fermi-Hubbard model that such a device can simulate. I then analyze this model numerically, investigating a variety of quantities in both bulk and local variants. These quantities require measurements that range from density operator tomography of half the system to simple charge sensing on two sites. Together, this comprehensively addresses the possibility of detecting MBL in

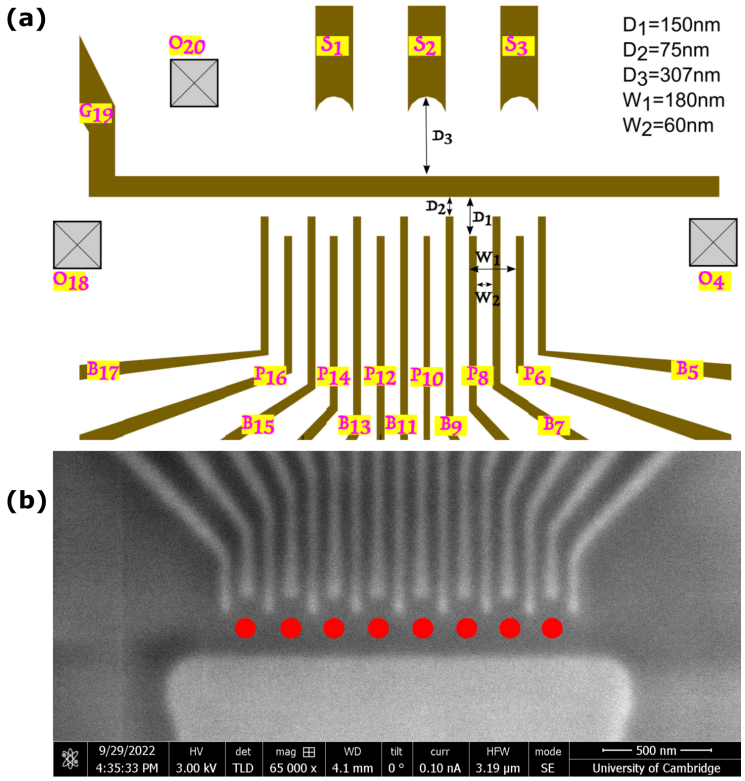

Figure 4.1: **(a)** The six-dot design for the specific characterized experimental device. In sec:qda-parameter I extract rough parameter ranges for the theoretical model that the device simulates from the pair of dots defined by the gates $G_{19} - B_{15} - B_{13} - B_{11}$ and addressed by plunger gates P_{14} and P_{12} respectively. **(b)** An SEM image of a fabricated array which is similar to the characterized design. Slight blurring of the SEM image is due to a layer of protective PMMA with an approximate thickness of 200 nm.

current generation QDA.

It is important to note here that research[2] suggests that attempting to isolate the ergodic-MBL transition in such small systems is prohibitively difficult - it is hard to make declarative statements about the thermodynamic transition without accessing both exponential time and length scales in microscopic analyses [12–14], and the small-system transition may belong to a different universality class than the transition in the thermodynamic limit [15]. Rather it is better to identify different regimes and investigate their properties away from the ergodic-MBL critical line. For this reason, and due to the fact that the size of modern QDAs are limited to up to about eight dots, I do not attempt to systematically investigate criticality in this

[2] And my own up-close and personal experience.

chapter. Rather I determine the conditions under which the different regimes can be *differentiated* in realistic experimental quantum dot arrays.

In Section 4.1.2 I introduce and discuss the model that quantum dot arrays simulate. In Section 4.1.4 I discuss the experimental device in question, namely a one-dimensional lateral array of electrostatically defined quantum dots, and then characterize such a device to extract rough ranges for the theoretical model parameters from experimental data. I define several quantities in both bulk and local variants in Section 4.1.5 which can be used to differentiate MBL from the other phases of the model. Finally, in Section 4.1.6 I analyze the model across the extracted parameter ranges and use the aforementioned quantities to develop a protocol for identifying MBL with minimal measurements on a realistic device. This research was carried out in conjunction with Dr. Jaliel and Prof. Smith at UCL and Cambridge respectively [16]. The bulk of this section is based on the preprint of our work in Ref. [17].

4.1.1 The Quantum Dot and Dot Arrays

The theoretical quantum dot is a highly confined system in which zero-dimensional effects can be seen [18], often interpreted as an 'artificial atom' of sorts in which the electronic properties of the system can be finely tuned and controlled [19]. As this is such a general idea, actual experimental implementations of quantum dots are numerous and varied. The physical quantum dots I will discuss are 'lateral' quantum dots, named for their structure. They are constructed from careful depletion of a two-dimensional electron gas (2DEG) formed by donor electrons introduced by silicon doping at the interface of a GaAs/AlGaAs heterostructure. The electrons in such a heterostructure are strongly confined to the boundary between the GaAs and AlGaAs layers by the electronic properties of the two materials, and further confinement is possible through judicial application of electromagnetic fields via gating on the structure's surface [20]. The dots are connected to each other by standard (screened) coulomb and exchange interactions between their electrons, and to the outside world by ohmic contacts; the two most notable of which are the 'source' and 'drain' contacts, through which a current can be passed. The electronic prop-

erties of these dots can be probed by charge sensing apparatus e.g. quantum point contacts. Two schematics of such lateral quantum dots are shown in Fig. 4.2. The precise details of dot fabrication is beyond the scope of this report; we will instead concern ourselves with a condensed matter approach to quantum dots arrays as simulators of the Fermi-Hubbard model. Much of this theory is drawn from the work of T. Hensgens (see Ref. [21]), who expanded on prior work by Yang et al. [22].

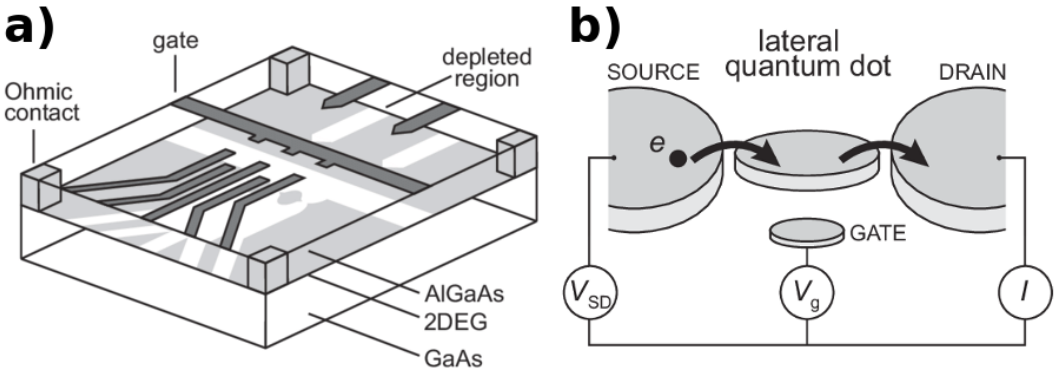

Figure 4.2: Schematics of lateral quantum dots. **a)** is a schematic of a lateral double-dot and explicitly shows the GaAs/AlGaAs heterostructure, the 2DEG at its interface (light grey region), top gating (dark grey regions), and the effect of gating in depleting the 2DEG (white regions). **b)** shows an instructive schematic of a lateral single dot. Both figures retrieved from Ref. [23].

The theory of quantum dot arrays starts with the features of an individual dot. The addition of an electron to a dot can only occur after the energetic cost due to coulomb interactions on that dot is surmounted. This is called 'coulomb blockade'. In addition to the coulomb blockade there is a quantum effect due to the tight confinement, wherein Pauli exclusion gives rise to a discrete (0D) energy spectrum [24]. Tunnelling through a single isolated dot depends solely on these two effects, the voltages V_{g1} applied to the dot itself, and the voltages V_s and V_d applied to the source and drain contacts. The unimpeded motion of an electron through the system, i.e. motion free of coulomb blockading effects, is only possible at certain gate voltages. This is illustrated in the schematic of Fig. 4.2**(b)**.

The immediate extension of the above idea is to consider a pair of coupled quantum dots, a quantum 'double-dot' system. The electrons in these two adjacent dots interact via (screened) coulomb and exchange interactions [20, 23]. The dots

may also experience cross-talk, in which voltages applied to specific dots or contacts can affect the other dots and contacts. These effects must be characterized for each double-dot system, and are extremely sensitive to the environment, damage sustained during use, and the precise fabrication of the system.

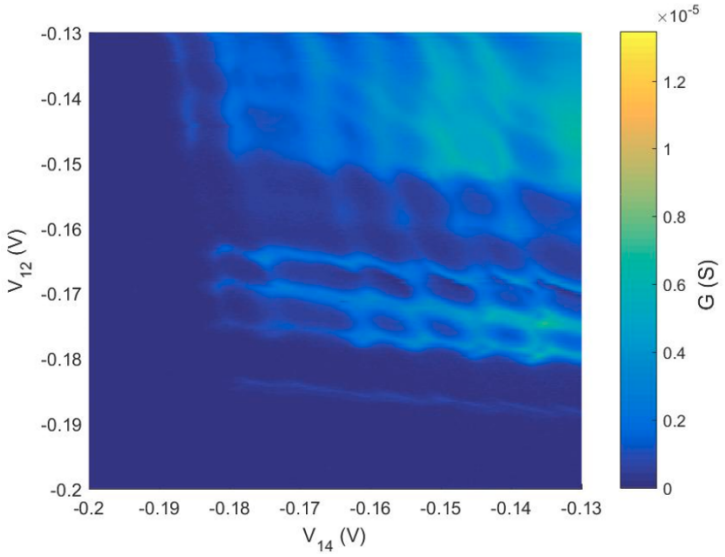

Figure 4.3: The charge-stability diagram of an experimentally realized lateral double-dot system. The conductivity peaks at phase boundaries between different equilibrium configurations, giving rise to the signature 'honeycomb' lattice. Analysis of this lattice allows us to characterize physical properties of the dots; from charging to interaction energies. When compared to the ground state occupancy diagrams of Fig. 4.5, it is clear that we can also determine many parameters of the Fermi-Hubbard model that this experimentally realized dot system simulates.

The de facto standard for characterizing these properties is by investigating stable, static, configurations of electrons on each dot. These configurations - the ground state of the combined double-dot system - can be altered by applying potentials V_{g1} and V_{g2} which induce local chemical potentials on each dot individually. The stable configurations are typically labelled by the number of electrons in each dot, e.g. $(0,1)$ or $(2,4)$. Hence, by scanning V_{g1} and V_{g2} and performing local charge sensing, these stable configurations can be found. The resulting diagram of stable regions as a function of the applied voltages, called the 'charge-stability' diagram is formed by a honeycomb of stable hexagonal regions in which small changes in V_{g1} and V_{g1} do not alter the ground state. The triple points where three of these

regions meet are where the double-dot system becomes conductive, and are the origin of the well-known 'conductance peaks'[3]. It is worth noting here that quantum tunnelling and thermal fluctuations can render the interface between two regions conductive as well, which registers on experimental charge-stability diagrams as visible boundaries between ground states. In practice the charge-stability regions are probed by applying a small potential difference across the system and measuring the current that flows through it; revealing the conductive corners (and edges) of the stable regions. The result of this process for an experimental realization of a double-dot in the middle of a larger array is shown in Fig. 4.3 [16]. The shape and size of these honeycombs are ultimately governed by cross-talk between the dots, the on-site coulomb and 0D effects, and the two-site coulomb and exchange interactions. Adding more quantum dots makes these effects more interrelated and harder to characterize, but does not change their essential nature.

4.1.2 Quantum Dot Arrays as Fermi-Hubbard Simulators

In the discussion of the previous section, we can see the shadow of the Fermi-Hubbard model as cast by experimentally realizable quantum dot arrays. There is a discrete lattice defined by the geometry of the quantum dot array itself, on-site fermionic exclusion laws, tunnelling between sites, and coulomb and exchange interactions. In essence, all the ingredients of the Fermi-Hubbard model are latent in quantum dot arrays; and it makes sense that such an array could simulate the theoretical model well. If we assume a single active energy level per site (an assumption we justify and discuss in more detail at the end of this section), the full extended

[3]The mechanism that causes this is an incredibly elegant bit of physics which is unfortunately irrelevant to this thesis. Nevertheless, I summarize it in this paean of a footnote. The triple point is where three stable configurations which differ from each other by at most one electron meet - consider e.g. (0,0), (0,1), and (1,0). At the triple point, all three are degenerate and so moving between these configurations costs no energy. This means that processes are allowed here which are forbidden at all other points. One such process might be (0,0)→(1,0)→(0,1)→(0,0), which corresponds to an electron *entering* on the left, then travelling to and exiting on the right. This process, and the reverse process (0,0)→(0,1)→(1,0)→(0,0), are respectively forwards and backwards tunnelling of electrons through the double-dot, i.e. a flow of current. This is typically represented in literature by little circular arrows around the triple points, with the direction of current denoted by the direction of the arrow. Hence, conductance is only non-zero at the triple points, where such cyclical flows can occur.

Fermi-Hubbard model that such devices simulate is as follows:

$$H = \sum_{\langle i,j\rangle,\sigma} \tau_{i,j,\sigma} \left(c^{\dagger}_{i,\sigma} c_{j,\sigma} + \text{h.c.} \right) + \sum_{\langle i,j\rangle} V_{i,j} n_i n_j + \sum_{j=1}^{L} U_j n_{j,\uparrow} n_{j,\downarrow} + \sum_{j=1}^{L} h_j n_j \quad (4.1)$$

with open boundary conditions, and where $\langle i, j\rangle$ runs over all nearest neighbours. The index $\sigma \in \uparrow, \downarrow$ labels spin. The operator $n_{j,\sigma} = c^{\dagger}_{j,\sigma} c_{j,\sigma}$ is the number operator for site j in the spin sector σ, and $n_j = \sum_{\sigma} n_{j,\sigma}$ is the total number operator for site j. The parameters of the model $\tau_{i,j,\sigma}$, $V_{i,j}$, U_j, and h_j are dependant on the physical features of the quantum dot array, and are related to the typical tools used to characterize interacting quantum dots: namely charge-stability diagrams [10].

In general this model admits no easy analytic solution. Despite conservation of total spin and charge numbers it exhibits no translational invariance and is strongly interacting; though for a spin-polarized system, imposed e.g. by a weak magnetic field, the U_j terms vanish entirely. This model is entirely a function of the number operators for $\tau_{i,j,\sigma} = 0$, and as such is trivially diagonalizable (in the number basis of n_j) at this point; this corresponds to the 'classical' picture of quantum dots in the constant interaction model, wherein the system's ground states are classical ground states of charges on a network [20]. For a brief overview of the theory of classical conductor networks and the constant interaction model, see Appendix C).

As I show later in Section 4.1.4, and as summarized in Table 4.1, the on-site interaction energy U for the systems I consider ends up being significantly larger than all other energy scales. This suppresses any process which results in more than one excess electron per site[4]. Thus, provided the disordered chemical potential energies h_j do not exceed U, the spin degrees of freedom do not enter into the dynamics and can be safely neglected. This can also be artificially enforced by polarizing the electrons such that only a single spin species persists; by e.g. applying a global magnetic field to the system. Thus, for sufficiently high $U \gg \tau$, $U \gg V$, and $U \gg h$, the theoretical model which our experimental quantum dot array simulates reduces

[4] In the corresponding $t - J$ model, any effects that rely on spin degrees of freedom are second order and their energies end up being about an order of magnitude lower than all others.

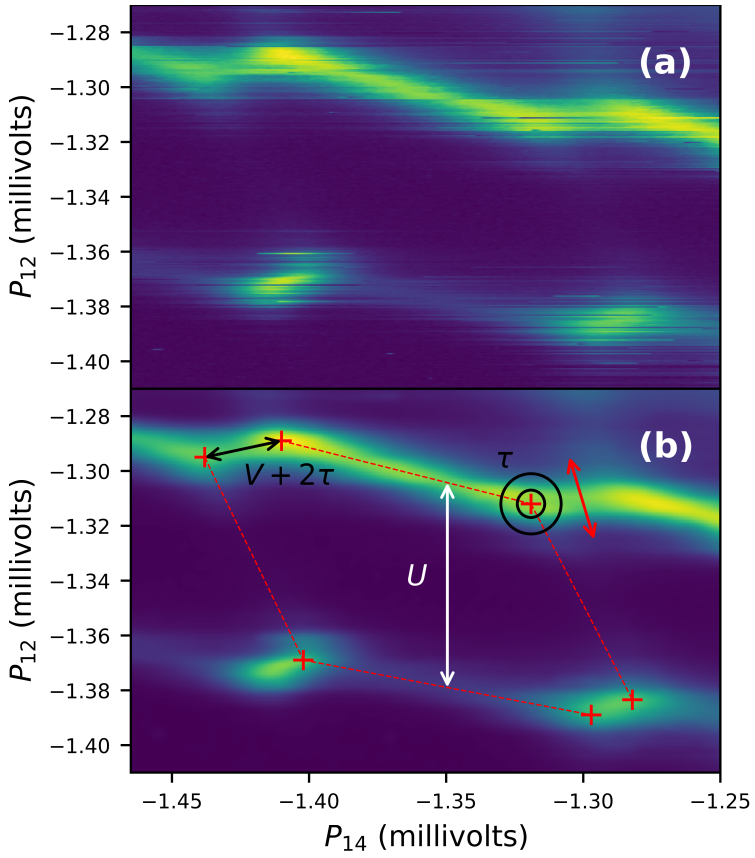

Figure 4.4: **(a)** A typical experimental honeycomb cell of the charge-stability diagram obtained by differential conductance measurements on the two dots defined by the gates $G_{19} - B_{15} - B_{13} - B_{11}$ in the middle of a device similar to that shown in Fig. 4.1. Bright (dark) regions indicate higher (lower) measured values of thhe differential conductance as a function of the two local plunger gate voltages P_{14} and P_{12}. **(b)** A Gaussian smoothing of the raw data shown in panel **(a)** with a schematic overlay of how the parameters of the theoretical model that the device simulates are extracted from the geometry of the honeycomb cell.

from Eq. (4.1) to the spinless Fermi-Hubbard model of

$$H = \tau \sum_{j}^{L-1} \left(c_j^\dagger c_{j+1} + \text{h.c.} \right) + V \sum_{j}^{L-1} n_j n_{j+1} + \sum_{j}^{L} h_j n_j, \tag{4.2}$$

where $n_j = c_j^\dagger c_j$ is the number operator at site j. The parameters τ and V are the tunnelling and nearest-neighbour coulomb interaction energies respectively, and the h_j are random energies drawn uniformly from the interval $[-h, h]$; with h tuning the overall disorder strength. To be completely clear, we have assumed (i) a single active energy level per site in constructing Eq. (4.1) and (ii) an (effective) single

species of electron in deriving Eq. (4.2) from Eq. (4.1).

I note here several features of the Hamiltonian of Eq. (4.2) which are of direct relevance. The system maps directly onto an extended XXZ model (see Appendix E) via the Jordan-Wigner transformation, and so inherits an insulating phase at $V/\tau = 2$. For $V/\tau = 0$ the system is non-interacting and, in the thermodynamic limit, should localize for all $h/\tau > 0$; this is Anderson localization [25] - which we do not further consider here. For $0 < V/\tau < 2$ the system is conducting and interacting and so should many-body localize for sufficient h/τ, whilst at $V/\tau > 2$ the system is insulating. For these reasons, the ergodic-MBL transition can only be meaningfully discussed in the regime $0 < V/\tau < 2$, and the ability to differentiate the ergodic regime, interaction-induced insulation due to high V/τ, and disorder-induced MBL becomes critically important when we seek to definitively identify the last in an exploratory experimental context. The systems I consider are also very small, as they are realistic models of fully tunable experimental quantum dot arrays. Thus the system is suspect to a range of pathologies. Edge effects are non-trivial, the phase transitions are expected to smear out - with e.g. Anderson localization visible for small, non-zero, V/τ - and the nature of the MBL transition being generally suspect, potentially not reflecting behaviour in the thermodynamic limit at all.

4.1.3 Mapping Between Experimental Charge-Stability Diagrams and Theoretical Hamiltonian Parameters

Let us now turn our attention to how the model parameters map onto an experimental charge-stability diagram. To facilitate this process, I preempt the proceeding section by introducing Fig. 4.4 - an experimentally determined charge-stability diagram of a real current generation quantum dot array [16]. Overlaid onto this diagram are visual indicators of how the Hamiltonian parameters map onto the experimental diagram - I discuss these below. I also provide the theoretical charge-stability diagram by calculating exact ground states of the Hamiltonian Eq. (4.1) - where each row corresponds to a different value for the tunnelling term $\tau_{i,j,\sigma} = \tau = \text{const.}$, and where the rightmost two columns are the results of two edge detection algorithms

from which one can extract precise regions of charge-stability.

The energy U is the simplest parameter to consider, it is simply the cost of adding a new electron to the dot, including both charging and zero-dimensional energies [20]. This can be determined from the charge-stability diagram by measuring the vertical distance between two classical ground state electron configurations, i.e. the potential we need to overcome to add a single electron to a single site [10]. In Fig. 4.4, I have selected an example honeycomb cell without a contribution from the zero-dimensional level spacing; thus this article works with a 'worst case' scenario where U/τ is not strengthened by zero-dimensional effects.

The nearest-neighbour Coulomb repulsion V is related to the shortest distance between two phases which differ by a single additional electron on *both* sites, i.e. the energy required to add two electrons to neighbouring sites after overcoming the necessary on-site energy requirements. Due to additional hybridization caused by τ, this distance is actually proportional to $V + 2\tau$ [21].

Unfortunately, whilst this simple kind of numeromancy works well for the part of the Hamiltonian diagonal in number operators, the effect of the tunnelling - typically weak - is slight and subtle. The effect of the tunelling energy on the shape of the charge-stability diagram is mediated through the hybridization of neighbouring classical ground states of identical total electron number. This in turn broadens the distance between triple points and phase boundaries, and causes rounding of the phase boundaries near the classical triple points. This is shown in Fig. 4.5, wherein each row corresponds to a different tunnelling energy τ, and where the deformation of the charge-stability diagram as a function of τ is clearly visible. This is especially true when looking at the boundaries of the stable regions after appropriate post-processing and edge-detection. From the leftmost column of Fig. 4.5, we can see the blurring of the phase boundaries between adjacent stable regions of constant total number. This is a manifestation of the hybridization between neighbouring $\tau = 0$ ground (Fock) states into new ground states of the $\tau > 0$ system. This in turn manifests as phase boundaries becoming conductive, and can be seen experimentally as the broadening of the characteristic conductance peaks.

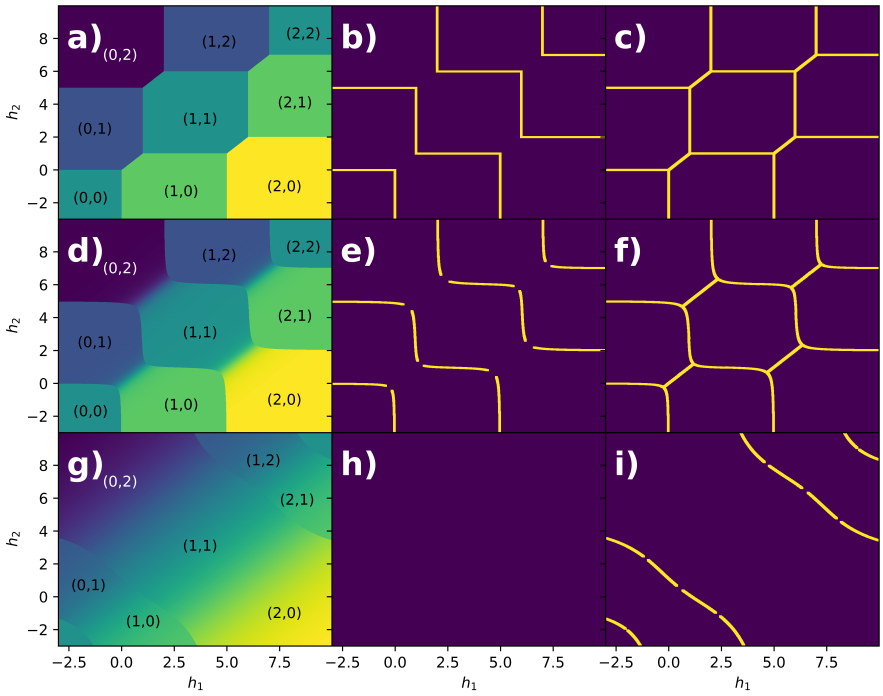

Figure 4.5: **a**), **d**), **g**) show ground state occupancy numbers for a two-site Fermi-Hubbard model with $U_j = U = 5$, $V_{i,j} = V = 1$, in the **a**) no tunnelling $\tau_{i,j,\sigma} = 0$, **d**) weak tunnelling $\tau_{i,j,\sigma} = 1/4$, **g**) strong tunnelling $\tau_{i,j,\sigma} = 2$ parameter regimes respectively. Each tuple shows the number configuration deep in each phase. The column **b**), **e**), **h**) shows the results of naïve edge detection on respective occupancy diagrams, and the column **c**), **f**), **i**) shows the results Canny edge detection [26].

As such, a non-zero τ has a wide range of effects, all of which are rather subtle and which are difficult to isolate in experimental charge-stability diagrams. Such identification requires both an experimental resolution orders of magnitude higher than those typically accessible, as well as some way of turning off τ, and *only* τ, completely. Ultimately, there are three prevailing ways of extracting τ from experimental data. Firstly, by analyzing the extent to which phase boundaries are curved [27] - clearly an impossibility for the noisy data of Fig. 4.4. Secondly, by extracting the tunnelling rate from Larmor oscillations observed over time as in [28, 29] - impossible given the static nature of our charge-stability diagram. Thirdly, by numerically fitting a line cut of the charge-stability diagram along a detuning axis

$V_1 - V_2$ (the red double-headed arrow in Section 4.1.6) to the analytic form of the steady-state conductance through an open double-dot model, or the response of a sensing dot; both of which should broaden with increasing τ [10, 11, 20]. This last approach has been met with considerable success, but requires a characterization of the leads. However, when characterizing a pair of dots in the middle of an array, it becomes much less tractable. Despite this, it is the prevailing method among the three suggested ones that may be possible in future work. As such I discuss it in more detail in Appendix D.

I note here that I am only considering rough parameter ranges, with an eye to addressing whether or not accessing MBL is even possible in current-generation or near-future devices. Thus I sidestep the delicate issue of extracting τ *precisely*, by instead roughly estimating the range of possible values it can take. As noted above, triple points are separated by a distance proportional to $V + 2\tau$. Thus I estimate rough ranges on this broadening (and thus τ) by estimating the maximum and minimum radii of the smeared-out triple points (shown as black rings in Section 4.1.6). Whilst a detailed characterization of τ is desirable, these rough estimates are sufficient to give us the range of possible τ values across which we must understand MBL in order to determine its accessibility in QDA [5].

4.1.4 Accessible Parameter Ranges in a Current-Generation Quantum Dot Arrays

Clearly our ability to freely simulate the theoretical Fermi-Hubbard model is savagely curtailed by the limitations of current-generation quantum simulators. Namely, given a specific characterization of a quantum dot array, only a few of the phases detailed at the end of the preceding section may be accessible. In this section I introduce and detail an experimental realization current-generation quantum dot array. I then extrapolate just such a characterization of a pair of sites in the middle of the device into limitations on the regimes that such a device may access.

[5] Moreover, τ can be directly controlled by tuning the voltages applied to the barrier gates which separate dots, as evidenced by the ability to 'pinch off' a dot (isolate it) before e.g. a measurement. This makes τ the parameter which is easiest to control *in situ* - without having to fabricate a new device.

The experimental devices I consider are lateral arrays of electrostatically defined quantum dots formed by selectively depleting electrons using nano-fabricated gate electrodes on the surface of a GaAs/AlGaAs heterostructure. The specific device used as a benchmark has a gate pattern which defines a linear array of six quantum dots, the design of which is shown in Fig. 4.1**(a)**. A scanning electron microscope (SEM) image of a similar (eight-dot) device that was fabricated is shown in Fig. 4.1**(b)**, where the positions of the quantum dots are illustrated by red circles. These are both simply larger versions of the designs often used in multi-dot experiments (see e.g. Refs. [10, 30]).

Tunnelling rates between adjacent dots are controlled through the voltages applied to the barrier gates B_j between neighbouring dots, where j is the gate number. On-site chemical potentials are controlled by voltages applied to the plunger gates P_j. The leftmost and the rightmost dots are also tunnel-coupled to the left and right reservoirs, respectively. The long middle bar gate, labelled G_{19} in Fig. 4.1**(a)**), is the top barrier for all wire gates below; and the three sensing gates, labelled $S_{1(2)(3)}$ in Fig. 4.1**(a)**, are quantum point contact charge detectors. The non-linear conductance characteristics of these detector gates can be used as a sensitive probe of the local electrostatic environment [31], which in turn can be used to measure local charge fluctuations. In practice, individual gate voltages affect not only the parameters they are designed to control but, through capacitive cross-talk, also affect other electrochemical potentials and tunnel barriers. However, this effect can be compensated for by using virtual gates: linear combinations of multiple gate voltages chosen such that only a single electrochemical potential or tunnel barrier is addressed [10, 32].

The design of the specific six-dot device from which model parameters will eventually be extracted is shown in Fig. 4.1**(a)**. The fabrication of this device uses a Si-doped GaAs/$Al_xGa_{1-x}As$ heterostructure, with a two-dimensional electron gas 90nm below the surface, a mobility of 9×10^5 cm^2/Vs, and an electron concentration of 1.62×10^{11}cm^{-2}. All gates are fabricated in a layer of Ti/Au of thickness 5/20nm, evaporated on the bare substrate. The device was cooled in a dilution refrigerator with a base temperature of $T \sim 70$mK. The electron temperature, how-

ever, is estimated to remain at $\sim$ 100mK. Extracted from their individual Coulomb diamonds (not shown), the on-site charging energy E_C is estimated to be $\sim$ 1.3meV, and the zero-dimensional level spacing of an individual dot to be $\sim 400\mu$eV.

Charge-qubit coherence times were not characterized, but I take them to be approximately $1-10$ns, which is in conservatively line with other characterizations in similar systems [33, 34]. Though it is worth noting here that silicon-based devices and spin-qubits have coherence times orders of magnitude greater [35–38], and may be a lucrative setting in which to investigate MBL as well.

Characterization of two dots in the middle of the array, defined by the gates $G_{19}-B_{15}-B_{13}-B_{11}$, is carried out by scanning the applied plunger gate voltages P_{12} and P_{14} across a range of values and measuring the differential conductance across the double-dot system. This yields a charge-stability diagram comprised of 'honeycomb' cells wherein the boundaries between stable electronic configurations admit the flow of current and appear as bright regions (high differential conductance). A typical example of the honeycomb cells obtained from this analysis is shown in Fig. 4.4 **(a)**, which I will use to determine accessible parameter ranges as per Section 4.1.3.

Parameters	Minimum τ	Maximum τ
V/τ	3.727	0.603
U/τ	12.941	4.792

Table 4.1: Table of upper and lower bounds on the considered parameter ranges for Eq. (4.2) extrapolated from the features of the experimental charge stability diagram of Fig. 4.4.

Over Fig. 4.4**(b)**, a Gaussian kernel-density smoothing of the raw experimental data in Fig. 4.4**(a)**, I have manually identify suspected triple points - denoted by black crosses. I have then taken minimum (inner) and maximum (outer) broadening radii - denoted by the inner and outer black circles respectively. The phase boundaries are derived from lines connecting these triple points and - in conjunction with the range of the radii - yields ranges of values for τ, $V+2\tau$, and U as annotated, and as discussed in Section 4.1.3. The resulting estimated ranges are summarized

in Table 4.1. In each case, the on-site Coulomb interaction U is found to be much larger than both τ and V, justifying the assumptions that (i) there is a single active energy level per site and (ii) the system is effectively spinless. These estimated ranges encompass extant characterizations of multi-dot arrays in e.g. Ref. [10]. Finally, I note that the h/τ is freely tunable by altering the on-site chemical potentials by changing plunger gate voltages, and is thus only limited by the restriction that $U \gg h$.

4.1.5 Probing Quantities

It is now time to turn our attention to actually identifying the MBL regime in realistic QDA systems. To this end, I introduce here three quantities which will be used to probe the phase diagram of Eq. (4.2) across the parameter ranges of Table 4.1. Two of these quantities I have introduced before in Chapter 2; they are the von Neumann entropy S and the widely-used imbalance $\mathcal{I}$, both of which I briefly reintroduce here. The last quantity of interest is the number entropy S_N, which I discuss here in more detail. All quantities vary first in their experimental accessibility and secondly - as I show in Section 4.1.6 - their capability when it comes to differentiating regimes in the phase diagram of Eq. (4.2).

The von Neumann entropy when applied to a bi-partite pure state unambiguously quantifies the entanglement across the bi-partition. It has been used extensively in the context of MBL theory and experiment, including in Chapter 2 of this very thesis, and serves here as a benchmark for the other quantities [39–43]. Here, it takes the form of an entropy *density*: $S(\rho(t)) = -\mathrm{Tr}[\rho(t)\log_2\rho(t)]/L_\rho$, where L_ρ is the size of the subsystem $\rho(t)$. In experiment, observation of the von Neumman entropy would require full tomography of the density operator of the region of interest - a prohibitively expensive and difficult task - but it serves as a crucial benchmark nonetheless.

The imbalance, widely used in MBL [5, 44–46], is used to determine how much a system has deviated from an initial charge configuration. It is directly re-

lated to standard auto-correlation functions. Here, I define it as

$$\mathcal{I}(\rho(t)) = \frac{2}{L_\rho}\sum_j \mathrm{Tr}\left[\rho(0)n_j\right]\mathrm{Tr}\left[\rho(t)n_j\right] \tag{4.3}$$

where j runs over the physical sites of the subsystem $\rho(t)$ and where - in the case of an initial charge density wave state such that n_j has $\rho(0)$ as an eigenstate - it reduces to the conventional statement of the imbalance as the difference between occupancy numbers on odd and even sites. If the charge configuration of $|\psi(t)\rangle$ becomes uncorrelated to the initial configuration of $|\psi(0)\rangle$ then the imbalance saturates to zero $\mathcal{I}(t) = 0$, whereas if they remain (anti-)correlated it persists as a finite non-zero value $\mathcal{I}(t) > 0$ ($\mathcal{I}(t) < 0$). In experiment $\mathcal{I}(\rho(t))$ requires only charge sensing on the relevant sites, which is significantly easier than the state tomography required by the von Neumann entropy.

The number entropy is a curious quantity which has seen some use in MBL [42, 47, 48], and which is simply the entropy of the discrete probability distribution $p(\rho(t), n)$ of finding n particles in the subsystem $\rho(t)$. It is defined as

$$S_N(t) = -\frac{1}{L_\rho}\sum_N p(\rho(t), n = N)\log_2 p(\rho(t), n = N). \tag{4.4}$$

This quantity is directly related to the von Neumann entropy by $S = S_N + S_C$ where S_C is the configurational entropy: the contribution to the entanglement due to correlations between different configurations of a fixed number of constituent particles. We can compute the distributions from the density operator by constructing projectors $P_N = \sum_r |N_r\rangle\langle N_r|$ where $|N_r\rangle$ are the N-particle states in the number basis that span the reduced Hilbert space of $\rho(t)$. The probability is then given by $p(\rho(t), n = N) = \mathrm{Tr}[\rho(t)P_N]$. I calculate an ergodic limit of the number entropy here, which I use to benchmark numerical results.

I start by assuming that, given L sites populated by N_0 electrons, the computational microstates which conserve N_0 are equally probable i.e. that the microcanonical ensemble gives the correct physical description of the equilibrated system at late time [49]. The problem of deriving the probability distribution $p_k(n)$ of observ-

ing n electrons within k selected sites becomes straightforward. The probability $p_k(n=N)$ is simply the probability of detecting N occupied sites and $k-N$ empty sites, multiplied by the multiplicity $\binom{k}{N}$ of such microstates:

$$p_k(n=N) = \binom{k}{N} \underbrace{\left[\prod_{j=0}^{N-1} \frac{n_0 - j}{L-j}\right]}_{\text{occupied}} \underbrace{\left[\prod_{j=0}^{k-N-1} 1 - \frac{n_0 - N - j}{L-N-j}\right]}_{\text{empty}} \tag{4.5}$$

The number entropy S_N of such an infinite-temperature subsystem is then readily calculated according to Eq. (4.4) of the main text with $\rho(t) \to \rho_{\text{th}}$. This quantity serves - in a similar capacity as the page entropy - as a thermal limiting case for the number entropy [50].

I also consider both bulk and local variants of the quantities by considering three different subsystems, the full system $\rho_{\text{f}}(t) = |\psi(t)\rangle\langle(t)\psi|$, half of the system $\rho_{\text{hc}}(t)$, and two sites in the middle of the system $\rho_2(t)$. The quantities are computed using the equations in Section 4.1.5 using the bulk or local reduced density operators according to Table Table 4.2. Experimentally, the imbalance and number entropy require identical local charge-sensing measurements only, and are highly experimentally tractable.

Quantity	Bulk	Local
VN Entropy	$S^{(b)}(t) = S(\rho_{\text{hc}}(t))$	$S^{(l)} = S(\rho_2(t))$
Imbalance	$\mathcal{I}^{(b)}(t) = \mathcal{I}(\rho_{\text{f}}(t))$	$\mathcal{I}^{(l)}(t) = \mathcal{I}(\rho_2(t))$
Number Entropy	$S_N^{(b)}(t) = S_N(\rho_{\text{hc}}(t))$	$S_N^{(l)}(t) = S_N(\rho_2(t))$

Table 4.2: Summary of bulk and local variants of the quantities discussed in Section 4.1.5. Bulk quantities are calculated over the state of the full system $\rho_{\text{f}}(t)$ or half the chain $\rho_{\text{hc}}(t)$, local quantities are calculated over two sites in the middle of the device $\rho_2(t)$.

The number entropy requires the same charge sensing measurements as the imbalance, but - as shown later in Section 4.1.6 - yields signatures similar to the von Neumann entropy. This becomes useful in that the number entropy can identify phases that the imbalance cannot without requiring the prohibitively difficult state tomography of the full von Neumann entropy. Moreover, the local variants of the

quantities shown in the last column of Table 4.2, require measurements only on two sites; making their calculation even simpler in experiment.

4.1.6 Results and Outlook

Here I investigate the phase diagram of Eq. (4.2) at time t_f after initialization in a charge density wave state wherein every other site is occupied at time $t = 0$. I vary V/τ and h/τ, and analyze the quantities (both bulk and local variants) discussed in Section 4.1.5. Given the upper and lower bounds extracted in Section 4.1.4, I investigate the phase diagram across the intervals $V/\tau \in [0,4]$ and $h/\tau \in [0,6]$. I consider both 'realistic' and 'ideal' versions of the same system.

The 'realistic' system addresses sizes of $L = 8$ sites, intermediate time scales of $\tau t_f/h = 150$ which (for reasonable tunnelling energies $\tau \sim 50-100\mu eV$) are within typical charge-qubit coherence times for these systems ($t_f \sim 1-10$ns) [33, 34], no time-averaging - just using the result at the final time t_f - and the number of disorder samples limited to 50 realizations. Additionally, I introduce large absolute ± 0.1 and relative $\pm 5\%$ uncertainties (box-distributed) in the parameters h/τ and V/τ such that the couplings are non-isotropic and random for each disorder realization. This accounts for small changes in these couplings due to cross-talk, and errors in the fabrication and characterization of the device.

The results of this analysis are shown in Section 4.1.6, wherein panels **(a)**, **(b)**, and **(c)** show the bulk von Neumann entropy, Imbalance, and Number entropy at t_f respectively, and panels **(d)**, **(e)**, and **(f)** show the local variants. Red dashes lines indicate the expected transition at $V/\tau = 2$ and an ergodic-MBL crossing at $h/\tau \sim 3$. The phase diagrams of the von Neumann entropy and number entropy are qualitatively similar, with a build-up of both entropies in the thermal regime that falls off as h/τ or V/τ increase. Surprisingly, the imbalance doesn't seem to register the metallic-insulator transition at $V/\tau = 2$, instead staying close to its thermal value of zero for all values of V/τ for sufficiently low disorder strength h/τ. This suggests that the imbalance alone cannot unambiguously detect the presence of the MBL regime: if a transition is seen in h/τ, it is entirely possible that the system is *already* in an insulating regime that the imbalance is simply agnostic to.

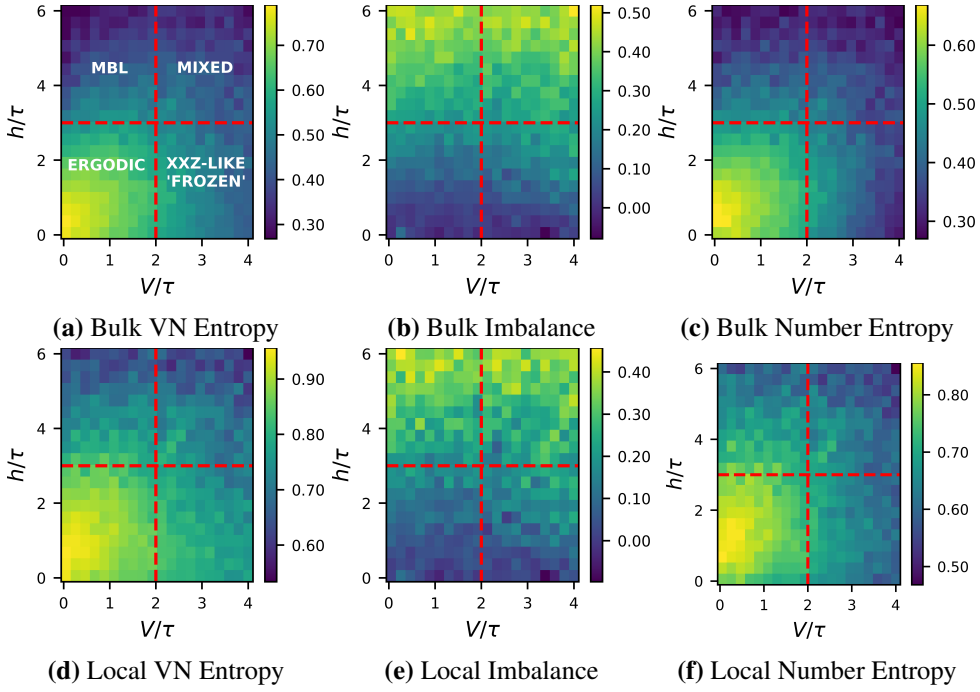

(a) Bulk VN Entropy **(b)** Bulk Imbalance **(c)** Bulk Number Entropy

(d) Local VN Entropy **(e)** Local Imbalance **(f)** Local Number Entropy

Figure 4.6: Disorder-averaged late-time quantities across the full $V-h$ phase diagram for the realistic system; initialized in a charge-density wave configuration. The realistic system consists of $L=8$ sites, total evolution times of $\tau t_f = 150$, no time-averaging (the final value at t_f is simply read out), and disorder-averaging over only 50 samples per (V,h) coordinate.

As such, differentiation between the thermal, MBL, and insulating regimes requires a different quantity. The number entropy requires the same measurements as the imbalance (i.e. charge sensing as opposed to full state tomography) but is also sensitive to the transition in V/τ. Thus by post-processing the results of a large number of charge measurements in two different ways, the imbalance and number entropy can both be calculated and compared, with the former sensitive only to the MBL transition, and the latter sensitive to both the MBL and insulating transition.

Perhaps the most striking feature of Section 4.1.6 is that the qualitative features of the bulk and local phase diagrams for individual quantities are consistent. For the purpose of differentiating the thermal, MBL, and insulating regimes, local measurements on a few sites seem to suffice. In conjunction with the above discussion, this leads to a simple protocol for detecting MBL in realistic QDA: perform charge-sensing measurements on a few dots in the middle of the array, then post-process these measurements differently to construct the local imbalance and local

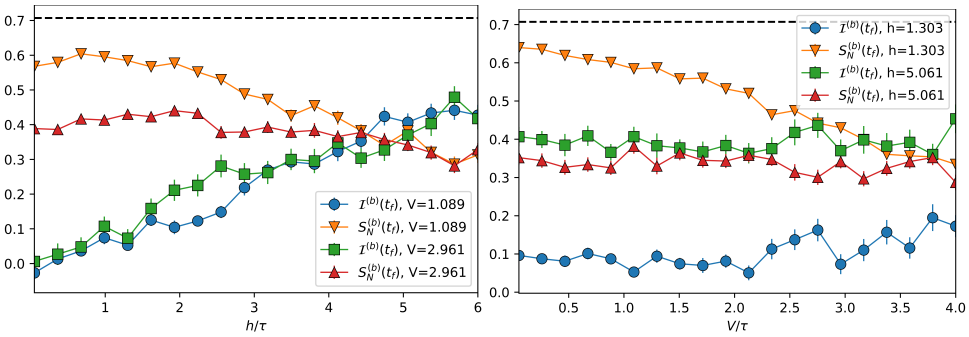

(a) Bulk Imbalance and Number Entropy against h/τ

(b) Bulk Imbalance and Number Entropy against V/τ

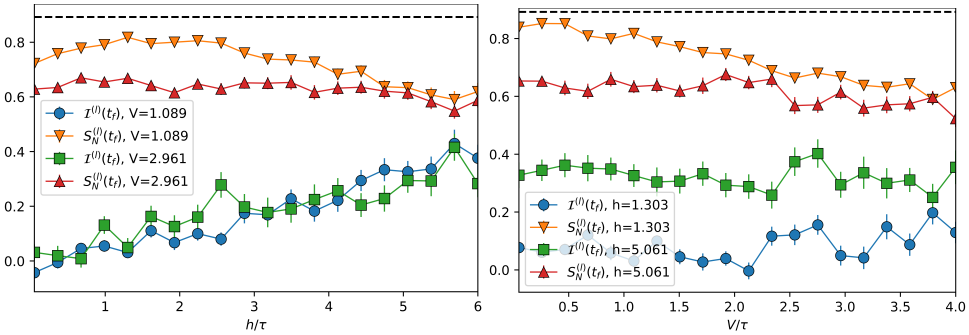

(c) Local Imbalance and Number Entropy against h/τ

(d) Local Imbalance and Number Entropy against V/τ

Figure 4.7: Slices of the phase diagrams of Section 4.1.6 (the realistic $L = 8$ model) for **(a)** and **(c)** fixed values of V/τ on both sides of the transition point between thermal and insulating phases at $V/\tau = 2$, and **(b)** and **(d)** fixed values of h/τ on both sides of the crossover from thermal to MBL regimes at $h/\tau = 3.5$; error bars shown where visible.

number entropy. Reapeating this protocol as we scan h from a low to a high value will show a transition in both the number entropy and imbalance if the system is MBL, and only the imbalance if the system is insulating.

I also examine individual slices of the phase diagrams of Section 4.1.6 in Section 4.1.6, to emulate the kind of results one would expect to see from an experiment which scans h/τ or V/τ whilst holding the other constant. Such an experiment is far simpler (especially in the case of scanning h/τ which can be freely tuned by modifying plunger gate voltages) than determining the full phase diagram. Panels **(a)** and **(b)** of Section 4.1.6 show the bulk imbalance and number entropy as we hold either V/τ and h/τ fixed on both sides of the MBL and metal-insulator transition and scan the other parameter respectively. Panels **(c)** and **(d)** of Section 4.1.6 show the local variants. The black dashed line in each panel shows the thermal value of

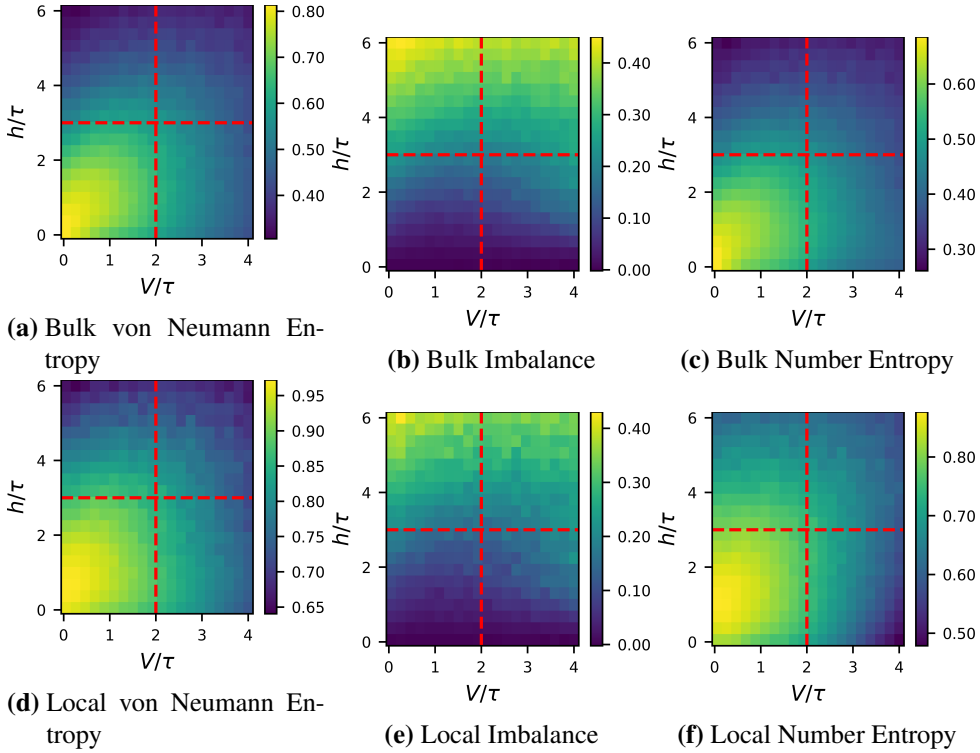

(a) Bulk von Neumann Entropy

(b) Bulk Imbalance

(c) Bulk Number Entropy

(d) Local von Neumann Entropy

(e) Local Imbalance

(f) Local Number Entropy

Figure 4.8: Time and disorder-averaged steady-state quantities across the full $V-h$ phase diagram for the ideal system; initialized in a charge-density wave configuration. The ideal system consists of $L=10$ sites, exponential total evolution times of $\tau t_f = 10^{10}$, time-averaging over the final third of the total evolution time, and disorder-averaging over 512 samples per (V,h) coordinate.

the number entropy, a benchmark of ergodicity in the system, which I introduced at the end of Section 4.1.5.

The form of the imbalance is agnostic to changes in the interaction strength V/τ; with each pair of imbalance curves in each panel having similar functional forms. The only difference is in panels **(b)** and **(d)** in which the imbalance is significantly higher for high h/τ and easily differentiated from the low h/τ case; though they are roughly invariant as V/τ is scanned. The number entropy is clearly sensitive to both parameters, staying fixed for sufficiently high V/τ or h/τ as the other parameter is scanned; but showing a clear decrease with increasing V/τ or h/τ as the other is held at a low constant value. Panel **(b)** shows this difference in the behaviour of the number entropy for different values of V/τ most clearly. The high-h/τ number entropy curve is roughly constant, whilst the low-h/τ curve shows a decrease with increasing V/τ. Moreover, the number entropies are most

readily differentiated in the thermal regime where they diverge, meeting again for sufficiently h/τ. Importantly, this difference in behaviour becomes much harder to distinguish in **(c)**; in which both number entropy curves are much closer together and their functional forms are harder to differentiate. This means that fixing V/τ and extracting local imbalance and number entropy values for different h/τ may be - by itself - insufficient to differentiate between MBL and insulating behaviour. The experimentalist may have to supplement this analysis by either considering bulk quantities instead, or by finding a way to vary V/τ such that the imbalance and number entropy curves in panels **(b)** or **(d)** can be directly differentiated instead.

I repeat the above analysis for an 'ideal' system by lifting the conservative constraints placed on evolution times, number of disorder realizations, and parameter characterization errors. I consider a system of $L = 10$ sites, exponential time scales of $\tau t_{\mathrm{f}} = 10^{10}$, late-time time-averaging - wherein I average over the final third of the evolution time to eliminate remaining fluctuations - and 512 disorder realizations. Additionally, there are no absolute and relative uncertainties in the parameters h/τ and V/τ.

The results of this analysis of an ideal system are shown in Section 4.1.6, and are qualitatively similar to the corresponding results for the realistic system. Again, the imbalance is agnostic to changes in V/τ and cannot detect the insulating regime at $V/\tau > 2$, again in contrast to the von Neumann and number entropies which identify both this transition and the ergodic-MBL crossover at $h/\tau \sim 3.5$. Strikingly, the local variants which use measurements on only two sites in the middle of the array are qualitatively similar to the bulk variants, indicating that local measurements are enough to identify the different regimes.

Individual slices of the phase diagrams of Section 4.1.6 are shown in Section 4.1.6, wherein we fix V/τ or h/τ and scan the other respectively. The behaviours noted in the discussion of Section 4.1.6 are much clearer in the larger, ideal system. The imbalance is clearly agnostic to changes in V/τ, as evidenced by its constancy in panels **(b)** and **(d)** of Section 4.1.6. Moreover, the imbalance curves in panels **(a)** and **(c)** respectively are almost identical. This supports the

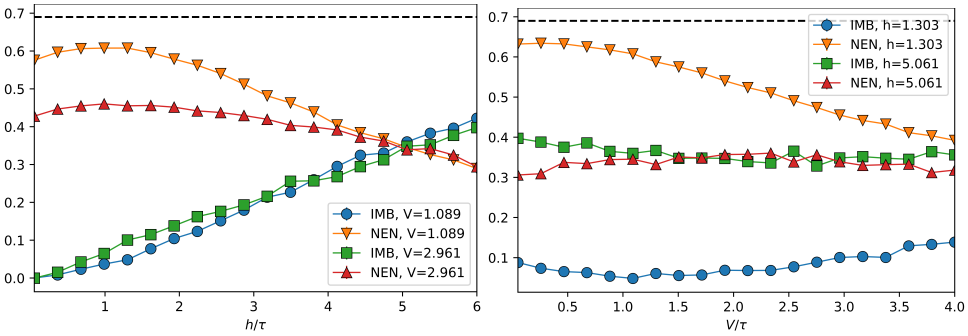

(a) Bulk Imbalance and Number Entropy against h/τ

(b) Bulk Imbalance and Number Entropy against V/τ

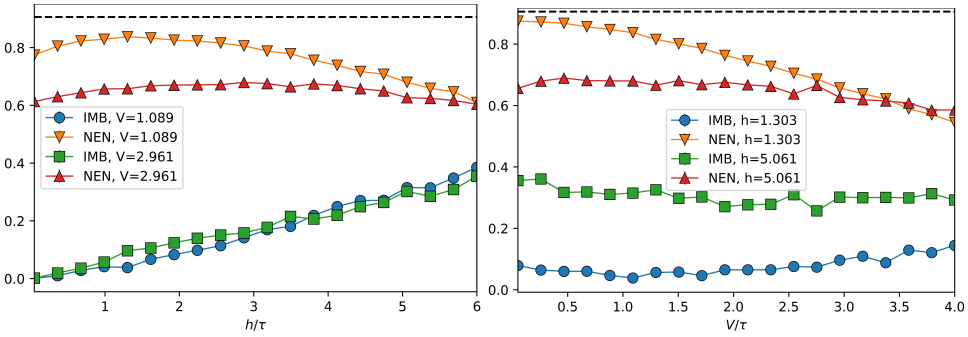

(c) Local Imbalance and Number Entropy against h/τ

(d) Local Imbalance and Number Entropy against V/τ

Figure 4.9: Slices of the phase diagrams of Section 4.1.6 (the ideal $L = 10$ model) for **(a)** and **(c)** fixed values of V/τ on both sides of the transition point between thermal and insulating phases at $V/\tau = 2$, and **(b)** and **(d)** fixed values of h/τ on both sides of the crossover from thermal to MBL regimes at $h/\tau = 3.5$; error bars shown where visible.

protocol we propose which requires different post-processing on charge measurements to construct both the imbalance and number entropy in tandem. The number entropy has clearly different behaviour as both V/τ and h/τ vary, staying fixed for sufficiently high V/τ or h/τ. Panel **(b)** shows this behaviour most clearly, with both the imbalance and number entropy constant with increasing V/τ for high disorder, and with imbalance constant but number entropy decreasing with increasing V/τ for low disorder.

I note here that the decision to restrict the analysis to a small number of disorder realizations, and the use of large absolute and relative uncertainties in all parameters, represents a worst-case scenario. Thus, experimental results are likely to be clearer than those presented in this article. The results of Section 4.1.6 for an ideal system and above discussion show that differentiating between the MBL and

insulating regimes is a much easier task with these worst-case restrictions lifted. Despite this, differentiation between these regimes is possible even in the conservative realistic model. Provided that the charging energies are high enough that h/τ can be freely tuned, local charge sensing is enough to identify MBL, and unambiguously differentiate it from insulating behaviour due to strong electron-electron interactions, in current-generation QDA.

I suggest that both the sensitivity of the number entropy and insensitivity of the imbalance to the transition in V/τ can be explained by a type of 'rolling' behaviour, in which the charge-density wave moves coherently through the system. In essence, V/τ is so strong that excitations cannot exist in neighbouring sites (similar to Rydberg-blockaded systems [51–53]) and due to the fact that total particle number is conserved: the dynamical state of the system oscillates between the states $|\circ,\bullet,\circ\cdots\rangle$ and $|\bullet,\circ,\bullet\cdots\rangle$ (where $\circ$ corresponds to an empty dot, and $\bullet$ to an occupied dot). This would register an imbalance which looks thermal, but a probability distribution $p(\rho(t),n=N)$ sharply peaked around $N=L_\rho/2$ - and thus a near-zero number entropy. I support this suggestion with a brief numerical analysis in which I investigate the overlap of a dynamical state in a single, typical, disorder profile, with both charge-density wave states. Interestingly, see similar behaviour can also be found in systems with an odd number of sites, suggesting a more slightly more complicated explanation which I defer to future study.

First I initialize a system in the charge-density wave $|\psi(0)\rangle = |\bullet,\circ,\bullet,\cdots\rangle$ (where $\circ$ corresponds to an empty dot, and $\bullet$ to an occupied dot) and select a typical disorder profile of strength $h/\tau = 1$. In Fig. 4.10 I then investigate the overlap of the state $|\psi(t)\rangle$ with $|\psi(0)\rangle$ (Loschmidt echo) in panel **(a)** and its overlap with the complementary charge-density wave state $|\circ,\bullet,\circ,\cdots\rangle$ in panel **(b)**. I compute the overlap as the expectation value squared: $|\langle\psi(t)|\psi_{\text{target}}\rangle|^2$. For low V/τ (thermal regime), both curves drop rapidly to low values and remain there. But as V/τ is increased we can see sharp revivals in the overlap of $|\psi(t)\rangle$ with both charge-density wave states. The first peak in panel **(a)** (after $t=0$) occurs after the first peak in panel **(b)** and at approximately the same time difference as the first peak in panel

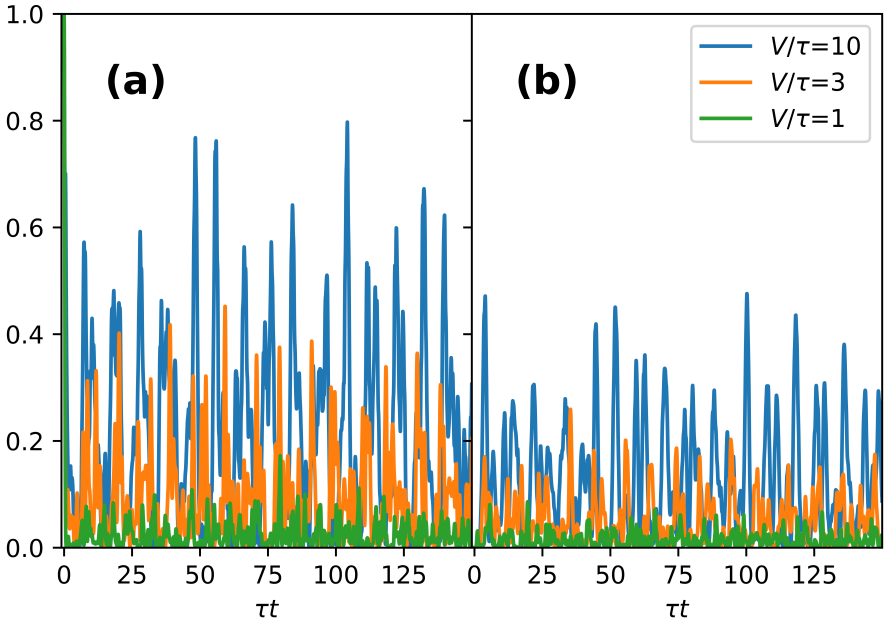

Figure 4.10: Numerical evidence of a coherent oscillation of a charge-density wave between two configurations as V/τ is varied. For a system initialized in the state $|\bullet,\circ,\bullet,\cdots\rangle$ **(a)** shows overlap with the initial state and **(b)** shows the overlap with the inverted state $|\circ,\bullet,\circ,\cdots\rangle$. System hamiltonian is a typical disorder-realization of strength $h/\tau = 1$.

(b) does from $t = 0$. This suggests that the 'rolling' behaviour explanation may be a good approximation to the dynamics of the state; and thus a more detailed investigation is warranted. Such an investigation is, however, beyond the immediate scope of this thesis.

The findings of this section show that MBL is accessible in state-of-the-art QDA, but that its identification is not a simple task. The key limitation to detecting MBL in modern quantum dot arrays is ensuring high enough on-site charging energies such that they cannot be surmounted by the large applied random chemical potentials required to localize the system. This may be improved by e.g. decreasing τ, but that requires a corresponding increase in charge-qubit coherence times such that total evolution times are large enough to see localization. This could perhaps be achieved by designing free-standing dots that isolate the system from phonons. Working within these limitations I first characterized an experimental device and extrapolated that characterization into a worst-case model. I then numerically de-

termined the phase diagram of the device as a function of disorder and interaction strength; identifying an insulating regime which may be mistaken for MBL. Finding that the widely-used imbalance is agnostic to this phase, I then proposed an alternative protocol based on the number entropy - which requires the same measurements as the imbalance - and which successfully differentiates MBL from the thermal and insulating regimes. This protocol relies only on local charge-sensing measurements, which are readily accessible in modern quantum dot experiments. In addition. we find that performing these measurements on two sites in the middle of the system yields qualitatively similar results as bulk analyses, drastically reducing the number and complexity of measurements required.

4.2 Statistical Properties of Twin-Rail Quantum Dot Arrays

In addition to strictly one-dimensional settings like that of the previous section, quantum dot arrays (QDAs) naturally provide an experimental setting in which to investigate quasi-one-dimensional, or even two-dimensional, behaviour. The properties of true two-dimensional QDAs of any considerable size is beyond the scope of this thesis, and indeed requires a technological finesse beyond the grasp of current experimental capabilities. However, twin-rail QDAs *do* exist, and provide a fertile ground for the simulation of quasi-one-dimensional systems [54]. In this section, I introduce and investigate the critical properties of a spin-ladder description of such twin-rail QDAs.

I start by introducing the experimental system in Section 4.2.1 and the antiferromagnetic Heisenberg ladder that simulates it in Section 4.2.2. I then introduce several quantities of interest, including singlet-triplet profiles and the fidelity susceptibility, in Section 4.2.3. The results of applying these quantities to the system are discussed in Section 4.2.4, wherein I interrogate their ability to reliably detect the system's phase crossover.

4.2.1 The Experimental Twin-Rail Quantum Dot Array

Here I briefly give an overview of the kind of experimental setup available to us in the context of twin-rail QDAs. I also briefly discuss the motivations behind this section. Much of what follows is drawn from ongoing research and private communication with Liza Morozova and Dr. Zhang in Prof. Vandersypen's group at TU Delft Ref. [55].

The QDAs in question are 'twin-rail', i.e. $2 \times L$ arrays, which are driven through two broad operating regimes[6], a 'working' regime wherein the dots interact, and a 'measurement' regime wherein pairs of dots are isolated from each other. In the working regime, the energy scales of longitudinal and transverse nearest-neighbour interactions are isotropic up to some - potentially significant - uncertainties, and are tuned to be within an order of magnitude of each other. These energies (in units of $\hbar = 1$) can be freely tuned in the interval of $10 - 100$MHz. In the measurement regime, longitudinal couplings are pinched off over a duration of a few nanoseconds such that only transverse couplings remain. The state of these isolated transverse double-dots, called 'rungs', can then be measured via singlet-triplet measurements; a process that takes place sequentially over rungs in a time of approximately 20μs. Nearest-neighbour SWAP gates may also be enacted during the measurement regime by carefully turning on and off specific transverse and longitudinal couplings.

This setup introduces two major restrictions which inform my theoretical analysis. Firstly, only singlet-triplet measurements are allowed; though we may use short range SWAP gates to post-process the final state. Secondly, any results must be robust to the quenching of the longitudinal couplings during the few nanoseconds over which the system is driven from the working to the measurement regime. This manifests as a question of adiabaticity - if the quench is diabatic then the state, and thus the information encoded in it, is preserved.

[6]There is technically a third 'initialization' regime wherein certain states are prepared and the couplings tuned, but it doesn't factor into my theoretical and numerical analysis.

4.2.2 The Antiferromagnetic Heisenberg Ladder

The QDAs discussed in the preceding section define a series of spin qubits that can be modelled by a twin-rail antiferromagnetic Heisenberg ladder (AFHL),

$$H = J_{\parallel} f(t) \sum_{j=1,\alpha}^{L-1} \eta_{j,\alpha} \mathbf{S}_{j,\alpha} \cdot \mathbf{S}_{j+1,\alpha} + J_{\perp} \sum_{j=1}^{L} \eta'_j \mathbf{S}_{j,A} \cdot \mathbf{S}_{j,B} \tag{4.6}$$

where the $\mathbf{S}_{j,\alpha} = (S^x_{j,\alpha}, S^y_{j,\alpha}, S^z_{j,\alpha})^\top$ are vectors of standard spin-1/2 operators $S^{x/y/z}_{j,\alpha}$ acting on site j and rail $\alpha \in \{A,B\}$. The parameter $J_{\parallel}$ tunes the strength of the intra-rail couplings, and $J_{\perp,j}$ tunes the inter-rail couplings. The smooth function $f(t) = [1 - \tanh((t - t_f/2)/t_w)]/2$ is used to quench the intra-rail couplings from their maximum value to zero as the system is driven from the working regime to the measurement regime, where t_f is the total time taken to quench the couplings and we take $t_w = t_f/5$ as the quench width throughout. This limits most of the quench's effect to the interval $t_f/4 < t < 3t_f/4$, as can be seen in Fig. 4.12(d). The $\eta_{j,\alpha}$ and η'_j are uniformly distributed in the interval $\eta_{j,\alpha}, \eta'_j \in [1-\eta, 1+\eta]$ and account for experimental inaccuracies that may lead to anisotropic couplings. As indicated by the name, we take all couplings as antiferromagnetic $J_{\perp}, J_{\parallel} \geq 0$ and $0 \leq \eta \leq 1$.

For antiferromagnetic couplings, each neighbouring pair of sites energetically prefers to anti-align and thus form singlet states - as such the overall ground state is generally a resonating valence bond state of all such possible singlet configurations [56]. Clearly, when one term dominates (and assuming isotropic couplings), singlets tend to accumulate along a single axis - either between the rails for $J_{\perp} \gg J_{\parallel}$ or along the rails for $J_{\parallel} \gg J_{\perp}$. In the former case the ground state is a unique product state of singlets $|\psi^s_j\rangle = (|\uparrow\rangle_{j,A}|\downarrow\rangle_{j,B} - |\downarrow\rangle_{j,A}|\uparrow\rangle_{j,B})/\sqrt{2}$ on each site j distributed across the rails A and B, $|\psi^{GS}_{J_{\perp} \gg J_{\parallel}(t)}\rangle = \prod_j |\psi^s_j\rangle$, whilst in the latter case the ground state is simply a product of the Heisenberg chain groundstates along each rail.

In actuality, this model exhibits a phase transition at precisely $J_{\perp} = 0$. We can understand this as a function of the Haldane conjecture, i.e. that the excitation spectra of antiferromagnetic Heisenberg chains with half-integer spin are gapless, and that of chains with integer spin are gapped [57, 58]. At $J_{\perp} = 0$ the ground state

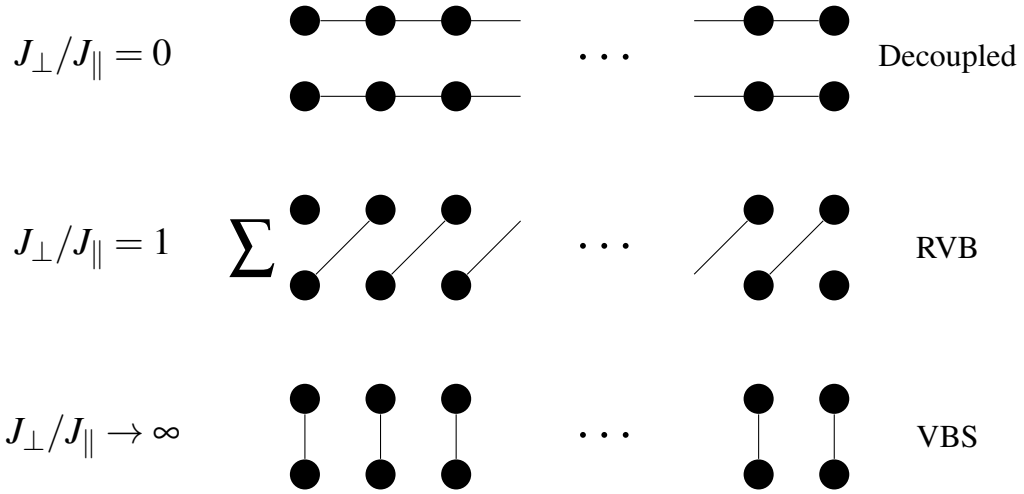

Figure 4.11: Schematic of the ground states of the antiferromagnetic Heisenberg ladder. As $J_\perp/J_\parallel$ increases, the state interpolates from a product state of Heisenberg ladders, through an RVB state of possible singlet-triplet configurations, to a VBS state comprised of singlets along the rungs. The specific RVB state shown occurs at exactly $J_\perp = J_\parallel$, and has high overlap with the states that have singlets distributed across next-nearest neighbours.

becomes a product state of two half-integer chains and so the system is gapless; deviating from $J_\perp = 0$ results in an effective integer-spin ladder which is gapped. As the degeneracy of the ground state has changed, the system must have definitionally passed through some ground-state phase transition.

In practice, the $J_\perp > 0$ regime exhibits a very notable crossover. Firstly, the ground state is close to a product state of two antiferromagnetic Heisenberg chain ground states at small $J_\perp > 0$. Secondly, a resonating valence bond (RVB) state similar to the Haldane phase of a spin-1 Haldane chain for large $J_\perp$, and finally the dimerized phase discussed above at $J_\perp \to \infty$. In this intermediate regime, centred around $J_\perp = J_\parallel$, all spins prefer to anti-align with their nearest-neighbours, with neither transverse nor longitudinal interactions dominating. This frustration results in spins *aligning* with next-nearest neighbours, resulting in a state which is very close to a simple product state of triplets across next-nearest neighbours[7]. The structure of these ground states across the phase crossover are schematically shown in Fig. 4.11.

[7]Rewriting this state in terms of singlets and triplets over nearest-neighbours again recovers the RVB picture of the ground state in this regime.

4.2.3 Singlet-Triplet Measurements and Fidelity Susceptibility

Given that they are the only kind of measurements immediately available to us in experiment, it is worth discussing singlet-triplet measurements in detail here. In particular I discuss a method of compressing measurement outcomes into a singlet-triplet 'profile', a statistical distribution which may be more amenable in experiment after averaging over many experimental rungs. The singlet-triplet measurement basis and these compressed statistics have seen use in quantum dot arrays before, specifically in characterizing the Heisenberg chain ground state [59]. I characterize these statistics by considering the Kullback-Liebler divergence of the determined probability distribution and the theoretical distribution given by the system at $J_\perp = 0$. This gives us a concrete way to investigate the transition and crossover regions discussed previously. I also introduce the fidelity susceptibility, widely used to herald phase transitions, as a diagnostic tool. The fidelity susceptibility is functionally useless in experiment - it is near impossible to measure - but is invaluable in theory.

The core of singlet-triplet profiles are simple projective measurements made onto singlet or triplet states across each rung:

$$\mathbf{P}^s_j = |\psi^s_j\rangle\langle\psi^s_j|, \quad \mathbf{P}^t_j = 1 - \mathbf{P}^s_j. \tag{4.7}$$

The action $\mathrm{Tr}[\mathbf{P}^{s(t)}_j \rho] = p^{s(t)}_j$ on some state ρ yields the probability of finding the pair of sites (j,A) and (j,B) in a singlet (triplet) state. We can thus build up a profile of measurement outcomes by considering products of all possible strings of the projectors of Eq. (4.7). Each possible outcome string $x = x_1 x_2 \cdots x_L$ where $x_j \in \{s,t\}$ corresponds to an operator $\mathbf{P}^x = \prod_j \mathbf{P}^{x_j}_j$. Partitioning strings with an equal number M of triplet outcomes into the sets X_M, and aggregating the corresponding projectors yields

$$\mathbf{P}(m_t = M) = \sum_{x \in X_M} \mathbf{P}^x. \tag{4.8}$$

The projectors defined in Eq. (4.8), when applied to a given state, yield a discrete probability distribution $p(m_t)$ describing the probability of measuring m_t triplets in

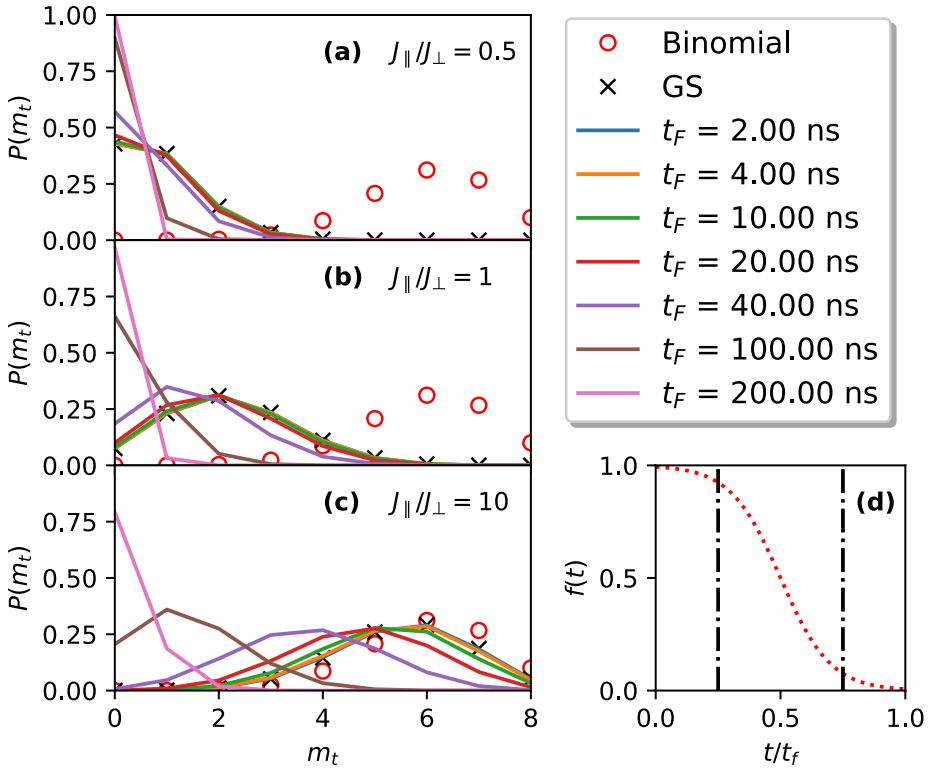

Figure 4.12: Panels (a)-(c) show singlet-triplet profiles for a system of $L = 8$ rungs without disorder $\eta = 0$, with varying $J_\parallel/J_\perp$ and quench times t_f. The binomial distribution describing the profile deep in the $J_\parallel/J_\perp \to \infty$ regime is centred around $3L/4$ and is shown as red circles. Panel (d) shows the shape of the quench $f(t)$ for $t_f = 1$. The characteristic energy scale is taken as $J_\perp = 100$ MHz, and evolution times are calculated accordingly.

total across all L rungs in the system.

Clearly as $J_\parallel/J_\perp \to 0$, singlets accumulate on the rungs, and the singlet-triplet profile becomes increasingly peaked around m_t, with the distribution becoming a Kronecker delta distribution $p(m_t) \to \delta_{m_t,0}$ in the extreme limit. For a system instead dominated by intra-rail couplings $J_\parallel/J_\perp \to \infty$, the resulting probability distribution closely follows a thermal distribution which yields a binomial distribution centred around $3L/4$.

The fact that the singlet-triplet profile probability distributions of the system deep within specific regimes are exactly known is extremely useful here. It allows us to define a distance of the system from those regimes in terms of the Kullback-

Liebler divergence

$$D_{\mathrm{KL}}\left[p(m_t)\|f_B(m_t)\right] = \sum_{M=0}^{L} p(M)\log\left[\frac{p(M)}{f_B(M)}\right], \tag{4.9}$$

where $f_B(m_t) \equiv f_B(L, m_t, q = 3/4)$ is the binomial distribution describing L trials yielding exactly m_t successes with success probability $q = 3/4$.

I also consider the fidelity susceptibility χ_F which is, though far less experimentally tractable, a quantum geometric quantity that allows us to probe generic phase transitions without appealing to a specific order parameter [60]. The fidelity susceptibility has also found use in the context of quantum sensing, as it is proportional to the quantum fisher information, an intrinsic property of a system which limits the precision of measurements that said system can be used to make [61]. The fidelity susceptibility gives us a direct quantity with which to compare our analyses of the singlet-triplet measurement statistics. The fidelity susceptibility is the coefficient of the second order term in the Taylor expansion of the logarithm of the quantum fidelity, defined as

$$\chi_F(\lambda) = -2\frac{\partial^2 \ln F(\lambda,\varepsilon)}{\partial\varepsilon^2}\bigg|_{\varepsilon=0} \tag{4.10}$$

where $F(\lambda,\varepsilon) = |\langle\psi^{GS}(\lambda)|\psi^{GS}(\lambda+\varepsilon)\rangle|$ is the fidelity between the ground state of the system $|\psi^{GS}(\lambda)\rangle$ and the ground state of the system $|\psi^{GS}(\lambda+\varepsilon)\rangle$ after some small perturbation[8] of the driving parameter λ. The fidelity itself spans a range of orders of magnitude, a behaviour which is captured by use of the logarithm. In our case, the driving parameter $\lambda = J_{\|}/J_{\perp}$ carries us across a crossover between two different regimes with two very different ground states. Thus, in the crossover region the ground state should change rapidly for small perturbations ε; this will register a rapid growth of $\chi_F(\lambda)$ around the critical value of $\lambda = \lambda_c$. Thus, as we address larger systems, a diverging fidelity susceptibility serves as evidence of a quantum crossover.

[8] Note that the first derivative of the fidelity vanishes as $F(\lambda,0)$ is a maximum.

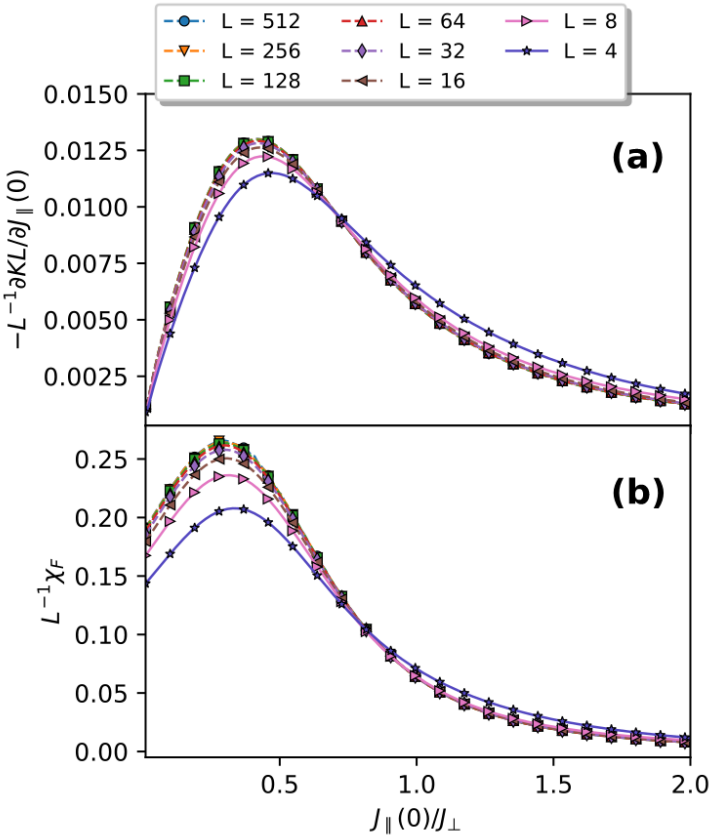

Figure 4.13: Results for exact ground states (no transport) of the antiferromagnetic Heisenberg ladder as a function of $J_{\parallel}/J_{\perp}$ at varying length scales. Solid lines show exact results, dotted lines show DMRG results. Panel **(a)** shows the Kullback-Liebler divergence of the singlet-triplet profile to the binomial distribution centred around $3L/4$. Panel **(b)** shows the fidelity susceptibility.

4.2.4 Results and Outlook

The results of applying the singlet-triplet profile projectors of Eq. (4.8) to the ground states of the antiferromagnetic Heisenberg ladder Hamiltonian of Eq. (4.6) for zero disorder $\eta = 0$ and a range of coupling ratios $J_{\parallel}/J_{\perp}$ and quench times t_f are shown in Fig. 4.12**(a)-(c)**. Results for exact ground states are shown as black crosses, and the binomial distribution which the system follows in the extreme limit $J_{\parallel}/J_{\perp} \to \infty$ are shown as red circles.

The system unilaterally exhibits adiabatic transport towards the $J_{\parallel}/J_{\perp} = 0$ ground state for large quench times. This is manifested as a drift of the singlet-triplet profile towards a Kronecker delta function as t_f increases. For short quench times, this drift is negligible and the system remains close to the true ground state.

In practice, as the experimental device is limited to frequencies of up to 100MHz for $J_{\parallel}$ and $J_{\perp}$; the real quench times for $J_{\parallel}/J_{\perp} = 10$ are ten times lower than the effective quench times shown in the legend of Fig. 4.13. This is important as the red 20ns line in Fig. 4.13**(c)**, which would correspond to a 2ns quench in the real system, suffers slightly from the adiabatic drift discussed above. Thus, for extreme values of $J_{\parallel}/J_{\perp}$, the quench in the experimental twin-rail device may be adiabatic; and the resulting state after the quench is not a reliable copy of the true ground state. Despite the fact that I do consider the effects of adiabatic transport in this section, much of the interesting crossover behaviour is actually restricted to the regime where the transverse and longitudinal couplings are roughly commensurate $J_{\parallel} \sim J_{\perp}$. Thus, it is reasonable to state that the experimental device is capable of reliably producing ground states within the regime of interest.

I next consider the gradient of the Kullback-Liebler divergence defined in Eq. (4.9), and the fidelity susceptibility defined in Eq. (4.10). I use exact diagonalization to retrieve exact ground states of small systems $L < 16$, and use two-site DMRG to determine ground states of larger systems $L \geq 16$. The fidelity susceptibility is computed using a small but finite value for $\varepsilon = 10^{-4}$ and a discretized version of Eq. (4.10): $\chi_F = -2\ln F(\lambda, \varepsilon)/\varepsilon^2$. The Kullback-Liebler divergence is calculated for small systems $L < 16$ according to Eq. (4.9). For larger systems $L \geq 16$ where the enumeration of all possible strings x is impossible, I instead calculate the probability of measuring a triplet state p^t_j on each rung j, and construct a binomial distribution from the average $\sum_j p^t_j/L$. This determined distribution is then substituted into Eq. (4.9) as $p(m_t)$. In practice, the probabilities p^t_j are relatively uniform across the system, and this approach is justified. After normalizing both quantities by system size L, the results of these calculations are shown in Fig. 4.13.

From Fig. 4.13(a) we can see that the gradient of the Kullback-Liebler divergence peaks in the region $0 < J_{\parallel}/J_{\perp} < 1$, indicating that the statistics of the ground state are rapidly changing in this region. The fidelity susceptibility shown in Fig. 4.13(b) also peaks in this region, supporting the existence of a rapidly changing ground state and thus a quantum crossover between the two regimes in this region.

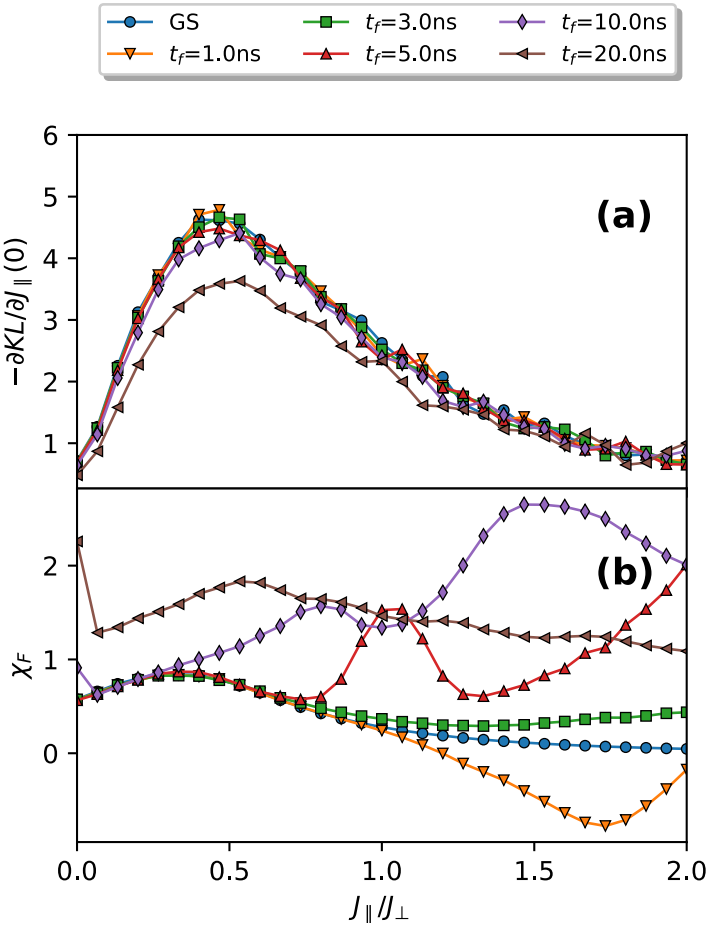

Figure 4.14: Results for ground states subject to significant preparation errors $\eta = 0.2$, and transport during a quench time t_f as a function of $J_\parallel/J_\perp$. Panel **(a)** shows the gradient of the Kullback-Liebler divergence of the singlet-triplet profile to the binomial distribution centred around $3L/4$. Panel **(b)** shows the fidelity susceptibility.

The most interesting features of these graphs are that both are clearly extensive in L, both have crossing points at different but close values of $J_\parallel/J_\perp$, and they are qualitatively very similar to each other. The first two facts, that they are extensive in L and exhibit scale invariance at very specific points, may suggest a kind of scaling behaviour. However, I was unable to find any meaningful data collapse using the continuous phase transition finite size scaling approach (see Section 1.3.3.1 and Section 2.2.4). Whilst this does not preclude the existence of some kind of phase transition in this region, it does support the supposition that the system is in fact undergoing a crossover through ground states of similar structure rather than a

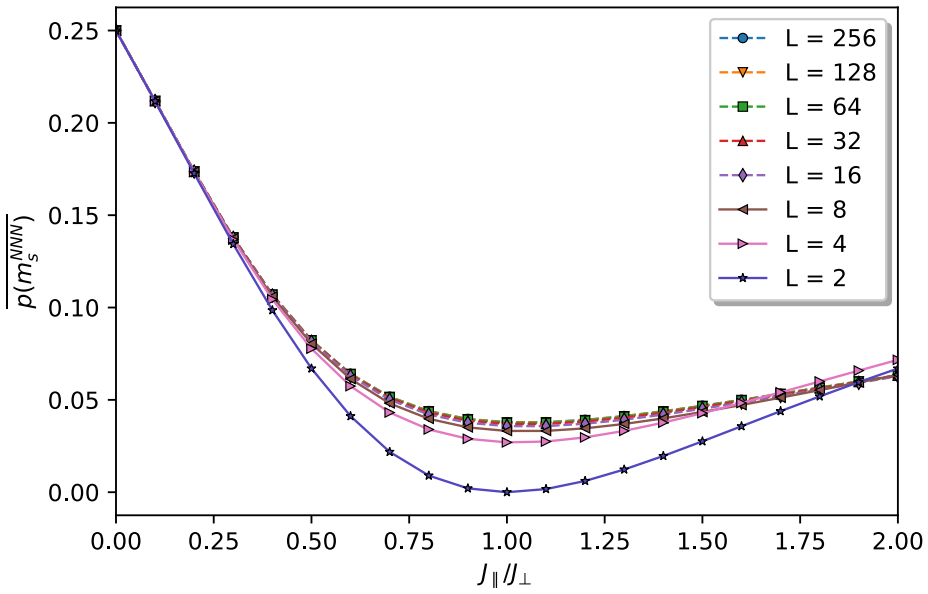

Figure 4.15: Probability of measuring next-nearest-neighbours in singlet states, averaged over the entire system. Overall ground states are exact (no transport).

true quantum phase transition. The last fact, that the two graphs are qualitatively very similar, suggests that the measurable Kullback-Liebler divergence is a good experimental replacement for the fidelity susceptibility in this system. They both intuitively address the same underlying thing, a rapidly changing ground state, and produce a similar characteristic signature of the crossover behaviour.

Moreover, when I consider a realistic experimental system of $L = 4$ rungs with variable quench times and anisotropic disorder $\eta > 0$, the results for the Kullback-Liebler divergence do not significantly change. This is constrast to the fidelity susceptibility results which - whilst initially well-behaved for short quench times and low values of $J_\parallel/J_\perp$ - become erratic and unpredictable as both increase. These behaviours are shown in Fig. 4.14 for significant disorder strengths $\eta = 0.2$ and 512 sample realizations of Eq. (4.6), corresponding to errors of up to 20% in the preparation of $J_\parallel$ and $J_\perp$ in each sample. The Kullback-Liebler divergences and fidelity susceptibilities are calculated *individually* and the results are then averaged. The gradient of the Kullback-Liebler divergence is computed after this averaging. Remarkably, even for the significant 20% error in array preparation, the crossover is still clearly visible in Fig. 4.14. This suggests that, for realistic quench times and

errors in Hamiltonian perparation, quantum dot arrays are still highly reliable simulators of the antiferromagnetic Heisenberg ladder and present a promising avenue to the experimental investigation of ground states thereof.

Finally, given the possibility of experimentally enacting nearest-neighbour SWAP gates after the quench, it may be possible to directly investigate the state of the system around $J_{\|}/J_{\perp} = 1$ which should be close to a valence bond solid of triplets distributed across next-nearest-neighbours [56]. This is schematically shown in Fig. 4.11. Post-quench, one could simply enact SWAP gates between disjoint pairs of sites along one of the rails; concentrating the entangled states of half of the L next-nearest-neighbour pairs into $L/2$ of the rungs. These $L/2$ rungs can then be measured in the singlet-triplet basis to come up with an average system-wide probability $\overline{p(m_s^{NNN})}$ of measuring next-nearest-neighbours in a singlet state. At $J_{\|}/J_{\perp} = 1$, this average probability should be at a minimum. The result of explicitly calculating $\overline{p(m_s^{NNN})}$ for a range of system sizes is shown in Fig. 4.15, wherein this behaviour is seen exactly. Again, exact diagonalization for small systems is shown as solid lines, and two-site DMRG for large systems is shown as dotted lines; calculation of $\overline{p(m_s^{NNN})}$ in both cases is carried out by computing the outcome of few-site next-nearest-neighbour projectors. As system size L increases, the curves collapse into a single line suggesting that this crossover persists in the thermodynamic limit. A key feature of this approach is that the measurement outcomes for individual strings x do not need to be experimentally calculated. Indeed if the outcome of one next-nearest-neighbour measurement is typical, then $\overline{p(m_s^{NNN})}$ can be determined by the application of a single SWAP gate and subsequent measurement. In systems which have high readout errors, this may present an even more promising method of investigating ground state phase transitions than the singlet-triplet profile and quantities derived thereof.

4.3 Information Leakage in Transmon-Based Quantum Computers

The foundational idea of this section is that quantum computers must necessarily trace a razor's edge between localization and chaos [62, 63]. This makes intuitive sense. If it is too difficult to change the internal state of a highly localized system then the system is useless for the purposes of computation. If the system is too delocalized then control is an issue, and the underlying natural dynamics may push the system into states that are undesirable. Thus, modern quantum computing devices must necessarily thread this needle. Burdened by this narrative, a natural follow-up question to ask is how much information *exactly* is lost due to the underlying dynamics. As I showed in Chapter 2, the internal dephasing that occurs in even highly localized systems can erase the information encoded within. Can this be leveraged into a quantitative analysis of how much information a quantum computer bleeds over time whilst idle?

Much of what follows is drawn from ongoing research and private communication with Dr. Dooley at Prof. Goold's group at Trinity College Dublin Ref. [64]. In Section 4.3.1 I introduce the model which simulates IBM's devices: the transmon array, and discuss some of its features. In Section 4.3.2 I introduce the specific IBM device in question, and analyse information loss in said device by comparing the informational quantities with calibration data taken directly from IBM.

4.3.1 The Transmon Array Hamiltonian

The gold standard of modern quantum computation takes the form of arrays of superconducting qubits: nanoscale or mesoscale solid-state electrical circuits that can occupy discrete quantum states. The basic building block of such a circuit is the Josephson junction which, at different regimes of operation, can form different kinds of effective qubit. For the purposes of this chapter, each Josephson junction can be abstracted into a box through which a certain number $\hat{n}_j$ of quasi-particles (Cooper pairs) are flowing, and the Josephson phase $\hat{\phi}_j$. The Hamiltonian of an

array of such junctions can be written as

$$H = 4\sum_j E_j^C \hat{n}_j^2 - \sum_j E_j^J \cos\hat{\phi}_j + T\sum_{\langle i,j\rangle} \hat{n}_i \hat{n}_j \tag{4.11}$$

where E_C is the charging energy, E_J is the Josephson energy, and T is a capacitive coupling between neighbouring junctions. For low E_j^J, this model is almost diagonal in the basis of the number operators $\hat{n}_j$. For high E_j^J the model is instead diagonal in the basis of the phase operators $\hat{\phi}_j$. This latter regime is used by IBM in their quantum computers, which are readily accessible to the wider scientific community.

I here derive a more useful form of Eq. (4.11) in terms of these flux qubits. Assuming for a moment that $T = 0$, one can diagonalize the first two terms of Eq. (4.11) by taking $\hat{n}_j = i n_j^{\text{zpf}}(\hat{c}_j^\dagger - \hat{c}_j)$ and $\hat{\phi}_j = \phi_j^{\text{zpf}}(\hat{c}_j^\dagger + \hat{c}_j)$. The $\hat{c}_j^{(\dagger)}$ operators describe 'transmon' quasi-particles satisfying standard bosonic commutation relations, and the numbers $\phi_j^{\text{zpf}} = \sqrt{\langle 0|\hat{\phi}_j^2|0\rangle}$ and $n_j^{\text{zpf}} = \sqrt{\langle 0|\hat{n}_j^2|0\rangle}$ are zero-point fluctuation frequencies for each individual transmon. Expanding the cosine, truncating at fourth order in the $\hat{c}_j^{(\dagger)}$ operators, and defining a total transmon number $\hat{a}_j = \hat{c}_j^\dagger \hat{c}_j$ yields

$$H = \sum_j \left[E_j^J {\phi_j^{\text{zpf}}}^2 + 8E_j^C {n_j^{\text{zpf}}}^2 n - \frac{1}{2}E_j^J {\phi_j^{\text{zpf}}}^4\right]\left(\hat{a}_j + \frac{1}{2}\right) - \frac{1}{2}E_j^J {\phi_j^{\text{zpf}}}^4 \hat{a}_j^2 \tag{4.12}$$

where I have neglected the fast-oscillating terms that don't conserve total transmon number. The zero-point fluctuations satisfy $n_j^{\text{zpf}}\phi_j^{\text{zpf}} = 1/2$ (in units of $\hbar = 1$) and are given by [65]:

$$n_j^{\text{zpf}} = -\frac{1}{\sqrt{2}}\left(\frac{E_j^J}{8E_j^C}\right)^{\frac{1}{4}}, \quad \phi_j^{\text{zpf}} = -\frac{1}{\sqrt{2}}\left(\frac{8E_j^C}{E_j^J}\right)^{\frac{1}{4}}. \tag{4.13}$$

Inserting these into Eq. (4.12), reintroducing the nearest-neighbour coupling term proportional to T, and neglecting constant contributions to the energy, yields the

Hamiltonian

$$H = \sum_j \left(\omega_j + \frac{\delta_j}{2} \right) \hat{a}_j + \frac{\delta_j}{2} \hat{a}_j^2 + \sum_{\langle i,j \rangle} \tau_{ij} \left(\hat{c}_j^\dagger \hat{c}_j + \text{h.c.} \right) \tag{4.14}$$

where $\omega_j = \sqrt{8 E_j^J E_j^C}$ are the harmonic frequencies and $\delta_j = E_j^C$ are the anharmonic frequencies. The tunnelling frequencies τ_{ij} are readily computed as:

$$\tau_{ij} = \frac{T}{4\sqrt{2}} \left[\frac{E_i^J E_j^J}{E_i^C E_j^C} \right]^{\frac{1}{4}} . \tag{4.15}$$

The Hamiltonian of Eq. (4.14) governs the underlying natural dynamics of an array of transmon qubits in the low-energy regime for $E_j^J \gg E_j^C \gg T$. In particular, the main IBM devices operate around the regime of $E_j^J \sim 10\text{GHz}$, $E_j^C \sim 250 - 300\text{MHz}$, and $T \sim 3 - 6\text{MHz}$; with typical gate times of around $t^G = 400 - 600\text{ns}$ and readout lengths of $t^R = 650 - 700\text{ns}$. In the context of the working Hamiltonian of Eq. (4.14), this corresponds to a parameter regime around $\omega_j \sim 5\text{GHz}$, $\delta_j \sim 250 - 300\text{MHz}$, and $\tau_{i,j} \sim 5 - 10\text{MHz}$. Of these parameters, IBM characterises two of them ω_j and δ_j every few days for most devices. Values for $\tau_{i,j}$ are, to the best of my knowledge, not publicly available. Though they are back-calculable from CNOT gate times, I find that in literature a fixed value of T around the range given is simply imposed.

As a final note, the model of Eq. (4.14) is clearly MBL, as site-to-site local disorder far exceeds all other energy scales. Recent works have investigated this property in the specific context of IBM's quantum computing devices, and have found that such devices tread a careful line between localization and chaos [62, 63, 66].

4.3.2 Idle Information Loss in Quantum Computers

The specific device I will be investigating here is IBM's publicly available seven-qubit Perth device. The architecture forms a kind of H-junction wherein two parallel rails of three qubits are connected by a single qubit. This is schematically shown in Fig. 4.16. The table of Fig. 4.16 shows the frequencies ω_j and anharmonicities δ_j of

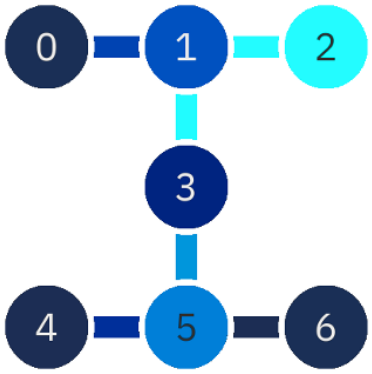

Qubit	ω_j (GHz)	δ_j (MHz)
0	5.15755	-341.525
1	5.03367	-344.369
2	4.86266	-347.272
3	5.12510	-340.442
4	5.15922	-333.367
5	4.97861	-346.022
6	5.15664	-340.454

Figure 4.16: (left) Schematic figure of IBM's Perth device with qubit labels. Brighter (darker) node colours correspond to higher (lower) values of the frequencies ω_j which are the main values driving localization in the device. **(right)** Table of qubit frequencies ω_j and anharmonicities δ_j as per calibration data retrieved from IBM's Perth device on 08/06/2023. Rounded to six significant figures.

each qubit as per calibration data retrieved from IBM's Perth device on 08/06/2023. After back-calculating the energies E_j^C and E_j^J, and given a fixed value for the raw tunnelling rate T, the renormalized tunnelling rates τ_{ij} can be calculated according to Eq. (4.15). These derived τ_{ij} for intermediate $T = 4$MHz and for the device in question are shown in Fig. 4.17**(a)** and all fall in the region of $4-5$MHz, in line with extant analyses. Two-qubit gate times t_{ij}^G for the device are shown in Fig. 4.17**(b)** and vary drastically, suggesting a range of underlying values of τ_{ij}. However, the results of each of these panels do not nicely line up - this may be due to the fact that CNOT gate times are generally a complicated function of the τ_{ij} or that Eq. (4.15) does not account for e.g. the physical distance between qubits. Improvements are, however, difficult without knowing more about the exact physical architecture of IBM's devices, or about the intricate details regarding how CNOT gates are actually enacted [9].

Ultimately, all these parameters can all be fed into Eq. (4.14) to simulate an isolated version of IBM's Perth device. This model remains an accurate simulator of IBM's device as long as evolution times are restricted to be much smaller than the corresponding dephasing times. On the device in question, these times are on the

[9] This seems to be proprietary information, or information that is deliberately obfuscated. After contacting several people affiliated with IBM Quantum, I have received no concrete response to queries on this matter.

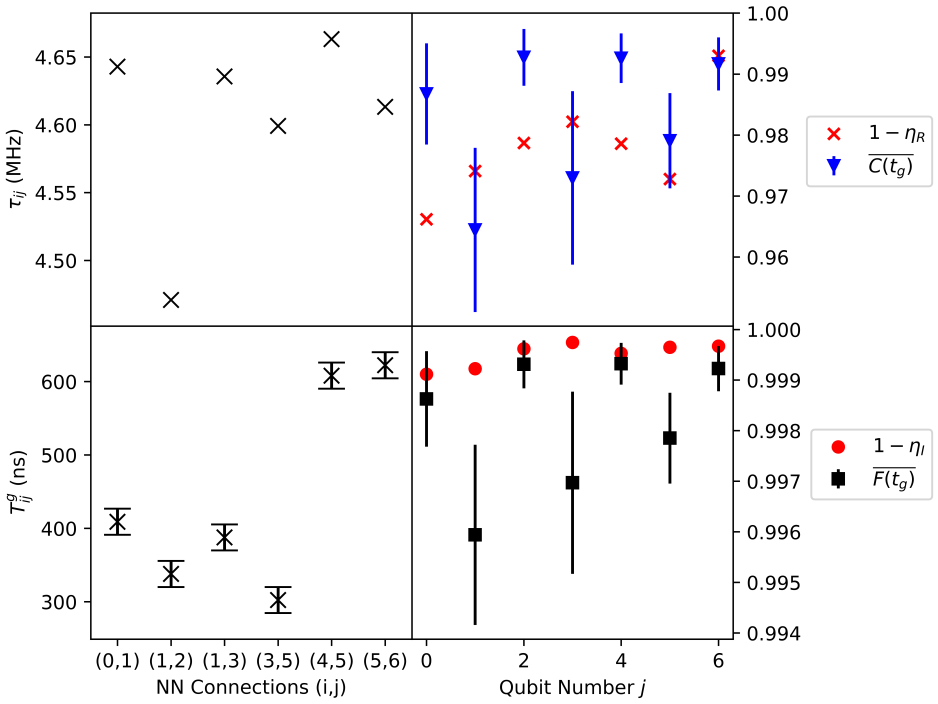

Figure 4.17: Panel **(a)** shows the derived tunnelling rates between nearest neighbour qubits, and **(c)** shows the CNOT gate times as per calibration data retrieved from IBM's Perth device on 08/06/2023. Panel **(b)** shows successful per-qubit readout probabilities (red crosses) and the time-averaged Holevo quantity (blue triangles with error bars). Panel **(d)** shows per-qubit identity fidelities (red circles) and the per-qubit colorred Loschmidt echo (black squares with error bars). Time-averaged quantities are calculated over typical readout times $650-700$ns, which correspond to extremely long gate times. Numerical results calculated for 4 active transmon levels.

order of a hundred microseconds. In the schematic, brighter (darker) node colours correspond to higher (lower) values of the frequencies ω_j. It is mainly the values of ω_j that drive localization in the device.

The main advantage of this architecture is that - after truncating the local Hilbert space to a few levels - the corresponding Hamiltonian admits fast brute-force exact diagonalization. This is important, as readout and gate times of ~ 700ns are difficult to numerically integrate given the high frequencies ω_j. In principle IBM's larger arrays could be accessed by e.g. time-evolving block decimation or other tensor network treatments, but there are more immediate extensions of my treatment that I cover in detail at the end of this section.

To characterize information loss I again invoke the Holevo quantity $C(t)$: the

classical capacity of a quantum channel, as defined in Section 2.1.2. The states $|m_j^{(k)}\rangle$ of the j-th qubit initialized in the k-th input state are initialized in the computational state $m_j^{(k)} \in \{0,1\}$, wherein I assume preparation does not involve the levels above this. I also utilize the simple fidelity between the initial state of each individual qubit and their final states $\rho_j^{(k)}(t) = \mathrm{Tr}_{i\neq j}[|m^{(k)}(t)\rangle]$, obtained by tracing out the qubits $i \neq j$ after unitary time evolution. These two quantities together should intuitively place constraints on two critical characterizing features of IBM's devices: the readout assignment error and the identity fidelity respectively.

The readout assignment error η_R - also referred to as the 'state preparation and measurement' or 'SPAM' error - is the error involved preparing a state then immediately measuring it. It is characterised by averaging the probabilities of preparing the state $|0\rangle$ and measuring it in the state $|1\rangle$, and that of preparing $|1\rangle$ and measuring $|0\rangle$. This is clearly a classical message transmitted via a quantum channel, and hence - if there are absolutely no preparation and measurement errors - its value is limited by the Holevo quantity. More specifically, for each individual qubit, $C(t^R) \geq 1-\eta_R$ where $t^R = 675$ns is the readout length for the Perth device. To determine $C(t^R)$, I average $C(t^R) = \overline{C(t)}$ over the interval $650-700$ns, as high values of the frequencies induce rapid oscillations which cause fast fluctuations in all quantities.

The identity gate error η_I for the j-th qubit is the deviation from unity of the fidelity of that qubit with its initial state after natural evolution over a single gate time t^G. This quantity for the j-th qubit should be bounded by the Loschmidt echo $F(t) = \mathrm{Tr}[\rho_j^{(k)}(t)|m_j^{(k)}\rangle\langle m_j^{(k)}|] = 1-\eta_I$. In real devices, η_I is actually determined via randomized benchmarking [67–71]. I also average $F(t^G) = \overline{F(t)}$ over the interval $650-700$ns which corresponds to extreme gate times; thus the results for $F(t)$ are very conservative - as some gate times are as low as ~ 300ns.

The results of this analysis are shown in Fig. 4.17**(b)** for the time-averaged Holevo quantities $\overline{C(t)}$ and readout errors η_R and Fig. 4.17**(d)** for the time-averaged Loschmidt echo $\overline{F(t)}$ and identity fidelity $1-\eta_I$. Again, η_I and η_R are directly retrieved from the calibration data of IBM's Perth device on 08/06/2023. As expected, in Fig. 4.17**(b)** the readout errors are consistent with the inequality $C(t^R) \geq 1-\eta_R$.

The same cannot be said of Fig. 4.17**(d)**, wherein the inequality $F(t^G) \geq 1 - \eta_I$ is satisfied only be the qubits 0, 2, 4, and 6. In fact in both panels, the values of $\overline{C(t)}$ and $\overline{F(t)}$ for qubits 0, 2, 4, and 6, are significantly higher than the corresponding quantities for the qubits 1, 3, and 5. IBM's data does not reveal a similar structure - with the central qubit 3 actually having the lowest errors η_I and η_R in the entire device. Interestingly, the qubits 0, 2, 4, and 6, are edge qubits: having at most a single nearest-neighbour. This restricts their dynamics and reduces the rate at which information can leak from them. This confluence of this fact with the fact that IBM's data does not have a similar issue suggests several possibilities.

Firstly, IBM may characterize its qubits *individually* by isolating them from the rest of this device. If this is true, then the *actual* errors η_R and η_I that afflict the device during the runtime of a real many-body program may be significantly higher than IBM's characterizations. Secondly, that there exist some meaningful long-distance interactions that the model of Eq. (4.14) doesn't account for. If so, then characterizing these long-distance interactions is necessary as they clearly have an impact on the dynamics of at least the edge qubits over short timescales of a single gate time. Finally, the values of the τ_{ij}, or the way in which they enter into the dynamics of the device, are incorrect - and off by as much as an order of magnitude[10]. This represents a problem for a lot of extant literature and ongoing research, as the interplay between τ_{ij} and the other parameters in Eq. (4.14) is precisely what makes these computers *quantum*. This can be addressed by IBM providing direct characterizations of the τ_{ij} along with the rest of the publicly available device parameters.

The preliminary work of this section can be readily extended by investigating the possible avenues detailed above. Direct extensions also include addressing the larger IBM devices using tensor network treatments, including noise and moving to open-system dynamics to study the interplay between internal information scrambling and information loss to the environment, and incorporating long-range

[10]Indeed, a conversation I had with Oliver Dial - CTO at IBM Quantum - suggests that this may be the case; he suggested values of $\tau_{ij} \sim 1 - 2$MHz as opposed to the value of $\tau_{ij} \geq 5$MHz often cited in literature.

or higher order effects into the model. However, I also mention an interesting idea that warrants further study. The most obvious way by which localization can be strengthened and thus information leakage reduced in the system is by lowering the tunnelling rate relative to some other parameter, e.g. τ_{ij}/ω_j. However, a lower tunnelling rate corresponds to higher gate times - it takes longer to enact two-qubit gates because the interaction that mediates those gates has been reduced in strength. This is an example of the notion of it being 'hard to change the internal state of a localized system' that I discussed in the introductory paragraphs of this section. An interesting question takes the form of balancing these two effects. Higher τ_{ij} mean more information loss, but faster programs, and the burgeoning question of 'balance between localization and chaos' becomes clearer once we view it as an optimization over τ_{ij} for different problems. This may present a potential avenue for optimizing quantum computers on a per-program basis, or as a general informational framework for balancing localization and chaos.

4.4 Outlook

In this chapter, I have investigated informational aspects of various current generation or near-future NISQ devices. These analyses suggest additional ways in which condensed matter and quantum information theory can be connected. Firstly, in Section 4.1, I analysed the dynamics of a one-dimensional lateral array of quantum dots using the von Neumann entropy, number entropy, and conventional imbalance. The objective was to determine whether MBL is accessible in modern QDAs, with model parameters informed by actual experiment in Section 4.1.4. Quantum dot arrays are highly tunable, and thus represent a potentially lucrative testbed for quantum simulation; a detection of MBL would evidence this fact with a concrete case study. Using these quantities I identified a 'frozen' insulating phase which similar to but distinct from MBL. Any identification of MBL in QDAs would require disambiguation from this phase. The findings of Section 4.1.6 show that the number entropy and von Neumann entropy yield similar results, and that - in concert with the imbalance - the number entropy can be used to disambiguate the frozen and

MBL phases. This result persists when considering measurements on only a few sites in the middle of the system. My results for this device altogether suggest that MBL is indeed accessible in near-future quantum dot arrays with only few-site local charge sensing measurements.

Secondly, I consider a twin-rail QDA that realizes an AFHL in Section 4.2. Another potential use of QDAs is the preparation and analysis of ground states. To that end I determine the effect of a diabatic quench on the ground state of the AFHL over a crossover between a two phases. By exploiting the known statistics of singlet-triplet measurement outcomes in an extreme limit, I define a Kullback-Liebler divergence between those statistics and the statistics determined by experiment. I also investigate the fidelity susceptibility which is suspected to act as a general indicator for phase transitions. I find that the divergence yields similar results to the fidelity susceptibility - with both clearly capable of detecting the phase crossover. By incorporating realistic disorder and quench times, again informed by discussions with an experimental group, I find that the divergence remains a useful and manifestly measurable signature of ground state phase transitions in current generation twin-rail QDAs.

Finally, in Section 4.3, I have investigated idle information loss in transmon arrays like those which comprise the architecture of IBM's superconducting quantum computers. Again, my model parameters are all informed by actual characterizations of IBM's Perth device. By invoking the Holevo quantity as introduced in Section 2.1.2 of Chapter 2 and the state fidelity, I quantity how accurately classical information encoded within, and the quantum state of, individual qubits is preserved over gate and readout times. The results of this inquiry place constraints on how much information a transmon-based quantum computer can preserve over time *even when isolated from an environment*. I find that identity fidelities and readout errors are close to these absolute limits, and suggest that IBM's devices (and those similar) can be improved by strategically strengthening the localizing effects that limit this idle information loss. Given the results of this section, I also contend that IBM should provide characterizations of tunnelling rates alongside the other

parameters.

Ultimately, the results of this chapter form case studies for how to apply information-theoretic ideas to realistic modern NISQ devices. These case studies have in turn revealed several interesting features regarding MBL, the statistics of measurement outcomes, and information leakage in modern quantum computers.

References

[1] Rahul Nandkishore and David A. Huse. Many-body localization and thermalization in quantum statistical mechanics. *Annual Review of Condensed Matter Physics*, 6(1):15–38, mar 2015.

[2] Fabien Alet and Nicolas Laflorencie. Many-body localization: An introduction and selected topics. *Comptes Rendus Physique*, 19(6):498–525, sep 2018.

[3] Dmitry A. Abanin and Zlatko Papić. Recent progress in many-body localization. *Ann. Phys. (Leipzig)*, 529(7):1700169, 2017.

[4] Dmitry A. Abanin, Ehud Altman, Immanuel Bloch, and Maksym Serbyn. Colloquium: Many-body localization, thermalization, and entanglement. *Rev. Mod. Phys.*, 91(2):21001, 2019.

[5] Michael Schreiber, Sean S. Hodgman, Pranjal Bordia, Henrik P. Lüschen, Mark H. Fischer, Ronen Vosk, Ehud Altman, Ulrich Schneider, and Immanuel Bloch. Observation of many-body localization of interacting fermions in a quasirandom optical lattice. *Science*, 349(6250):842–845, 2015.

[6] Henrik P. Lüschen, Pranjal Bordia, Sean S. Hodgman, Michael Schreiber, Saubhik Sarkar, Andrew J. Daley, Mark H. Fischer, Ehud Altman, Immanuel Bloch, and Ulrich Schneider. Signatures of many-body localization in a controlled open quantum system. *Physical Review X*, 7(1), Mar 2017.

[7] Jae-yoon Choi, Sebastian Hild, Johannes Zeiher, Peter Schauß, Antonio Rubio-Abadal, Tarik Yefsah, Vedika Khemani, David A Huse, Immanuel

Bloch, and Christian Gross. Exploring the many-body localization transition in two dimensions. *Science*, 352(6293):1547–1552, 2016.

[8] J. Smith, A. Lee, P. Richerme, B. Neyenhuis, P. W. Hess, P. Hauke, M. Heyl, D. A. Huse, and C. Monroe. Many-body localization in a quantum simulator with programmable random disorder. *Nat. Phys.*, 12(10):907–911, 2016.

[9] P. Roushan, C. Neill, J. Tangpanitanon, V. M. Bastidas, A. Megrant, R. Barends, Y. Chen, Z. Chen, B. Chiaro, A. Dunsworth, A. Fowler, B. Foxen, M. Giustina, E. Jeffrey, J. Kelly, E. Lucero, J. Mutus, M. Neeley, C. Quintana, D. Sank, A. Vainsencher, J. Wenner, T. White, H. Neven, D. G. Angelakis, and J. Martinis. Spectroscopic signatures of localization with interacting photons in superconducting qubits. *Science*, 358(6367):1175–1179, 2017.

[10] T. Hensgens, T. Fujita, L. Janssen, Xiao Li, C. J. Van Diepen, C. Reichl, W. Wegscheider, S. Das Sarma, and L. M. K. Vandersypen. Quantum simulation of a fermi–hubbard model using a semiconductor quantum dot array. *Nature*, 548(7665):70–73, aug 2017.

[11] Uditendu Mukhopadhyay, Juan Pablo Dehollain, Christian Reichl, Werner Wegscheider, and Lieven MK Vandersypen. A $2\times$ 2 quantum dot array with controllable inter-dot tunnel couplings. *Applied Physics Letters*, 112(18):183505, 2018.

[12] R. K. Panda, A. Scardicchio, M. Schulz, S. R. Taylor, and M. Žnidarič. Can we study the many-body localisation transition? *EPL*, 128(6):40–42, 2019.

[13] Piotr Sierant and J Zakrzewski. Can we observe the many-body localization? *arXiv preprint arXiv:2109.13608*, 2021.

[14] Piotr Sierant and Jakub Zakrzewski. Challenges to observation of many-body localization. *Phys. Rev. B*, 105:224203, Jun 2022.

[15] Vedika Khemani, D. N. Sheng, and David A. Huse. Two universality classes

for the many-body localization transition. *Phys. Rev. Lett.*, 119:075702, Aug 2017.

[16] G Jaliel and C Smith. Private Communication.

[17] Alexander Nico-Katz, Gulzat Jaliel, Paola Atkinson, Thomas A Mitchell, David A Ritchie, Charles G Smith, and Sougato Bose. Identifying many-body localization in realistic dot arrays. *arXiv preprint arXiv:2301.08246*, 2023.

[18] Dieter Bimberg, Marius Grundmann, and Nikolai N Ledentsov. *Quantum dot heterostructures*. John Wiley & Sons, 1999.

[19] Marc A Kastner, Olivier Klein, Theodore M Lyszczarz, Paul M Mankiewich, David C Shaver, Shalom Wind, David Abusch-Magder, David J Goldhaber-Gordon, and Nicole Y Morgan. Artificial atoms. Technical report, Research Laboratory of Electronics (RLE) at the Massachusetts Institute of . . . , 1994.

[20] W. G. van der Wiel, S. De Franceschi, J. M. Elzerman, T. Fujisawa, S. Tarucha, and L. P. Kouwenhoven. Electron transport through double quantum dots. *Rev. Mod. Phys.*, 75:1–22, Dec 2002.

[21] Toivo Hensgens. *Emulating Fermi-Hubbard physics with quantum dots: from few to more and how to*. PhD thesis, Delft University of Technology, 2018. Casimir PhD series 2017-47.

[22] Song Yang, Abolfazl Bayat, and Sougato Bose. Entanglement-enhanced information transfer through strongly correlated systems and its application to optical lattices. *Phys. Rev. A*, 84:020302, Aug 2011.

[23] R. Hanson, L. P. Kouwenhoven, J. R. Petta, S. Tarucha, and L. M. K. Vandersypen. Spins in few-electron quantum dots. *Rev. Mod. Phys.*, 79:1217–1265, Oct 2007.

[24] Leo P Kouwenhoven, DG Austing, and Seigo Tarucha. Few-electron quantum dots. *Reports on Progress in Physics*, 64(6):701, 2001.

[25] P. W. Anderson. Absence of diffusion in certain random lattices. *Phys. Rev.*, 109:1492–1505, Mar 1958.

[26] John Canny. A computational approach to edge detection. *IEEE Transactions on Pattern Analysis and Machine Intelligence*, PAMI-8(6):679–698, 1986.

[27] Xin Wang, Shuo Yang, and S. Das Sarma. Quantum theory of the charge-stability diagram of semiconductor double-quantum-dot systems. *Phys. Rev. B*, 84:115301, Sep 2011.

[28] Zhan Shi, C. B. Simmons, Daniel R. Ward, J. R. Prance, R. T. Mohr, Teck Seng Koh, John King Gamble, Xian Wu, D. E. Savage, M. G. Lagally, Mark Friesen, S. N. Coppersmith, and M. A. Eriksson. Coherent quantum oscillations and echo measurements of a si charge qubit. *Phys. Rev. B*, 88:075416, Aug 2013.

[29] Bao-Chuan Wang, Bao-Bao Chen, Gang Cao, Hai-Ou Li, Ming Xiao, and Guo-Ping Guo. Coherent control and charge echo in a gaas charge qubit. *Europhysics Letters*, 117(5):57006, may 2017.

[30] F. R. Braakman, P. Barthelemy, C. Reichl, W. Wegscheider, and L. M. K. Vandersypen. Long-distance coherent coupling in a quantum dot array. *Nature Nanotechnology*, 8(6):432–437, Jun 2013.

[31] M. Field, C. G. Smith, M. Pepper, D. A. Ritchie, J. E. F. Frost, G. A. C. Jones, and D. G. Hasko. Measurements of coulomb blockade with a noninvasive voltage probe. *Phys. Rev. Lett.*, 70:1311–1314, Mar 1993.

[32] C. Volk, A. M. J. Zwerver, U. Mukhopadhyay, P. T. Eendebak, C. J. van Diepen, J. P. Dehollain, T. Hensgens, T. Fujita, C. Reichl, W. Wegscheider, and L. M. K. Vandersypen. Loading a quantum-dot based "qubyte" register. *npj Quantum Information*, 5, apr 2019.

[33] T. Hayashi, T. Fujisawa, H. D. Cheong, Y. H. Jeong, and Y. Hirayama. Coherent manipulation of electronic states in a double quantum dot. *Phys. Rev. Lett.*, 91:226804, Nov 2003.

[34] K. D. Petersson, J. R. Petta, H. Lu, and A. C. Gossard. Quantum coherence in a one-electron semiconductor charge qubit. *Phys. Rev. Lett.*, 105:246804, Dec 2010.

[35] J. Gorman, D. G. Hasko, and D. A. Williams. Charge-qubit operation of an isolated double quantum dot. *Phys. Rev. Lett.*, 95:090502, Aug 2005.

[36] J. R. Petta, A. C. Johnson, J. M. Taylor, E. A. Laird, A. Yacoby, M. D. Lukin, C. M. Marcus, M. P. Hanson, and A. C. Gossard. Coherent manipulation of coupled electron spins in semiconductor quantum dots. *Science*, 309(5744):2180–2184, 2005.

[37] Hendrik Bluhm, Sandra Foletti, Izhar Neder, Mark Rudner, Diana Mahalu, Vladimir Umansky, and Amir Yacoby. Dephasing time of gaas electron-spin qubits coupled to a nuclear bath exceeding 200 μs. *Nature Physics*, 7(2):109–113, Feb 2011.

[38] Erika Kawakami, Thibaut Jullien, Pasquale Scarlino, Daniel R. Ward, Donald E. Savage, Max G. Lagally, Viatcheslav V. Dobrovitski, Mark Friesen, Susan N. Coppersmith, Mark A. Eriksson, and Lieven M. K. Vandersypen. Gate fidelity and coherence of an electron spin in an si/SiGe quantum dot with micromagnet. *Proceedings of the National Academy of Sciences*, 113(42):11738–11743, oct 2016.

[39] Jens H. Bardarson, Frank Pollmann, and Joel E. Moore. Unbounded growth of entanglement in models of many-body localization. *Phys. Rev. Lett.*, 109:017202, Jul 2012.

[40] Maksym Serbyn, Z. Papić, and Dmitry A. Abanin. Universal slow growth of entanglement in interacting strongly disordered systems. *Phys. Rev. Lett.*, 110:260601, Jun 2013.

[41] Kai Xu, Jin Jun Chen, Yu Zeng, Yu Ran Zhang, Chao Song, Wuxin Liu, Qiujiang Guo, Pengfei Zhang, Da Xu, Hui Deng, Keqiang Huang, H. Wang,

Xiaobo Zhu, Dongning Zheng, and Heng Fan. Emulating Many-Body Localization with a Superconducting Quantum Processor. *Phys. Rev. Lett.*, 120(5):050507, 2018.

[42] Alexander Lukin, Matthew Rispoli, Robert Schittko, M. Eric Tai, Adam M. Kaufman, Soonwon Choi, Vedika Khemani, Julian Léonard, and Markus Greiner. Probing entanglement in a many-body-localized system. *Science*, 364(6437):256–260, 2019.

[43] Rozhin Yousefjani, Sougato Bose, and Abolfazl Bayat. Non-algebraic entanglement growth in long-range many-body localized systems. *arXiv preprint arXiv:2201.03716*, 2022.

[44] David J. Luitz, Nicolas Laflorencie, and Fabien Alet. Extended slow dynamical regime close to the many-body localization transition. *Phys. Rev. B*, 93(6):060201, 2016.

[45] Pranjal Bordia, Henrik Lüschen, Sebastian Scherg, Sarang Gopalakrishnan, Michael Knap, Ulrich Schneider, and Immanuel Bloch. Probing slow relaxation and many-body localization in two-dimensional quasiperiodic systems. *Phys. Rev. X*, 7(4):041047, 2017.

[46] Henrik P. Lüschen, Pranjal Bordia, Sebastian Scherg, Fabien Alet, Ehud Altman, Ulrich Schneider, and Immanuel Bloch. Observation of slow dynamics near the many-body localization transition in one-dimensional quasiperiodic systems. *Phys. Rev. Lett.*, 119:260401, Dec 2017.

[47] Maximilian Kiefer-Emmanouilidis, Razmik Unanyan, Michael Fleischhauer, and Jesko Sirker. Evidence for unbounded growth of the number entropy in many-body localized phases. *Physical Review Letters*, 124(24), jun 2020.

[48] Roopayan Ghosh and Marko Žnidarič. Resonance-induced growth of number entropy in strongly disordered systems. *Phys. Rev. B*, 105:144203, Apr 2022.

[49] Luca D'Alessio, Yariv Kafri, Anatoli Polkovnikov, and Marcos Rigol. From quantum chaos and eigenstate thermalization to statistical mechanics and thermodynamics. *Advances in Physics*, 65(3):239–362, May 2016.

[50] Don N. Page. Average entropy of a subsystem. *Physical Review Letters*, 71(9):1291–1294, aug 1993.

[51] Cheng-Ju Lin and Olexei I Motrunich. Exact quantum many-body scar states in the rydberg-blockaded atom chain. *Physical review letters*, 122(17):173401, 2019.

[52] Hannes Bernien, Sylvain Schwartz, Alexander Keesling, Harry Levine, Ahmed Omran, Hannes Pichler, Soonwon Choi, Alexander S. Zibrov, Manuel Endres, Markus Greiner, Vladan Vuletić, and Mikhail D. Lukin. Probing many-body dynamics on a 51-atom quantum simulator. *Nature*, 551(7682):579–584, Nov 2017.

[53] Vedika Khemani, Chris R Laumann, and Anushya Chandran. Signatures of integrability in the dynamics of rydberg-blockaded chains. *Physical Review B*, 99(16):161101, 2019.

[54] LMK Vandersypen, H Bluhm, JS Clarke, AS Dzurak, R Ishihara, A Morello, DJ Reilly, LR Schreiber, and M Veldhorst. Interfacing spin qubits in quantum dots and donors—hot, dense, and coherent. *npj Quantum Information*, 3(1):34, 2017.

[55] L Vandersypen, L Morozova, and X Zhang. Private Communication.

[56] Steven R White. Equivalence of the antiferromagnetic heisenberg ladder to a single s= 1 chain. *Physical Review B*, 53(1):52, 1996.

[57] F Duncan M Haldane. Continuum dynamics of the 1-d heisenberg antiferromagnet: Identification with the o (3) nonlinear sigma model. *Physics letters a*, 93(9):464–468, 1983.

[58] Li-Hua Pan and Chang-De Gong. A note on haldane's conjecture. *Journal of Physics: Condensed Matter*, 20(21):215232, apr 2008.

[59] Johnnie Gray, Abolfazl Bayat, Reuben K. Puddy, Charles G. Smith, and Sougato Bose. Unravelling quantum dot array simulators via singlet-triplet measurements. *Phys. Rev. B*, 94:195136, Nov 2016.

[60] Lei Wang, Ye-Hua Liu, Jakub Imriš ka, Ping Nang Ma, and Matthias Troyer. Fidelity susceptibility made simple: A unified quantum monte carlo approach. *Physical Review X*, 5(3), jul 2015.

[61] Xingjian He, Rozhin Yousefjani, and Abolfazl Bayat. Stark localization as a resource for weak-field sensing with super-heisenberg precision, 2023.

[62] Christoph Berke, Evangelos Varvelis, Simon Trebst, Alexander Altland, and David P. DiVincenzo. Transmon platform for quantum computing challenged by chaotic fluctuations. *Nature Communications*, 13(1), may 2022.

[63] Joachim Cohen, Alexandru Petrescu, Ross Shillito, and Alexandre Blais. Reminiscence of classical chaos in driven transmons. *PRX Quantum*, 4(2):020312, 2023.

[64] J Goold and S Dooley. Private Communication.

[65] Jens Koch, Terri M. Yu, Jay Gambetta, A. A. Houck, D. I. Schuster, J. Majer, Alexandre Blais, M. H. Devoret, S. M. Girvin, and R. J. Schoelkopf. Charge-insensitive qubit design derived from the cooper pair box. *Phys. Rev. A*, 76:042319, Oct 2007.

[66] Simon-Dominik Börner, Christoph Berke, David P DiVincenzo, Simon Trebst, and Alexander Altland. Classical chaos in quantum computers. *arXiv preprint arXiv:2304.14435*, 2023.

[67] Emanuel Knill, Dietrich Leibfried, Rolf Reichle, Joe Britton, R Brad Blakestad, John D Jost, Chris Langer, Roee Ozeri, Signe Seidelin, and David J

Wineland. Randomized benchmarking of quantum gates. *Physical Review A*, 77(1):012307, 2008.

[68] Easwar Magesan, Jay M Gambetta, and Joseph Emerson. Scalable and robust randomized benchmarking of quantum processes. *Physical review letters*, 106(18):180504, 2011.

[69] Easwar Magesan, Jay M Gambetta, and Joseph Emerson. Characterizing quantum gates via randomized benchmarking. *Physical Review A*, 85(4):042311, 2012.

[70] Timothy Proctor, Kenneth Rudinger, Kevin Young, Mohan Sarovar, and Robin Blume-Kohout. What randomized benchmarking actually measures. *Physical review letters*, 119(13):130502, 2017.

[71] Jonas Helsen, Ingo Roth, Emilio Onorati, Albert H Werner, and Jens Eisert. General framework for randomized benchmarking. *PRX Quantum*, 3(2):020357, 2022.

Chapter 5

Conclusions and Outlook

"It is good to see that in the end, when all is said and done – love prevails."

— bell hooks

"You're Sougato's new student? Welcome to the family!"

— Anonymous
Said to me by a stranger,
whose name I have forgotten,
on my first day as a physicist.

In this thesis, I have forged several new interdisciplinary connections between the fields of quantum information theory and condensed matter physics. These connections have, in turn, yielded insight into how information in many-body quantum systems can be stored, tracked, manipulated, and lost.

The work of Chapter 2 places the notion of memory in many-body quantum systems on a firm quantitative footing. Whereas memory has heretofore been probed implicitly, my provision of a set of criteria, a few exemplary quantifiers of memory, and concrete case studies in non-ergodic MBL and scarred settings respectively, lay the groundwork for future investigation of memory effects. This work also sheds some light on the potential structure of the MBL phase. Future research in this field could involve a more detailed examination of memory in non-ergodic systems: now that we know information can be *stored* in these systems, can

it be *manipulated*. This could pave the way for the integration of condensed matter systems into existing quantum computational architectures.

Chapter 3 exploits the idea of compression that is latent in the matrix product state representation of many-body quantum state. I use this to develop a novel geometric measure of entanglement in many-body quantum which is highly successful at detecting ground state phase boundaries. By investigating the ergodic-MBL transition, I also find it to be a valuable tool in analysing phase transitions that occur across the whole spectrum. Interpreting this measure as a quantification of entanglement-complexity, my work demonstrates its value in condensed matter systems where ground states may not be separable but still have simple area-law entanglement structures. This work represents a step forward in terms of which tools are available to the theoretical physics community when probing unknown ground state phase diagrams. Future work could delve deeper into compressability, the tensor network description of quantum states may admit e.g. information bottleneck bounds which limit how easily certain states can be compressed and decompressed using a fixed network. Not only would such an analysis yield more insight into tensor networks themselves, but it could lead to advanced quantum compression algorithms - quantum versions of the algorithms that laid the foundation for modern computation.

The concluding Chapter 4 addresses informational aspects of realistic current or near-future NISQ devices. The work in this section reveals an insulating phase of matter in quantum dot arrays, and exploits information-theoretic quantities to differentiate this phase from MBL. This paves the way for near-future detection of MBL in quantum dot arrays using local charge sensing measurements. I also examine twin-rail quantum dot arrays realizing an antiferromagnetic Heisenberg ladder; revealing that by exploiting the Kullback-Liebler divergence, an experimentally accessible probe of ground state crossovers in the array can be constructed. Additional numerical evidence suggests that the preparation of ground states and the probing of ground state crossovers is a realistic possibility in current generation quantum dot arrays. Finally I examine information loss in transmon arrays which simulate the

natural underlying dynamics of IBM's superconducting quantum computers. This examination reveals that internal idle information loss - where information is not lost to the environment, but instead becomes distributed non-locally - is significant. This kind of idle information loss would occur even if the device were fully isolated from the environment, and so characterizing it provides an upper limit on how reliable these devices are. The sum total of the results of this chapter demonstrates the value of the informational approach in practical, realistic, experimental settings. Future work could include more detailed analysis of information loss in quantum computers, as well as potentially novel error-correcting codes that exploit the precise features of the underlying many-body quantum dynamics of the device.

Ultimately, this thesis has taken the form of fugues: varied related investigations surrounding the same broad themes that connect condensed matter and quantum information theory. Themes of memory, compression, probability, the non-local distribution of information, and information leakage. Taken in concert, the results of this thesis paint a picture of how to reliably analyze the flow of information in condensed matter systems, and present concrete case studies in how to do so. The concluding exploratory parts of each chapter demonstrate how rich and full of additional questions these themes are. With quantum computers still in their infancy, and the many-body quantum frontier as wide and exciting as ever; the nature and role of information in these systems seems, to me, increasingly relevant. My concluding contention is simple: to talk about information in condensed matter systems requires us to reach beyond the basic language of correlation functions, von Neumann entropies, and OTOCs. To paraphrase Claude Shannon for the final time: how much richer a source is Finnegan's Wake than Basic English [1]. And how much richer then must the informational universe be than the small fragment that I have studied here.

References

[1] Claude Elwood Shannon. A mathematical theory of communication. *The Bell system technical journal*, 27(3):379–423, 1948.

Appendices

A Derivation of the Hierarchy of Memory Quantifiers

Here I derive the first two inequalities in the memory hierarchy $1-\overline{S(t)} \geq \overline{C(t)} \geq \overline{I_c(t)} \geq \overline{I_s(t)}$ discussed in Section 2.2.3. I also discuss a few technical nuances and justifications for the construction of $\overline{I_s(t)}$. I derive the inequalities for a single ensemble of initial probabilities $\{p_k\}$ and final quantum states $\{\rho^{(k)}(t)\}$. Clearly, if it holds for each individual ensemble, it holds for the disorder and environment (channel) average over those ensembles as well. I denote each quantity for a single channel realization using the index r, e.g. $\overline{S(t)} = \frac{1}{N_r}\sum_r S^r(t)$ where N_r is the number of samples. I suppress this index on the density operators $\rho^{(k)}(t)$ themselves for readability. Thus, the hierarchy derived here for the largest three quantities is *stricter* than that stated in the main text: $1-S^r(t) \geq C^r(t) \geq I_c^r(t)$.

The first inequality $1-S^r(t) \geq C^r(t)$ trivially follows from the definition of the normalized von Neumann entropy over the ensemble:

$$S^r(t) = \frac{1}{l}\sum_k p_k S(\rho^{(k)}(t)) \tag{1}$$

where $S(\rho) = -\mathrm{Tr}\rho\log_2\rho$; and the definition of the Holevo quantity:

$$C^r(t) = \frac{1}{l}S\left(\sum_k p_k \rho^{(k)}(t)\right) - \frac{1}{l}\sum_k p_k S(\rho^{(k)}(t)). \tag{2}$$

By taking the difference of the two quantities $\Delta^r_{SC}(t)$ and noting that the second term

in the Holevo quantity is just $S^r(t)$, it follows:

$$\Delta^r_{SC}(t) = 1 - S^r(t) - C^r(t) = 1 - \frac{1}{l} S\left(\sum_k p_k \rho^{(k)}(t)\right) \tag{3}$$

where the second term clearly saturates to its maximum value of unity as $\sum_k p_k \rho^{(k)}(t)$ approaches the identity. As such $\Delta^r_{SC}(t) \geq 0$ and the inequality $1 - S^r(t) \geq C^r(t)$ follows. This provides an intuitive understanding of the Holevo quantity as a modification to $1 - S^r(t)$; accounting for how much information is *accessible* at time t rather than how useful the $\rho^{(k)}(t)$ are as an instantaneous alphabet.

The derivation of the second inequality is slightly more involved, first requiring that the CMI $I^r_c(t)$ is shown to be a fully decohered version of the Holevo quantity $C^r(t)$. This is covered in the discussion and derivation preceding Eq. (2.24) in the main text, but I will repeat it here for completeness. I will carry out the derivation in the computational basis, but in principle any suitable basis can be used instead. In the computational basis, and given the $\{p_k\}$ *a priori*, the joint probability $p(k,k',t)$ of sending the state k and measuring the state k' at time t is determined entirely by the diagonal elements of $\rho^{(k)}(t)$:

$$p(k,k',t) = p_k \rho^{(k)}_{k'k'}(t) \tag{4}$$

the classical mutual information can be then computed according to the well-known formula

$$I^r_c(t) = \frac{1}{l} \sum_{kk'} p(k,k',t) \log_2 \frac{p(k,k',t)}{\sum_s p(k,s,t) \sum_{s'} p(s',k',t)} \tag{5}$$

where the first marginal distribution $\sum_s p(k,s,t)$ resolves trivially to p_k by the unit-trace condition (see Eq. (4)). The second marginal distribution $\sum_{s'} p(s',k',t)$ involves all message states and is generally non-trivial. Evaluating the first marginal

distribution, splitting up the logarithm, and cancelling relevant terms yields:

$$\begin{aligned} I_c^r(t) =& \frac{1}{l}\sum_{kk'} p_k \rho_{k'k'}^{(k)}(t) \log_2 \rho_{k'k'}^{(k)}(t) \\ & - \frac{1}{l}\sum_{kk'} p_k \rho_{k'k'}^{(k)}(t) \log_2 \sum_{s'} p_{s'} \rho_{k'k'}^{(s')}(t) \end{aligned}$$

where I note that, by constructing an operator with the $\rho_{k'k'}^{(k)}(t)$ as eigenvalues, the sums over k' can be replaced with appropriate traces and some terms will take the form of von Neumann entropies. A naturally suitable operator is the fully decohered (in the computational basis) operator $\rho_D^{(k)}(t)$, defined as the leading diagonal of $\rho^{(k)}(t)$:

$$\rho^{(k)}(t) \;\rightarrow\; \rho_D^{(k)}(t) = \mathrm{diag}\left(\rho_{11}^{(k)}(t), \rho_{22}^{(k)}(t), \cdots, \rho_{2^l 2^l}^{(k)}(t)\right) \tag{6}$$

which trivially has the $\rho_{k'k'}^{(k)}(t)$ as eigenvalues. I can then recast $I_c^r(t)$ in terms of traces as follows:

$$\begin{aligned} I_c^r(t) =& \frac{1}{l}\sum_{k} p_k \mathrm{Tr}\left[\rho_D^{(k)}(t) \log_2 \rho_D^{(k)}(t)\right] \\ & - \frac{1}{l}\mathrm{Tr}\left[\left(\sum_k p_k \rho_D^{(k)}(t)\right) \log_2 \left(\sum_s p_s \rho_D^{(s)}(t)\right)\right] \end{aligned}$$

which, when rewritten in terms of the von Neumann entropy $S(\rho) = -\mathrm{Tr}\rho\log_2\rho$, yields the Holevo quantity over decohered states $\rho_D^{(k)}(t)$:

$$I_c^r(t) = \frac{1}{l} S\left(\sum_k p_k \rho_D^{(k)}(t)\right) - \frac{1}{l}\sum_k p_k S(\rho_D^{(k)}(t)). \tag{7}$$

demonstrating, by analogy to Eq. (2), that the configurational mutual information is just the Holevo quantity with all states fully decohered in the computational basis. Though I have chosen the computational basis for the derivation, any suitable (orthonormal) basis can be used. One can intuit that different choices of basis yield different diagonal elements in the $\rho_D^{(k)}(t)$, and act as effective modifications to the eigenvalues of all the $\rho^{(k)}(t)$ at once. The Holevo quantity is 'optimal' in the sense that it uses the true eigenvalues of the $\rho^{(k)}(t)$, equivalent to performing measure-

ments in the eigenbasis of each individual $\rho^{(k)}(t)$.

I now derive the second strict inequality $C^r(t) \geq I_c^r(t)$ by defining the difference:

$$l\Delta_{CI}^r(t) = lC^r(t) - lI_c^r(t) \tag{8}$$

where I have multiplied by l to suppress the normalization constants and avoid notational clutter in the derivation to come. Inserting the Holevo quantity of Eq. (2) and the dephased Holevo form of the CMI of Eq. (7), and fully expanding the von Neumman entropies yields:

$$\begin{aligned} l\Delta_{CI}^r(t) = &- \mathrm{Tr}\left[\left(\sum_k p_k \rho^{(k)}(t)\right) \log_2 \left(\sum_k p_k \rho^{(k)}(t)\right)\right] \\ &+ \sum_k p_k \mathrm{Tr}\left[\rho^{(k)}(t) \log_2 \rho^{(k)}(t)\right] \\ &+ \mathrm{Tr}\left[\left(\sum_k p_k \rho_D^{(k)}(t)\right) \log_2 \left(\sum_k p_k \rho_D^{(k)}(t)\right)\right] \\ &- \sum_k p_k \mathrm{Tr}\left[\rho_D^{(k)}(t) \log_2 \rho_D^{(k)}(t)\right]. \end{aligned}$$

I now remark that the operators $\log_2 \rho_D^{(k)}(t)$ and $\log_2 \sum_k p_k \rho_D^{(k)}(t)$ are diagonal by definition, so any matrix multiplication between them and another operator will only involve the diagonal elements of both. Thus, all the $\rho_D^{(k)}(t)$ *outside* those logarithms can be replaced by the corresponding original operators $\rho^{(k)}(t)$. I perform this replacement, collect like terms, and manipulate $l\Delta_{CI}^r(t)$ into a revealing form:

$$\begin{aligned} l\Delta_{CI}^r(t) = &- \mathrm{Tr}\left[\left(\sum_k p_k \rho^{(k)}(t)\right)\left(\log_2 \left(\sum_k p_k \rho^{(k)}(t)\right) - \log_2 \left(\sum_k p_k \rho_D^{(k)}(t)\right)\right)\right] \\ &+ \sum_k p_k \mathrm{Tr}\left[\rho^{(k)}(t)\left(\log \rho^{(k)}(t) - \log \rho_D^{(k)}(t)\right)\right] \end{aligned}$$

in which both terms clearly take the form of quantum relative entropies $S(\rho||\sigma) = \mathrm{Tr}[\rho(\log_2 \rho - \log_2 \sigma)]$. Explicitly, one can rewrite $\Delta_{CI}^r(t)$ as follows (re-introducing

the normalization factor):

$$\Delta^r_{CI}(t) = -\frac{1}{l} S\left(\sum_k p_k \rho^{(k)}(t) \,\middle\|\, \sum_k p_k \rho^{(k)}_D(t)\right) + \frac{1}{l}\sum_k p_k S\left(\rho^{(k)}(t) \,\middle\|\, \rho^{(k)}_D(t)\right)$$

in which, by the joint convexity of the quantum relative entropy, the second term is greater than or equal to the first. As such, $\Delta^r_{CI}(t) \geq 0$ and the Holevo quantity upper bounds the CMI $C^r(t) \geq I^r_c(t)$. This can be understood in two highly intuitive ways: (i) the CMI is 'suboptimal' with respect to the Holevo quantity in the sense that it uses a single, fixed, measurement basis (ii) decoherence and measurements cannot increase the information accessible in a system.

I conclude with a brief discussion of the single-site mutual information (SSMI) $\overline{I_s(t)}$. The final inequality $\overline{I_c(t)} \geq \overline{I_s(t)}$ can be intuitively understood as follows: the SSMI is constructed using repeated partial traces and projections on the systems used in the construction of the CMI. Such operations cannot increase the information in a system, and so we expect the CMI to systematically upper-bound the SSMI. This has been convincingly verified numerically in Section 2.2.4. Finally, in the definition of the SSMI in Eq. (2.16), I average over individual sites and messages in an order that may appear arbitrary: taking the site average at the level of individual probabilities, and the message average at the level of disorder/environment (channel) averaging. My justifications follow four ideas: (i) an average must be taken, without averaging the protocol sends a single message with probability unity, and as such cannot bear information. This can be verified by inspection of the definition of $\overline{I_s(t)}$ in the main text (ii) For a given site, the rest of the message forms part of the environment (iii) I define the SSMI analogously to the conventional imbalance which averages over each site per realization (iv) results (not shown) for taking the combined order - with both site and message averaging at the level of individual probabilities - yield no scaling results, and show an overall decrease in informational content with increasing system size; indicating that this decoding protocol is essentially useless.

B Diagrammatic Tensor Notation

Diagrammatic tensor notation, alternatively named Penrose notation for its originator Roger Penrose in Ref. [1], is a visual depiction of tensors and tensor networks. The mathematical rules of tensor manipulation have corresponding diagrammatic representations and so the tedious process of calculation and tally-keeping of indices is abstracted away into doodles that are readable at a glance.

The basic object, the tensor itself, is represented as a blob with legs attached: each leg corresponds to an index of that tensor. Legs going up correspond to contravariant indices (up indices), and legs going down correspond to covariant indices (down indices); though this is often ignored for indices that are contracted over or in situations where the difference is irrelevant. The tensor $A^{\mu}_{\nu\eta}$ for example is shown in panel **a)** of Fig. B.1. Contractions over pairs of indices are drawn simply by connecting the indices in question; the tensor network $B^{\mu}_{\nu}C^{\eta}_{\mu}$ for example is shown in panel **b)** of Fig. B.1.

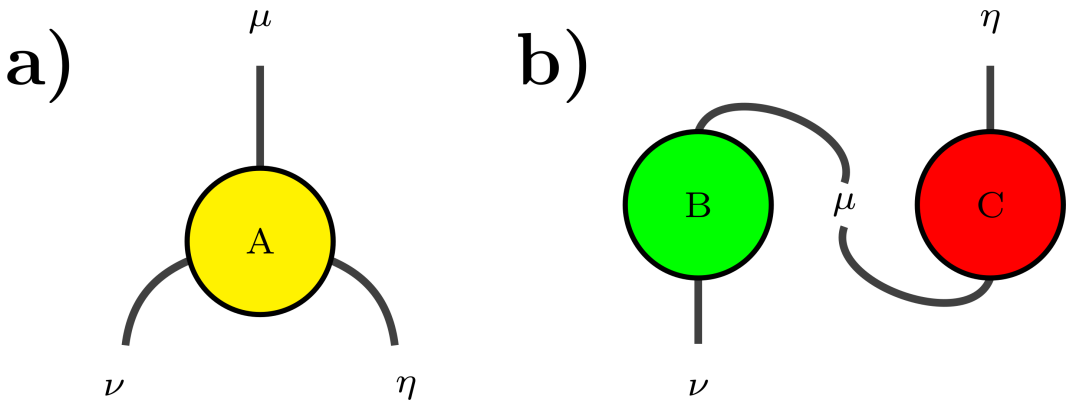

Figure B.1: Schematics showing the basics of diagrammatic 'Penrose' notation for tensor networks. Panel **a)** shows the diagrammatic representation of the tensor $A^{\mu}_{\nu\mu}$, and **b)** shows the diagrammatic representation of the contraction $B^{\mu}_{\nu}C^{\eta}_{\mu}$.

The standard tensor manipulations then become simple diagrammatic tricks. For example, raising or lowering an index via the metric tensor corresponds to extending the corresponding leg until it points upwards or downwards. More complicated algorithms can also be readily represented, consider the singular value decomposition of Eq. (3.4) (in which I have omitted any notion of upper or lower indices), which has been drawn diagrammatically in Fig. B.2. Note that the contraction over

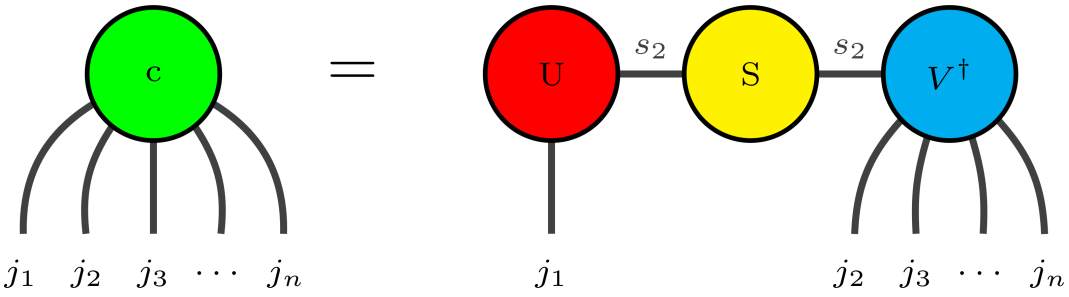

Figure B.2: A diagrammatic version of the singular value decomposition of Eq. (3.4).

the single index s_2 is represented by two contractions over the same index s_2 going into and out of S, this can be understood either as equivalent to the promotion of S to a diagonal tensor of increased rank, or as notational convenience in representing a contraction over three indices.

C The Constant Interaction Model and Semi-Classical Conductor Networks

The celebrated constant interaction model is the de facto starting point for analyses of quantum dot systems. The two core assumptions of the constant interaction model are as follows: (i) the quantized energy levels are unaffected by, and manifest as simple energetic contributions to, the classical Coulomb interactions between electrons. It is in this sense that the model is semi-classical. (ii) the Coulomb interactions between a single electron on the j-th dot and all other electrons in the system are parametrized by a constant capacitance c_j [2]. We can thus determine the ground state properties of the classical ($t = 0$) dot array by considering the electrostatics problem of minimizing the total energy of a network of capacitively coupled conductors.

I consider just such a network of N classical conductors henceforth, with each conductor capacitively coupled to all the others and to ground. These conductors each describe a single conducting element of the *entire* quantum dot system: gates, leads, and dots. At electrostatic equilibrium, the charge Q_j on a given conductor j

must be balanced with the charge in every capacitor to which it is coupled:

$$Q_j = \sum_{k=0}^{N} c_{jk}(V_j - V_k) \tag{9}$$

where c_{jk} is the capacitive coupling between conductors j and k, and where V_j is the electric potential on the j-th conductor. I fix $V_0 = 0$ as the potential of the ground $j = 0$. One can see quite clearly that Eq. (9) is some weighted linear sum of the potentials V_j where the weights can be extracted by explicitly separating the potential differences and the $k = j$ terms:

$$Q_j = c_j j \underbrace{(V_j - V_j)}_{=0} + \left(\sum_{\substack{k=0 \\ k\neq j}}^{N} c_{jk} \right) V_j - \sum_{\substack{k=0 \\ k\neq j}}^{N} c_{jk} V_k \tag{10}$$

$$= c_j V_j - \sum_{\substack{k=0 \\ k\neq j}}^{N} c_{jk} V_k \tag{11}$$

where I have defined $c_j = \sum_{k=0,k\neq j}^{N} c_{jk}$. This c_j is a constant for each conductor in the network, and is the eponymous 'constant' capacitance discussed in the opening paragraph of this section. We can now rewrite Eq. (9) as a matrix equation:

$$\vec{Q} = C\vec{V} \tag{12}$$

where the elements of the vectors $\vec{Q}$ and $\vec{V}$ are the Q_j and V_j as defined above. The elements of the matrix C are given by Eq. (11) with diagonal elements c_j and off-diagonal elements $-c_{jk}$. Finally, the total electrostatic energy U of this network is given by the sum of the electrostatic energies U_j of each individual node:

$$U_j = \frac{1}{2} \sum_{k=0}^{N} c_{jk}(V_j - V_k)^2 \tag{13}$$

in the expansion of the squared binomial $(V_j - V_k)^2$, one can notice that $k = j$ terms are zero and that cross terms of the form $V_j V_k$ cancel as we evaluate the sum over all N nodes. This leaves us exclusively with terms proportional to the V_j^2, and by

a similar method as employed in Eq. (11) gives us a familiar equation for the total electrostatic energy U:

$$U = \vec{V} \cdot C\vec{V} = \vec{Q} \cdot C^{-1}\vec{Q} \tag{14}$$

where the final step follows from Eq. (12) and the commutativity of the dot product. In a physical quantum dot array, we can assuredly characterise all the relevant capacitances; though the other quantities are not necessarily all known. The potentials of voltage sources such as plunger and barrier gates are well-controlled, but the charge on each dot is given by a self-consistent electrostatics problem involving these controlled voltages. I henceforth call the nodes with known applied voltages 'voltage sources' and all other nodes 'charge nodes'. The incorporation of such a voltage source essentially corresponds to a node with a large charge on it $Q_j \to \infty$ and an equivalently large capacitive coupling to ground $C_0 \to \infty$ such that $V_j \to Q_j/C_0$ is fixed. We can then reformulate Eq. (12) as:

$$\begin{bmatrix} \vec{Q}_c \\ \vec{Q}_v \end{bmatrix} = \begin{pmatrix} C_{cc} & C_{cv} \\ C_{vc} & C_{vv} \end{pmatrix} \begin{bmatrix} \vec{V}_c \\ \vec{V}_v \end{bmatrix} \tag{15}$$

where $\vec{Q}_c$ and $\vec{Q}_v$ are vectors of charges on the conductors which are charge nodes and voltage sources respectively. The $\vec{V}_c$ and $\vec{V}_v$ are vectors of the electrostatic potentials on charge nodes and voltage sources respectively. The C_{cc}, C_{cv}, C_{vc}, and C_{vv} matrices contain the capacitive couplings between charge-charge, charge-voltage, and voltage-voltage conductors respectively.

This gives us a rather convenient method for extracting the electrostatic energy of an array of classically interacting quantum dots, given the capacitances of all couplings and all the voltages applied to source/drain leads, and the plunger gates. We simply consider the electrostatic energy equation Eq. (13) as applied to the part of Eq. (15) corresponding to the vector of charge node charges $\vec{Q}_c$. The voltages on the charge nodes can be computed as:

$$\vec{V}_c = C_{cc}^{-1}\left(\vec{Q}_c - C_{cv}\vec{V}_v\right) \tag{16}$$

and thus the total electrostatic energy of just the charge nodes (the quantum dots) as:

$$U_c = \frac{1}{2}\vec{V}_c \cdot C_{cc}\vec{V}_c \tag{17}$$

If we then rewrite the charge on each charge node $Q_j = -N_j|e|$ as some number N_j of fundamental charges e, we find:

$$\vec{Q}_c = -|e|\vec{N} = -|e|\,[N_1, N_2, N_3, \cdots, N_n]^\top \tag{18}$$

where n is the number of charge nodes, i.e. the number of quantum dots in an array. Given a known set of applied voltages $\vec{V}_v$, characterizable inter-dot capacitances which are the elements of C_{cc}, and capacitances between dots and the gates and leads which are the elements of C_{cv}, we can always solve Eq. (17) as a function of the dot occupancies $\{N_j\}$ using Eq. (16) and Eq. (18),

$$U_c(\vec{N}) = \frac{1}{2}C_{cc}^{-1}\left(-|e|\vec{N} - C_{cv}\vec{V}_v\right)^2. \tag{19}$$

We can then find the classical equilibrium states of such a system by - for a fixed set of voltage source potentials and capacitances - finding the values $\{N_j\}$ which maximize the electrostatic energy U_c without exceeding zero. Transition lines which demarcate different equilibrium states as a function of gate voltages yield the well-known classical 'honeycomb' charge stability diagrams. These classical diagrams can be readily obtained by constructing chemical potential objects:

$$\mu_j(\vec{N}, \vec{N}') = U_c(\vec{N}) - U_c(\vec{N}') \tag{20}$$

where $\vec{N}$ and $\vec{N}'$ are two different number configurations. At phase boundaries this quantity should vanish for $\vec{N} \neq \vec{N}'$.

For a double quantum dot system coupled in series to leads to the left L and right R, and to plunger gates $g1$ and $g2$ on each dot 1 and 2 respectively, we have four

voltage sources: $L, R, g1, g2$ with a corresponding voltage source potential vector:

$$\vec{V}_v = [V_L, V_{g1}, V_{g2}, V_R]^\top \tag{21}$$

and two charge nodes $1, 2$ with a corresponding charge node charge vector:

$$\vec{Q}_c = -|e|[N_1, N_2]^\top \tag{22}$$

our capacitance matrices are given by:

$$C_{cv} = C^{[cv]} = -\begin{pmatrix} c_{L,1} & c_{g1,1} & c_{g2,1} & c_{R,1} \\ c_{L,2} & c_{g1,2} & c_{g2,2} & c_{R,2} \end{pmatrix} \tag{23}$$

and

$$C_{cc} = \begin{pmatrix} C_1 & -c_{1,2} \\ -c_{2,1} & C_2 \end{pmatrix} \tag{24}$$

where $c_{\alpha,\beta}$ is the capacitance between node α and node β, and $C_{1(2)} = \sum_\alpha c_{\alpha,1(2)}$ is the sum of all capacitances coupled to dot $1(2)$. In this case:

$$C_1 = c_{L,1} + c_{g1,1} + c_{g2,1} + c_{R,1} \tag{25}$$

$$C_2 = c_{L,2} + c_{g1,2} + c_{g2,2} + c_{R,2} \tag{26}$$

We also note that Eq. (24) is trivially invertible:

$$C_{cc}^{-1} = \frac{1}{C_1 C_2 - c_{1,2} c_{2,1}} \begin{pmatrix} C_2 & c_{2,1} \\ c_{1,2} & C_1 \end{pmatrix} = \begin{pmatrix} \widetilde{C}_2 & \widetilde{c}_{2,1} \\ \widetilde{c}_{1,2} & \widetilde{C}_1 \end{pmatrix} = \widetilde{C}^{[cc]} \tag{27}$$

Substitution of the above equations into Eq. (19), explicitly writing out the matrix multiplications, and collecting terms gives us a tensor representation of the full form for the total classical electrostatic energy of a double dot:

$$U(N_1, N_2) = \frac{1}{2}\left[|e|^2 \widetilde{C}^{[cc]}_{\alpha\beta} N_\alpha N_\beta + |e| \widetilde{C}^{[cc]}_{\alpha\beta} C^{[cv]}_{\beta\gamma} V_\gamma N_\alpha + |e| \widetilde{C}^{[cc]}_{\beta\alpha} C^{[cv]}_{\beta\gamma} V_\gamma N_\alpha + \widetilde{C}^{[cc]}_{\alpha\beta} C^{[cv]}_{\beta\gamma} C^{[cv]}_{\alpha\delta} V_\gamma V_\delta\right] \tag{28}$$

where I have implied Einstein's summation convention. Note that the two terms proportional to $|e|$ are identical if we make the reasonable assumption that $c_{1,2} = c_{2,1} = C_m$. Numerical contraction of the above network can be used to readily find electrostatic energies of a characterized quantum double dot at any occupancy (N_1, N_2). I conclude by noting that this is all straightforwardly generalizable for larger dot arrays, and that the costly matrix inversion C_{cc}^{-1} need only be performed once if the capacitances are independent of applied gate voltages.

D The Lorentzian Tunnelling Curve for Quantum Double-Dots

Evaluation of the steady-state rate equations $\dot{\rho} = 0$ for a double-dot system yields coefficients which can then be used to evaluate the steady-state current at resonance (the conductance peak) through said system. Such a current can then be fitted to experimental data to determine the value of parameters in the theoretical model of the experimental system. I will go through this process in detail for the two-site extended Fermi-Hubbard model, showing that the current through a double-dot at resonance takes a Lorentzian form [3, 4].

Consider a quantum double-dot system occupied by a single species of fermion. The system can either be empty $|\circ\circ\rangle$, left-occupied $|\circ\bullet\rangle$, right-occupied $|\bullet\circ\rangle$, or fully-occupied $|\bullet\bullet\rangle$. The extended Fermi-Hubbard Hamiltonian incorporating a nearest-neighbour interaction V and on-site chemical potentials $\varepsilon_1 = \delta\varepsilon, \varepsilon_2 = -\delta\varepsilon$ then reads as follows:

$$H = -\tau(|\circ\bullet\rangle\langle\bullet\circ| + \text{h.c.}) + V|\bullet\bullet\rangle\langle\bullet\bullet| + \delta\varepsilon|\bullet\circ\rangle\langle\bullet\circ| - \delta\varepsilon|\circ\bullet\rangle\langle\circ\bullet| \tag{29}$$

which can be represented in the above basis as the following matrix:

$$H = \begin{bmatrix} 0 & 0 & 0 & 0 \\ 0 & -\delta\varepsilon & -\tau & 0 \\ 0 & -\tau & \delta\varepsilon & 0 \\ 0 & 0 & 0 & V \end{bmatrix} \tag{30}$$

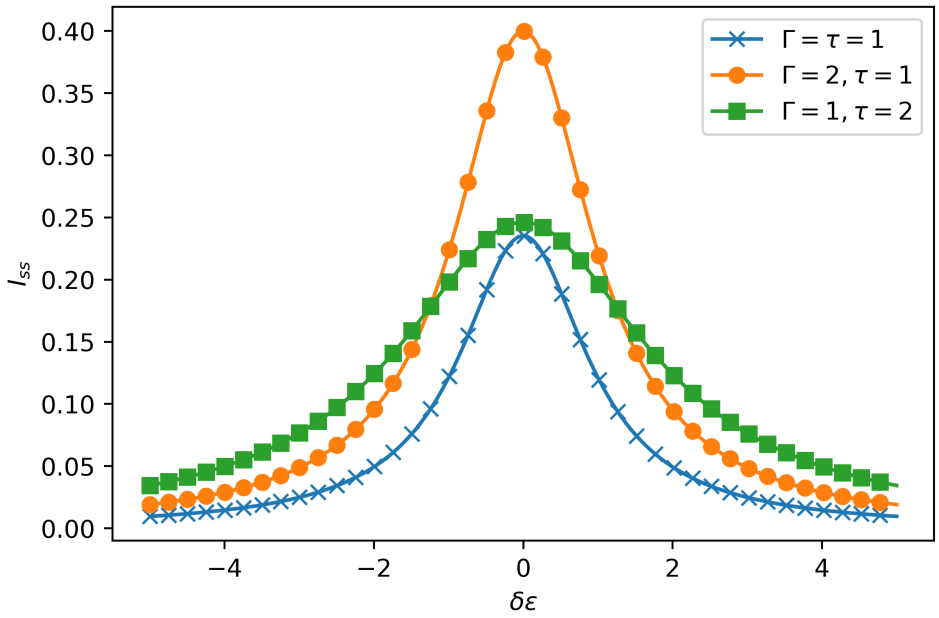

Figure D.1: The Lorenztian function of Eq. (46) for three different parameter regimes. Blue crosses indicate $\Gamma = \tau = 1$, the reference regime. Orange circles indicate an increase just in $\Gamma = 2$, and a dramatic rise in the Lorenztian's height, but not its width. Green squares indicate an increase just in $\tau = 2$, and a broadening of the peak without much extra height. Altogether, this suggests that Γ mostly tunes the height of the Lorenztian, and τ the width; allowing us to easily fit the Lorenztian to any set of data points.

and where I also define two jump operators as follows:

$$L_1 = \frac{1}{\sqrt{2}}\left(|\bullet\circ\rangle\langle\circ\circ| + |\bullet\bullet\rangle\langle\circ\bullet|\right)$$
$$L_2 = \frac{1}{\sqrt{2}}\left(|\circ\circ\rangle\langle\circ\bullet| + |\bullet\circ\rangle\langle\bullet\bullet|\right)$$

with equivalent matrix representations:

$$L_1 = \frac{1}{\sqrt{2}}\begin{bmatrix} 0 & 0 & 0 & 0 \\ 0 & 0 & 0 & 0 \\ 1 & 0 & 0 & 0 \\ 0 & 1 & 0 & 0 \end{bmatrix} \quad L_2 = \frac{1}{\sqrt{2}}\begin{bmatrix} 0 & 1 & 0 & 0 \\ 0 & 0 & 0 & 0 \\ 0 & 0 & 0 & 1 \\ 0 & 0 & 0 & 0 \end{bmatrix} \tag{31}$$

with the identity condition $\sum_j L_j^\dagger L_j = \mathbb{I}$ resolved by some other jump operators

$\{L_{j>2}\}$ which will carry no weighting in the eventual construction of the Lindblad equation. The two jump operators L_1 and L_2 respectively correspond to tunnelling from the left lead into the left dot, and from the right dot to the right lead. The rates of the reverse processes are assumed to be negligible (see schematic **b)** of Fig. 4.2).

By assuming that the tunnelling rates into Γ_1 and out of Γ_2 the double-dot system are equal $\Gamma_1 = \Gamma_2 = \Gamma$ and construct the Lindblad equation as follows:

$$\dot{\rho}(\rho) = i[\rho, H] + \Gamma\left(L_1\rho L_1^\dagger + L_2\rho L_2^\dagger - \frac{1}{2}\left(L_1^\dagger L_1\rho + \rho L_1^\dagger L_1 + L_2^\dagger L_2\rho + \rho L_2^\dagger L_2\right)\right). \tag{32}$$

Explicit evaluation of the steady-state equation $\dot{\rho}(\rho) = 0$ on the general density matrix:

$$\rho = \begin{bmatrix} \rho_{\circ\circ,\circ\circ} & \rho_{\circ\circ,\circ\bullet} & \rho_{\circ\circ,\bullet\circ} & \rho_{\circ\circ,\bullet\bullet} \\ \rho_{\circ\bullet,\circ\circ} & \rho_{\circ\bullet,\circ\bullet} & \rho_{\circ\bullet,\bullet\circ} & \rho_{\circ\bullet,\bullet\bullet} \\ \rho_{\bullet\circ,\circ\circ} & \rho_{\bullet\circ,\circ\bullet} & \rho_{\bullet\circ,\bullet\circ} & \rho_{\bullet\circ,\bullet\bullet} \\ \rho_{\bullet\bullet,\circ\circ} & \rho_{\bullet\bullet,\circ\bullet} & \rho_{\bullet\bullet,\bullet\circ} & \rho_{\bullet\bullet,\bullet\bullet} \end{bmatrix} \tag{33}$$

subject to hermiticity $\rho = \rho^\dagger$ and normalization $\mathrm{Tr}[\rho] = 1$ conditions yields a system

of seventeen linear equations, of which only ten are linearly independent:

$$\dot{\rho}_{\circ\circ,\circ\circ} = 0 = \frac{\Gamma}{2}\rho_{\circ\bullet,\circ\bullet} - \frac{\Gamma}{2}\rho_{\circ\circ,\circ\circ} \tag{34}$$

$$\dot{\rho}_{\circ\circ,\circ\bullet} = 0 = \left(-\frac{3\Gamma}{4} - i\delta\varepsilon\right)\rho_{\circ\circ,\circ\bullet} - i\tau\rho_{\circ\circ,\bullet\circ} \tag{35}$$

$$\dot{\rho}_{\circ\circ,\bullet\circ} = 0 = \left(-\frac{\Gamma}{4} + i\delta\varepsilon\right)\rho_{\circ\circ,\bullet\circ} + \frac{\Gamma}{2}\rho_{\circ\bullet,\bullet\bullet} - i\tau\rho_{\circ\circ,\circ\bullet} \tag{36}$$

$$\dot{\rho}_{\circ\circ,\circ\bullet} = 0 = \left(iV - \frac{\Gamma}{2}\right)\rho_{\circ\circ,\bullet\bullet} \tag{37}$$

$$\dot{\rho}_{\circ\bullet,\circ\bullet} = 0 = -\Gamma\rho_{\circ\bullet,\circ\bullet} - i\tau\rho_{\circ\bullet,\bullet\circ} + i\tau\rho_{\bullet\circ,\circ\bullet} \tag{38}$$

$$\dot{\rho}_{\circ\bullet,\bullet\circ} = 0 = \left(-\frac{\Gamma}{2} + 2i\delta\varepsilon\right)\rho_{\circ\bullet,\bullet\circ} - i\tau\rho_{\circ\bullet,\circ\bullet} + i\tau\rho_{\bullet\circ,\bullet\circ} \tag{39}$$

$$\dot{\rho}_{\circ\bullet,\bullet\bullet} = 0 = \left(-\frac{3\Gamma}{4} + iV + i\delta\varepsilon\right)\rho_{\circ\bullet,\bullet\bullet} + i\tau\rho_{\bullet\circ,\bullet\bullet} \tag{40}$$

$$\dot{\rho}_{\bullet\circ,\bullet\bullet} = 0 = \frac{\Gamma}{2}\rho_{\circ\circ,\circ\bullet} + \left(-\frac{\Gamma}{4} + iV - i\delta\varepsilon\right)\rho_{\bullet\circ,\bullet\bullet} + i\tau\rho_{\circ\bullet,\bullet\bullet} \tag{41}$$

$$\dot{\rho}_{\bullet\bullet,\bullet\bullet} = 0 = \frac{\Gamma}{2}\rho_{\circ\bullet,\circ\bullet} - \frac{\Gamma}{2}\rho_{\bullet\bullet,\bullet\bullet} \tag{42}$$

$$\mathrm{Tr}[\rho] = 1 = \rho_{\circ\circ,\circ\circ} + \rho_{\circ\bullet,\circ\bullet} + \rho_{\bullet\circ,\bullet\circ} + \rho_{\bullet\bullet,\bullet\bullet} \tag{43}$$

from which one can immediately note, through Eq. (37), that $\rho_{\circ\circ,\bullet\bullet} = 0$. The next thing to note is that the equations Eq. (35), Eq. (36), Eq. (40), and Eq. (41)) form an independent subsystem of equations in $\rho_{\circ\circ,\circ\bullet}$, $\rho_{\circ\circ,\bullet\circ}$, $\rho_{\circ\bullet,\bullet\bullet}$, and $\rho_{\bullet\circ,\bullet\bullet}$ which can be mutually solved without invoking the normalization condition Eq. (43). As such, no term can enter this subsystem of equations which is not proportional to one of these elements. This essentially means that this subsystem of equations is eventually reducible to:

$$\rho_{\circ\circ,\bullet\circ} \propto \rho_{\circ\circ,\circ\bullet} \propto \rho_{\circ\bullet,\bullet\bullet} \propto \rho_{\bullet\circ,\bullet\bullet} \propto 0$$

Hence, all of the involved matrix elements (and their hermitian conjugate counterparts) are equal to zero as well.

We can now explicitly solve the remaining equations to determine the non-zero elements of the steady-state density operator. Noting from Eq. (34), Eq. (42), and

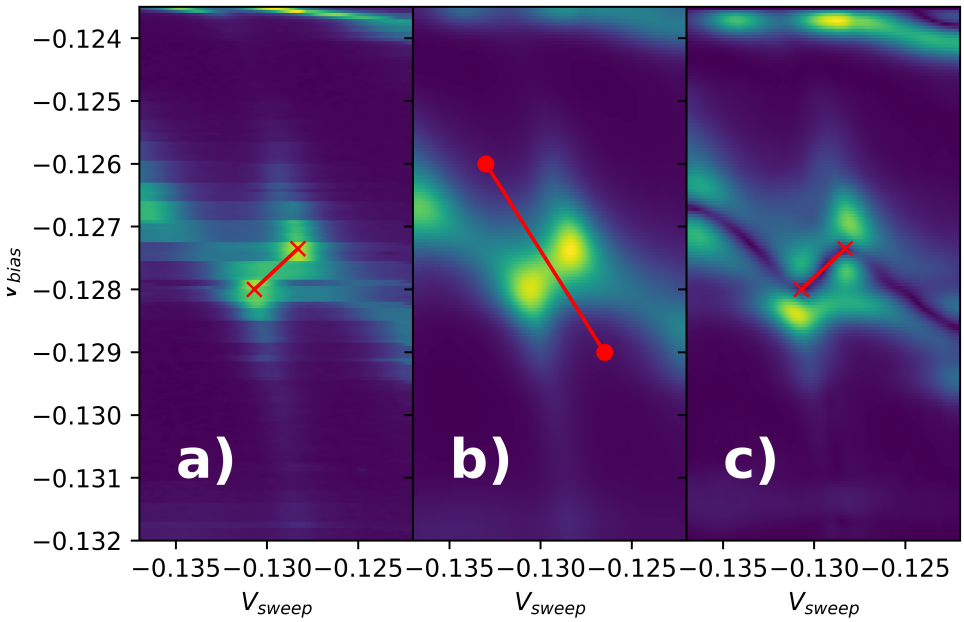

Figure D.2: Differential conductance of a quantum double-dot in a parameter regime close to a pair of triple points. **a)** shows the experimental data which, despite clear triple points, is too noisy to extract anything except a rough estimate of the avoided crossing energy gap $V + 2\tau$ (the length of the red line with crossed ends). **b)** is the same data, but smoothed by a radially symmetric gaussian kernel, from here it is possible to estimate τ by extracting the coulomb peak across the stable regions with same total number (the data points that fall on the red line with circle ends) and fitting it to the Lorenztian of Eq. (46). **c)** Sobel edge detection of the smoothed data, may provide a more accurate value of the avoided crossing energy gap $V + 2\tau$.

Eq. (43) that:

$$\rho_{\circ\circ,\circ\circ} = \rho_{\circ\bullet,\circ\bullet} = \rho_{\bullet\bullet,\bullet\bullet} = \frac{1}{3}(1 - \rho_{\bullet\circ,\bullet\circ}) \tag{44}$$

which we can use, along with the fact that $\rho_{\circ\bullet,\bullet\circ} = \rho^*_{\bullet\circ,\circ\bullet} = \alpha + i\beta$, to solve the two remaining equations Eq. (38) and Eq. (39). Using Eq. (39) we find:

$$\rho_{\bullet\circ,\bullet\circ} = 1 - \frac{6\beta\tau}{\Gamma} \tag{45}$$

and using Eq. (38), by setting the real part to zero separately, we find:

$$\alpha = -\frac{4\delta\varepsilon\beta}{\Gamma}$$

which we then use in conjunction with setting the imaginary part of Eq. (38) to zero to find:

$$\beta = \frac{2\Gamma\tau}{\Gamma^2 + 16\left(\delta\varepsilon^2 + \tau^2\right)}.$$

We can now construct a simple steady-state current $I_{\mathrm{ss}} = -i\tau(\rho_{\bullet\circ,\circ\bullet} - \rho_{\circ\bullet,\bullet\circ}) = 2\beta\tau$ from the forwards and backwards tunnelling rates between the dots, which gives us a steady-state current through the dot of:

$$I_{\mathrm{ss}} = \frac{4\Gamma\tau^2}{\Gamma^2 + 16\left(\delta\varepsilon^2 + \tau^2\right)}. \tag{46}$$

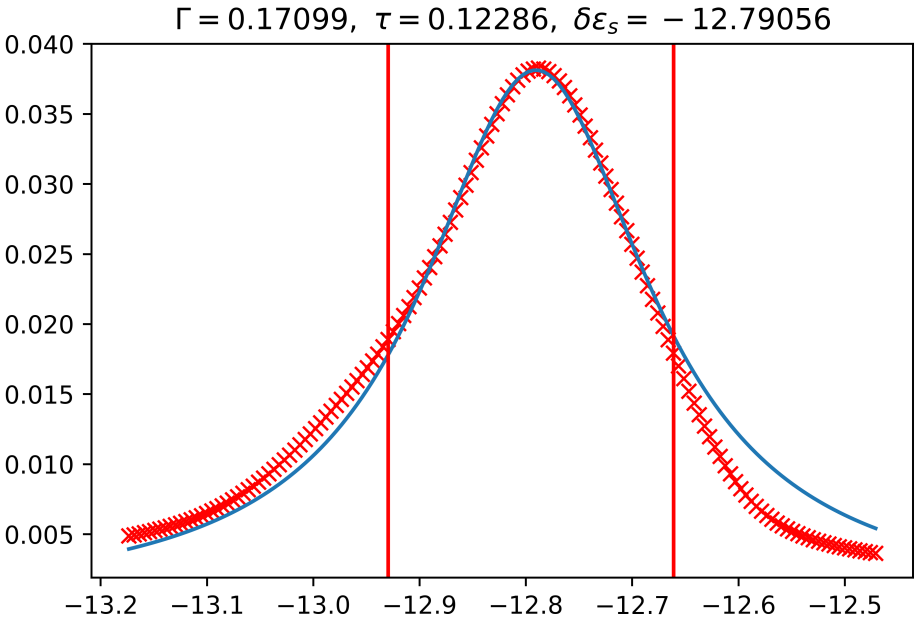

Figure D.3: Optimal fit (blue line) of the Lorenztian function of Eq. (46) to the data points (red crosses) extracted along the red line of Fig. D.2. The x-axis is $V_{\mathrm{sweep}} - V_{\mathrm{bias}}$, which, assuming that cross-talk is negligible at resonance, is the energy difference $\delta\varepsilon$ between the two dots.

The form of the steady-state current I_{ss} is a Lorentzian function of the level gap $\delta\varepsilon$, and its shape for various choices of the parameters Γ and τ are shown in Fig. D.1. This current is conceptually equivalent to the conductance of the system against bias voltage and thus the signature conductance peaks of a double dot should be fitted nicely by an appropriately scaled Lorentzian function. Successful fitting

of such a function, and its comparison to Eq. (46), should allow us to extract values of Γ and τ. In fact, this fitting process is made relatively simple due to the feature, as is clearly shown in Fig. D.1, that τ mostly controls the width of the Lorentzian and Γ mostly controls the peaks' height. Intuitively, this is just a restatement of the well-known fact that larger lead couplings Γ allow more current to flow through the system, and that larger inter-dot couplings τ cause the two dots to hybridize.

E Mapping the Fermi-Hubbard Model to the XXZ Spin Chain

The spinless Fermi-Hubbard model of Eq. (4.2) can be mapped onto an spin-1/2 XXZ model by means of a standard Jordan-Wigner transformation. I start by identifying the two states of each site - occupied or unoccupied - with the two spin-1/2 states - spin-up and spin-down. I then relate the fermionic creation and annihilation operators with the spin-1/2 raising and lowering operators $c_j^\dagger \to S_j^+$ and $c_j \to S_j^-$, and impose the standard fermionic anti-commutators by applying highly non-local Jordan-Wigner string operators such that the final transformation takes the form:

$$c_j^\dagger = \left(\prod_{k<j} \sigma_j^z\right) S_j^+ \tag{47}$$

$$c_j = \left(\prod_{k<j} \sigma_j^z\right) S_j^- \tag{48}$$

where the σ_j^z is the standard Pauli Z operator. In practice, due to the fact that $(\sigma_j^z)^2 = 1$, many of these Jordan-Wigner strings cancel and one can often manipulate the final Hamiltonian into a local form. Substituting Eq. (47) and Eq. (48) into the Hamiltonian Eq. (4.2), and simplifying the Jordan-Wigner strings, yields the model

$$\begin{aligned} H = \tau \sum_j^{L-1} \left(S_j^+ \sigma_j^z S_{j+1}^- + \text{h.c.}\right) \\ + V \sum_j^{L-1} S_j^+ S_j^- S_{j+1}^+ S_{j+1}^- + \sum_j^L h_j S_j^+ S_j^- \end{aligned}$$

which we can simplify further by noting that $S_j^+ S_j^- = S_j^z + 1/2$, that $S_j^+ \sigma_j^z = -S_j^+$, and by invoking the definition of $S_j^\pm = S_j^x \pm i S_j^y$; where S_j^α are the standard spin-1/2 operators. Under these simplifications, the model now takes the form

$$\begin{aligned} H = -2\tau \sum_j^{L-1} \left(S_j^x S_{j+1}^x + S_j^y S_{j+1}^y \right) \\ + V \sum_j^{L-1} \left(S_j^z S_{j+1}^z + S_j^z + S_{j+1}^z + 1 \right) \\ + \sum_j^L h_j \left(S_j^z + 1/2 \right) \end{aligned}$$

wherein the negative overall phase of the tunnelling term proportional to t is irrelevant to the physics of the system: we can e.g. simply relabel every other site such that, for odd j, $S_j^{x/y} \to -S_j^{x/y}$, and S_j^z is left unchanged. I eliminate all constant terms which do not contribute to the physics of the system, and note that - since the Hamiltonian conserved total particle number, its Jordan-Wignerization equivalently conserves total spin. Thus we can neglect all terms proportional to $\sum_j^L S_j^z$, which appear in the sum over single-site operators proportional to V such that $\sum_j^{L-1} S_j^z + S_{j+1}^z = -S_1^z - S_L^z + \sum_j^L S_j^z$. Collecting terms, and performing these substitutions gives us an extended XXZ Hamiltonian

$$\begin{aligned} H = 2\tau \sum_j^{L-1} \left(S_j^x S_{j+1}^x + S_j^y S_{j+1}^y + \frac{V}{2t} S_j^z S_{j+1}^z \right) \\ - V \left(S_1^z + S_L^z \right) + \sum_j^L h_j S_j^z \end{aligned}$$

which exhibits an XXZ transition at $V = 2\tau$, makes clear the importance of edge effects in small systems by explicit inclusion of the dangling S_1^z and S_L^z operators.

F Colophon

The numerical tools used throughout this thesis are modifications and extensions of several important python packages. First and foremost is quimb, a package for simulating many-body quantum systems and managing tensor networks [5]. Other

crucial packages include tenpy, another package for managing tensor networks [6], and pyfssa, a package for carrying out data collapse and finite size scaling analyses [7, 8]. This document was set using LaTeXand BibTeX, and composed with the Overleaf online text editor.

References

[1] Roger Penrose. Applications of negative dimensional tensors. *Combinatorial mathematics and its applications*, 1:221–244, 1971.

[2] R. Hanson, L. P. Kouwenhoven, J. R. Petta, S. Tarucha, and L. M. K. Vandersypen. Spins in few-electron quantum dots. *Rev. Mod. Phys.*, 79:1217–1265, Oct 2007.

[3] W. G. van der Wiel, S. De Franceschi, J. M. Elzerman, T. Fujisawa, S. Tarucha, and L. P. Kouwenhoven. Electron transport through double quantum dots. *Rev. Mod. Phys.*, 75:1–22, Dec 2002.

[4] NC Van der Vaart, SF Godijn, Yu V Nazarov, CJPM Harmans, JE Mooij, LW Molenkamp, and CT Foxon. Resonant tunneling through two discrete energy states. *Physical review letters*, 74(23):4702, 1995.

[5] Johnnie Gray. quimb: a python library for quantum information and many-body calculations. *Journal of Open Source Software*, 3(29):819, 2018.

[6] Johannes Hauschild and Frank Pollmann. Efficient numerical simulations with Tensor Networks: Tensor Network Python (TeNPy). *SciPost Phys. Lect. Notes*, page 5, 2018. Code available from `https://github.com/tenpy/tenpy`.

[7] Andreas Sorge. pyfssa: a scientific python package for finite-size scaling analysis at phase transitions. 2015.

[8] Oliver Melchert. autoscale.py - a program for automatic finite-size scaling analyses: A user's guide. 2009.